Contents

Chapter 1

Introduction

1.1 Surfaces

In observing the world around us, we predominantly look at the surface of objects. They form the boundaries between the gaseous world surrounding us and that of the ordered world of solids and liquids. The processes occurring at surfaces are influenced by both. Gases can adsorb and perhaps react on surfaces and change their chemical composition. A well known example of this is the oxidation of iron, better known as rust. On the other hand there is the three-dimensional periodicity of the solid, which is reflected in the two-dimensional structure at the surface. As the surface atoms do not feel the presence of neighboring atoms at one side, the surface may be inwardly or outwardly relaxed or reconstructed. These effects may have dramatic influences on the electronic properties and geometrical structure of the outermost layers. These layers determine many of the chemical and physical properties of the material, such as reactivity and electron emissivity. The intriguing fundamental aspects of surfaces and their many technological applications make them interesting objects for study. The many aspects which are studied include, amongst others, geometric, electronic and dynamical properties of surfaces. In addition, their interactions with photons, atoms, molecules, ions and clusters are explored.

The study of the interaction of atoms and molecules with solid surfaces has been stimulated by the desire to understand and control chemical reactions in heterogeneous catalysis and semiconductor processing [1]. Many different experimental approaches, from Auger electron spectroscopy (AES) and low-energy electron diffraction (LEED) to scanning tunnel microscopy (STM) and high resolution electron energy loss spectroscopy (HREELS) have been applied to explore the binding of atoms and molecules at surfaces [2,3]. Apart from these "static" techniques, which characterize the structure and binding sites at surfaces, additional techniques have been developed, which explore the dynamics and mechanisms of particle/surface interactions, such as molecular beam scattering and low-energy ion beam scattering.

In addition to being important probes for the investigation of (parts of) chemical reactions at surfaces, beam scattering experiments also serve as excellent tools for the investigation of the structure and composition of surfaces and interfaces. A number of important and widely used experimental techniques are based on the scattering of ions from surfaces, e.g. secondary ion mass spectrometry (SIMS), low-energy ion scattering (LEIS),

medium-energy ion scattering (MEIS) and Rutherford backscattering (RBS). Together with the development of these experimental techniques, new applications related to the study of particle/surface interactions emerged. These include semiconductor processing for the fabrication of microelectronic devices which require doping of semiconductor material by implantation with sufficiently energetic ions. For the preparation of these materials, reactive ions beams, molecular beams and plasma etching may be used for surface modifications and/or thin-film deposition [4].

Another area of research requiring the details of mechanisms in ion/surface interactions, is fusion research and technology. The knowledge of processes such as neutralization, the formation of positive and negative ions, and the penetration into the solid is important for a basic understanding of plasma/wall interactions, divertor physics and negative ions sources. In addition, particle/surface interactions are believed to be important in atmospheric chemistry and to processes occurring when space-craft are in low-earth-orbit colliding with particles in the upper atmosphere [5].

Recently, the mechanisms governing the dissociation of large polyatomic ions scattered from surfaces have been explored [6]. The interest is stimulated by the challenge of developing a mass spectrometric technique, which helps resolve structures of large (bio)molecules. Here, the difficult step is the generation of structurally relevant fragment ions, which are subsequently analyzed by mass spectrometric tools. Until recently, collisional activation of molecular ions with gas phase target atoms has been used. An alternative approach is to collide the polyatomic ions with a surface, so called surface-induced dissociation (SID) [6]. Here, as opposed to gas phase scattering, fragmentation in SID gives a better defined energy transfer in the collision and, hence, more structural information concerning the parent ions. However, efficient neutralization occurs when ions are scattered from metal surfaces, which complicates the detection of the scattered ion signal. In addition, many of the basic phenomena related to polyatomic ion/surface collisions are still not understood.

1.2   Survey of particle-surface interactions

With help from molecular beam and ion beam technology a vast range of incident particle energies can be attained, enabling the experimentalist to study the rich physical and chemical phenomena related to particle/surface interaction at various experimental conditions. In Fig. 1.1 a selected number of physical and chemical processes are depicted which can occur over the incident energy range from 10 meV to 10 MeV (upper abscissa); an energy range spanning 9 orders of magnitude. On the lower abscissa, the equivalent translational temperatures are depicted and the usual terminology for the incident energy ranges is displayed. With molecular beam machines incident energies roughly between 20 meV and 3 eV can be attained. This technique is based on gas expansion through a (heated) nozzle. For special conditions, the incident energy range can be extended to 10 eV, which requires heavy particles to be seeded in a jet of light particles [7]. For very low incident energies (20-50 meV), and for light particles such as helium and hydrogen, quantum mechanical effects such as diffraction and single phonon exchange play a role in the surface interaction. For higher incident energies and/or heavier particles, the de Broglie wavelength of the incident particles becomes significantly smaller than the typical interatomic distances of the
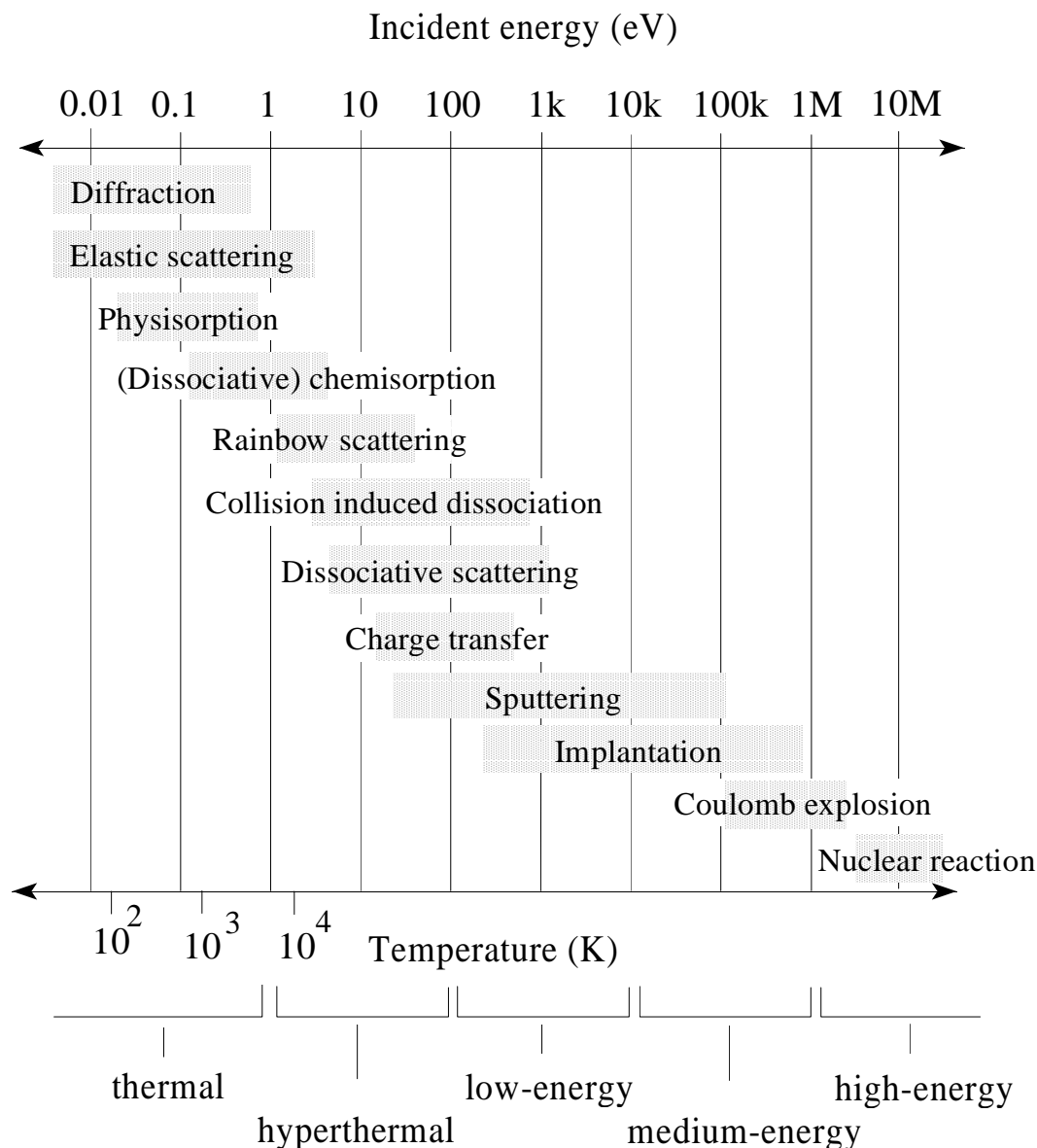
Incident energy (eV)

Figure 1.1 *A selected number of particle/surface processes depicted over the incident energy at which they are usually studied.*

crystal lattice (5 Å) and the scattering process can be treated by classical mechanics, i.e. hard cube models and hard sphere models. For these conditions a number of processes can occur: the incident molecule can either elastically scatter from the potential barrier walls or get trapped in the potential wells leading to physisorption (Van der Waals attraction), chemisorption or dissociative chemisorption [8]. Once adsorbed on the surface, chemical reactions can occur and/or desorption of (product) particles. The surface can be considered flat or slightly corrugated. The interaction is dominated by the attractive potential and the potential barriers leading to adsorption. However, the repulsive parts of potentials also play a role.

For incident energies above 10 eV, the repulsive potential (Pauli repulsion) starts to dominate the interaction and the surface can be considered corrugated. These incident energies can be achieved by ion beam technology, although it is difficult to get sufficiently high intensities (> 1 nA/cm^2) because at very low incident energies (< 100 eV) the space charge effect causes a reduction of the beam intensities. In addition, problems with extensive neutralization of scattered low-energy ions play a role. In the incident energy range 10-to 500-eV, rainbow scattering is important [9]. Moreover, impulsive excitation of scattered molecular ions occurs, leading to collision-induced dissociation (CID) [6]. For incident molecular ions at metal surfaces, charge transfer processes dominate the interaction, leading to neutralization, negative ion formation and dissociative scattering. These processes occur also at higher incident energies, ranging from 100 eV to 10 keV; the so-called low-energy regime [10]. The surface appears more open to the incident particles and penetration of the surface occurs. The energetic particles can modify the surface due to sputtering, etching reactions and/or deposition. The penetration into the solid is employed in surface structure analysis techniques such as LEIS, with which the structure of the topmost layer is studied [11]. The efficient neutralization of incoming ions which penetrate the solid makes this technique very surface sensitive.

At medium-energies between 10 keV and 1 MeV, most particles enter the crystal lattice; the particles can deeply penetrate into the solid and be implanted. Ion energies above 0.5 MeV can be reached with the use of a Van der Graaff accelerator. This is used for doping semiconductor materials and depth profiling of the solid/interface region [12]. Above hundreds of keV, the role of screening on the scattering potential is very weak and the interaction can be described by a Coulombic interaction (Rutherford scattering) between the incident ion and the crystal nuclei. For molecular ions incident at energies in the upper-keV and MeV range, Coulomb explosions are important in the interaction [13]. At these high incident energies, a diatomic molecule is effectively stripped of a number of electrons upon entering the solid. The molecules dissociate, and, thereafter, the fragments repel each other by their mutual Coulomb force.

At the very high energy side (> 1MeV) nuclear fusion (and fission) reactions can occur [14]. This has an application in the detection of H atoms chemisorbed and/or embedded under a surface, which are very hard to detect with conventional methods. A 6.385 MeV ^{15}N$^+$ beam is directed at a surface initiating the resonance nuclear reaction ^{1}H(^{15}N$, \alpha\gamma$)^{12}C with the chemisorbed H atoms. This fusion reaction has a resonance width which is very small; about 1.8 keV at collisions energies of 6.385 MeV. When the ^{15}N$^+$ have penetrated more than one atomic layer, the ions have suffered energies losses equivalent to the resonance width, assuring either surface sensitive detection or appreciable depth resolution.

1.3 Electron transfer at surfaces

In the experiments presented in this thesis, the incident energies of the ions range from 10 eV to 1 keV; an energy regime in which electron transfer processes dominate the interaction. In the sections that follow, we briefly summarize the important charge transfer processes of atomic and diatomic ions incident on metal surfaces.

In Fig. 1.2 two schematic potential energy diagrams are depicted, showing the relevant
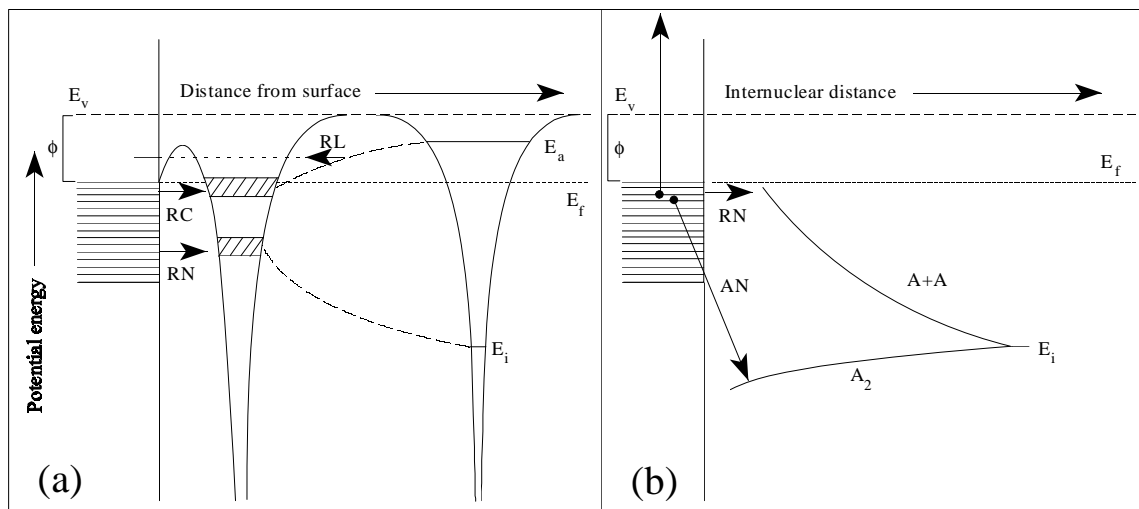
Figure 1.2 *One electron energy diagram of an ion and atom (a) and molecule (b) in front of a metal surface. E_f is the Fermi energy of the solid, the difference to the vacuum energy E_v is the work function ϕ. The ion has the ionization level E_i and the neutral atom or molecule has the affinity level E_a. The possible electron transfer processes are explained in the text.*

electron transfer processes of an atomic and/or diatomic ion near a metal surface. On the left hand side of both figures is the metal conduction band with work function ϕ. E_v and E_f are the vacuum level and Fermi level of the solid, respectively. In Fig. 1.2(a) the ionization potential E_i of the projectile is depicted. E_v gives the energy of a neutral atom or molecule. In close approach to the surface, E_i shifts up due to the image charge interaction and a broadening of this level occurs due to the overlap of the metallic and the atomic wave functions. In Fig. 1.2(a) this level is schematically depicted as a function of distance to the surface. The overlap of the wave functions of the metal and the particle allows for resonant neutralization (RN) to occur. Likewise, when a neutral particle approaches the surface the affinity level E_a shifts down due to the image charge attraction, and broadens. Resonant electron capture (RC) can occur if the atomic and metal wave functions overlap and, subsequently, negative ions are formed. On the exiting trajectories, depopulation of this level occurs, which lead to resonant loss (RL) processes.

In Fig. 1.2(b), the molecular potential curves (A_2, A+A) as a function of internuclear distance are depicted, where E_v gives the energy of a molecular ion A_2^+. The positive molecular ion can be neutralized into the ground state of the molecule by Auger neutralization (AN); the excess energy is carried away by another electron which is ejected into the vacuum. The ion can also be neutralized into an excited state, which can either be a bonding state or a non-bonding state, of which the latter gives rise to dissociation. Dissociation of diatomic ions through electron attachment is feasible at incident translational energies below the ground state dissociation energies of the neutral molecules. This is because dissociation occurs through electronically excited neutral states which are more weakly bound than the grounds state of the neutral species [15].

Dissociation can also occur via the temporary formation of a negatively charged molecular ion, which is referred to as harpooning [16,17]. During the time that the negative

molecular ion exists, i.e. for the time duration between electron hops, the intra-molecular vibrational coordinate will be displaced. Subsequently, backdonation of the electron occurs and the molecule will emerge as a vibrationally excited neutral with some of the excited states lying within the dissociative continuum.

1.4   Collision-induced dissociation

Not only can charge transfer processes promote dissociation of molecular ions incident at surfaces, the impulsive collision with the surface atoms can also cause the breaking of the molecular bond, in the event that the translational energy of the incident particle is sufficiently high. In the collision-induced dissociation mechanism, translational energy is converted into rovibrational energy of the scattered particle. This CID mechanism is not as efficient as dissociation through electron attachment as discussed in the previous section; for CID to occur, incident translational energies exceeding the bond energy by a factor 4 or 5 are needed to break the molecular bond of diatomics which are scattered from well defined single crystal surfaces.

Many studies have been performed in order to elucidate the mechanisms governing the CID process in the cases of diatomic ions and molecules scattered from metal surfaces. These studies give detailed information on, among others, the role of incident translational energy, vibrational energy and the orientation of the molecule's internuclear axis. Conclusions from those studies are briefly summarized below. Note that we schematically discuss a number of limiting cases, in order to set the stage. In reality, combinations of parameters are important for determining the outcome of the scattering event, which again can be combinations of outcomes.

The decisive factor determining the break-up of the molecule is its incident translational energy E_i. Closely related is the angle of incidence; at very grazing angles of incidence the normal component, $(E_n = E_i \cos^2 \theta_i)$, of the incident translational energy has to be considered (E_n scaling) [15].

A parameter relevant for the excitation mechanism is the surface corrugation. A number of studies have shown that, when scattering from a highly corrugated surface (schematically shown in Fig. 1.3(a)), the dissociative scattering event is governed by a rotationally mediated mechanism [18–20]. If the centrifugal forces are larger than the chemical bond strength, dissociation occurs due to centrifugal stretching of the molecular bond. In this mechanism, the impact parameter b (Fig. 1.3(a)) plays an important role [21]. Rotational excitation was first invoked to explain dissociative scattering from a "flat" surface. When scattering occurs off a "flat" surface, vibrational excitation dominates the interaction as is schematically depicted in Fig. 1.3(b). This mechanism assumes the transfer of the incident translational energy into vibrational energy by compression of the molecular bond (T-V transfer). This is highly dependent on the initial vibrational phase of the molecule; molecules which are initially compressed upon collisions are most likely to dissociate [22]. Clearly, the T-V transfer will be highly dependent upon the individual masses of nuclei of the molecule and the surface atoms (Fig. 1.3(c)), analogous to what is found in gas phase scattering [23]. In addition, the alignment of the molecular axis relative to the surface normal when the molecule strikes the surface has a large influence on the outcome of the
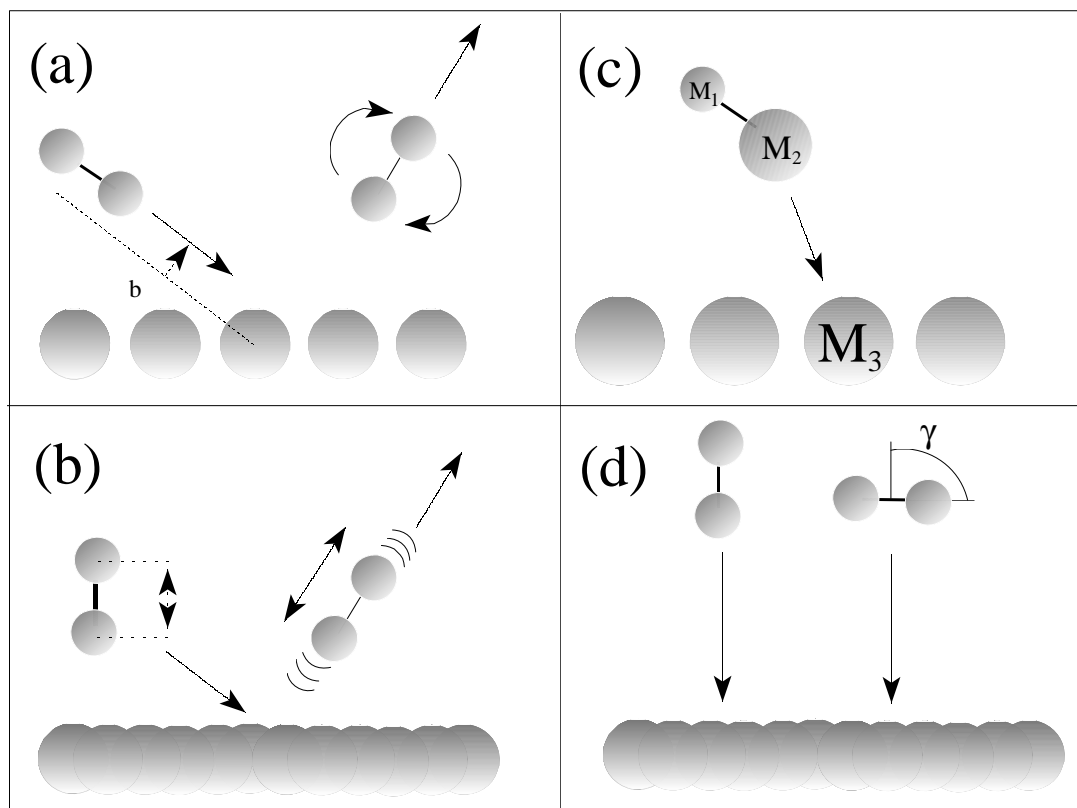
Figure 1.3 *Schematic illustration of several important processes and parameters in collision-induced dissociation: (a) rotationally excitation from corrugated surface, (b) vibrational excitation from a "flat" surface, (c) the mass-effect and (d) the alignment of the molecular axis relative to the surface normal.*

scattering event [18,21,24]. Molecules which have their internuclear axis aligned with the surface normal prior to the collision, experience the greatest degree of bond compression upon impact, and hence, the largest T-V transfer (Fig. 1.3(d)).

In contrast to the numerous diatomic ion/surface studies which have been carried out, data concerning polyatomic ion/surface scattering are limited. In this thesis, we explore the mechanisms that underly dissociation of polyatomic ions "large" compared to diatomic ions. In a systematic way, several experimental parameters are varied: the incident translational energy of the ions, the surface corrugation, the "type" of surface: metal (conductor) and liquid (non-conductor). Throughout this thesis, energy and angular analysis is performed on the scattered product ions which enables us to study the influence of the impact parameter on the CID process directly. In the final chapter, a comparison is made between the scattering of a di-,tri-and tetra atomic ion from a liquid surface; indirectly, the problem of the approach geometry on reactivity is addressed.

1.5   Liquid surfaces

Traditionally, the interaction between polyatomic ions and metal surfaces is studied. However, recently more attention has been focused on the scattering from non-metallic surfaces such as oxides [25,26], self-assembled monolayers (SAMs) [27–29] and thin films of an inert polymer oil such as a perfluoropolyether (PFPE) [30,31]. The interest is stimulated by the desire to reduce the efficient neutralization which occurs at metal surfaces. This reduction is needed if a mass spectrometric technique is to be developed which is based on surface-induced dissociation (SID) [6,30]. The liquid PFPE surface appears to be a promising candidate; the neutralization yields are significantly lower compared to metal surfaces and a liquid has the additional advantage that the surface layer is renewed because of the high mobility of the liquid molecules [30]. However, many of the fundamental processes occurring in (poly)atomic ion/liquid surface scattering are not fully understood or even explored; among these are the energy transfer mechanisms to the surface and to internal energy of the scattered ions. These impulsive energy transfer processes are studied in detail in Chapter 4 and 6 of this thesis.

1.6   Overview of this thesis

This thesis can be divided into two parts. In the first part (Chapter 2), experiments and simulations of hydrogen ions scattered from metal surfaces are described. It presents a comparative study on negative ion formation in the scattering of a proton beam off both a clean and a barium covered Ag(111) surface. In this chapter, some of the important scattering processes occurring at solid surfaces are introduced. These are illustrated by classical trajectory calculations which are performed on the H/Ag(111)-system.

In the second part of this thesis (Chapter 3,4 and 6), experiments concerning polyatomic fluorocarbon ions scattered from metal surfaces (Chapter 3) and a liquid surface (Chapter 4 and 6) are presented. In these chapters, the scattering dynamics and dissociation of polyatomic ions is discussed and the mechanisms behind these processes are explored. Chapter 5 describes the design and performance of a new low-energy ion beamline. This beamline is built because of the desire to vary the incident translational energy of the ions between roughly 10 and 1000 eV. With the former beamline, only particles with energies above 100 eV could be obtained. In addition, the new beamline is capable of producing beams of ions with a high mass resolution and a low energy spread.

The different ion/surface interactions studied in this thesis are summarized in Table 1.1. The various aspects of these processes are indicated and references are made to the chapters where these can be found.

Table 1.1 *Summary of the ion/surface scattering processes studied in this thesis. References are made to the chapters where these can be found.*

Physical process	Aspect	Chapter
Neutralization	(CF_3^+) (H^+)	3,2
Electronic dissociation	(CF_3^+)	3
Negative ion formation	Low/high work function	2,3
	Polyatomic ions	3
	Atomic	2,4
Collision-induced dissociation	Incident translational energy	3,4,6
	Surface corrugation	3
	Metals (conductor)	3
	Liquid (non-conductor)	4,6
	Approach geometry	6
	Impact parameter	3,4,6
Scattering dynamics	Surface rainbows	3,4,5
	Trajectory analysis	2
	Effective surface mass	4,6
	Binary collision model	2,3,4,6
Penetration	(Electronic) stopping	2
	Trajectory analysis	2
Surface structure	Atomic geometry	2
	End group determination	4,6

Chapter 2

Low-energy hydrogen ion scattering from metal surfaces: Trajectory analysis and negative ion formation

Abstract

A comparative study on negative ion formation in the scattering of a proton beam from both a clean and a barium covered Ag(111) surface is presented. The angular and energy dependence of the backscattered negative hydrogen ions as a function of incoming and azimuthal angles has been determined for a beam energy of 750 eV. The backscattered negative particles emerge from the surface as well as from deeper layers of the crystal. The angular dependence of the outgoing particles shows a very rich structure which is explained by shadowing and blocking of the incoming and outgoing particles. In addition, the angular dependence of the outgoing neutral particles is determined. The essential features appear the same, but distinct differences can be observed. These are due to changes in the probability for negative ion formation as a function of outgoing angle. The energy distributions of the outgoing particles suggest a large penetration depth along the crystal channels. We have performed classical trajectory calculations which simulate the angular distributions of the backscattered particles very well. These calculations also show considerable penetration of particles into the bulk of the crystal and complicated zig-zag trajectories through the bulk before leaving the crystal. The (electronic) stopping inside the Ag solid is at least one or two orders of magnitude smaller (< 0.3 eV/$\mathring{A}$ at $E = 700$ eV) than the values found in literature. Comparing the Ag(111) data and the data of Ag(111) covered by one monolayer barium, we conclude that the barium atoms occupy lattice positions of the crystal. The overlayer must contain vacancies to accommodate the large size mis-match between the barium atoms and those of the substrate.

2.1 Introduction

The study of the interaction of low-energy ions with surfaces has received considerable attention from a multitude of disciplines within chemistry and physics [10,11]. In particular the charge exchange mechanisms governing the interaction have been studied in great detail because of their technological relevance in catalysis and surface processing [32,33]. A

fundamental understanding of ion/surface collisions is also important for analytical techniques that involve the detection of backscattered low-energy ions leaving the surface, such as low-energy ion scattering (LEIS) and secondary ion mass spectrometry (SIMS), where it is important to know the ionization probabilities in order to draw conclusions [11,34].

Another important area of research involving ion/surface collisions is fusion research and technology [35]. Here, a detailed knowledge of the neutralization and subsequent positive and negative ion formation in ion/surface collisions is important for a basic understanding of plasma/wall interactions, divertor physics and negative ion sources [36]. Negative ion formation has received considerable attention; negative hydrogen ion yields up to 30% have been found for positive ions scattered off low work function surfaces, such as Cs or Ba covered metal surfaces [32]. The study of penetration into the crystal lattice is also important for a better understanding of plasma/wall interactions and divertor physics [37–40].

The mechanisms governing negative ion formation in the scattering of protons at low work function surfaces have received considerable attention from the surface science community in recent years, experimentally as well as theoretically [32,35,41–43]. In those studies, emphasis was primarily put on determining the yields of negative ions and the charge exchange mechanisms. The differential conversion efficiency η has been determined for certain scattering conditions, where $\eta = I(H^-)/[I(H^-) + I(H^0)]$ and I the intensity for ions and neutrals measured with the same detection efficiency. To our knowledge, the scattering dynamics has not been studied in great detail for hydrogen ions with incident energies ranging from 100-eV to 1 keV, scattered from metal surfaces at incoming angles where considerable penetration is important. However, trajectory calculations have been carried out for hydrogen atoms scattered off single-crystal surfaces at glancing angles, where no penetration is observed and the particles are scattered in the specular direction [44]. Some studies have been performed involving penetration of hydrogen into the solid, although no trajectory analysis was performed in those investigations [45,46].

In the case of scattering a beam of protons from a metal surface, the neutralization is assumed to occur along the incoming trajectory; before the positive ion collides with the surface it is neutralized into an excited state via resonant neutralization (RN) and subsequently Auger de-excited (AD) into the ground state. Effectively, neutral hydrogen atoms are scattered from the surface. Sufficiently close to the surface the affinity level, located at 0.7 eV below the vacuum level, shifts down due to the image force attraction and broadens because of the overlap of atomic and metallic wave functions, which allows negative ions to be formed in a resonant process. On the exiting trajectory, depopulation of the affinity levels occurs.

In recent years, the interest in negative ion formation from non-metallic surfaces has increased [47,48]. In those studies, it was found that negative ion yields up to 70%, and even 100%, could be obtained for O and F scattering off alkali halide surfaces under certain conditions; i.e. highly energetic beams (> 10 keV) incident at glancing angles. Also high yields of negative hydrogen ions have been found for low-energy ion scattering (< 5 keV) from oxide surfaces [49]. The results from the oxide surfaces were interpreted in much the same way as scattering off the alkali halide surfaces; the surface is considered to be ionic and the hole that is created in the formation of the negative ion is localized and does not travel along with the negative ion. Recently, we observed large negative hydrogen ion yields

in H^+ scattering from a graphite surface [36].

Detailed trajectory analyses have been carried out for noble gas ions and alkali ions scattered off metal surfaces in the incident energy range between 10 eV and 1 keV [9,11,33]. The scattering dynamics of alkali ions from metal surfaces has been studied in great detail, both experimentally and with the help of classical trajectory calculations [33,50,51]. For those systems it was found that scattering occurs primarily with the outermost layer of the solid. Charge transfer dynamics in these systems has also been studied in detail [32,33]. By correlating their experimental results and calculations, Cooper and coworkers found evidence for a trajectory dependent charge transfer event [52].

Recently, a trajectory effect in negative hydrogen ion formation has been suggested in model calculations of hydrogen particles scattered from a stepped metal surface. The fraction of negative ions turned out to be highly dependent on the step density at the surface, and whether the steps were going up or down [53]. Those calculations model previously obtained experimental observations very well [54].

Clearly, a careful analysis of the trajectories of scattered ions is important for a detailed understanding of ion-surface interactions; it is crucial for unraveling local effects and trajectory effects in neutralization and negative ion formation [52,55]. In this chapter we discuss the trajectories of scattered negatively charged and neutral hydrogen atoms from incoming positive ions with energies around 700-eV on single-crystal metal surfaces. The interaction of the incident hydrogen particles and the crystal atoms is governed by a sequence of binary collisions in this incident energy range [11,55]. The collision kinematics and dynamics allows for elemental analysis and structure studies of the outermost layer of a solid. The experimental results are analyzed with the help of computer simulations, and explained by shadowing and blocking effects. Noble gas ions such as He and Ne are used in scattering experiments because of their high neutralization efficiencies if scattered from layers deeper than the topmost layer. Backscattered neutrals remain hidden from the detector. Hydrogen particles, however, have a much smaller shadow cone, which makes them more suited to use in the low incident energy regime for structure analysis. This was already recognized by MacDonald and coworkers in the scattering and detection of positive hydrogen ions [45,56]. However, in the present study we use an alternative approach by probing scattered negative hydrogen ions, which give the opportunity of obtaining structural information to several layers depth. To our knowledge, the present study is the first structure analysis using the detection of scattered negatively charged hydrogen ions.

The scattering dynamics of atoms and ions reflected from single crystal surfaces has been studied over a wide range of incident energies, from the thermal and hyperthermal energy regime (meV and eV range), where the surface can be considered a hard wall [7], to the keV range, where the binary interaction between the incident particles and the surface atoms becomes important and penetration into the solid occurs [11]. In the intermediate energy range from 10-to 100-eV rainbow scattering is important [9]. The surface is highly corrugated but no penetration into the solid occurs. At very high incoming energies (> 100 keV), the interaction between the nuclei of the particles becomes important, and the interaction is essentially point-like [12].

In an earlier paper, we studied negative hydrogen ion formation in the scattering of a beam of protons from two monolayers of barium deposited onto Ag(111) [57]. We found negative ion yields of about 20% for outgoing angles smaller than 60°; the negative ion
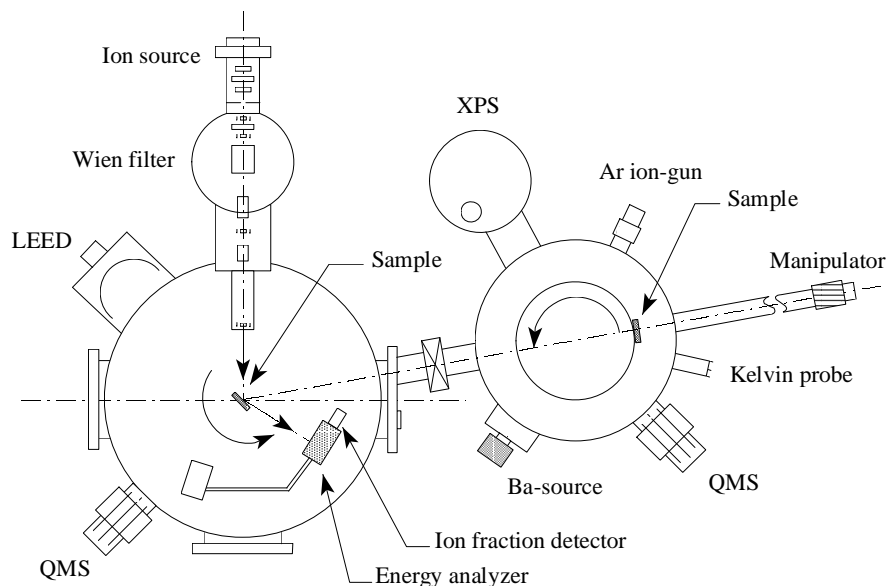
Figure 2.1 *The ion scattering chamber (left) and sample preparation chamber (right). The differentially pumped electron impact source is mounted on the scattering chamber.*

fraction decreased for larger outgoing angles. All angles were defined with respect to the surface normal. A simple model, describing resonant charge transfer calculated by the non-perturbative coupled angular modes (CAM) method, which also takes the parallel velocity effect into account [57,58], described the measured negative ion fractions very well. Structure was observed in the angular distributions of the negative ions, which was assigned to scattering from second layer atoms of the crystal.

In this chapter, we present a detailed experimental study and classical trajectory calculations of the scattering of hydrogen particles from a clean Ag(111) surface and one covered with a monolayer of barium. The angular distributions of the backscattered negative ions reveal a peak structure which suggests that considerable penetration into the solid occurs in the incident energy regime around 700-eV. With the help of classical trajectory calculations we assign the peaks to classes of trajectories. The simulated angular spectra are in good agreement with the measured spectra. Further, we comment on the energy losses the ions have suffered on both the clean and barium covered Ag(111) surfaces, and also on the final charge state of the scattered particles.

2.2   Experimental

2.2.1   Apparatus

The experimental set-up is depicted in Fig. 2.1. Briefly, it consists of two UHV chambers. In one (base pressure of 4×10^{-11} mbar), the crystal can be cleaned and characterized by X-ray photoelectron spectroscopy (XPS), thermal desorption spectroscopy (TDS) and work
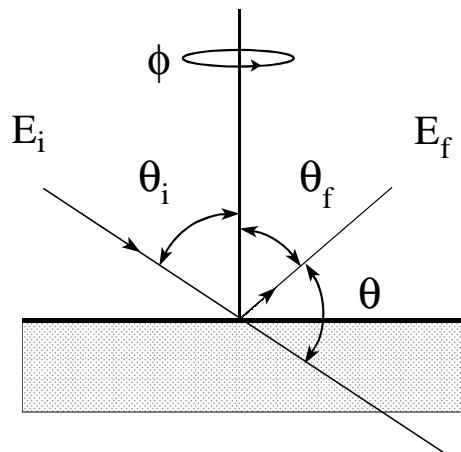
**Figure 2.2** *Definition of the scattering geometry: the incoming angle θ_i, the outgoing angle θ_f and azimuthal angle ϕ.*

function measurements. The work function measurements are done with a Kelvin probe. The crystal can be transferred under UHV to a two-axis goniometer in the second chamber (base pressure of 1×10^{-10} mbar). This goniometer allows rotation of the target around an axis parallel to the surface, to change the incoming angle θ_i (which is measured with respect to the surface normal) and rotation around the surface normal, to change the azimuthal angle ϕ. This is schematically depicted in Fig. 2.2. The total scattering angle θ is defined as: $\theta = 180°$ - $(\theta_i + \theta_f)$, with θ_f the outgoing angle of the particles. On this chamber, a differentially pumped electron impact source (VG, AG 60) is mounted which produces the H^+ ions. The incident energies of the ions can be varied between 100 and 1250 eV. The ion beam is purified using a Wien-filter. Typical currents at the crystal position between 1 and 2 nA are measured. The scattered positive and negative ions are detected with a 90° cylindrical electrostatic energy analyzer, which has an energy resolution of $\Delta E/E =$ 0.08. In the scattering plane, the detector can be rotated from 45° to 180° with respect to the incoming beam and out of plane detection from $-15°$ to 90° is possible. The angular resolution of the detector is around 0.5°. Adjacent to this detector, a fraction detector is mounted, with which the differential conversion efficiency η can be determined, where η = $I(H^-)/[I(H^-) + I(H^0)]$ and I is the energy integrated intensity of the ions or neutrals. Particles entering the detector are detected by a channeltron. However, prior to detection, the ions are neutralized by reflection from a tungsten surface. In this way, a possible difference in detection efficiency for neutrals and ions is eliminated. When a retarding potential is applied at the entrance of the detector only the neutral particles are detected, if grounded, the total particle intensity is measured.

2.2.2 The crystal

The Ag(111) crystal is cut by spark erosion and polished mechanically. The misalignment of the (111) surface is less than 0.05° as determined by Von Laue diffraction. The crystal was cleaned by repeated sputter and anneal cycles. Typically, a sputter treatment consists of 15
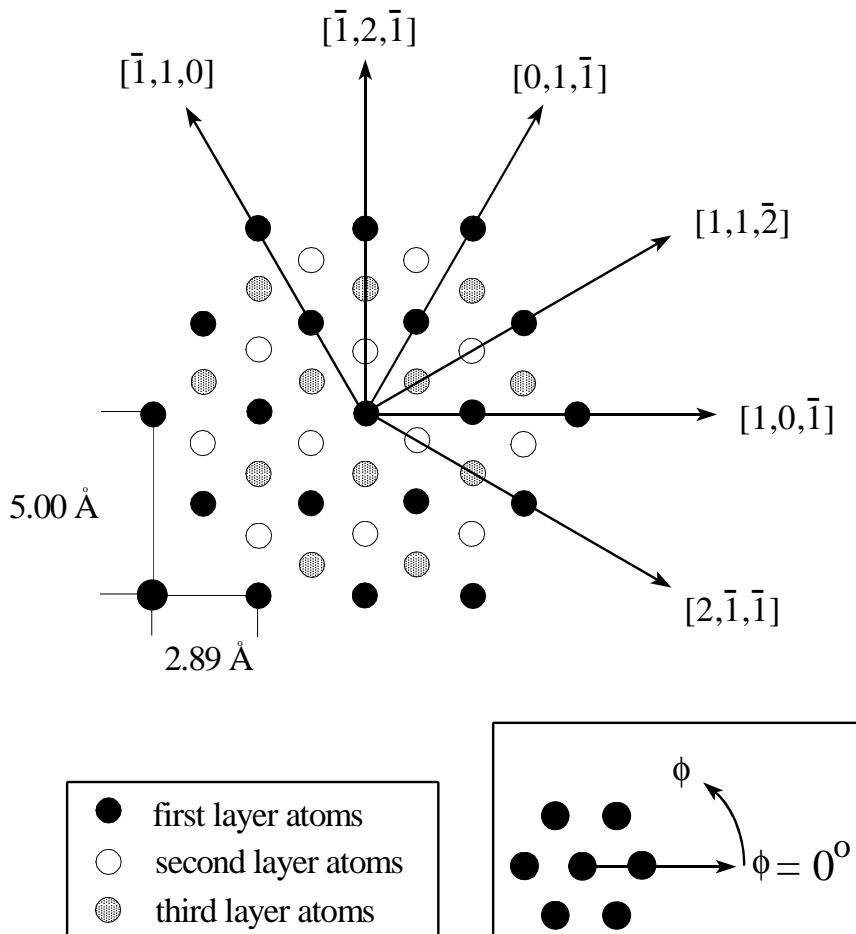
Figure 2.3 *Crystallographic drawing of the (111) face of a Ag crystal. The crystal directions and the definition of ϕ are indicated.*

min. of 800 eV Ar^+ bombardment at normal angle of incidence for a crystal current density of $5\times10^{-6}A/cm^2$. The crystal temperature during sputtering is 573 K. For annealing the crystal temperature is kept at 673 K for 15 min. The surface cleanliness is checked by XPS and work function measurements. The crystal orientation is drawn in Fig. 2.3, in which the crystallographic directions are plotted. The $(10\bar{1})$ direction is defined as $\phi = 0°$. All the spectra in this chapter were measured with a crystal near room temperature. Good reproduction of earlier data [57] was found.

Onto the Ag(111) surface, barium is deposited from a SAES-Getter source. The pressure during dosing was below 2×10^{-10} mbar. The barium overlayer was previously characterized using Auger electron spectroscopy (AES), XPS, work function measurements, medium-energy ion scattering (MEIS) and low-energy H^+ scattering [43,59,60]. In the latter case, backscattered H^- ions were detected [59]. This work indicated that a monolayer of barium is initially grown, after which a rather open overlayer structure is formed by Poisson growth. It further showed that the overlayer grows epitaxially. Due to the difference in size of the
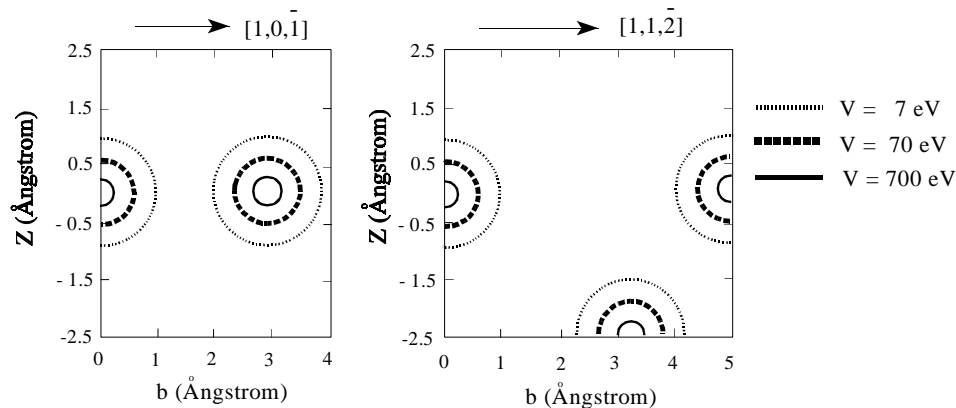
Figure 2.4 *Two sections through the potential energy surfaces for the H-Ag system along two symmetry planes given by the surface normal and the $(10\bar{1})$ (left) and $(11\bar{2})$ (right) axis. Drawn is the static potential felt by the incoming H atom when it reaches the surface as a function of distance z to the surface and the impact parameter b along that particular direction.*

adsorbate and substrate atoms, the first layer appears to be incomplete and must contain vacancies. The work function of a clean Ag(111) surface is 4.7 eV. When the surface is covered with one monolayer of barium the work function decreases to 2.4 eV [43].

2.2.3 Measurement procedure

In a three-dimensional intensity distribution $I(\theta_f, E_f)$ measurement, the incoming angle θ_i and the azimuthal orientation ϕ are kept constant. The detector is kept in the scattering plane at a fixed outgoing angle, θ_f. The intensity I of the positive and negative ions is measured as a function of their final energy E_f by scanning the detector voltage. This procedure is repeated for various outgoing angles. In an azimuthal scan, the incoming angle, outgoing angle and final energy are kept constant. The intensity of the ions or neutrals is measured as a function of azimuthal angle by rotating the crystal around its axis.

2.3 Computational

2.3.1 The potential

At incident energies which are high compared to the depth of the Ag-H potential well, only the repulsive part of the interaction potential is important for scattering. The repulsive Ag-H pairpotential was calculated using the Hartree-Fock-Slater (HFS) linear combination of atomic orbital method [61]. The results of this calculation are shown elsewhere [20]. The calculation can be approximated by a Born-Mayer potential which is of the form $V = A\exp(-\beta r)$ [51,61]. The parameters are given by $A = 3691.7$ eV and $\beta = 7.134$ Å^{-1}. To give an impression of the range of the potential, we show in Fig. 2.4 two sections through the H-Ag interaction potential for two symmetry planes given by the surface normal and

the $(10\bar{1})$ and the $(11\bar{2})$ axis, which represent the azimuthal angles $\phi = 0°, 60°, ...$ and $\phi = 30°, 150°, ...,$ respectively. For the energies used in our experiment ($E_i \sim 700$ eV), the crystal is quite open and, consequently, the particles can easily penetrate the crystal lattice.

2.3.2   The computer code

The computer code, written to simulate the scattering of the incoming particles at a crystal lattice, has been described extensively in the past [51,61] and is briefly summarized here. The code has been developed for collisions at (hyper)thermal energies and is rather inefficient in the present study compared to computer codes such as MARLOWE [11,62]. Nevertheless, satisfactory results are obtained.

Newton's equations are solved exactly for an hydrogen atom approaching a silver lattice, consisting of 321 atoms. The lattice is represented by 5 layers. In the first layer 88 atoms are placed, the second 74, the third 61, the fourth 54 and the fifth 44. The layers are placed on the Ag(111) lattice position sites. Thermal vibrations are taken into account using a so-called Einstein lattice [51]. These vibrations are generated using random displacements, according to the Boltzman distributions. The lattice is placed at T=300 K. The opening angle of the detector is set at 2°. The impact parameters are chosen systematically on a grid over the entire surface unit cell.

In a full three-dimensional calculation, a large number of hydrogen atoms are implanted into the crystal lattice or, otherwise, scattered out of the detection plane and, hence, are not detected. To obtain reasonable statistics, over 1×10^6 trajectories must be calculated. To gain more insight in the scattering dynamics and to reduce the number of trajectories, we performed calculations with the so-called "chain-model" [63]. Here, the impact parameters are chosen aligned with the rows of the surface atoms; essentially 2-dimensional calculations are performed on a 3-dimensional crystal since the scattering is restricted to the plane given by the surface normal and the incoming angle. The calculations were done at T=0 K and T=300 K, in order to study the influence of the thermal motion of the crystal atoms. To assure that only in-plane scattering occurs in the chain calculations at T=300 K, the crystal atoms are only displaced in the scattering plane.

2.3.3   Classical trajectory calculations: Chain-model and particle trajectories

Before discussing the experimental results we describe the "chain-model" in more detail and show trajectory calculations which serve as an easy reference in the discussion of our experimental results. In addition, some of the important scattering processes are introduced. Fig. 2.5(a) shows a symmetry plane given by the surface normal and the $(11\bar{2})$ axis of the Ag(111) surface. In this graph, calculated trajectories of 750 eV H^0 with impact parameters along the $(11\bar{2})$ axis are plotted. For all trajectories, the incoming angle of the beam is 40°. Thermal vibrations of the crystal atoms have not been included in this calculation. Considerable penetration into the crystal lattice is observed. We consider the trajectories from left to right. The trajectory of the H atom associated with the first trajectory (*1*) undergoes a head-on collision with a first layer atom. In these kinds of collisions, the highest energy transfer to the surface atoms occurs; a maximum elastic energy loss of 28 eV
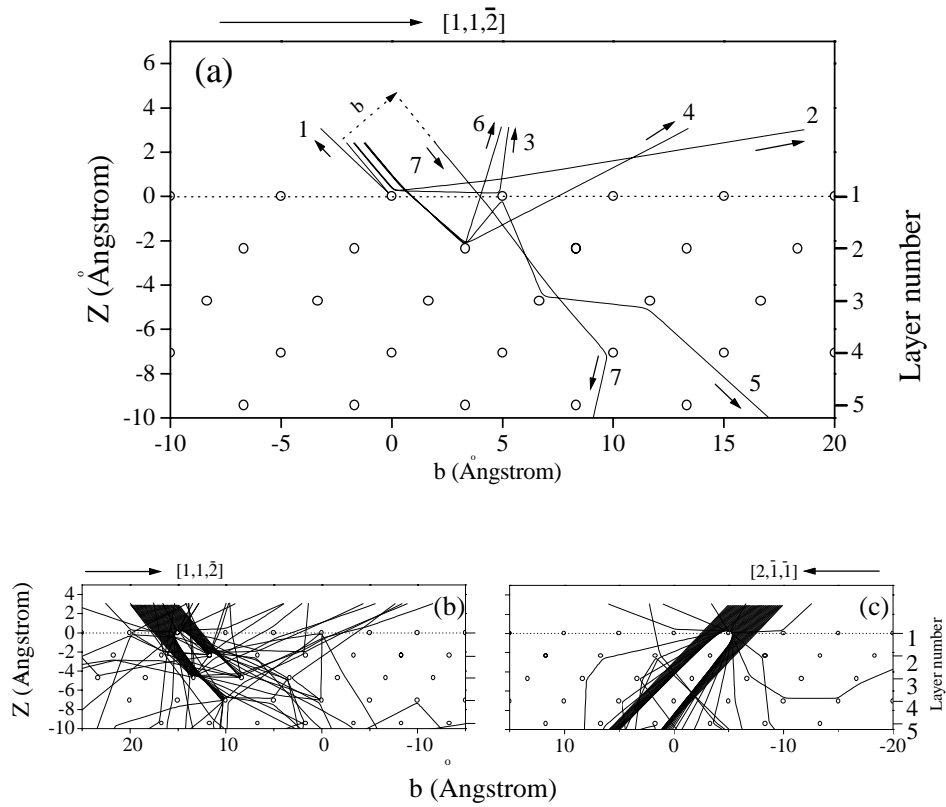
Figure 2.5 *Calculated trajectories for 750 eV H^0 with impact parameters along the (a) (11$\bar{2}$) with 7 trajectories, (b) (11$\bar{2}$) with 100 trajectories and (c) (2$\bar{1}\bar{1}$) axis of the Ag(111) surface. The beam is incident at $\theta_i = 40°$.*
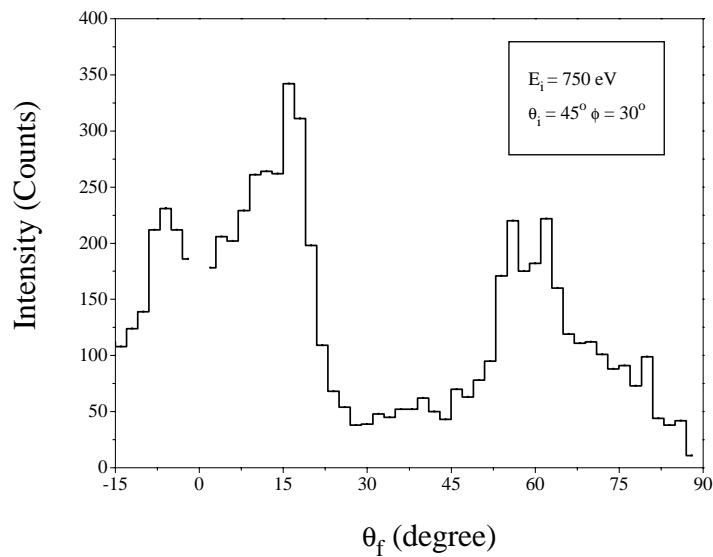

Figure 2.6 *Calculated angular spectra for scattering of 750 eV H^0 along the (11$\bar{2}$) axis of the Ag(111) surface. The beam is incident at $\theta_i = 40°$.*

arises for a total scattering angle of 180°. If after backscattering another surface atom is hit, this is referred to as a *hard-double* collision. With increasing impact parameter b, the atom goes through smaller total scattering angles; the particles are observed at larger θ_f. For a total scattering angle of 60° ($\theta_f = 80°$), an energy loss of 7 eV occurs (traj. (*2*)). As the impact parameter is increased further, the scattering angles become even shallower and the scattered particles can hit another surface atom in a so-called *double* collision (traj. (*3*)). The presence of this second surface atom limits the total scattering angle and gives rise to a so-called surface rainbow [9]; the rainbow angle is the angle where the "single" and "double" collision peaks merge. When the impact parameter is increased further, penetration into the solid occurs. The presence of the surface atom creates a region behind it where the particles cannot penetrate, the so-called "shadow cone" [11]. This is illustrated in Fig. 2.5(b), where 100 calculated trajectories are displayed. Here, a flux of particles concentrated just outside this cone is observed which is called the "focusing effect" [11]. At large enough impact parameters the particles can scatter from the second layer. They can scatter directly back into the vacuum (traj. (*4*)) or, at $\theta_f = 40°$, the particles are "blocked" by the first layer. An example of this is trajectory (*5*), which is "blocked" and subsequently scattered back into the solid. At larger impact parameters the particles can again escape from the solid (traj. (*6*)). Here, we can observe again the "focusing effect"; at the edges of the shadow cone of the first layer we observe an enhanced yield of particles. If the impact parameter is sufficiently large we can shoot the particle directly into the solid as is illustrated with trajectory (*7*). The calculated angular spectrum of the backscattered hydrogen particles is shown in Fig. 2.6. In this spectrum, a clear minimum is observed at $\theta_f = 40°$ and the maxima in intensity are observed next to the minimum, at $\theta_f = 15°$ and $\theta_f = 60°$.

In Fig. 2.5(c) calculated trajectories for the same scattering condition along the $(2\bar{1}\bar{1})$ axis are shown. Here, the second and subsequent layers are "shadowed" by the first layer atoms. As a consequence, significantly more penetration occurs compared to scattering along the $(11\bar{2})$ axis (Fig. 2.5(b)), as the lower lying layers do not contribute directly to the backscattered signal. When we compare Fig. 2.5(b) and Fig. 2.5(c), we observe much more backscattering for scattering along the $(11\bar{2})$ axis than along the $(2\bar{1}\bar{1})$ axis. This is discussed in more detail when we present the experimentally obtained azimuthal scans.

2.4   Results and analysis

2.4.1   Experimental results

Scattering of H^+ from clean Ag(111)

Fig. 2.7 shows the energy and angular distributions of backscattered negative ions for 700 eV H^+ scattering off clean Ag(111) along the $(11\bar{2})$ (a,c,e) and $(2\bar{1}\bar{1})$ (b,d,f) azimuthal directions. These azimuthal directions are defined as $\phi = -30°$ and $\phi = 30°$, respectively. Spectra for three different incoming angles are plotted; $\theta_i = 40°$ (a,b), $\theta_i = 60°$ (c.d) and $\theta_i = 70°$ (e,f). Fig. 2.7(a) shows scattering along the $(11\bar{2})$ direction for an incoming angle of 40°. Two peaks can be observed at $\theta_f = 18°$ and $\theta_f = 58°$. These peaks are found at an energy position which corresponds to elastic scattering from a single Ag atom. Consequently, a
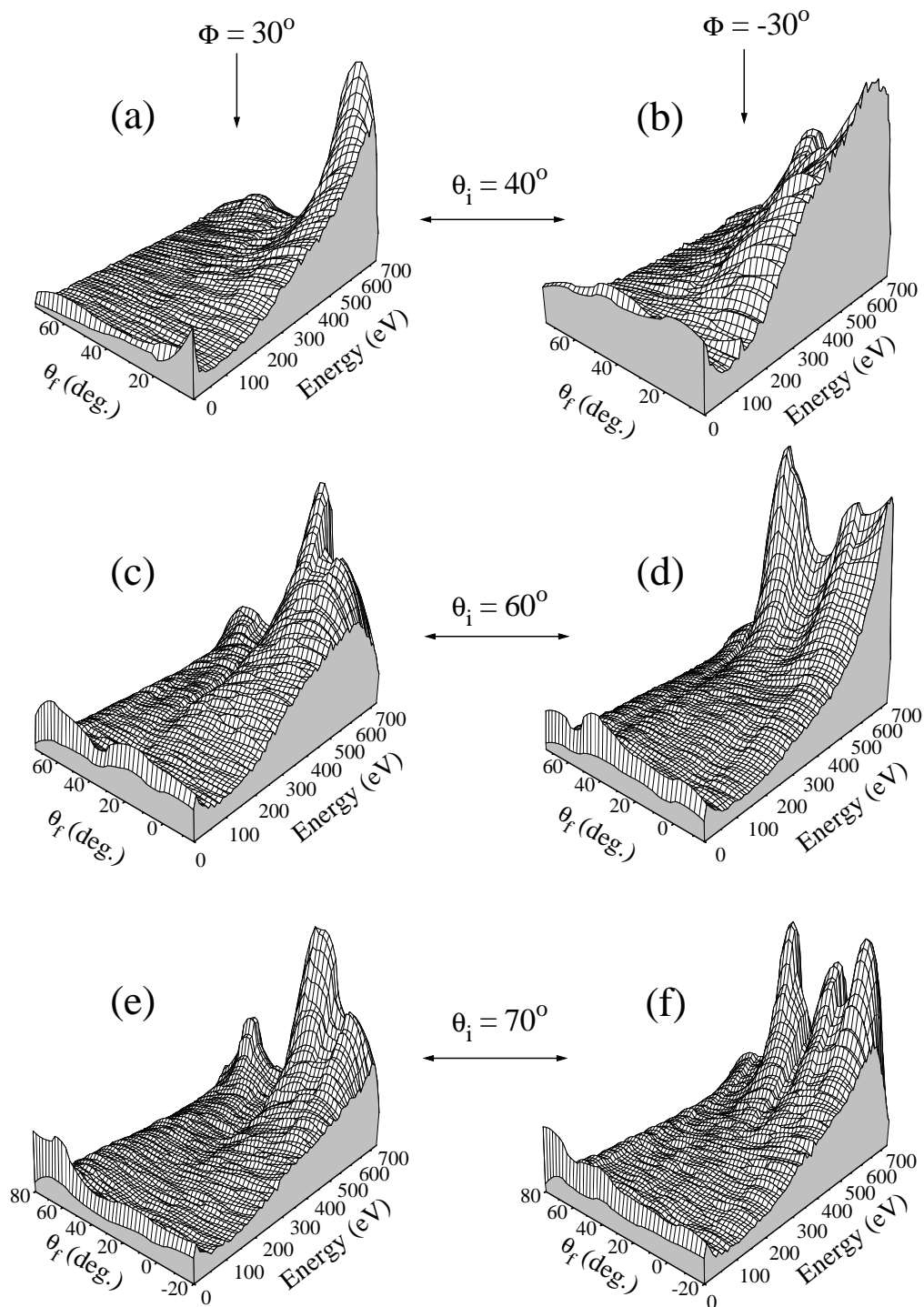
Figure 2.7 *Three-dimensional intensity distributions $I(\theta_f, E_f)$ for 700 eV H^+ from clean Ag(111) along the $(11\bar{2})$ (a, c, e)) and $(2\bar{1}\bar{1})$ (b, d, f)) azimuths for $\theta_i = 40°$ (a,b), $\theta_i = 60°$ (c,d) and $\theta_i = 70°$ (e,f). The measured intensities are plotted on a linear scale. Negatively charged hydrogen ions are detected. No correction for the energy-dependent transmission of the energy analyzer has been made.*

binary collision model between an H (M=1) and an Ag (M=109) atom can be applied to explain the energy losses at the peak positions in the energy distributions. Fig. 2.7(b) shows scattering along the $(2\bar{1}\bar{1})$ direction. The incoming angle and energy are the same as in Fig. 2.7(a), but the energy distributions appear much broader and also the peak structures in the angular domain have changed. The energy losses the particles have suffered can be as large as 500 eV. However, the maximum energy loss in a binary collision between an H atom and an Ag atom is smaller than about 0.037 times the initial energy E_i, which suggests that the particles have traveled through many atomic layers before exiting the solid. Probably, a combination of elastic energy losses and electronic stopping is responsible for the observed energy losses. In Fig. 2.7(c) and (d) the incoming angle has been changed to $60°$. The azimuthal orientations are identical to those in Fig. 2.7(a) and (b), respectively. The energy distributions for $\theta_i = 60°$ (c) have broadened compared to $\theta_i = 40°$ (a). Spectra (d) shows a narrowing compared to spectra (b). Most likely, particles penetrate deeply into the crystal for certain combinations of θ_i and ϕ. Fig. 2.7(e) and (f) show scattering for $\theta_i = 70°$. Now, the energy distributions have comparable widths. These particular scattering geometries do not give a penetration like that observed in Fig. 2.7(b) and (c). The peak positions in the outgoing angle seem to be independent of the incoming angle, which is an indication that these are due to the crystal structure. Similar peak structures have been observed for other system [57,64,65]. The negative ions are primarily observed at small outgoing angles; at very grazing outgoing angles no negative ions are observed. This difference can be explained with the normal and parallel velocity effect in negative ion formation [32].

To examine in more detail the peak structures in the outgoing angle we performed angular scans at one fixed final energy. Fig. 2.8 shows angular distributions of H$^-$ for 750 eV H$^+$ from clean Ag(111). The negative ions with a final energy of 708 eV are detected. Results for four different angles are shown, $\theta_i = 40°$ (a,e), $\theta_i = 60°$ (b,f), $\theta_i = 70°$ (c,g) and $\theta_i = 80°$ (d,h). Scattering occurs along the $(11\bar{2})$ (a to d) and $(2\bar{1}\bar{1})$ (e to h) azimuthal direction. For $\theta_i = 40°$ and $\phi = 30°$ (Fig. 2.8(a)), we clearly observe the two peaks at $\theta_f = 18°$ and $\theta_f = 58°$, which were present in Fig. 2.7(a). The absence of the scattering signal around $\theta_f = 35°$ was attributed to blocking of H atoms scattered from the second layer by atoms of the first layer (section 2.3.3). The measured angular spectrum has all the same features as the calculated spectrum which was displayed in Fig. 2.6. When we change the incoming angle to more grazing angles of incidence (b to d), we observe also a peak at $\theta_f = -5°$. This peak could not be observed for smaller angles of incidence because of the limited range of the energy analyzer. The peak positions are independent of the incoming angle, indicating that they are due to the exiting part of the trajectories the particles follow. At very grazing angles of incidence ($\theta_i = 80°$, Fig. 2.8(d)), we observe the appearance of a split peak around $\theta_f = 76°$. This can be attributed to a surface rainbow, giving two closely spaced peaks in the forward direction. It is remarkable that even for such grazing angles of incidence, penetration into the crystal lattice is observed.

Fig. 2.8(e) to (h) show scattering along the $(2\bar{1}\bar{1})$ azimuth. Three distinct peaks can be observed, around $\theta_f = -10°$, $10°$ and $42°$. Once again, the positions of the peaks are independent of the incoming angle. For $\theta_i = 80°$, two closely spaced peaks are observed around $\theta_f = 76°$. These can again be attributed to a surface rainbow. Scattering along the $(10\bar{1})$ azimuth or $\phi = 0°$ also gives rise to peaks in the angular distributions, data which
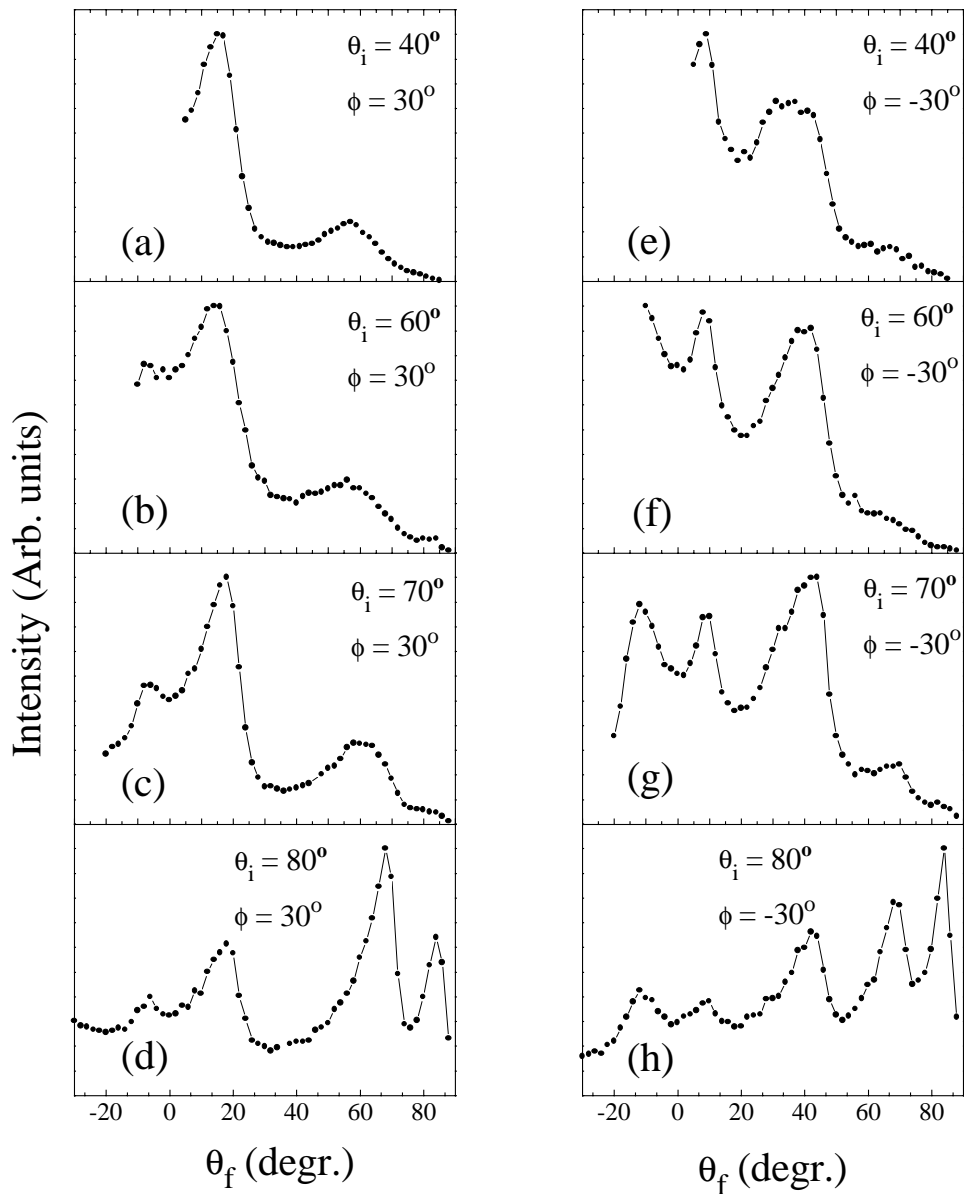
**Figure 2.8** *Angular distributions of* H^- *for 750 eV* H^+ *from clean Ag(111). The negative ions with an energy of 708 eV are detected. Results for four different angles is shown:* $\theta_i = 40°$ *(a,e),* $\theta_i = 60°$ *(b,f),* $\theta_i = 70°$ *(c,g), and* $\theta_i = 80°$ *(d,h). Scattering occurs along the (11$\bar{2}$) (a to d) and (2$\bar{1}\bar{1}$) (e to f) azimuthal direction.*
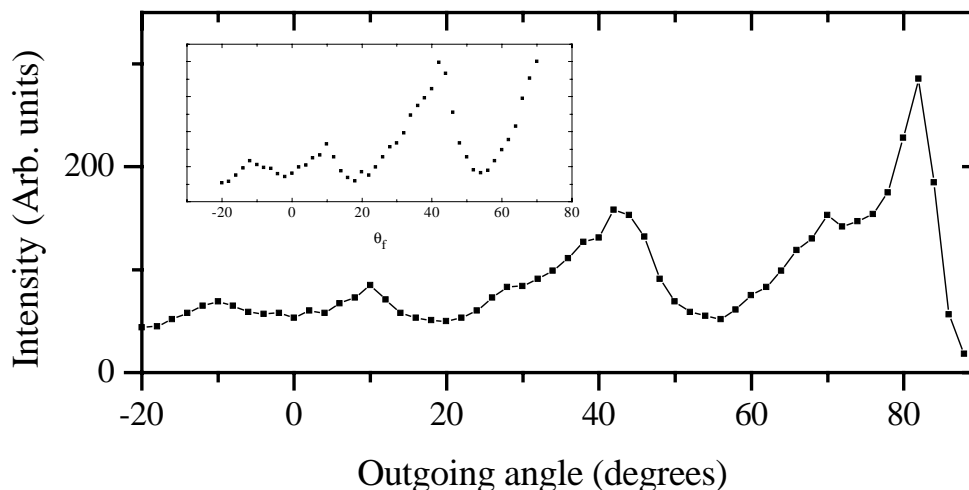
Figure 2.9 *Energy integrated angular distribution of H atoms for 750 eV H^+ from clean Ag(111) along the ($2\bar{1}\bar{1}$) azimuth. Data are taken at $\theta_i = 70°$. The inset shows data between $\theta_f = -20°$ and $\theta_f = 70°$.*

was previously published in Ref. [59].

To check whether the peak structures in the angular distributions are only due to the structure of the crystal, we also measured the angular distributions of the backscattered neutral hydrogen atoms, which are shown in Fig. 2.9. The incoming energy of the hydrogen ions is 750 eV and $\theta_i = 70°$, scattering takes place along the ($2\bar{1}\bar{1}$) azimuth; the same scattering conditions as employed in Fig. 2.8(g) for backscattered negative ions. The total yield of the backscattered neutral particles is measured with the fraction detector; the energy integrated angular distribution is measured. The angular distribution is strongly peaked around $\theta_f = 82°$, a peak which was not observed in the negative ion case and can be attributed to surface rainbow scattering [9]. The peak structures between $\theta_f = -20°$ and $\theta_f = 60°$ (see inset) are the same as for the backscattered negative ions. The peaks are located at the same positions and also the relative peak heights are similar.

Another method to investigate the penetration into the crystal lattice is to perform azimuthal scans. Fig. 2.10 (left panel) shows the azimuthal dependence of the backscattered H^- ions for 750 eV H^+ incident at clean Ag(111) and $\theta_i = 40°$. The ions with a final energy of 708 eV are detected. Scans are performed at four different outgoing angles: (a) $\theta_f = 5°$, (b) $\theta_f = 20°$, (c) $\theta_f = 40°$ and (d) $\theta_f = 60°$, respectively. The spectra show a 120° symmetry which indicates that more than one layer is involved in the scattering process. For $\phi = -30° \pm 120°$ clear minima are observed in the spectra. This is because the first layer shadows the second layer and subsequent deeper layers, which allows for substantial penetration into the crystal lattice (see Fig. 2.5). The azimuthal scans reveal that the $\phi = 0°, \pm60°, \dots$ directions contribute equally to the backscattered signal. For these directions, the particles are focused into the surface channels and can be reflected by the second layer. The peaks that change significantly in intensity with outgoing angle are located at $\phi = -90°, 30°, \dots$. For these directions, at $\theta_f = 5°$ and $\theta_f = 20°$, the particles are
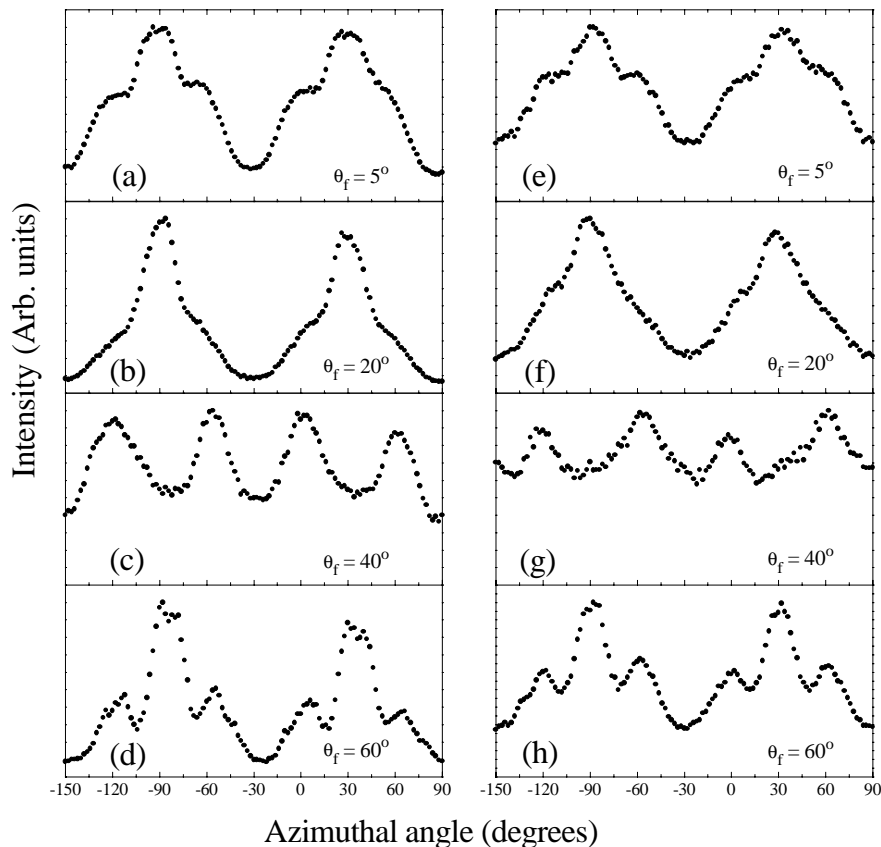
Figure 2.10 *Azimuthal dependence of backscattered* H^- *ions in scattering of* H^+ *from clean Ag(111) (left) and a monolayer of barium covered Ag(111) (right) for* $\theta_i = 40°$. *The data are taken at* $E_i = 750$ *eV and ions with a final energy of 708 eV (left) and 672 eV (right) are detected.*

scattered directly from the second layer and for $\theta_f = 40°$, the particles reflecting from the second layer are blocked by the first layer. For $\theta_f = 60°$ the particles show an increased yield because of the focusing effect; the particles can escape from the solid (see section 2.3.3).

As a final point, in H^+ scattering off Ag(111) the relative yield of backscattered positive ions is very low ($< 10^{-6}$) and they are hard to detect. In the case of H_2^0 and H_2^+ scattering from Ag(111), only first layer scattering was observed; the azimuthal scans showed a clear $60°$ symmetry of the backscattered H^+ ions, which were formed in a reionization process [19].

Scattering of H^+ from Ba/Ag(111)

Covering the surface with barium and, hence, lowering the work function of the surface leads to an increase in negative ion yield [32,57]. Fig. 2.11(a) shows the contour plot for H^- for 700 eV H^+ incident on Ag(111) covered by one monolayer of barium along the $(2\bar{1}\bar{1})$ azimuth. The data are taken at $\theta_i = 60°$. The contour plot for scattering of H^+ on clean Ag(111) is also shown in Fig. 2.11(b) for the same scattering geometry and incident
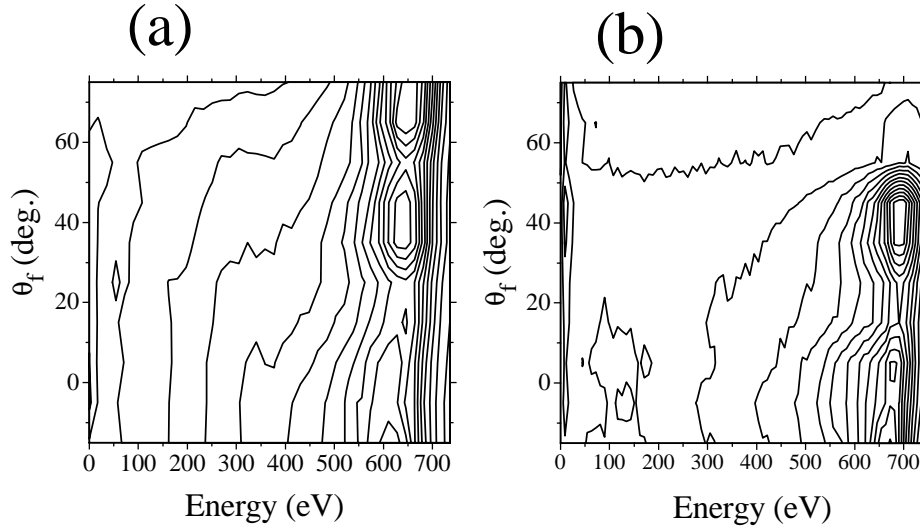
Figure 2.11 *Contour diagrams of backscattered negative ions for (a) 700 eV* H^+ *from barium covered Ag(111) at* $\theta_i = 60°$ *along the* $(2\bar{1}\bar{1})$ *azimuth and (b) for scattering of* H^+ *on clean Ag(111) for the same scattering geometry and incident energy. No correction for the energy-dependent transmission of the energy analyzer has been made.*

energy. This contour plot corresponds to the energy and angular distribution depicted in Fig. 2.7(d). The peaks in the angular distributions are located at the same positions as for the clean Ag(111) case, which indicates that the barium atoms are positioned at lattice position sites of the crystal. However, there are some remarkable differences for the two surfaces: (i) the energy distributions for scattering of Ba/Ag(111) are significantly broader than those measured from Ag(111), (ii) the peak positions of the energy distributions are shifted to lower energies by about 40 eV, for scattering of Ba/Ag(111), (iii) at grazing exit angles ($\theta_f > 50°$), a relative increase in negative ion yield is observed, (iv) the yield of negative ions has increased from <1 % for clean Ag(111) to around 20% for Ba/Ag(111).

To examine in more detail the effect of the barium overlayer on the negative ion signal, we display in Fig. 2.12, the energy distributions for two different outgoing angles, $\theta_f = 35°$ and $\theta_f = -15°$; these are cuts through the three-dimensional intensity distributions presented in Fig. 2.11. In Fig. 2.12(a) the energy distributions for scattering from Ag(111) are shown. For larger scattering angles the measured peak energy position shifts to lower energies; more energy is transferred to the surface. These peak positions agree with the peak positions calculated from the binary collision formula, with $M_H = 1$ and $M_{Ag} = 109$ [10,11,34]. Fig. 2.12(b) shows the energy distributions for scattering from Ba/Ag(111). Clearly, the peak positions are observed at lower energies than in Fig. 2.12(a). The elastic scattering positions, as calculated from the binary collision formula, are indicated with arrows; the particles have suffered an additional energy loss of 50 eV. For larger scattering angles, the peak positions shift to lower energies. In addition, a considerable broadening of the peaks is observed. For $\theta_f = 35°$, the width (FWHM) is about 120 eV in the case of the clean Ag(111) and 145 eV in the case of scattering from the Ba/Ag(111) surface. In Fig. 2.12(c) the peak positions in the energy distributions are depicted for scattering from Ag(111) and Ba/Ag(111) as a
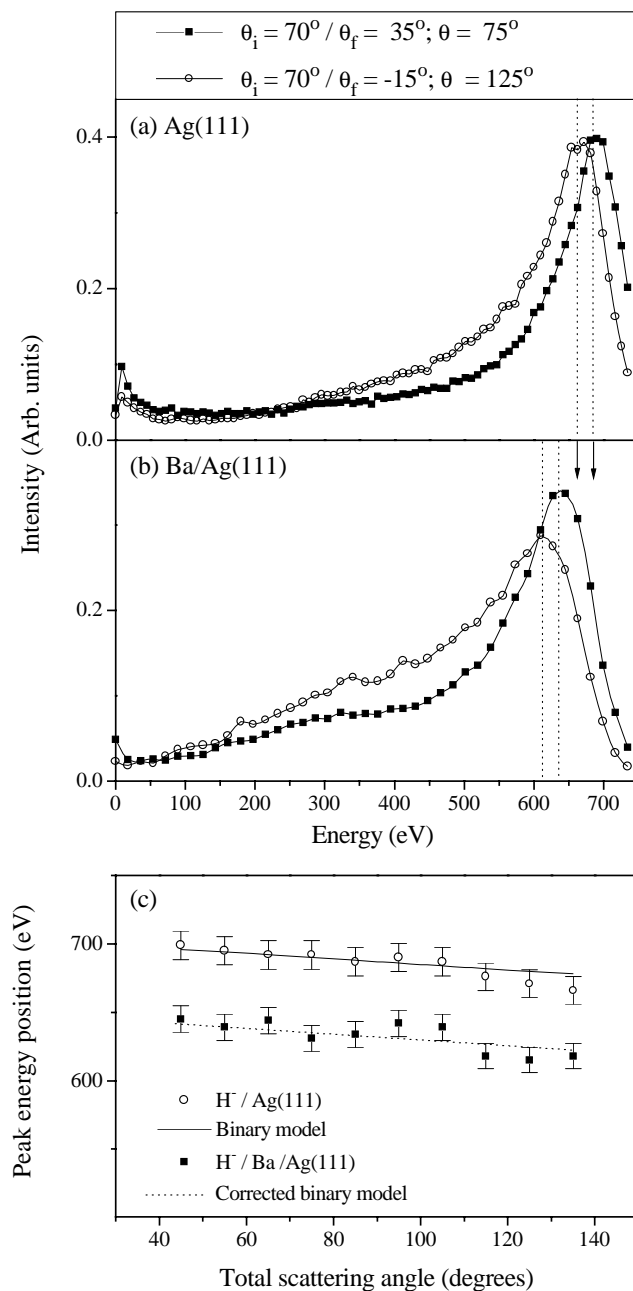
Figure 2.12 *Intensity distributions of backscattered negative ions for 700 eV H$^+$ at $\theta_i = 70°$ on (a) clean Ag(111) and (b) on barium covered Ag(111) surface. (c) shows the peak energy positions as a function of total scattering angle θ for scattering of these surfaces. The lines in figure (c) were calculated from the binary collision model for the H on Ag system (solid line) and corrected for H on Ba/Ag (dashed line).*

function of total scattering angle. The solid line gives the calculated energy position as extracted from the binary collision formula; clearly, the data points are described fairly well by this model calculation. The measured energy losses from the Ba/Ag(111) surface are much larger than are to be expected on the basis of the binary collision formula. The dashed line gives the energy positions for elastic scattering displaced to lower energies by about 50 eV, to obtain a fit with the data points. The energy losses with outgoing angle are reproduced by the binary collision model. However, the 50 eV additional energy loss is due to inelastic effects.

Fig. 2.10 (right) shows the azimuthal dependence of the H^- yield for 750 eV H^+ incident at one monolayer of barium covered Ag(111). The ions with final energies of 672 eV are detected. The scans appear identical to the spectra taken for clean Ag(111) (left), except the background signal seems to be higher. The results of the angular and azimuthal scans appear to clearly indicate that the barium atoms are located at lattice positions of the Ag(111) substrate.

Until now, we have attributed the observed structure in the azimuthal scans to particles following different kinds of trajectories in the solid/surface region. We did not take crystallographic effects in neutralization or negative ion formation probabilities into account. A way to check the validity of this assumption is performing an azimuthal scan with the fraction detector and determining the fraction of negative ions as a function of the azimuthal orientation of the crystal. This approach was previously applied by Närmann and coworkers in their study on crystallographic effects in charge exchange processes [55]. They studied He^+ from Ni(110) at grazing angles of incidence, and found minima in the charge fraction $He^+/(He^0 + He^+)$ along the major crystallographic directions. This effect was attributed to different trajectories and different contributions of Auger neutralization and "dynamic resonant loss processes". Also van Slooten at al. follow this procedure in Ref. [66].

Fig. 2.13 shows the azimuthal dependence of backscattered (a) H^0 and (b) H^- particles in scattering of H^+ from two layers of barium covered Ag(111) for $\theta_i = 40°$ and $\theta_f = 40°$. The data are taken at E_i=1250 eV and the energy integrated signals are measured with the fraction detector. The signals for neutral atoms and negative ions show identical behaviour. The fraction $I(H^-)/[I(H^-) + I(H^0)]$ shows no variation with azimuthal angle as can be seen in Fig. 2.13(c); its value is constant at 0.22, in agreement with a previous study [57]. We do not observe crystallographic effects in negative ion formation within the experimental error and therefore we conclude that observed structures in the azimuthal scans are merely due to scattering effects.

Fig. 2.14 shows the H^- signal for different final energies: (i) 1160 eV (ii) 900eV, (iii) 600 eV, (iv) 400 eV and (v) 200 eV, respectively. The initial conditions, incident energy and angles, are the same as for Fig. 2.13. The absolute intensities are scaled. For the highest final energies, the minima in intensity are observed along the $(2\bar{1}\bar{1})$ and $(11\bar{2})$ azimuthal directions. The minimum around $\phi = -30°$ is attributed to shadowing and, around $\phi = 30°$, to blocking. We observe the disappearance of the dip in the $(11\bar{2})$ azimuthal direction when the final detection energy is lowered. The dip in the $(2\bar{1}\bar{1})$ direction remains, even at the lowest detection energies. The origin of this phenomenon is unclear. From the behaviour observed in Fig. 2.13 and Fig. 2.14, we conclude that the negative ions and neutral atoms have identical energy distributions. We can not determine the energy distributions of the neutrals directly in the present experiment.
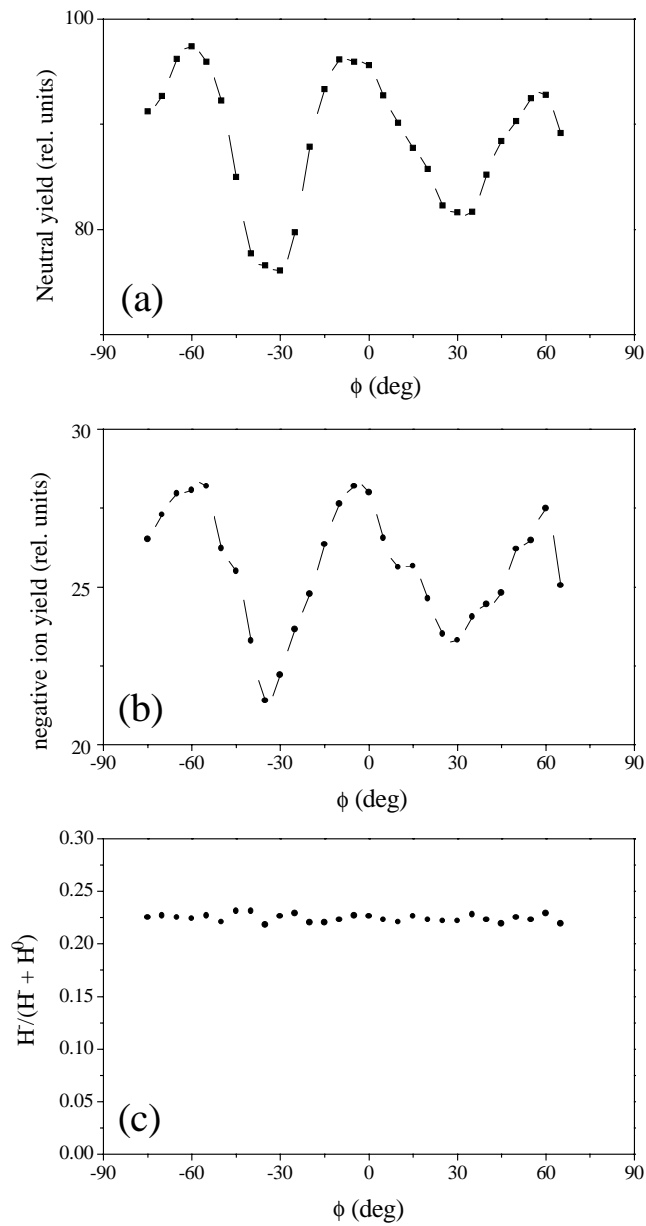
Figure 2.13 *Azimuthal dependence of backscattered (a)* H^0 *and (b)* H^- *particles in scattering of* H^+ *from two layers of barium covered Ag(111) for* $\theta_i = 40°$ *and* $\theta_f = 40°$. *The data are taken at* $E_i=1250$ *eV and the energy integrated signals are measured. Also shown (c) is the fraction of negative ions.*
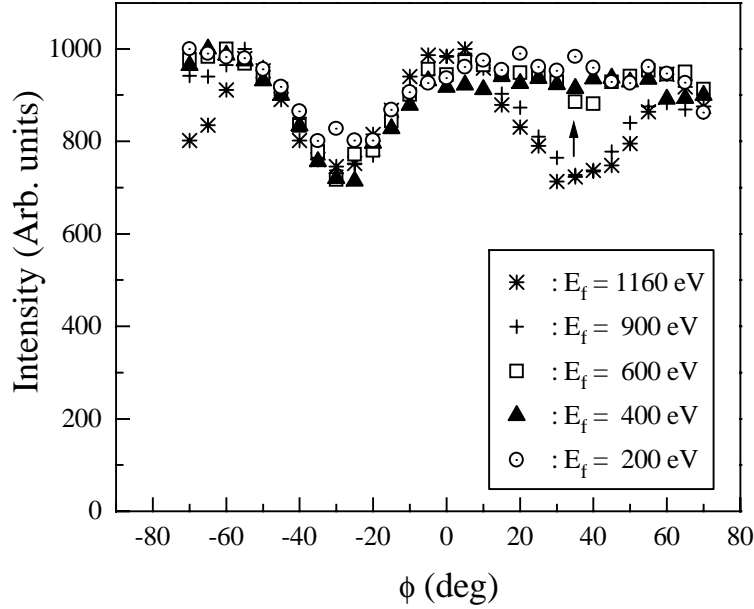
Figure 2.14 *The azimuthal dependence of the* H⁻ *signal for different final energies: (i) 1160 eV (ii) 900eV, (iii) 600 eV, (iv) 400 eV and (v) 200 eV. The scattering conditions are the same as in the previous figure.*

2.4.2 Classical trajectory calculations

To assign the peaks in the angular distributions to classes of trajectories, we performed classical trajectory calculations. Fig. 2.15(a) displays the calculated angular spectra for 750 eV H scattering from the Ag(111) surface with impact parameters aligned along the $(2\bar{1}\bar{1})$ azimuth. The crystal temperature is set at 0 K, $\theta_i = 70°$ and 20,000 trajectories are calculated. The calculated spectra show the same peak structures as were observed for experimental angular distributions, although in this case the peaks are much narrower. The positions of the peaks in the calculations agree fairly well with those observed in the experimental results. The calculated peaks are located at $\theta_f = -10°, 10°, 44°, 70°$ and $82°$, respectively. In the chain calculation only trajectories are considered that scatter in the plane given by the surface normal and the incoming angle. This is only a small fraction of the scattering events that take place; when the impact parameters are not chosen exactly on top of the crystal row, extensive out-of-plane scattering occurs [63,67].

At the backscattering directions two additional peaks are observed at $\theta_f = -78°$ and $\theta_f = -56°$; these were not observed in the experiment because of the limited range of the detector position. The peak at $\theta_f = -78°$ is attributed to a backward rainbow. The rainbow position is shifted towards the surface normal by about 4° compared to the rainbow in the forward scattering direction. In the forward scattering direction relatively soft collisions lead to rainbow scattering, and in backward scattering hard collisions are important. In Fig. 2.16(a), calculated trajectories for 750 eV H^0 with impact parameters along the $(2\bar{1}\bar{1})$ axis of the Ag(111) surface leading to (1) "back-" and (2) "forward-" scattered rainbows are shown. The inset shows at what distances the particles approach the surface for both
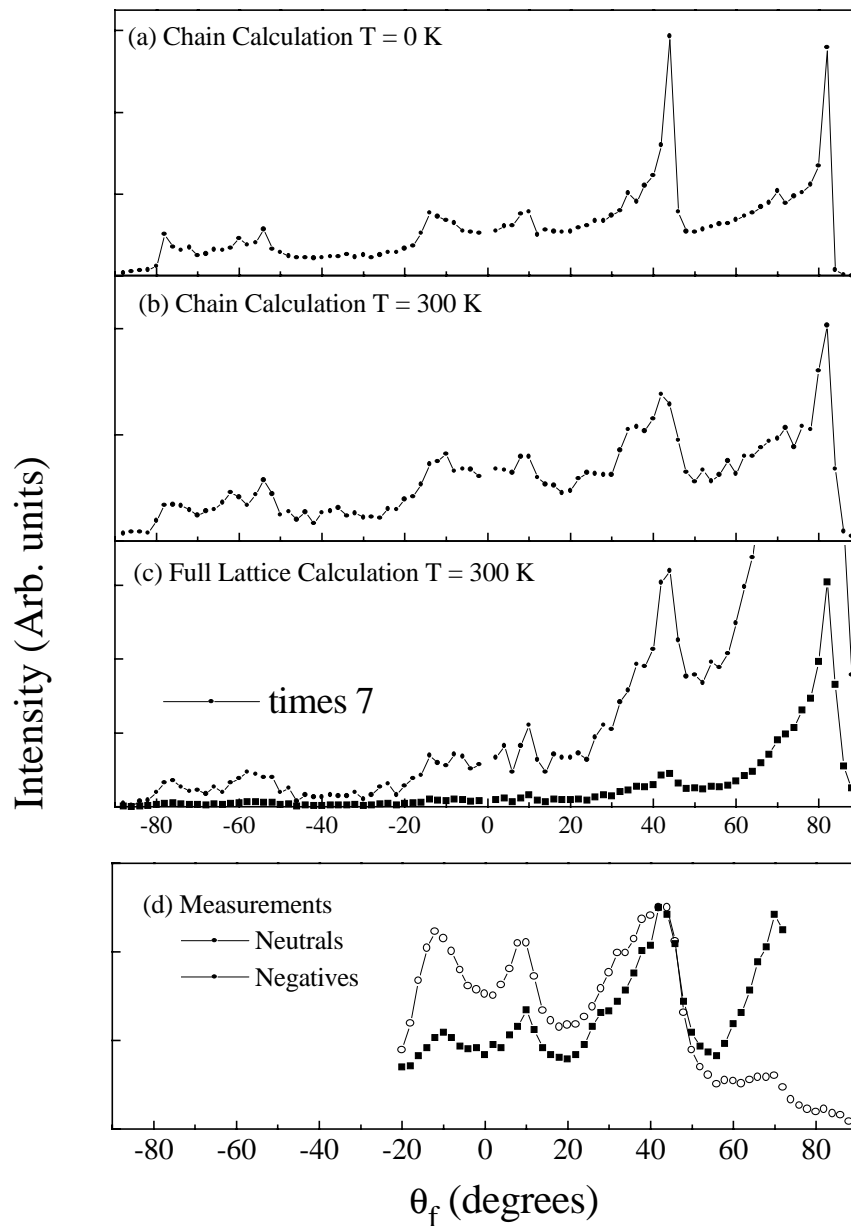
Figure 2.15 *Calculated angular spectra for 750 eV H scattering from the Ag(111) surface along the $(2\bar{1}\bar{1})$ azimuth, for $\theta_i = 70°$. (a) "chain" calculation for T=0 K. (b) "chain" calculation for T=300 K. (c) 3D calculation for T=300 K. In (d) the measurements for scattered neutrals and negatives are displayed.*
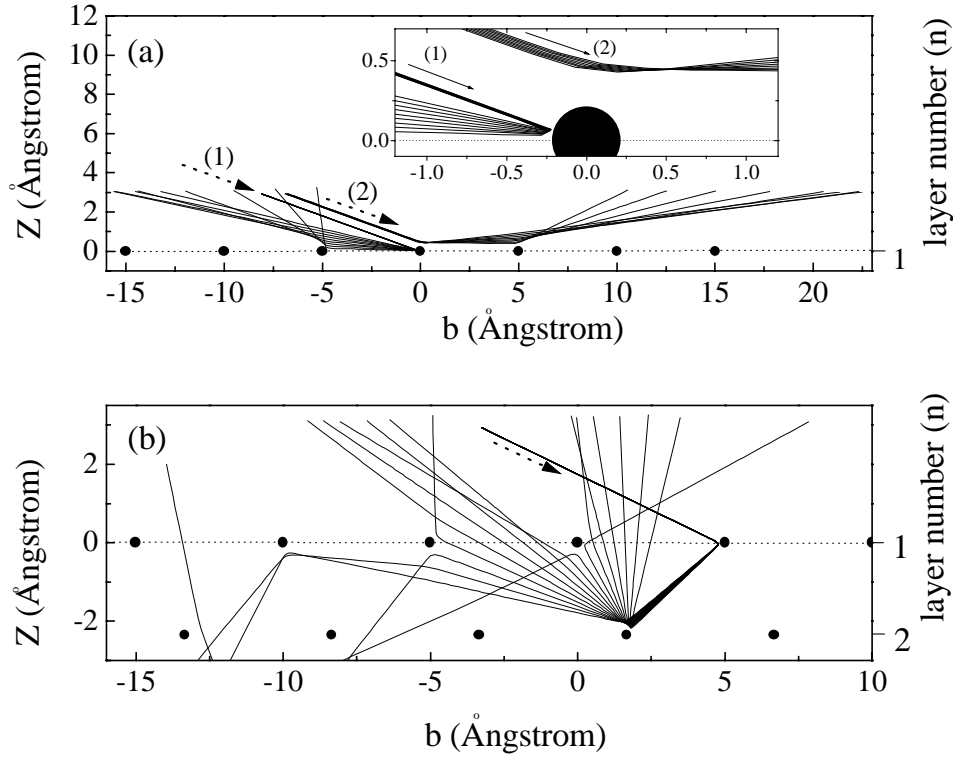
Figure 2.16 *Calculated trajectories for 750 eV H^0 with impact parameters along the $(2\bar{1}\bar{1})$ axis of the Ag(111) surface leading to (a1) "back-" and (a2) "forward-" scattered rainbows. The inset shows at what distance the particles approach the surface. (b) shows scattering from the second via the first layer. The initial beams are incident at $\theta_i = 70°$.*

cases. The initial beams are incident at $\theta_i = 70°$. For the forward scattered rainbow, the particles originate from about 0.45 Å above the surface. For the backward rainbow the particles originate from much closer to the surface plane (<0.06 Å), giving rise to cut-off angles at smaller θ_f; the single and double collision peaks merge in the direction towards the surface normal. The difference in intensity between the two rainbow peaks can be explained considering the impact parameter regions that lead to forward and backward rainbow scattering. The regions with impact parameters between $1.14 < x < 1.32$ lead to forward and the much smaller region $-0.06 < x < -0.03$, which means significantly less trajectories, contribute to the backward scattering rainbow. The impact parameter x is expressed in Å and refers to the projection of the impact parameter b (Fig. 2.5(a)) in $(2\bar{1}\bar{1})$ direction of the surface plane.

The peak at $\theta_f = -56°$ is observed in scattering along the $(11\bar{2})$ axis (Fig. 2.6). This direction is the same as the $(2\bar{1}\bar{1})$ direction rotated over 180°. The peak was attributed to particles directly scattered from the second layer; particles at smaller outgoing angles are "blocked" by the first layer (see section 2.3.3). Calculated trajectories that contribute to the peak at $\theta_f = -56°$, are displayed in Fig. 2.16(b). In this plot, we observe particles which are scattered from the second layer after an initial hard collision with a first layer atom. Once again, particles at smaller outgoing angles are blocked by the first layer atom which
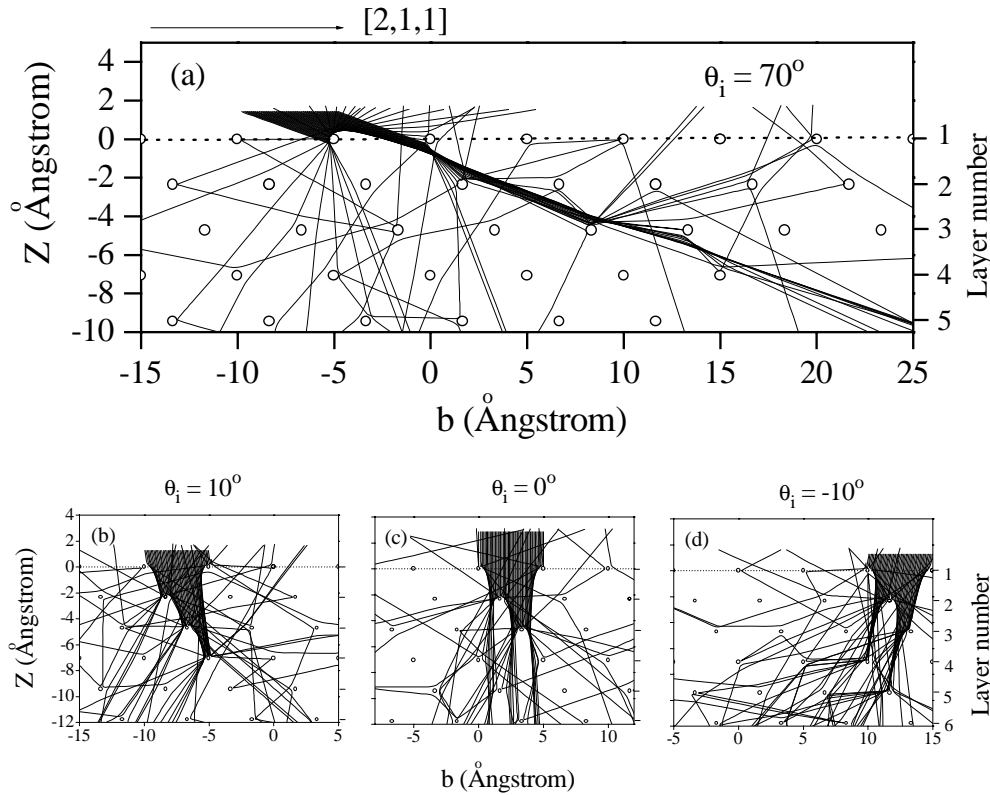
Figure 2.17 *Calculated trajectories for 750 eV H^0 with impact parameters along the (2$\overline{1}\overline{1}$) axis of the Ag(111) surface. The beams are incident at (a) $\theta_i = 70°$,(b) $\theta_i = 10°$, (c) $\theta_i = 0°$ and (d) $\theta_i = -10°$.*

gives rise to a shadow cone as can clearly be observed.

In Fig. 2.15(b) the thermal vibrations of the crystal atoms are included (T=300 K). The average displacements of the crystal atoms is approximately 0.01 $\mathring{A}$ [68]. Once more, 20,000 trajectories are calculated with impact parameters centered over the top-layer atom chains. In the angular spectra a significant broadening of the peaks is observed compared to the T=0 K case, but the calculated peak positions are not affected. The rainbow is the dominant feature in the spectrum and its appearance remains sharp. The backscattered rainbow is also still observed. For systems where the range of the potential is of the same order as the internuclear distances between the surface atoms, the backward rainbow is very sensitive to surface temperature, and disappears at sufficiently high temperatures [9,63,69]. Our results show that backscattered rainbow is still observed at T=300 K. In the H-Ag system the range of the potential is an order of magnitude smaller than the internuclear distance between the surface atoms allowing an initial hard collision followed by a soft collision as shown in Fig. 2.16(a1).

In a 3D calculation at T=300 K, even better agreement with the experimental data is obtained. However, to get reasonable statistics, 50 times more trajectories (i.e. 1×10^6) are calculated than was required in the chain calculations. The calculation is shown in Fig. 2.15(c). The impact parameters are no longer chosen aligned with the rows of the surface

atoms, but systematically on a grid over the entire surface unit cell. The peak positions, their widths and the peak heights of the rainbow peak agree with the data (Fig. 2.15(d)). The yield of particles at large backscattering angles is underestimated due to the limited size of the crystal in the calculation (321 atoms). The most striking difference between the chain calculation and the 3D calculation is the increase of the rainbow peak relative to the other peaks originating from deeper in the crystal; out-of-plane scattering becomes important and the effect increases for multiple collisions. It seems that the peaks for sufficiently small energy losses can be explained by in-plane scattering, especially considering the good agreement between the experimental data and the chain calculations.

In Fig. 2.17(a), the calculated trajectories for 750 eV H^0 with impact parameters along the $(2\bar{1}\bar{1})$ axis of the Ag(111) surface are depicted. The beam is incident at (a) $\theta_i = 70°$ and the crystal temperature is set at 0 K; the same scattering conditions as in Fig. 2.15(a). We can see that the particles can penetrate deep into the crystal and that they follow complicated zig-zag trajectories through the crystal. Direct scattering from the third and fourth layers appears to be important.

A more direct way to check the origin of the peaks in the angular distributions is reversing the trajectories. This approach is valid because the energy losses the particles suffer at the peak positions are small. The peak maxima appear at the position for elastic scattering. We first look at the origin of the peaks located at $\theta_f = -10°$ and $10°$. In Fig. 2.17(b-d), beams of particles are incident at (b) $\theta_i = 10°$, (c) $0°$ and (d) $-10°$, respectively. For $\theta_i = -10°$ and $\theta_i = 10°$ direct scattering from the second, third, fourth and even fifth layers is observed. When a beam of particles is incident at $0°$ only direct scattering from the second and third layers is observed. The fourth layer is shadowed by the first and the fifth by the third. Now we can assign the two peaks in the angular spectra at $\theta_f = -10°$ and $10°$ to "direct" scattering from the fourth and fifth layers. At $\theta_f = 0°$ a minimum is observed which can be attributed to blocking of the particles by the second and third layers. The same approach can be made for the peak at $\theta_f = 44°$. Here, also "direct" scattering from the second, third and fourth layers is important. In the analysis the focusing effect is important. Next to a blocking minimum we find maxima in intensity due to the enhanced flux of particles at the edges of the shadow cones. The peak at $\theta_f = 70°$ is identified with a crystal channel identical to the one observed in Fig. 2.17(b), where $\theta_i = 70°$ and the particles penetrate along this direction.

Using the classical trajectory calculations, we can explain the experimentally observed peaks for scattering along the $(2\bar{1}\bar{1})$ azimuth which appear at $\theta_f = -10°, 10°, 44°, 70°$ and $82°$. Similar analyses can be performed for scattering along the $(11\bar{2})$ and $(10\bar{1})$ azimuths, which are not shown. The peaks in the angular distributions are detected at small energy losses and the classical trajectory calculations show only small energy losses for the limited crystal used (321 atoms). When we look at the angular distributions of the H^- at larger energy losses, particles that have traveled many layers deep before exiting the crystal are detected. In Fig. 2.18 the angular distributions are displayed of negative ions detected at several final energies between 44 and 690 eV. The initial scattering conditions are identical to those used in Fig. 2.7(g). The distance between the data points is rather large ($10°$) and we are only interested in variations in relative peak heights, not in absolute positions of the peaks, with final energy. The peak positions that were obtained in the classical trajectory calculations are indicated with dashed lines. For large detection energies, 690
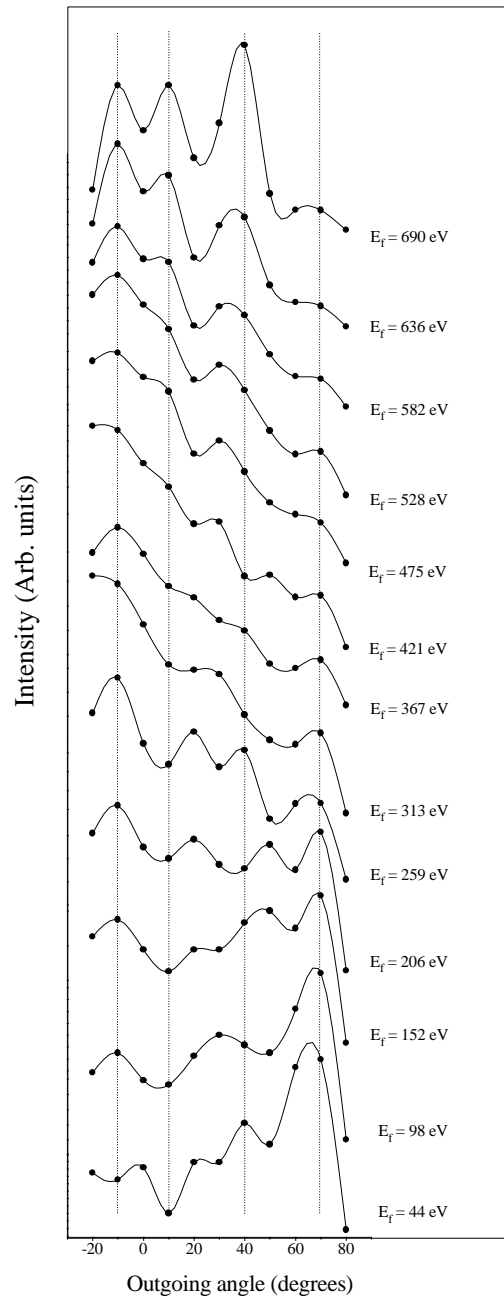
Figure 2.18 *Angular distributions of* H^- *for 750 eV* H^+ *from clean Ag(111). The negative ions are detected for several final energies between 44 and 690 eV. The beam is incident at* $\theta_i = 70°$ *along the* $(2\bar{1}\bar{1})$ *axis of the Ag(111) surface.*

eV $> E_f >$ 475 eV, the peaks appear roughly at the same positions. The peak at $\theta_f = 70°$ shows a remarkable increase at low detection energies 206 eV $> E_f >$ 44 eV, relative to other outgoing angles, which indicates that it is favorable for low energy particles to exit the crystal along this channel. The peak around $\theta_f = -10°$ is visible across the whole range of detection energies. The peak at $\theta_f = 10°$ is reduced and disappears for low detection energies. Between $\theta_f = 20°$ and $50°$ multiple peaks are observed and it is difficult to explain the peak position around $\theta_f = 44°$, due to the limited number of data points. It seems, however, that this peak is present going to lower detection energies. At very low detection energies we still observe the peak. Note that the overall intensity of the negative ions decreases at lower detection energies as observed in the energy distributions displayed in Fig. 2.12(a). The energy dependence of the angular distributions indicates that the structure of the crystal is important for all final detection energies and indicate that there are preferential exit channels for the backscattered particles.

2.5   Discussion

2.5.1   Penetration depth and energy losses

Scattering of H^+ from clean Ag(111)

The experimental results and classical trajectory calculations reveal that the number of particles reflected from the solid is highly dependent on the crystal azimuth along which scattering occurs. Experimentally, this is demonstrated in the azimuthal scans; for $\theta_i = 40°$, approximately 5 times more backscattering occurs along the $(11\bar{2})$ direction than along the $(2\bar{1}\bar{1})$ direction (see Fig. 2.10). In the classical trajectory calculations this is observed in Fig. 2.5(b) and (c) which are the $(11\bar{2})$ and $(2\bar{1}\bar{1})$ directions, respectively, and the ratio of $5:1$ is reproduced. The calculations indicate that for scattering along the $(11\bar{2})$ direction, about 25% of the *total* incident H particles are backscattered. However, this is a chain calculation and many particles can penetrate between the crystal rows. In the case of a 3D calculations and scattering along the $(2\bar{1}\bar{1})$ azimuth and $\theta_i = 70°$, the total reflection is about 20% and, consequently, 80% is implanted in the crystal lattice. However, the total amount of particles that is reflected in the experiment may be higher, because in the classical trajectory calculations we only consider a crystal lattice consisting of 5 layers; reflection from deeper layers was not taken into account.

In what follows, we make an estimate of the distances the particles have traveled inside the solid. With help of Fig. 2.17 we have made an analysis of the trajectories the particles have followed that give rise to the observed peaks at $\theta_f = -10°$ and $\theta_f = -10°$ for $\theta_i = 70°$. These peaks were assigned to trajectories coming "directly" from the fourth and fifth layers. When we take the minimal distance the particles have traveled to reflect from the fourth and fifth layers, these lengths are 35 Å and 45 Å, respectively. The extrapolated value for the stopping power of hydrogen in a Ag solid is given by 2.8 eV/Å, at translational energies of 700 eV [70]. This value is close to the value used by Van Wunnik at al. in H^+ scattering from a tungsten surface i.e. 3.0 eV/Å [71]. Note that these are extrapolated values, below 10 keV no experimental stopping power data are shown in Ref. [70]; a square root dependence with energy is assumed in the extrapolation procedure. When the particles have traveled

35 $\mathring{A}$, an energy loss of about 100 eV is expected. However, particles originating from the fourth layer are observed at a peak energy position, which can be explained solely on the basis of the binary collision model (see Fig. 2.12). From this we estimate that the (electronic) stopping power must be at least one or two orders of magnitude smaller than that extrapolated by Andersen and Ziegler [70], i.e. < 0.3 eV/$\mathring{A}$. When we assume a constant stopping power between energies of 700 and 200 eV, the particles that have suffered energy losses of 500 eV must have traveled over a distance larger than 1700 $\mathring{A}$. Particles that have experienced even larger energy losses must have traveled over distances on the order of μms.

Scattering of H^+ from Ba/Ag(111)

Some distinct differences in the H^- energy distributions are observed when scattering H^+ from a clean and from a barium covered Ag(111) surface. For the barium case, the energy distributions appear broader and for incoming energies of 700 eV, the peak positions are lowered by about 50 eV relative to those of scattering from a clean Ag(111) surface, for identical scattering conditions (Fig. 2.12). Moreover, scattering off two monolayers of barium leads to the same additional 50 eV energy loss [57], which indicates that these losses are not due to bulk properties of the barium. The tabulated value for the electronic stopping in bulk Ba is 1.0 eV/$\mathring{A}$ at energies of E=700 eV, 2.8 times smaller than the value in bulk Ag [70]. However, Ziegler and Andersen do not show any experimental data for the Ba case; the stopping powers are solely based on calculations.

The peak structures in the angular distributions are identical for scattering from a clean Ag(111) surface and from a Ag(111) surface covered with one monolayer of barium (see Fig. 2.11). The hydrogen particles must have followed identical trajectories for both surfaces, therefore the higher energy losses can not be explained by different trajectories and, hence, different elastic energy losses. Clearly, the additional energy losses must be related to a surface effect; either the lowering of the work function and/or the increase in electron density near the Fermi-level. The work function of a clean Ag(111) surface is 4.7 eV, while that of Ba/Ag(111) is 2.4 eV. In the case of scattering from a graphite surface (work function of 5 eV), an appreciable negative ion yield (about 20%) is measured, but the H^- are observed at the elastic scattering position of a H-C collision [36]. Also for scattering from Pt(111), with a work function of 5 eV, the energy losses can be explained by the binary collision formula [36]. However, in the case of H^+ scattering from Cs/W(110) (work function of 1.9 eV) the observed energy losses of the H^- are larger than expected on the basis of the binary collision model, between 5% and 15% instead of 0.5% as calculated by the binary collision model [71]. These observations suggest that scattering off a low work function surface leads to additional energy losses which can not be explained by the binary collision formula.

Higher energy losses for the H^- have also been observed in scattering H^+ from potassium covered Pd(110), compared to scattering off clean Pd(110) by Höfner and coworkers [72]. They attributed this to the lowering of the work function, which is associated with an increased electron charge density at the surface, giving rise to higher stopping powers. The effective interaction region is enhanced, leading to larger energy losses. These experiments were carried out for grazing angles of incidence. In our case, the particles do not spend

most of their time in the surface region, but deeply penetrate into the crystal lattice.

Possibly, electron capture and loss processes during the particle/surface interaction are responsible for the higher energy losses in the case of scattering off a low work function surface as suggested in Ref. [72]. In bulk material, dynamic loss and capture processes are supposed to contribute to the observed energy losses [73]. In ion/surface collision these occur, for low work function surfaces, on the incoming and outgoing trajectory. The times spent in the ion/surface interaction region are distinctly different for high and low work function surfaces, considering the shift of the affinity level due to the image force and the location of the Fermi-level. Recent experimental results of light ions scattered off Al(110) and K/Pd(110) indicate that calculated bulk friction coefficients cannot be used to explain the observed energy losses and that the friction of light ion is different at the surface and in the bulk [74].

The width of the hydrogen affinity level is at most 1.3 eV between 0.4 $\mathring{A}$ and 1.25 $\mathring{A}$ from the surface image plane, in the case of a barium surface [57]. Applying Heisenberg's uncertainty relationship, we obtain a typical transition rate w of 2×10^{14} s^{-1}. The velocity of an hydrogen particle of E = 700 eV is $v = 3.7 \times 10^{15}$ $\mathring{A}$s^{-1}. For particles leaving low work function surfaces, the affinity level will be resonant with the conduction band longer, allowing for more transitions and hence more friction, than for particles leaving a high work function surface, at the same $v_\perp$. However, more experiments and analyses is necessary to verify this conclusion.

2.5.2   Negative ion formation: Low and high work function surfaces

In a previous paper, we measured the negative ion fraction from a Ba/Ag(111) surface as a function of outgoing angle [57]. These data were reproduced very well by a simple model describing resonant charge transfer by the non-perturbative CAM method and taking into account the parallel velocity effect [57,58]. These data and calculations are depicted in Fig. 2.19(b) to allow for direct comparison with the values of clean Ag(111). Unfortunately, our ion fraction detector is not sufficiently sensitive to measure small ion fractions (i.e. < 1%) and determine these in scattering from a clean Ag(111) surface. However, we can make a rough estimate how the ion fraction behaves with outgoing angle, by comparing the angular distributions of the scattered negatives from both Ag(111) and Ba/Ag(111).

In Fig. 2.19(a) the normalized ratio (H_{Ag}^-/H_{Ba}^-) of angular distributions of the total yield of H$^-$ from Ag(111) and Ba/Ag(111) is shown. The three-dimensional intensity distributions, depicted in Fig. 2.11(a) and (b), were energy integrated. Fig. 2.19(a) shows, that between $\theta_f = -15°$ and $\theta_f = 45°$ the ratio is more or less constant. However, for larger outgoing angles ($\theta_f > 50°$) the ratio decreases significantly indicating that the negative ion fraction also decreases compared to the Ba case. In Fig. 2.19(b) the fraction from Ba/Ag(111) (*) and Ag(111) (•) as a function of outgoing angle are depicted. The fraction from Ag(111) is obtained by multiplying the fraction from Ba/Ag(111) by the ratio depicted in Fig. 2.19(a) and scaling it to 0.01. Clearly, the negative ion fraction in the Ag case decreases at smaller outgoing angles than in the Ba/Ag case. The high work function of the Ag(111) surface, allows for more time for the negative ion to back donate its electron for a similar $v_\perp$.
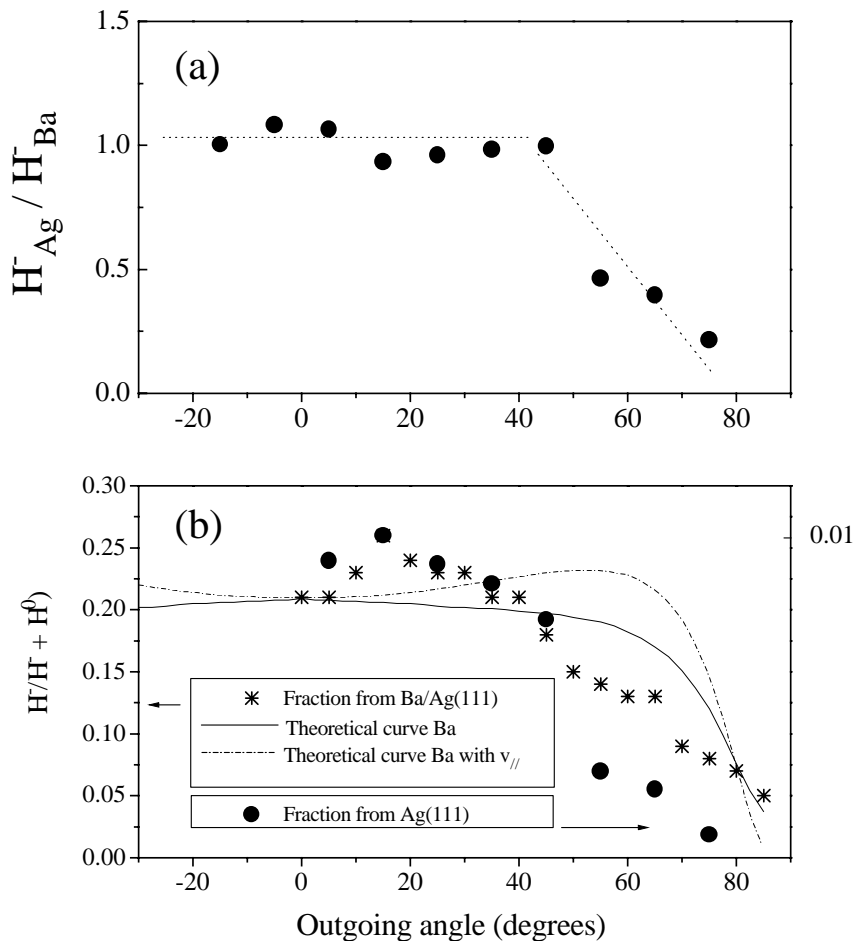
Figure 2.19 *(a) normalized ratio of the energy integrated angular distributions of H⁻ from Ag(111) and Ba/Ag(111). (b) negative ion fraction as a function outgoing angle from Ba/Ag(111) (∗) and Ag(111) (•). The lines give the results of a theoretical calculations with (dashed line) and without (solid line) the parallel velocity effect taken into account.*

The negative ionization probability depends on the normal velocity component ($v_\perp$) of the particles leaving the surface. In the low incident energy regime the parallel velocity component ($v_{//}$) is also important, to a lesser extent. If a trajectory dependent charge transfer event is to be observed, the experiments should be done with fixed θ_i and θ_f (i.e. fixing the normal and parallel velocity components). This is most easily done by looking at the charged fractions as a function of azimuthal angle [55,66]. In the current experiment we did not observe a change in negative ion yield for scattering along different crystallographic directions and, hence, no trajectory effect is observed. However, most hydrogen particles penetrate the crystal lattice as we demonstrated in our classical trajectory calculations. It may well be that a trajectory dependent charge transfer is present but that we are not sufficiently sensitive to detect it. Observing a trajectory dependent charge transfer in negative ion formation is complicated by the fact that most of the hydrogen particles come

from deep within the crystal lattice. On exiting the crystal lattice their final charge state is determined at some distance from the surface. The depopulation of the affinity level occurs at relatively large distances from the Ba/Ag(111) surface (> 1.6 Å) [57].

2.5.3 Surface structure analysis: Location of the barium atoms

The azimuthal scans and angular distributions of H^- scattered from clean Ag(111) and one monolayer of barium covered Ag(111) appear identical. Only the yield of negative ions as a function outgoing angle is different, which we attribute to different angular dependencies of negative ion formation. The scattering data, together with the classical trajectory calculations strongly suggest that the barium atoms occupy three-fold hollow sites of the Ag(111) lattice. The classical trajectory calculations indicate that if the barium atoms are located at positions other than the fcc three-fold hollow sites, the angular distributions would look dramatically different. Previous studies on the adsorption of barium on Ag(111) suggest the formation of a complete monolayer with a density of 0.61×10^{15} particles/cm^2, after which a rather open overlayer is formed by Poisson growth [43]. The results in the current chapter indicate that three-fold hollow (fcc) sites are occupied. The density of the barium overlayer is lower than that of the Ag substrate layer as was indicated by previously obtained MEIS results [43]. This was attributed to the larger size of the barium atoms. However, we can not give the long range order of the barium overlayer because we are not sensitive to that. Epitaxial growth with vacancies to accommodate the large adsorbate atoms have also been found by Lamble and King [75]. They studied the adsorption of Cs on Ag(111) with EXAFS and found a very open structure with all the Cs atoms sitting at the three-fold hollow sites. Perhaps a structural study using another structure sensitive technique will shed more light on the long range order of the barium overlayer.

Using the detection of backscattered negative hydrogen ions in ion beam crystallography studies with low-energy protons incident on metal surfaces, appreciable depth information can be obtained. In this chapter we have demonstrated that we can distinguish ions coming from the second layer and ions coming from the fourth and even the fifth layers. With the detection of backscattered positive ions this is not possible in the low incident energy regime, because of extensive neutralization of the ions when penetration into the solid occurs. This depth information can be achieved in LEIS, when backscattered neutrals are detected. However, in the case of negative ions (H^-) an electrostatic analyzer (ESA) can be used and, hence, energy analysis on the backscattered ions can be performed; elemental specific information can be obtained. Especially in conjunction with "conventional" LEIS using He^+ or Ne^+, the detection of negatively charged hydrogen ions gives additional information concerning the structures of overlayers deposited onto metal surfaces.

2.6 Summary and conclusions

In the scattering of H^+ from a clean and barium covered Ag(111) surface, reflection from deeper layers is observed. The backscattered negative and neutral hydrogen particles show the same angular and azimuthal dependencies. The differences in the angular behaviour is explained with a difference in negative ion formation as a function of outgoing angle. The final charge state of the particles is determined on exiting the surface layer. The

energy distributions of the negative ions indicate a large penetration depth along the crystal channels. Classical trajectory calculations reproduce the qualitative features of the angular distributions of the neutral and negative particles and an assignment of the trajectories has been made. The extrapolated HFS/LCAO Ag-H pair potential used in these calculations describes the interaction very well. For the scattering conditions used in this study, the interaction between the H atom and Ag atoms can be considered a sequence of binary collisions. The (electronic) stopping inside the Ag solid is at least one or two orders of magnitude smaller (< 0.3 eV/$\mathring{A}$ at E = 700 eV) than the values found in literature.

The energy losses of the detected H$^-$ in scattering from a clean Ag(111) surface are accounted for by the binary collision formula. In scattering from a Ba/Ag(111) surface, additional inelastic energy losses of the scattered ions are observed, which are due to the lowering of the work function and/or an increase of the electron density near the Fermi-level. The negative ion fraction in the Ag case decreases at smaller outgoing angles than in the Ba/Ag case. The high work function of the Ag(111) surface allows for more time for the negative ion to donate back its electron for a similar $v_\perp$. No trajectory dependent charge transfer events have been observed in scattering from a Ba/Ag(111) surface.

The angular distributions and azimuthal scans do not significantly change with covering the Ag(111) surface with one monolayer of barium. This indicates that the barium atoms must sit in the three fold hollow (fcc) sites of the surface. The layer must contain vacancies to accommodate the large barium atoms on the substrate. Appreciable depth information can be obtained in surface structure analysis studies via the detection of negatively charged low-energy hydrogen ions.

Chapter 3

Dissociative scattering of polyatomic ions from metal surfaces: $\mathrm{CF_3^+}$ on Ag(111) and Ba/Ag(111)

Abstract

The dissociative scattering of $\mathrm{CF_3^+}$ *ions from a clean Ag(111) and a barium covered Ag(111) surface was explored in the energy range 100-to 600-eV. Both negative ($\mathrm{CF_3^-}$, $\mathrm{CF_2^-}$ and $\mathrm{F^-}$) and positive ($\mathrm{CF^+}$ and $\mathrm{C^+}$) ions were formed. The complete dissociation of the $\mathrm{CF_3^+}$ ions into $\mathrm{C^+}$ fragments was found to be feasible at low (normal) incoming energies. We conclude that the breaking of three C-F bonds is due to concerted electronic and mechanical energy transfer. The azimuthal orientation of the crystal has a large influence on the degree of dissociation, which indicates the importance of direct momentum transfer. For the barium covered Ag(111) surface the negatively charged scattering products only showed $\mathrm{F^-}$ and the positives showed $\mathrm{CF^+}$ and $\mathrm{C^+}$ fragments. No negatively charged polyatomic ions are observed. The lowering of the work function facilitates resonant neutralization into the excited 3s Rydberg state of the neutral molecule. Consequently, the spectral features associated with Auger neutralization are not observed.*

3.1 Introduction

The interaction of polyatomic ions with surfaces plays an important role in many areas of physics and chemistry. These include plasma-wall interactions in fusion devices, etching reactions in the semiconductor industry, the study of chemical reactions at surfaces and recently mass spectrometry. In the latter case, the fragmentation of polyatomic ions at surfaces, so-called surface-induced dissociation (SID), is used as an alternative to fragmentation by collisions with noble gas atoms [30,76]. This is especially useful for the study of large molecules because the better defined energy transfer in the ion-surface collision can lead to specific fragment ions and hence, more structural information concerning the parent ions [77]. Important fundamental yet unknown processes involved in SID are the neutralization of the incoming parent ion and of the outgoing fragments, the (re)ionization processes and the dissociation mechanisms.

Several models have been proposed to describe ion-surface encounters for small diatomic ions [10]. The neutralization step is usually treated by one of two mechanisms: Auger neutralization (AN) or resonant neutralization (RN) [32,78]. The relative importance of these processes is still a matter of debate [79]. The dissociation mechanisms can be divided into electronic processes and collision-induced dissociation (CID). In the first case, an electron near the Fermi-level is captured into a dissociative neutral state [80] or dissociation occurs due to the temporary formation of a negative ion [16]. In CID, translational energy is transferred into internal energy leading to the rupture of a bond. This is a (predissociation) process where the rotational [19] and/or vibrational energy [81–83] content exceeds the dissociation energy of the molecule.

To distinguish between the different dissociation mechanisms we use different scattering geometries in our experiment. By varying the incoming angle θ_i and energy E_i, we can lower the normal energy ($E_n = E_i \cos^2 \theta_i$) and exclude CID [84], and hence focus on dissociation mediated by electronic processes. On the other hand, by increasing E_n we can study CID directly [17,83,85]. CID can also be studied by varying the azimuthal orientation of the crystal Φ and keeping E_i and the scattering geometry constant.

Only a few experiments have been performed on the scattering of large polyatomic ions on well defined surfaces. In this chapter we demonstrate for the first time the complete break-up of a low energy tetra-atomic ion colliding with a well defined solid surface. A dissociation mechanism is proposed. We study CF_3^+ ions incident on a Ag(111) surface and a barium covered Ag(111) surface.

In this chapter, we present energy and angular distributions of negative and positive fragment ions in scattering of 100-to 600-eV CF_3^+ from Ag(111) and barium-covered Ag(111). We try to identify the principal neutralization and dissociation mechanisms leading to the manifold of negative and positive fragment ions in our experimental study. To achieve this, the incoming energy and scattering geometry are varied in our experiment; this allows for scattering along different azimuthal orientations of the crystal with different incoming angle and outgoing angle. The two principal azimuths of the Ag(111), the $(01\bar{1})$ and $(\bar{1}2\bar{1})$, differ from one another in the atomic spacing along the rows and separation between the rows of the surface atoms, enabling us to study surface corrugation effects in dissociative scattering of polyatomic ions

This chapter is divided into five main sections. In section 3.2 the experimental set-up, sample preparation and time-of-flight measurements are described. In section 3.3 the experimental spectra are presented and analyzed. The mechanisms governing ion-surface interactions are discussed in section 3.4. The chapter ends with a summary of the most important results.

3.2   Experimental

3.2.1   Set-up

The experimental set-up is described in detail in chapter 2. The CF_3^+ ions were produced by electron impact on CF_4 and accelerated to kinetic energies between 100 and 600 eV. A Wien filter was incorporated in the beamline to remove possible contaminants from the ion beam. The crystal is mounted on a 2-axis goniometer in the ultrahigh vacuum (UHV) chamber

(base pressure of 1×10^{-10} mbar). The crystal was cleaned by repeated Ar^+ sputter and anneal cycles and the surface cleanliness was checked by X-ray photoelectron spectroscopy (XPS) [57]. XPS showed no trace of surface fluorine or carbon after experiments. The scattered ions were detected with a 90° cylindrical electrostatic energy analyzer, with an energy resolution of $\Delta E / E = 0.08$. The detector can be rotated in and out of the plane of incidence. Time-of-flight (TOF) measurements were carried out to identify the mass of the fragment ions. The deflection plates in the Wien filter were pulsed and the flight times of the different ions as a function of their energy were determined. Both the energy and the mass spectra of the fragment ions were independent of exposure time to the ion beam. The amount of contaminants or metastables in the primary beam was less than 0.01%. Neutrals could not be detected in our experiment. However, the positive and negative fragment ions are good probes to study the dissociation dynamics of CF_3^+ on Ag(111), as has been shown before for diatomics [17,86]. The electron affinities of the different (fluorinated) fragments are 1.8±0.2 eV for CF_3 [87], 0.18 eV for CF_2 [88], 0.45±0.05 eV for CF [89] and 3.40 eV for F [90].

3.2.2 Time-of-flight measurements and analysis

To identify the mass of the fragment ions in the energy spectrum, time-of-flight (TOF) measurements were carried out. These were done by pulsing the deflection plates in the Wien filter and measuring the time-of-flight spectra using a multichannel scaler (EG&G, turbo MCS). In these TOF-measurements, the energy analyzer was fixed at a particular acceptance energy. In this way we can determine the flight-times of the different (fragment) ions as a function of their energy and hence determine their mass. In the present experiment, all the detected ions are singly charged. A schematic overview of the experimental set-up is drawn in Fig. 3.1.

A pulse generator (Hewlett-Packard) is set at a repetition rate of 10 kHz, with rise and fall times of .1 μs and the pulses have a width of 30 ns and amplitude of 5 V. The pulses are amplified to 60 V by a wide band amplifier and subsequently fed into an oscilloscope and to one of the Wien filter plates. The other Wien filter plate is set to a constant voltage of -60 V. The signal of the pulse generator is also fed into a tail-pulse generator (rise time .05 μs, fall time 1 μs) for generating a start pulse for the MCS. The Wien filter is normally closed and the ions only pass for about 30 ns, every 100 μs. The flight times of the ions from the exit of the Wien filter to the channeltron are on the order of tens of μs and peaks widths (FWHM) of .3 μs are measured.

The mass assignment is done by :

$$t_{tot} = t_a + t_b \tag{3.1}$$

with t_a the flight time from Wien filter to crystal, t_b the flight time from crystal to detector and t_{tot} the total flight time as measured. This can be rewritten as:

$$t_{tot} = L_a \sqrt{\frac{M_1}{2eU_0}} + L_b \sqrt{\frac{M_2}{2e}} E_f^{-1/2} = C_0 + C_1 . E_f^{-1/2} \tag{3.2}$$

where
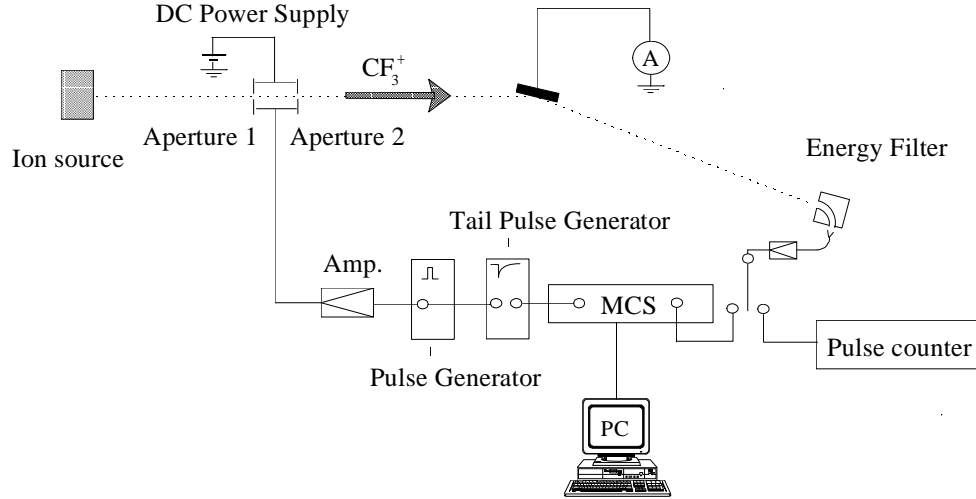
Figure 3.1 *Experimental set-up for time-of-flight measurements for the mass identification of the fragment ions.*

$$
\begin{aligned}
C_0 &= L_a \sqrt{\frac{M_1}{2eU_0}} \\
C_1 &= L_b \sqrt{\frac{M_2}{2e}}
\end{aligned}
$$

M_1 : mass of CF_3^+ ion

M_2 : mass of unknown fragment ion

e : elementary charge constant

U_0 : acceleration voltage of CF_3^+ ion

L_a : distance from Wien filter to crystal

L_b : distance from crystal to detector

E_f : fixed energy of energy analyzer

t_{tot} is now a linear function of $E_f^{-1/2}$ (C_0 is a constant). By determining the slope of this function we can estimate the mass of the fragment ion.

3.2.3   The sample

The Ag(111) crystal was cut by spark erosion and polished mechanically. The misalignment of the (111) surface is smaller than 0.05° as determined by Von Laue diffraction. The crystal was cleaned by repeated sputter and anneal cycles. Typically, a sputter treatment consists of 15 min. of 800 eV Ar^+ bombardment at normal angle of incidence for a crystal current density of $5 \times 10^{-6} A/cm^2$. The crystal temperature during sputtering is 573 K. For annealing the crystal temperature is kept at 673 K for 15 min. The surface cleanliness is checked by XPS and work function measurements. The crystal surface structure is drawn in Fig. 3.2, in which the crystallographic directions are shown. The $(10\bar{1})$ direction is defined as $\Phi = 0°$. The crystal orientations of the Ag(111) crystal have been accurately ($\sim 0.5°$) determined
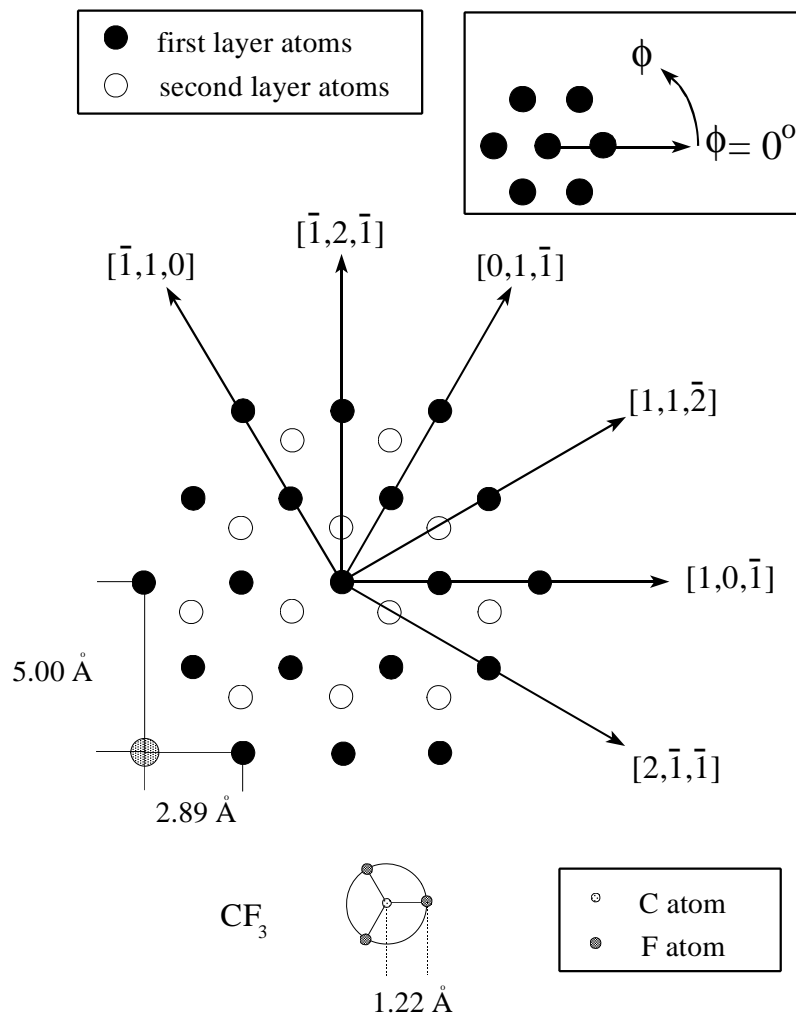
Figure 3.2 *Crystallographic drawing of the (111) face of a Ag crystal. The crystal directions and the definition of ϕ are indicated. Also shown are the bond lengths of the CF_3^+ ion.*

by H^+ scattering (see chapter 2). All the spectra in this chapter were measured with a crystal near room temperature. In addition, Fig. 3.2 displays the bond lengths of the CF_3^+ ion [91]. The ion is drawn in its planar geometrical structure, as calculated in Ref. [91]. The neutral displays an umbrella-like structure.

Barium is deposited onto the Ag(111) surface from a SAES-Getter source. The pressure during dosing was below 2×10^{-10} mbar. The barium overlayer was previously character-ized using Auger electron spectroscopy (AES), XPS, work function measurements, medium energy ion scattering (MEIS) and low energy H^+ scattering [43,59,60]. In the latter case, backscattered H^- ions were probed [59]. Previous work indicated that a monolayer of bar-ium is initially grown, after which a rather open overlayer structure is formed by Poisson growth and is epitaxially grown. All the barium atoms occupy three-fold hollow sites of the Ag(111) lattice. Due to the difference in size of the adsorbate and substrate atoms, the first layer appears to be incomplete and must contain vacancies. The work function of a

clean Ag(111) surface is 4.7 eV. When the surface is covered with one monolayer of barium the work function decreases to 2.4 eV [43].

3.2.4   Measurement procedure

In a typical measurement, the incoming angle θ_i and the azimuthal orientation Φ are kept constant. The detector is kept in the scattering plane at a fixed outgoing angle θ_f. The intensity I of the positive and negative ions is measured as a function of their final energy E_f by scanning the detector voltage. This procedure is repeated for various outgoing angles, so that a three-dimensional intensity distribution $I(\theta_f, E_f)$ is obtained. In an azimuthal scan the incoming angle, outgoing angle and final energy are kept constant. The intensity of the ions or neutrals is measured as a function of azimuthal angle by spinning the crystal around its axis.

3.3   Results and analysis

3.3.1   Scattering from clean Ag(111)

In the following sections, the results when CF_3^+ is scattered from Ag(111), and the yields of the scattered negative and positive fragment ions are determined. Scattering occurs along the two principal azimuths of the Ag(111) surface, the $(01\bar{1})$ and $(\bar{1}2\bar{1})$ directions. The peaks in the energy distributions can be described by single and double collisions of the incident particles with the Ag-atoms. The fragmented particles leave the surface with the same speed. These conclusions are verified with time-of-flight measurements.

Negative fragment ions

The energy distributions for the scattering of a beam of CF_3^+ ions from Ag(111) leading to negative fragment ions for different scattering geometries and incident energies are shown in Fig. 3.3. The measured intensities are plotted on a logarithmic scale. Fig. 3.3(a) shows scattering along the close packed direction $(01\bar{1})$, defined as $\Phi = 60°$. The data are taken at $\theta_i = 70°$, $\theta_f = 75°$ and $E_i = 500$ eV. Both angles are measured with respect to the surface normal. Three peaks are clearly visible and indicated with labeled arrows. For the mass assignment a double collision of CF_3 with the silver atoms is assumed. After scattering, the parent and fragmented particles leave the surface with the same speed and have a final energy which is proportional to their mass. TOF measurements at selected energies confirmed the mass assignment. Several TOF spectra for negative ions with final energies ranging from 35-to 420-eV are drawn in Fig. 3.4. The scattering geometry and beam energy are the same as in Fig. 3.3(a). For $E_f = 35$ eV we observe two peaks, at $t_1 = 23.2$ μs and at $t_2 = 33.7$ μs. These can be identified with (negatively ionized) sputtered particles and F^-, respectively. For $E_f = 145$ eV we observe a peak at t = 22.1 μs. This peak can be identified with F^-. For $E_f = 220$ eV, we observe three peaks, at $t_1 = 21.0$ μs, at $t_2 = 22.4$ μs and at $t_3 = 23.2$ μs. These can be identified with F^-, CF^- and CF_2^-, respectively. For $E_f = 310$ eV the CF_2^- fragment ion is observed at t = 22.1 μs. At $E_f = 420$ eV, the CF_3^- ion is observed at t = 22.3 μs. Because of the very low signal to noise ratio of the TOF
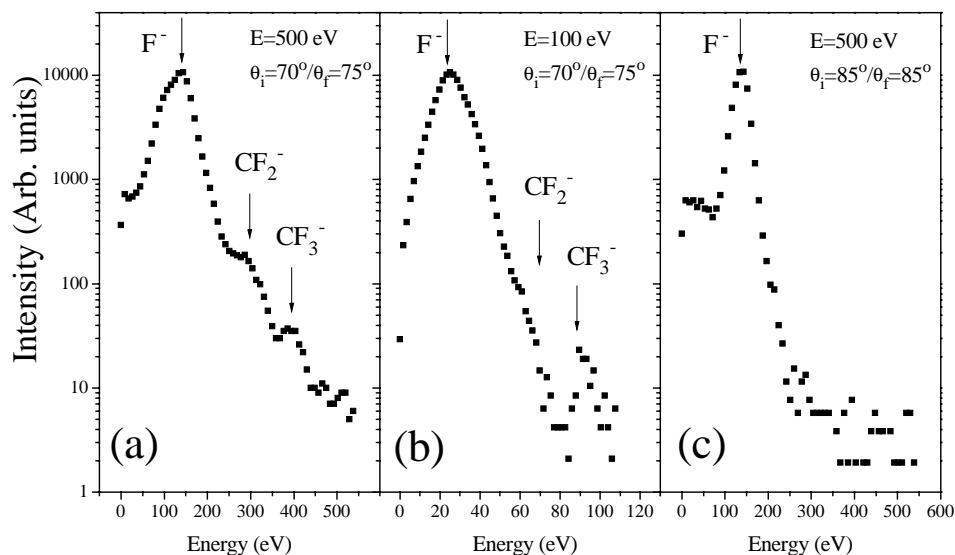
Figure 3.3 *Energy distributions for negative ions formed for different scattering geometries and incoming energies: (a) $\theta_i = 70°$, $\theta_f = 75°$, $E = 500\,eV$ and the $(01\bar{1})$ azimuth, (b) $\theta_i = 70°$, $\theta_f = 75°$, $E = 100\,eV$ and the $(01\bar{1})$ azimuth, and (c) $\theta_i = 85°$, $\theta_f = 85°$, $E = 500\,eV$ and the $(01\bar{1})$ azimuth. No correction for the energy dependent transmission of the energy analyzer has been made.*

experiments, no mass resolved energy spectra could be obtained. The TOF spectra show that CF_3^-, CF_2^-, CF^- and F^- are observed in the energy spectra. Also the assumption that the fragment ions leave the surface with the same speed is valid, thereby giving rise to the peak positions observed in the energy spectra. The dominant channel gives rise to F^-. We now investigate the incident energy dependence of the negative ion fragment signals.

In Fig. 3.3(b), the spectrum is shown for $E_i = 100$ eV. The scattering geometry is the same as in Fig. 3.3(a). Surprisingly, the CF_3^- peak is almost absent. The same behaviour is observed at more grazing angles of incidence with the incident energy held constant. In Fig. 3.3(c) a spectrum is shown for $\theta_i = 85°$, $\theta_f = 85°$ and $E_i = 500$ eV. Only the peak corresponding to F^- is observed. Thus we find that the CF_2^- and CF_3^- yields increase with increasing E_n ($E_n < 60$ eV). This is in dramatic contrast with the observations in previous studies on diatomic systems. For example, the scattering of O_2^+ from Ag(111), showed a decrease in molecular negative ion (O_2^-) yield relative to the atomic negative ion (O^-) yield with increasing E_n [17]. This was attributed to collision-induced dissociation of the molecular ions. It is clear that in our experiment another energy dependence is observed for the production of the negative parent ion, which is discussed in more detail in section 3.4.1.

In Fig. 3.5, the three-dimensional intensity distributions $I(\theta_f, E_f)$ and corresponding contour diagrams of the backscattered negative ions are plotted for 200 eV CF_3^+ ions incident on a Ag(111) surface. In both cases $\theta_i = 70°$ and scattering occurs along the $(01\bar{1})$ (a) and $(\bar{1}2\bar{1})$ (b) azimuths. The measured intensities are plotted on a linear scale. In these spectra only the F^- peak is observed which has its maximum around the specular direction for
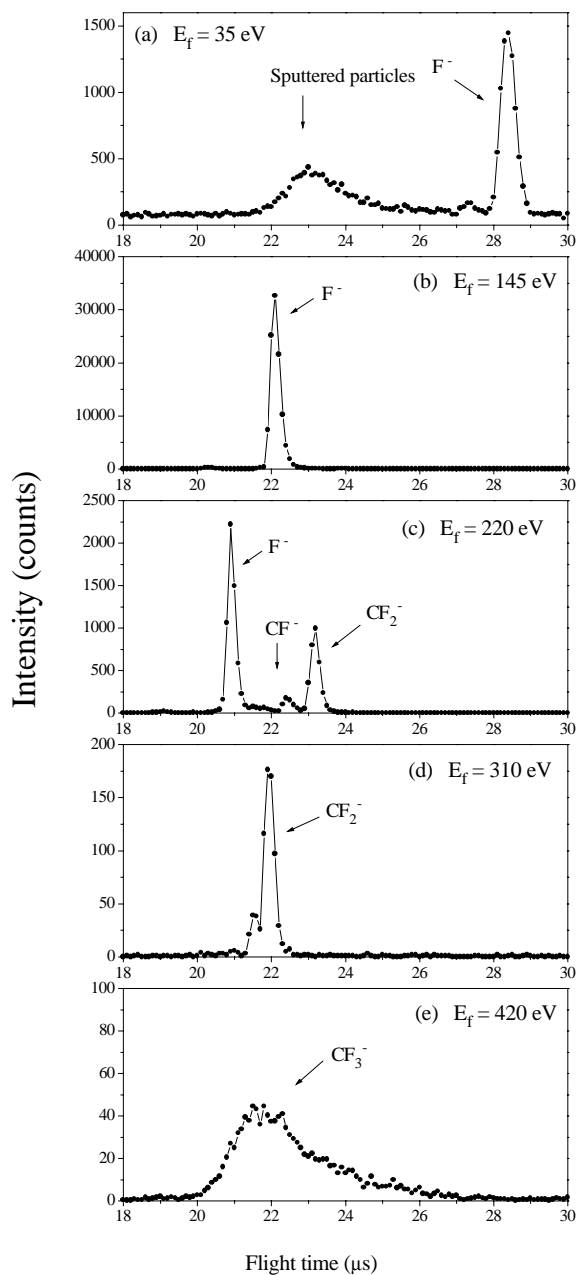
Figure 3.4 *Time-of-flight spectra for 500 eV CF_3^+ ions from Ag(111) along the $(01\bar{1})$ azimuth at different final energies: (a) $E_f = 35$ eV, (b) $E_f = 145$ eV, (c) $E_f = 220$ eV, (d) $E_f = 310$ eV and (e) $E_f = 420$ eV. The data are taken at $\theta_i = 70°$ / $\theta_f = 75°$.*
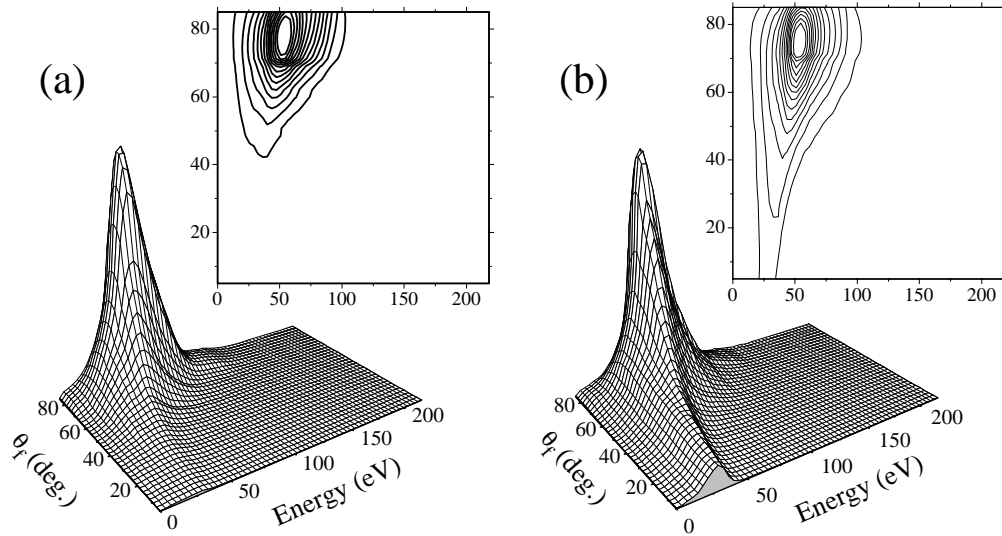
Figure 3.5   *Three-dimensional intensity distributions $I(\theta_f, E_f)$ and corresponding contour diagrams of negative ions formed in scattering of 200 eV CF_3^+ from Ag(111) along the $(01\bar{1})$ (a) and $(\bar{1}2\bar{1})$ (b) azimuths for $\theta_i = 70°$. The measured intensities are plotted on a linear scale. No correction for the energy-dependent transmission of the energy analyzer has been made.*

both azimuths. The angular distributions are sharply peaked, which indicates that not the impulsive collision but probable charge transfer leading to the removal of F atoms before the particle collides with the surface dominates the interaction. Scattering along the $(\bar{1}2\bar{1})$ leads to a broader angular distribution than scattering along the $(01\bar{1})$ direction, displaying the enhanced corrugation along the $(\bar{1}2\bar{1})$ direction.

Scanning the azimuth of the crystal and fixing the detection energy gives a symmetrical pattern corresponding to the hexagonal structure of the Ag(111) unit cell. These spectra are shown in Fig. 3.6 for (a) $E_f = 135$ eV and (b) $E_f = 400$ eV, the F^- and CF_3^- peak, respectively. The maxima in intensity are observed for scattering along low index directions. This behaviour has been observed before for O_2^+ scattering on Ag(111) and was attributed to more out of plane scattering along the higher index directions [92]. The dependence of the scattered intensity on the crystal azimuth rules out the possibility of defects being the origin of the experimental observations [93]. In Fig. 3.6(c) the ratio CF_3^- / F^- is depicted. Along the $\Phi = 0°, \pm 60°, \ldots$ directions, the close spaced directions, the intensity of the CF_3^- peak increases relative to the F^- peak intensity. This indicates that more survival of the CF_3^- occurs along the close spaced directions. This is even more apparent if we consider the energy distributions at different azimuthal orientations. Energy distributions for negative ions formed along the two major azimuthal orientations are depicted in Fig. 3.7. The data are taken at $\theta_i = 75°$, $\theta_f = 80°$, E = 500 eV along the (a) $(01\bar{1})$ and (b) $(\bar{1}2\bar{1})$ azimuths. In Fig. 3.7(a) we can clearly observe the CF_3^-, CF_2^- and F^- signals. At $E_f = 210$ eV the contribution of CF^- is observed, the presence of which was confirmed with the time-of-flight spectra depicted in Fig. 3.4. In Fig. 3.7(b) the same scattering geometry and E_i are used, but the azimuth of the crystal has been rotated through 30° and scattering takes place
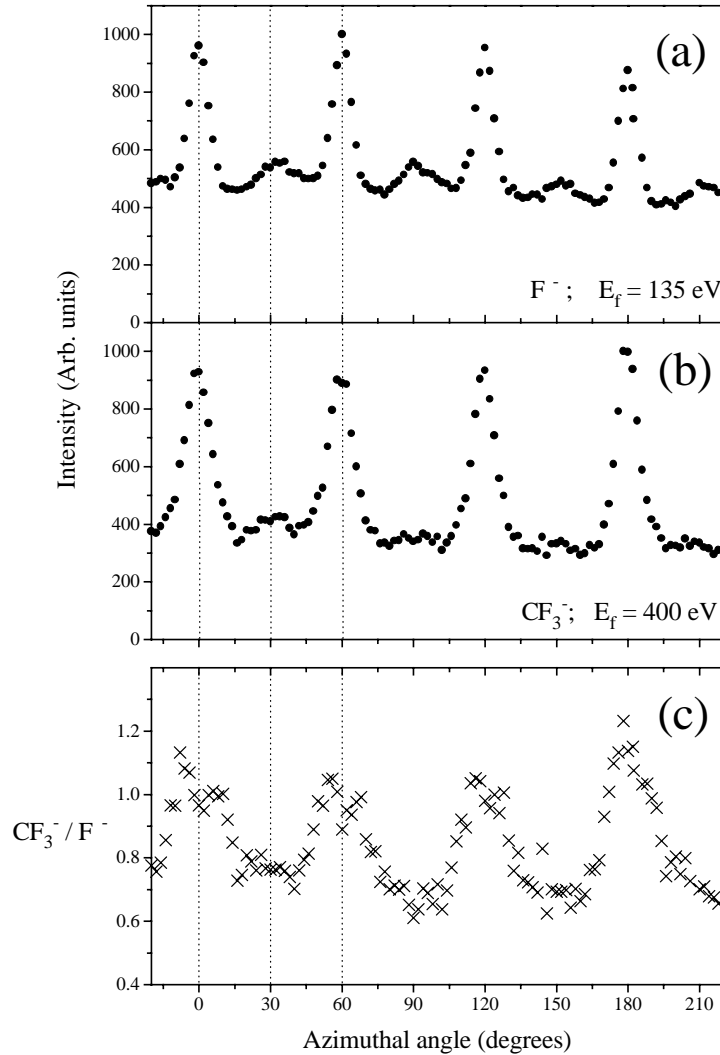
Figure 3.6 *Azimuthal dependence of backscattered* F^- *(top) and* CF_3^- *ions (center) in scattering of* CF_3^+ *from clean Ag(111) for* $\theta_i = 70°$ *and* $\theta_f = 75°$. *The data are taken at* $E_i = 500$ eV *and ions with a final energy of (a) 135 eV and (b) 400 eV are probed. (c) gives the ratio* CF_3^- / F^-.

along the open azimuthal direction $(\bar{1}2\bar{1})$ or $\Phi = 90°$. The F^- peak is still clearly visible, but the CF_2^- and CF_3^- peaks have diminished relative to the F^- peak.

In Fig. 3.8, the three-dimensional intensity distributions $I(\theta_f, E_f)$ and corresponding contour diagrams of the backscattered negative ions are plotted for 500 eV ions incident on a Ag(111) surface. In both cases the data are taken at $\theta_i = 40°$ and scattering occurs along the (a) $(01\bar{1})$ and (b) $(\bar{1}2\bar{1})$ azimuths. For these cases only the F^- ion is observed, which peaks at outgoing angles larger than specular. Also for both cases a peak near the surface normal is observed. The appearance of these angular distributions is indicative of surface rainbow scattering [9]. In Fig. 3.9 we have plotted the peak energy positions of the F^- as a function of total scattering angle θ for scattering along the $(01\bar{1})$ ($\times$) and $(\bar{1}2\bar{1})$ ($\bullet$) azimuthal directions. We can clearly see that the F^- ions leave the surface with less energy going to larger scattering angles, indicating more energy is transferred to the
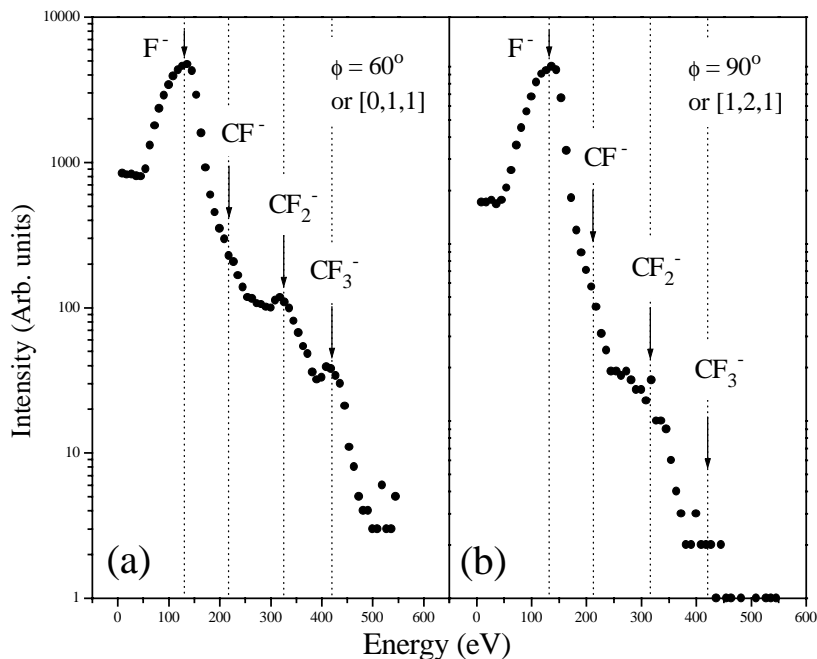
Figure 3.7 *Energy distributions for negative ions formed along different azimuthal orientations. The data are taken at $\theta_i = 75°$, $\theta_f = 80°$, $E = 500$ eV and the (a) $(01\bar{1})$ and (b) $(\bar{1}2\bar{1})$ azimuth. No correction for the energy dependent transmission of the energy analyzer has been made.*
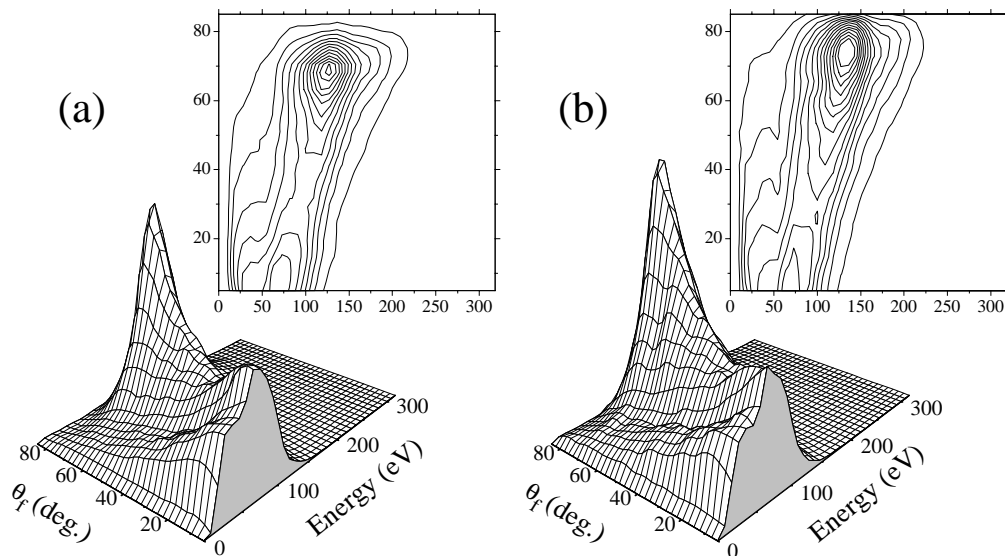
Figure 3.8 *Three-dimensional intensity distributions $I(\theta_f, E_f)$ and corresponding contour diagrams of negative ions formed in scattering of 500 eV CF_3^+ from Ag(111) along the $(01\bar{1})$ (a) and $(\bar{1}2\bar{1})$ (b) azimuths for $\theta_i = 40°$. The measured intensities are plotted on a linear scale. No correction for the energy-dependent transmission of the energy analyzer has been made.*
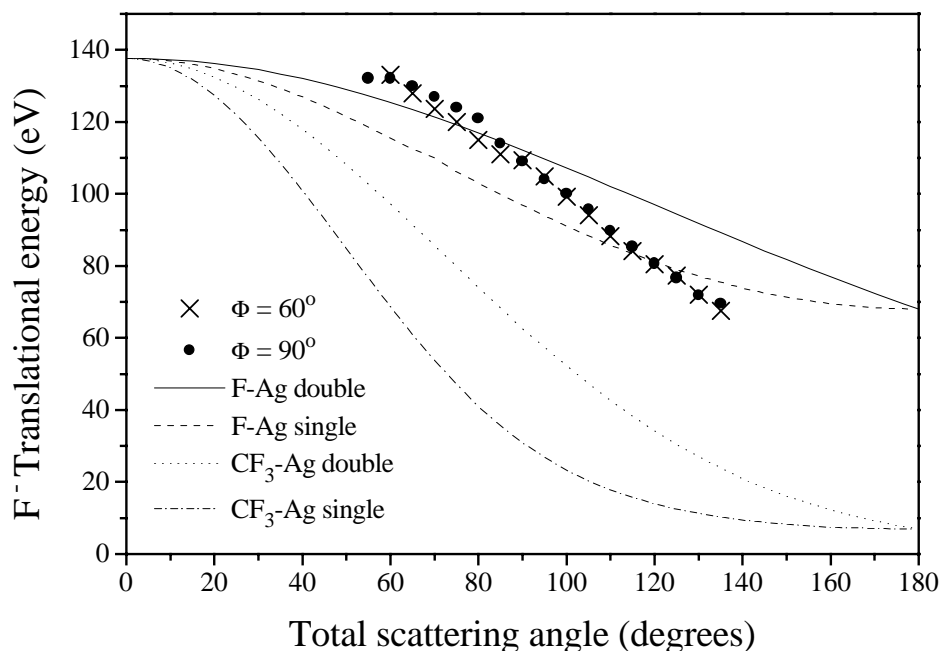
Figure 3.9 *Peak energy positions for identical scattering conditions as in Fig. 3.8 for scattering along $(01\bar{1})$ ($\times$) and $(\bar{1}2\bar{1})$ ($\bullet$). The lines in the figure were calculated from the binary collision model for F and CF_3 scattering from Ag(111).*

surface atoms. The *solid* line gives the translational energy of F atoms scattered from Ag atoms in a double collision applying the binary collision formula [10,11,34]. The *dashed* line gives the energy position of the F atoms in a single collision with the Ag atom. In both these cases, the dissociation of CF_3 molecules leading to F atoms is assumed to occur prior to the molecule/surface collision. In contrast, the *dotted* line gives the energy position of the F atoms if the entire CF_3 molecule scatters from the surface and the dissociation occurs after the collision, after which the fragments leave the surface with the same speed. The *dotted − dashed* line gives the energy position of the F atoms if the CF_3 molecule makes a single collision. At small scattering angles, the data points are best fit by the double scattering model for F from Ag, at larger scattering angles the data points are better described by a single collision model of a F atom scattered from the Ag surface. The present experimental results clearly indicate that the majority of the scattered F atoms are formed before the collision with the surface atoms.

Positive fragment ions

In Fig. 3.10, the energy and angular distributions of the backscattered positive ions along the two different azimuthal orientations are plotted for 500 eV CF_3^+ on Ag(111). In both cases $\theta_i = 70°$. The intensity is about two orders of magnitude lower and, remarkably, the fragmentation pattern is completely different from the negative ion case. Neither the parent ion CF_3^+ nor CF_2^+ is present and the peaks are assigned to C^+ and CF^+ fragments. Along
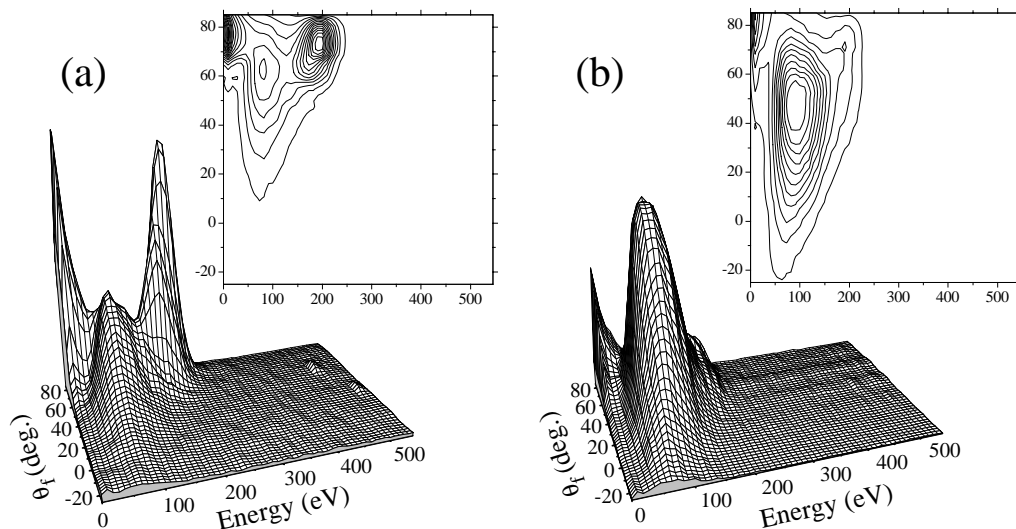
Figure 3.10 *Three-dimensional intensity distributions $I(\theta_f, E_f)$ and corresponding contour diagrams of positive ions formed in scattering of 500 eV CF_3^+ from Ag(111) along the $(01\bar{1})$ (a) and $(\bar{1}2\bar{1})$ (b) azimuths for $\theta_i = 70°$. The measured intensities are plotted on a linear scale. No correction for the energy-dependent transmission of the energy analyzer has been made.*

the close packed direction $\Phi = 60°$ (Fig. 3.10(a)), the CF^+ ions at $E_f = 195$ eV are strongly peaked around the specular direction. Apparently they are formed in rather soft collisions, presumably not from CF_3 neutrals after CID but from CF_2 or CF formed by charge transfer. The C^+ ions at $E_f = 82$ eV appear at larger scattering angles and show a broad angular distribution. The maximum in intensity is observed at $\theta_f = 65°$. This is an indication that the C^+ ions are formed in hard collisions with the surface atoms. When we scatter along the open azimuthal direction (Fig. 3.10(b)), we observe a decrease in CF^+ intensity and an increase in C^+ intensity. The angular distribution of the latter is even broader and shifted towards even larger scattering angles compared to the one in Fig. 3.10(a). The maximum in intensity is now observed at $\theta_f = 45°$. The peaks around 10 eV in both spectra can be attributed to sputtered positive ions from the surface [85]. In contrast to all other features, the 10 eV peak showed a slight increase with exposure time.

To examine the incident energy dependence of the backscattered positive ion signal along the two different azimuthal orientations, the translational energy of the incident CF_3^+ ions is varied from 200 eV to 400 eV. Fig. 3.11(a) to (c) display the three-dimensional intensity distributions $I(\theta_f, E_f)$ for scattering along the $(01\bar{1})$ azimuth for $\theta_i = 70°$ and incident energies: (a) 200 eV, (b) 300 eV and (c) 400 eV. For the lowest incident energies, only the CF^+ ion is observed, which displays a sharp angular distribution around the specular scattering direction. Only at an incident energy of 400 eV does the C^+ ion become apparent. For scattering along the $(\bar{1}2\bar{1})$ azimuth (Fig. 3.11(d) to (f)) essentially the same trends are observed. However, more fragmentation is observed for this case and the angular distributions of the C^+ ions are broader and shifted towards larger scattering angles as was also seen in Fig. 3.10 for an incident energy of 500 eV. Moreover, the onset of fragmentation
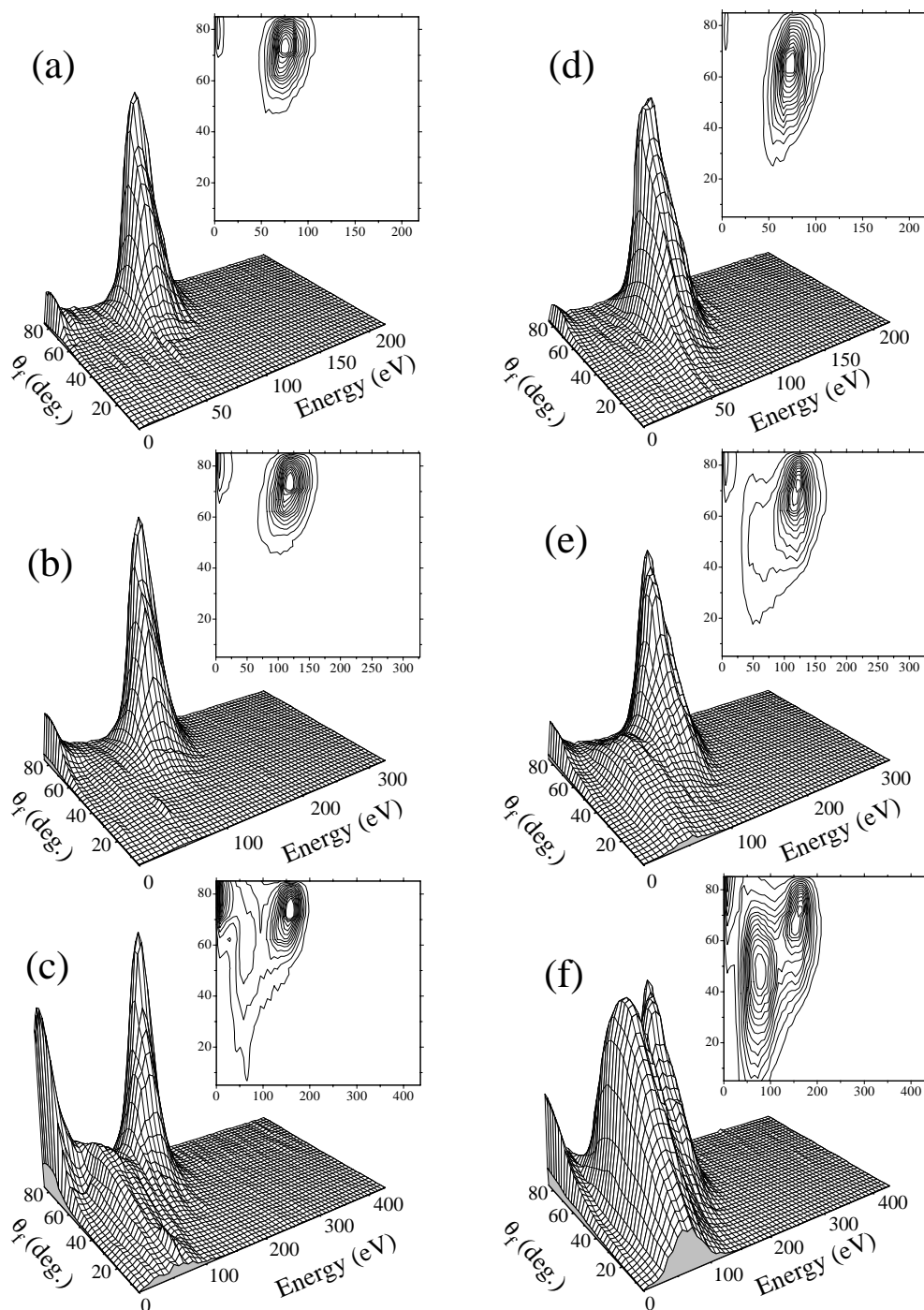
**Figure 3.11**   *Three-dimensional intensity distributions $I(\theta_f, E_f)$ of positive ions formed in scattering of 200 eV (a,d), 300 eV (b,e) and 400 eV (c,f) CF_3^+ from Ag(111) along the $(01\bar{1})$ (a,b,c) and $(\bar{1}2\bar{1})$ (d,e,f)) azimuths for $\theta_i = 70°$. The measured intensities are plotted on a linear scale. No correction for the energy-dependent transmission of the energy analyzer has been made.*
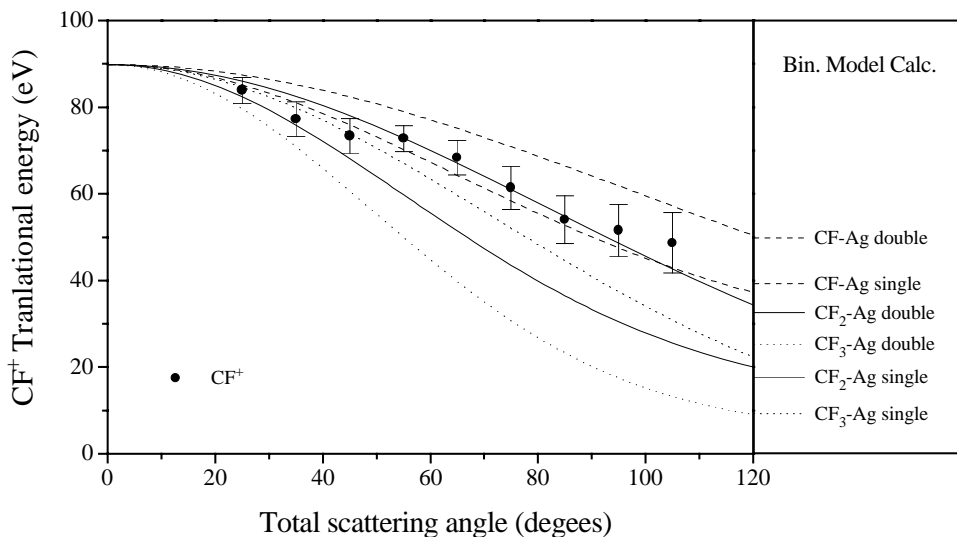
Figure 3.12 *The average translational energy of scattered CF^+ ions as a function of total scattering angle. The data are taken at $\theta_i = 70°$, and the initial energy of the CF_3^+ beam is 200 eV. The lines in the figure were calculated from the binary collision model for CF (dashed lines), CF_2 (solid lines) and CF_3 (dotted lines) for single and double scattering events.*

into C^+ occurs at lower incident translational energies. The angular distributions of the CF^+ ions is significantly broader than for scattering along the $(01\bar{1})$ azimuth (compare Fig. 3.11(a) and (d)) and the peak is observed at scattering angles larger than specular. The sputtered positive ion signal is significantly reduced for lower incident energies.

Fig. 3.12 displays the average translational energy of the scattered CF^+ ions as a function of total scattering angle for 200 eV CF_3^+ on Ag(111). The scattering occurs along the $(\bar{1}2\bar{1})$ azimuth. Clearly, more translational energy is lost going to larger scattering angles, indicating harder collisions of the incident particles with the surface atoms; hence more translational energy transfer to the surface atoms occurs for larger total scattering angles. For a total scattering angle of 25°, the CF^+ ion escapes with an average translational energy which is 42% of the initial CF_3^+ translational energy. For a total scattering angle of 95° this value is 25%. Larger scattering angles of the ions can be associated with smaller impact parameter collisions of the incident particles [94,95]. The energy and angular distributions of the scattered ions provide information on the influence of impact parameter in surface-induced dissociation. The lines in Fig. 3.12 are discussed in section 3.4.3.

Scattering along different azimuthal orientations of the crystal and fixing the detection energy again gives a symmetrical pattern corresponding to the hexagonal structure of the Ag(111) unit cell. These spectra are displayed in Fig. 3.13 for $E_f = 200$ eV and $E_f = 90$ eV, the CF^+ and C^+ peak, respectively. In this case, however, survival of the CF^+ ion is observed for scattering along low index directions. Scattering along high index directions gives more fragmentation, and hence the maximum yields of C^+ ions. These azimuthal scans and the energy-angular distributions of the fragment ions along the two principal azimuthal orientations clearly show the influence of the surface corrugation in polyatomic
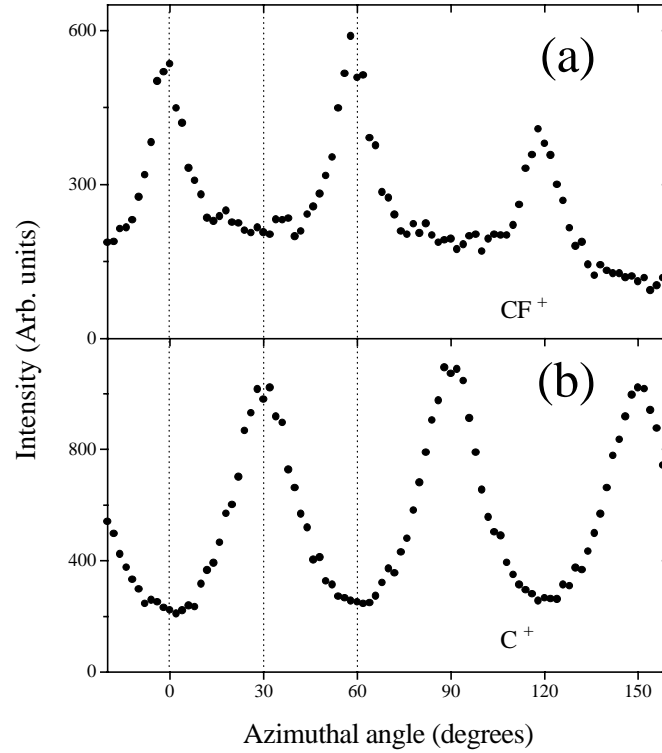
Figure 3.13 *Azimuthal dependence of backscattered* CF^+ *(top) and* C^+ *ions (bottom) in scattering of* CF_3^+ *from clean Ag(111) surface for* $E_i = 500$ *eV. The data are taken at* $\theta_i = 70°$, $\theta_f = 75°$ *and* $E_f = 200$ *eV (top), and* $\theta_i = 70°$, $\theta_f = 45°$ *and* $E_f = 90$ *eV (bottom).*

ion/surface scattering.

The incident energy dependence of the C^+ and CF^+ ion yields for CF_3^+ incident on Ag(111) along the close packed azimuthal direction is plotted in Fig. 3.14, for $\theta_i = 70°$ and the ions detected at $\theta_f = 65°$ and $\theta_f = 75°$ are summed. The C^+ intensity increases linearly with increasing incoming energy, while the CF^+ intensity decreases. The dip in intensity at the low energy side has observed been before by Murata at al. for other systems [81,96]. A threshold for C^+ appearance is observed at $E_i = 220$ eV, which corresponds to $E_n = 220 \cos^2 70° = 26$ eV.

Fig. 3.15 displays the average translational energy of the scattered CF^+ ions as a function of the incident CF_3^+ translational energy for two total scattering angles: (a) $35°$ and (b) $45°$, respectively. The incoming angle is $70°$ and scattering occurs along the $(01\bar{1})$ azimuth of the Ag(111) crystal. For both scattering angles, the average CF^+ translational energy displays a linear increase with CF_3^+ translational energy. Fig. 3.15(a) shows that upon collisions with the Ag(111) surface, the CF^+ escapes with 40% of the initial CF_3^+ translational energy for $\theta = 35°$. Similarly, Fig. 3.15(b) shows that the CF^+ fragment retains 37% of the incident CF_3^+ translational energy after it scatters from the surface over $\theta = 45°$. The lines in Fig. 3.15 are linear fits to the data points and are constrained to pass through the origin.
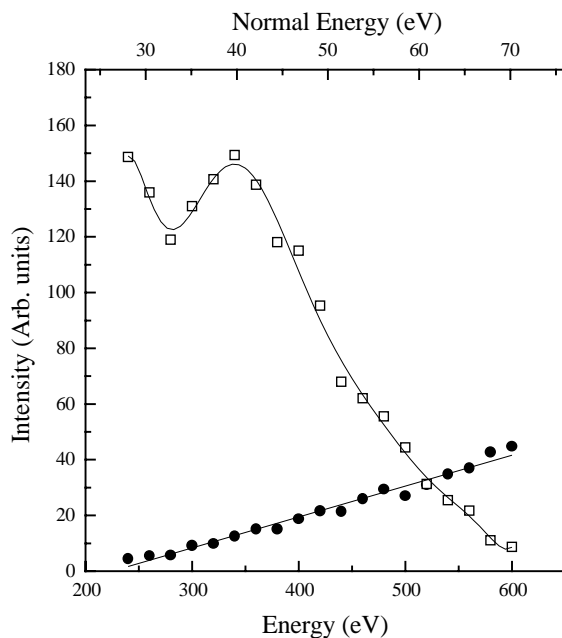
Figure 3.14 *Scattered ion yields as a function of incident energy for CF^+ (open squares) and C^+ (solid circles) with CF_3^+ incident on Ag(111) along the (01$\bar{1}$) azimuth, for $\theta_i = 70°$ and ions with $\theta_f = 65°$ and $\theta_f = 75°$ are detected; the sum is plotted. Lines are drawn to guide the eye. No correction for the energy dependent transmission of the energy analyzer has been made.*
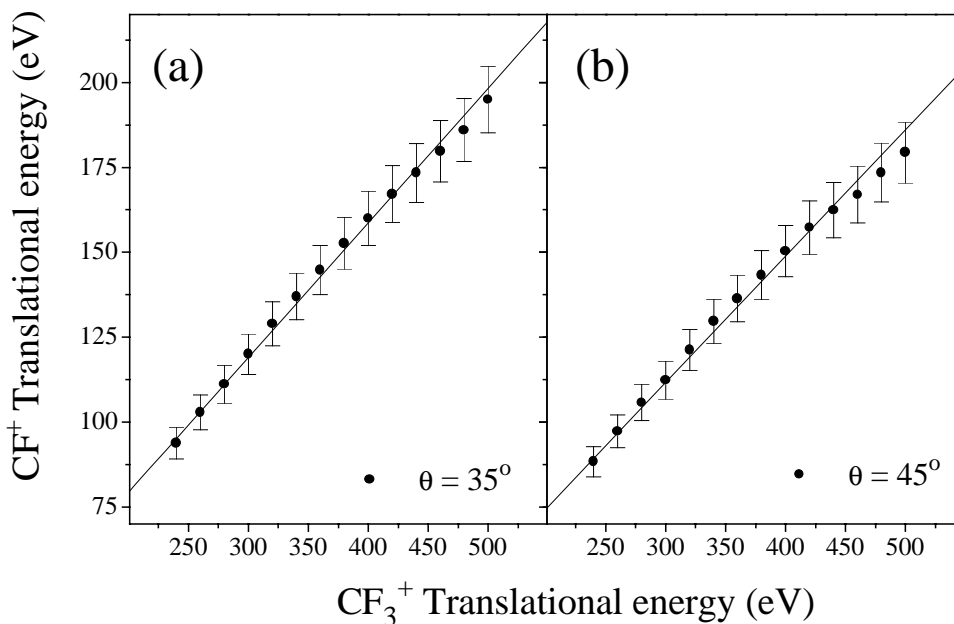
Figure 3.15 *The average translational energy of scattered CF^+ ions as a function of the CF_3^+ translational energy for two total scattering angles (a) 35° and (b) 45°. The data are taken at $\theta_i = 70°$ and, (a) $\theta_f = 75°$ and (b) $\theta_f = 65°$.*
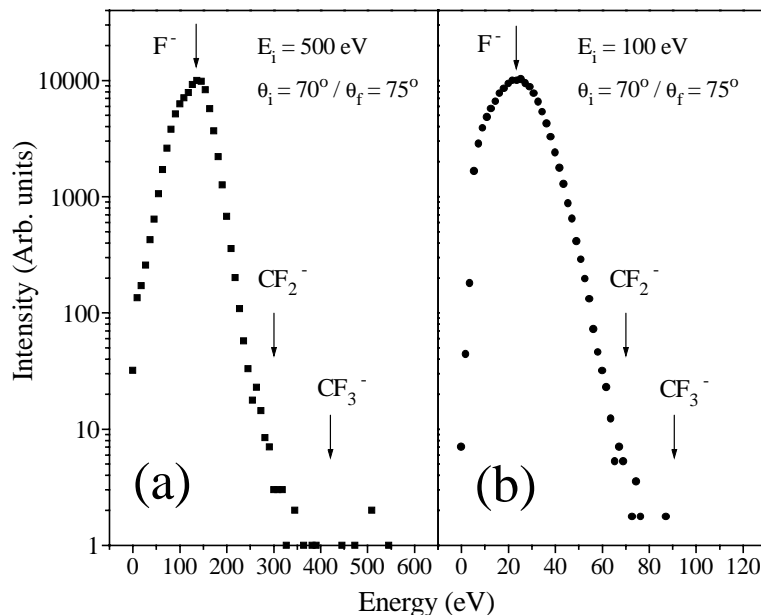
Figure 3.16 *Energy distributions for negative ions formed in scattering of CF_3^+ from a Ba/Ag(111) surface for two different incoming energies: (a) 500 eV and (b) 100 eV. The data are taken at $\theta_i = 70°$, $\theta_f = 75°$ and the $(01\bar{1})$ azimuth. No correction for the energy dependent transmission of the energy analyzer has been made.*

3.3.2 Scattering from barium-covered Ag(111)

In the following sections, the results when CF_3^+ is scattered off Ag(111) covered by one monolayer of barium. The Ba/Ag(111) system was extensively studied in chapter 2 of this thesis and in Refs. [43,59,60]. The work function of the surface is lowered from 4.7 eV for clean Ag(111) to 2.3 eV for Ba/Ag(111).

Negative fragment ions

The energy distributions for the scattering of (a) 500 eV and (b) 100 eV CF_3^+ ions from a barium covered Ag(111) surface leading to negative fragment ions are shown in Fig. 3.16. The data are taken at $\theta_i = 70°$, $\theta_f = 75°$ and scattering occurs along the $(01\bar{1})$ azimuth; the measured intensities are plotted on a logarithmic scale. The scattering geometry used, is the same as in Fig. 3.3(a) and (b) where the energy spectra for scattering from a clean Ag(111) surface are shown. Covering the surface with barium, and in this way lowering the work function of the surface, has a distinct effect on the production of negatively charged polyatomic ions. The energy positions of the polyatomic ions as were observed in the clean Ag(111) case, are indicated with labeled arrows. The CF_3^- and CF_2^- ions are not observed. Only F^- is present in the spectra, with a yield on the order of 20% of the incoming CF_3^+ ions. The F^- yield has increased by a factor of two compared to the clean Ag case. This relatively small increase in yield confirms the large number of negative ions observed in scattering off clean Ag(111). It is well known that lowering the work function results in a larger yield of negative ions [32]. For O_2^- and CO_2^- formation it has also been observed that
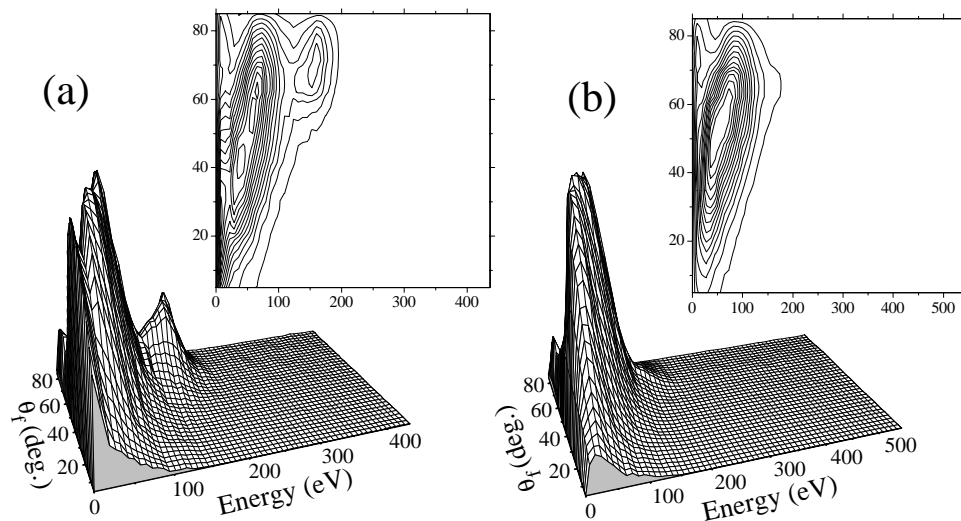
Figure 3.17 *Three-dimensional intensity distributions $I(\theta_f, E_f)$ and corresponding contour diagrams of positive ions formed in scattering of (a) 400 eV and (b) 500 eV CF_3^+ on Ba/Ag along the $(01\bar{1})$ azimuth. The incident angle is $\theta_i = 70°$. The measured intensities are plotted on a linear scale. No correction for the energy-dependent transmission of the energy analyzer has been made.*

the molecular ion yield increases when decreasing the work function [17,84]. In contrast, we observe a total absence of negatively charged polyatomic ions for CF_3^+ on Ba/Ag(111). By covering the surface with barium and hence lowering the work function, the neutralization pattern of the incoming ions is probably changed.

Positive fragment ions

In Fig. 3.17, the energy and angular distributions of the backscattered positive ions for (a) 400 and (b) 500 eV CF_3^+ on barium covered Ag(111) are shown. For these spectra $\theta_i = 70°$ and scattering takes place along the $(01\bar{1})$ azimuth of the crystal. In Fig. 3.17(a) we can observe that the same positive fragment ions as in the clean Ag(111) (Fig. 3.10(a)) case; the CF^+ and C^+ ions. However, the ratio between the intensities of the peaks has changed. The number of C^+ ions has increased relative to the number of CF^+. Also the angular distributions of the C^+ ions is broader for the Ba/Ag(111) case. The angular distribution of the CF^+ ions remains strongly peaked around the specular direction as is observed in CF_3^+ scattering off a clean Ag(111) surface. In Fig. 3.17(b), the angular and energy distribution of the backscattered positive ions for 500 eV CF_3^+ on Ba/Ag(111) is shown. The C^+ intensity has increased relative to CF^+ intensity compared to the 400 eV case, as is also observed in the clean Ag case.

The peaks at the very low energy side around 10 eV in the energy and angular distributions of the positive fragment ions can be attributed to sputtered positive ions from the surface [85,97], as in the clean Ag(111) case. However, for the Ba/Ag(111) case there seems to be an increase in sputtered positive particles. Once again, XPS data showed no trace of contamination on the surface. The sputtered particles can probably be assigned to

sputtered H$^+$ ions from the surface. The uptake of hydrogen from the background gas at a barium surface is larger than at a clean Ag(111) surface [43].

3.4 Discussion

In this section we discuss the processes that are important to the observation of the positive and negative fragment ions; these include neutralization, inelastic scattering, dissociation and negative ion formation. The energetic particles may have an effect on the surface such as sputtering, etching or deposition, and therefore may locally modify the surface. However, the currents used in the present experimental study are extremely low ~ 1 nA/cm^2. At these exposure rates it would take at least 10 hours of continuous impingement before every surface site is hit once. Therefore, the overall structure of the surface will not change significantly on the time scale of the experiment (1 to 3 hours). Hence, in what follows all effects that the energetic particles may have had on the surface are neglected.

Our discussion starts with the introduction of our dissociation model of CF$_3^+$ on Ag(111) and Ba/Ag(111). In the sections that follow, the individual steps of the model are discussed in more detail and a comparison is made to similar ion/surface scattering systems.

3.4.1 Dissociation model

For the discussion, it is convenient to describe the experimental results in terms of a series of consecutive events, which in reality may occur almost simultaneously. A scheme of the proposed charge transfer and dissociation steps of CF$_3^+$ on Ag(111) leading to the manifold of positive and negative ions is depicted below.

$$(a) \quad CF_3^+ \xrightarrow{AN} CF_3 \longrightarrow CF_3^- \xrightarrow{CID} ...$$

$$(b) \quad CF_3^+ \xrightarrow{1\,RN} CF_3^* \xrightarrow{2} CF_3^{*-}$$
$$\xrightarrow{3} F^- + CF_2 \xrightarrow{4} 2F^- + CF^+$$
$$\xrightarrow{5\,CID} C^+ + 2F^- + F$$
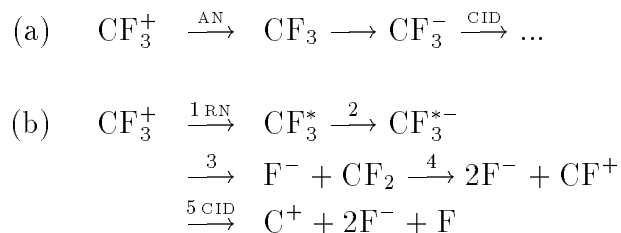
The first step in the ion-surface interaction is the neutralization of the incoming positive ion. This neutralization step is very efficient. No surviving CF$_3^+$ ions are observed. Resonant neutralization (RN) into an excited state is the most likely process. The excited neutral molecule is indicated by CF$_3^*$. *Ab initio* configuration interaction calculations show a stable Rydberg state at 4.3 eV below the vacuum level [98], which is accessible for resonant neutralization. No other accessible states have been found in the calculations. The Rydberg state has a high energy barrier to dissociation (about 3 eV) and therefore the C-F bond is not easily broken by the impulsive collision. Due to the high electron affinity, the attachment of a second electron, yielding a negative CF$_3^{*-}$ ion, as indicated by step (*2*), is easy. This is referred to as harpooning [17]. The CF$_3^{*-}$ ion undergoes a fast internal relaxation and the fluorine-carbon bond is easily broken (*3*). This is supported by the fact that the dissociation energy of the negative CF$_3^-$ ion is 1.7 eV lower than that for the neutral molecule [99]. Most

collisions will result in CF_2 and F^- particles, in agreement with the observation that F^- is the major dissociation channel and that CF_2^- is almost absent. The simultaneous formation of F^- and CF_2^- is energetically unfavorable due to the strong Coulomb repulsion between two negative ions. The formation of additional negative ions is possible in polar dissociation of the CF_2 molecules to produce CF^+ and F^- ions (*4*). This is the least endoergetic process to produce positive ions: indeed, CF^+ ions are observed to be formed in collisions leading to specular scattering and the yield shows an increase with decreasing incident ion energy. These particles also show a sharp specular angular distribution. If the CF^+ ion were formed in a reionization process of the CF molecule, a broader angular distribution and an increase in yield with increasing incoming energy would be expected [86]. The CF^+ ions can dissociate into C^+ fragment ions by an impulsive collision with the surface atoms (*5*). This is supported by the energy dependence of the CF^+ and C^+ ion signals: the CF^+ intensity decreases with increasing incident energy while the C^+ intensity increases. This behaviour has also been observed for CO^+ scattering on Pt(100) [86]. The azimuthal dependence of the positive ion signal indicates collision-induced dissociation of the CF^+ ion. Along an effectively more corrugated direction, harder collisions can take place and hence more dissociation occurs [18]. This is clearly reflected in the broader angular distribution and larger scattering angles of the C^+ ions along the open spaced azimuthal direction shown in Fig. 3.5(b).

When we look at the parent negative ion CF_3^-, we observe an increase in yield relative to the F^- yield at higher incoming normal energies. Because both products have a high electron affinity, we infer that the number of neutral parent CF_3 molecules relative to the F atoms increases with normal energy. If the ion comes closer to the surface, because of its higher incoming normal energy, more ions are Auger neutralized to the molecular ground state [78]. After attachment of an additional electron this leads to the formation of CF_3^- ions, as indicated in scheme (a). It has been shown in previous studies that Auger neutralization at short molecule-surface distances becomes competitive with resonant neutralization [82]. At the same energies, CID of CF_3^- becomes important. The impulsive collision is also reflected in the azimuthal dependence of the CF_3^- yield. Along an apparently more corrugated direction fewer polyatomic ions survive.

3.4.2 Dissociative electron attachment

In our dissociation scheme we infer that the major dissociation channel is electron attachment processes or harpooning. This leads to the loss of a F^-; i.e. $CF_3^+ + 2e^- \rightarrow CF_3^{*-} \rightarrow CF_2 + F^-$. In this scheme, we infer the temporary formation of a CF_3^{*-} Rydberg state, by consecutive resonant capture of two electrons. At an incident energy of 500 eV, the CF_3^+ ions travel at a speed of $v = 3.7 \times 10^{14} Å s^{-1}$ The normal velocity for an incoming angle of $70°$ is $v_\perp = 1.3 \times 10^{14} Å s^{-1}$. At $E_i = 100$ eV the ion travels with a speed of $v = 1.6 \times 10^{14} Å s^{-1}$ and a normal speed for an incoming angle of $70°$ of $v_\perp = 6 \times 10^{13} Å s^{-1}$ If we assume the electrons to be transferred at about 5 $Å$ [100], which seems reasonable for the population of a Rydberg state, the dissociation should occur in about 0.05 ps if the particle were to break-up before the collision with the surface atoms. This is in favorable agreement with values found in the literature [84]. The peak energy position of the scattered F^- ions (Fig. 3.9), clearly indicate they are formed before the CF_3 molecule collides with the surface

atoms.

Electron attachment processes leading to dissociation of diatomic ions have been observed in a number of studies [101]. However, the scattering of polyatomic ions from single crystal metal surfaces has not been studied in much detail. In a paper by Schmidt and coworkers, the catalytic dissociation of CO_2^+ incident on Pd(110) was explored [84]. The formation of a CO_2^{*-} state was suggested, where the first electron is captured in a Rydberg state. The reaction is given by: $CO_2^+ + 2e^- \rightarrow CO_2^{*-} \rightarrow CO + O^-$ [84]. When the crystal is covered by potassium, and hence the work function of the surface is lowered, all incoming CO_2^+ ions dissociate before Auger neutralization in the ground state occurs. This is similar to what we propose for the electronic dissociation of the incident CF_3^+ ions on Ag(111).

3.4.3   Collision-induced dissociation

In Fig. 3.14 a threshold is observed for the appearance of the C^+ ion. With increasing incident energy of the CF_3^+ ions, the yield of C^+ increases linearly and that of the CF^+ ions decreases. The appearance threshold energy can be associated with the threshold energy for the $CF^+ \rightarrow C^+/Ag(111)$ reaction. The endoergicity of this reaction is only 6.6 eV, the appearance threshold is about $E_n = 26\ eV$. This threshold is within the range of measured values for various other systems, including: $O_2^+ \rightarrow O^-/Ag(111)$ ($E_n = 15\ eV \pm 4eV$) [15], $NO^+ \rightarrow O^-/GaAs(110)$ ($E_i = 25$ eV) [82], $BF_2^+ \rightarrow BF^+/Au$ ($E_i = 20$ eV) and $BF^+ \rightarrow B^+/Ag(111)$ ($E_i = 35$ eV) [102]. The transfer of translational energy into rovibrational energy is known to occur with efficiencies ranging from 10 to 25% for different surfaces [6]. Most of the incident translational energy is transferred to the surface atoms.

The CF_3^- signal shows dissociation due to the impulsive collision. This only becomes obvious when we scatter along different azimuthal orientations of the Ag(111) crystal. Along the low index directions more survival is observed. In addition, the onset for CID occurs at lower incident translational energies for scattering along the open azimuthal directions, which is clearly observed for the positive ion signal (see Fig. 3.11). The angular distribution of CF^+ ions is significantly broader for scattering along the open azimuthal direction than for scattering along the close spaced direction.

In the case of scattering experiments of hyperthermal Xe atoms from single crystal surfaces, it has been demonstrated that there is a direct correspondence between the scattering angle and the impact parameter [94]. Larger scattering angles can be associated with small impact parameter collisions. In Fig. 3.12 we can observe that more energy is transferred to the surface atoms for larger scattering angles. The lines in this figure were calculated from the binary collision model for CF (dashed lines), CF_2 (solid lines) and CF_3 (dotted lines) for single and double scattering events. The data points are best described by CF-Ag single and CF_2-Ag double collisions, of which the latter are consistent with our dissociation scheme.

Our present experimental observations on scattering along different azimuthal orientations can be explained by a combination of two effects.

1. Along the open spaced directions, smaller impact parameter collisions are possible because less shadowing by the neighboring surface atoms occurs. This is reflected in the broadening of the angular distributions of the scattered particles [94]. Smaller

impact parameter collisions give rise to more dissociation, because these lead to harder collisions in which more translational energy transfer occurs. In the case of scattering along the open spaced direction the angular distributions are peaked more to the surface normal.

2. Different excitation mechanisms leading to CID are important for scattering along a "smooth" direction and "rough" directions [18,19]. We observe more dissociation along the open spaced directions at fixed total scattering angles.

That the azimuthal orientation of the crystal has a large influence on the degree of dissociation has been shown by Vicanek and Heiland [103,104]. Also Van den Hoek and Kleyn have shown that along the rougher direction more dissociation occurs in classical trajectory calculations for O_2 scattering from Ag(111) [18].

3.4.4 Negative ion formation

Negative ion formation has been studied in detail for atomic ions scattered from metal surfaces [32] (see also chapter 2 and references therein). The neutralization occurs along the incoming trajectory. The affinity level of the incident particle shifts down due to the image charge attraction and a broadening occurs due to the overlap of atomic and metallic wave functions. High yields of ions can be observed for low work function surfaces as was demonstrated in chapter 2 of this thesis and elsewhere [57]. H^+ is scattered from barium-covered Ag(111) giving rise to negative ion yields of about 20%, for certain scattering conditions. The negative ions are formed along the incoming trajectory or near the classical turning point.

Also negative molecular ions have been observed in scattering of positive molecular ions from surfaces. The first system to demonstrate this was $O_2^+ \rightarrow O_2^-/$Ag(111) [17]. Subsequently, it was observed for a number of other systems, including: $NO^+ \rightarrow NO^-/$Ag(111) [105], $CO^+ \rightarrow CO^-/$Ag(111) [105], $O_2^+ \rightarrow O^-/$Ag(111) [105], $CO_2^+ \rightarrow CO_2^-/$Pd(110) [84] and $NO^+ \rightarrow NO^-/$GaAs(110) [82]. For all these cases, neutralization into the ground state of the molecule is proposed, after which the affinity level is populated. The phase of the vibrational period can cause large shifts of the affinity level. This is inferred for the $O_2^-/$Ag(111) and $NO^-/$GaAs(110) system, with affinity levels located at 0 eV and 0.1 eV, respectively, relative to the vacuum level. In our case only a small fraction of the CF_3^+ is neutralized directly into the ground state. The affinity level of the CF_3 species is located 1.8 ± 0.2 eV below the vacuum level [87]. A concerted shift of the level due to image charge and expansion of the molecular bond can account for the observation of the negative parent ion.

3.4.5 Scattering from barium covered Ag(111)

When the Ag(111) surface is covered with 1 monolayer of barium, the work function decreases from 4.7 eV to 2.4 eV [43]. The 3s Rydberg state of CF_3, 4.3 eV below the vacuum level, is already resonant with the filled density of states far from the surface. Therefore, resonant neutralization will occur at large ion/surface separations and all the ions will be neutralized before they come close enough to the surface to allow Auger neutralization.

This channel is only competitive with the RN channel at short ion/surface distances, as has been shown for the clean Ag case and in other studies [82]. Therefore, only the resonant neutralization channel is operative in scattering of CF_3^+ ions off a Ba covered Ag (111) surface. The spectral features associated with Auger neutralization (the negatively charged polyatomic ions) are not observed. The observation of positive C^+ and CF^+ ions is associated with resonant neutralization, as shown in the dissociation scheme. Positive ions are still formed at the surface with a low work function. Increasing the energy of the incoming ions leads to an increase in C^+ and a decrease in CF^+, which is assigned to CID of the latter. CID is also reflected in the angular distributions of the ions. The CF^+ is strongly peaked around the specular direction and the C^+ shows a broad angular distribution which is shifted to larger scattering angles. This corresponds to harder collisions with the surface atoms in which more energy is transferred. These observations are also seen at the clean Ag(111) surface and are consistent with the proposed dissociation scheme.

A change in work function due to covering the surface with barium leads to a different amount of neutralization for the outgoing ions and explains the ratio difference in C^+ to CF^+ for Ba/Ag(111) compared to Ag(111). This was suggested earlier for O_2^+ from Ag(111) and K covered Ag(111) leading to O^- and O_2^- [17]. Harder collisions in the case of Ba/Ag(111) also explain the ratio difference. We already mentioned that barium forms an incomplete overlayer which contains vacancies. This surface is rougher than the clean Ag surface. We showed previously that the crystal structure has a large influence on the degree of dissociation by CID by comparing the fragmentation patterns for scattering of CF_3^+ along different azimuthal orientations of the clean Ag(111) crystal. For scattering along a more corrugated direction, more dissociation is found. The same features were observed for the barium covered surface. This is consistent with epitaxial growth of the barium overlayer on the Ag substrate (see chapter 2).

3.4.6   Surface rainbows

Fig. 3.8(a) and (b) clearly show the appearance of surface rainbow structures [9,18]. The angular distributions show a minimum around the specular scattering direction and two maxima near the surface normal and at angles larger than specular, which vary when we rotate the crystal around its azimuthal axis. Previously, the appearance of surface rainbows in dissociative scattering was observed in classical trajectory calculations for O_2 scattering from Ag(111) by Van den Hoek and Kleyn [9,18]. " Angular rainbows" were found for scattered O atoms which were formed in the impulsive collision of the O_2 with the Ag atoms. However, in the present study the energy position of the scattered F^- ions clearly indicates that the origin of the rainbows can be attributed to F atoms scattered from Ag surface atoms. The F^- ions are formed before the collision with the surface atoms. This reaction channel is given by: $CF_3^+ + 2e^- \rightarrow CF_3^{*-} \rightarrow CF_2 + F^-$. Therefore, we conclude that the angular rainbow structures are not due to CID of molecules, but due to individual atomic species scattered from the Ag(111) surface.
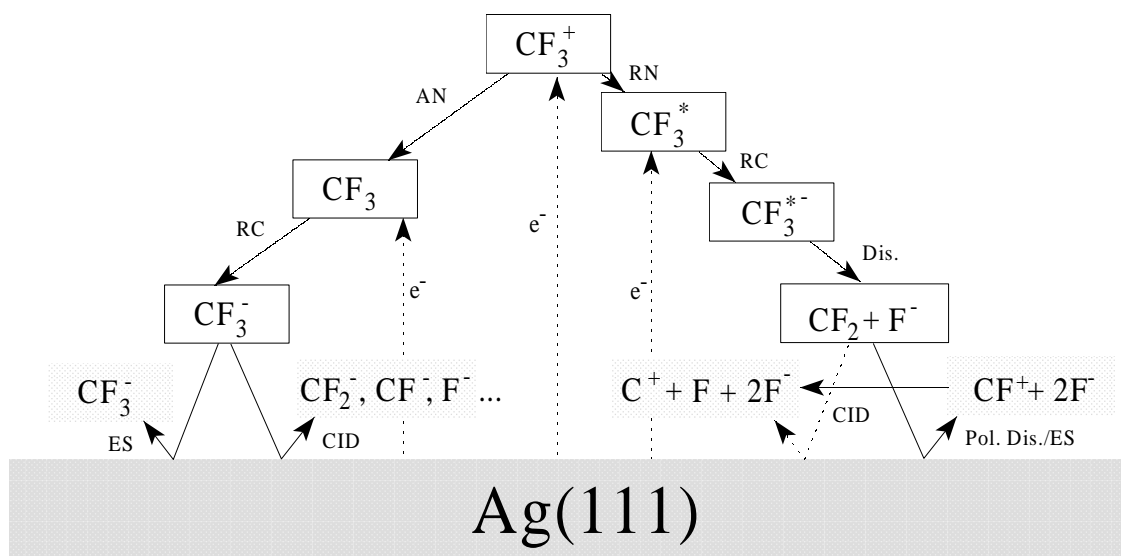
Figure 3.18 *Schematic illustration of several important processes occurring in scattering of CF_3^+ from (Ba/)Ag(111) leading to the observed fragment ions, RN = resonant neutralization, AN = Auger neutralization, RC = resonant capture, Dis. = dissociation, Pol. Dis. = polar dissociation, CID = collision induced dissociation and ES = elastic scattering.*

3.5   Conclusions

In the dissociative scattering of CF_3^+ ions from the clean Ag(111) surface, the major dissociation channel yields F^- ions. To a lesser extent CF_2^- and CF_3^- ions are observed. The positive channel shows C^+ and CF^+ ions. We have proposed an empirical model which explains the salient features of the data. It clearly shows that concerted electronic and collision-induced processes are important in the dissociative scattering of a polyatomic ion from a surface. In a combined process all bonds of the CF_3^+ ion can be broken in the ion-surface collision at relatively low (normal) energies. The results show that the dissociation is sensitive to the surface structure. We have depicted several important processes occurring in scattering of CF_3^+ from (Ba/)Ag(111) leading to the observed fragment ions in Fig. 3.18.

We have shown that at a low work function surface the neutralization of the incoming CF_3^+ solely proceeds via resonant neutralization into the first excited 3s Rydberg state of the neutral molecule. The spectral features associated with Auger neutralization, negatively charged molecular ions, are not observed. Only fragment ions associated with the resonant neutralization channel are observed.

Chapter 4

Dissociative scattering of polyatomic ions from a liquid surface: CF_3^+ on a perfluoropolyether film

Abstract

The dissociative scattering of CF_3^+ ions from a liquid insulating perfluorinated polyether surface was explored in the incident energy range 100-to 500-eV. We have measured the angular and energy distributions of the positive and negative fragment ions. The impulsive energy transfer to the liquid molecules and to internal energy of the scattered ions has been determined as a function of incoming energy and total scattering angle. The energy transfer in the ion/surface collision indicated scattering off the -CF_3 groups of the liquid molecules. The dissociation of the CF_3^+ ions was due to a single impulsive collision with these groups. The parent ion was observed as well as CF_2^+, CF^+ and C^+ ions. The degree of dissociation depends only on the total scattering angle and the incoming energy, as in gas phase scattering. Remarkably, negatively charged F^- fragment ions were also observed. These were formed in a process referred to as collisionally-induced "ion-pair" formation from neutrals leaving the surface. The important parameter which determined the internal energy uptake in the collision was the translational energy loss ΔE the parent ion suffered. Finally, a comparison has been made between scattering from a liquid perfluorinated polyether surface and a metal Ag(111) surface.

4.1 Introduction

The interaction of polyatomic ions with surfaces has been a topic of great scientific and technological interest over the last decades. One can think of such important processes as plasma-wall interactions in fusion devices, etching reactions in the semiconductor industry, chemical reactions at surfaces and surface-induced dissociation in mass spectrometry. Despite the great technological relevance of understanding ion-surface interactions, many of the fundamental processes are still obscure.

In the past, a great number of studies has been performed on the dissociative scattering of small polyatomic ions (i.e. di- and tri-atomics) from single-crystal surfaces [10,101,106–

108]. Several mechanisms have been proposed to explain dissociative scattering from these surfaces. These can roughly be divided into two categories: i) dissociation due to electron transfer processes [16,80] and ii) dissociation due to the impulsive collision with the surface, in which translational-to-internal energy transfer occurs [19,82,86]. These models have been adapted to explain the fragmentation of large polyatomic ions [6].

Among the important processes occurring in ion/surface collisions is the transfer of electrons. For the neutralization of the incoming ion, two mechanisms have been proposed: resonant neutralization (RN) and Auger neutralization (AN) [10,11]. It has been argued that resonant neutralization is favored over long distances. At short ion/surface distances Auger neutralization becomes competitive or even the dominant process [82].

The interest in unraveling the dissociation dynamics of *large* polyatomic ions colliding with surfaces is boosted by the application of surface-induced dissociation (SID) in mass spectrometry [6,30] which has been pioneered by Cooks and coworkers [109,110]. SID is used as an alternative to fragmentation by noble-gas atoms because in the case of scattering from surfaces a better defined energy transfer in the collision can lead to specific fragment ions and, hence, more structural information concerning the parent ions [77]. One of the major problems in applying surface-induced dissociation in mass spectrometers is the efficient neutralization of the incoming parent ions and outgoing fragment ions. Several surface modifications have been suggested to reduce the neutralization yields. Among these are the use of oxide surfaces [25,26], self-assembled monolayers (SAMs) [27–29] and recently thin films of an inert polymer oil such as a perfluoropolyether (PFPE) [30,31]. The latter compound efficiently reduces neutralization and has the additional advantage that the surface layer is renewed because of the high mobility of the liquid molecules [30].

In recent years, a number of groups has investigated the surface structure of the PFPE liquid [111–114]. Rare-gas atomic beam scattering experiments by Nathanson and coworkers suggest hard sphere like collisions of the rare-gases with $-CF_n$ (n=1-3) groups protruding from the surface occur [111,113]. That the PFPE surface is composed exclusively of $-CF_n$ (n=1-3) groups was confirmed by reactive ion scattering results of Cooks and coworkers [110] who found that ion-surface reactions exclusively lead to the pick-up of F atoms. They conclude that scattering from F and $-CF_3$ groups occurs and that the oxygen atoms must be buried under the topmost layers [110]. These results have been confirmed by a recent angular resolved photoelectron spectroscopy study by Pradeep and coworkers [114,115] in which it is concluded that a high degree of order exists on the PFPE liquid surfaces. Also, they have inferred that the surface is primarily composed of functional groups like $-CF_3$ and $-CF_2$, which are oriented nearly perpendicular to the surface.

In previous studies concerning SID of polyatomic ions, much insight was gained in the phenomenology of the processes occurring [6]. The data suggest that the same excitation processes are operative in gas phase collision-induced dissociation and surface-induced dissociation [6]. However, since most of the SID studies are performed at a fixed scattering geometry, no information concerning the angular distributions of the fragment ions is obtained. Occasionally, the incoming angle has been changed but the total scattering angle was kept constant because the detector was placed at a fixed position. In a number of studies the energy transfer to the surface was determined [97]. However, this has not been studied in great detail, i.e. not as a function of incoming energy and outgoing angle. Since these data are lacking it is hard to make definite claims about the scattering mechanism.
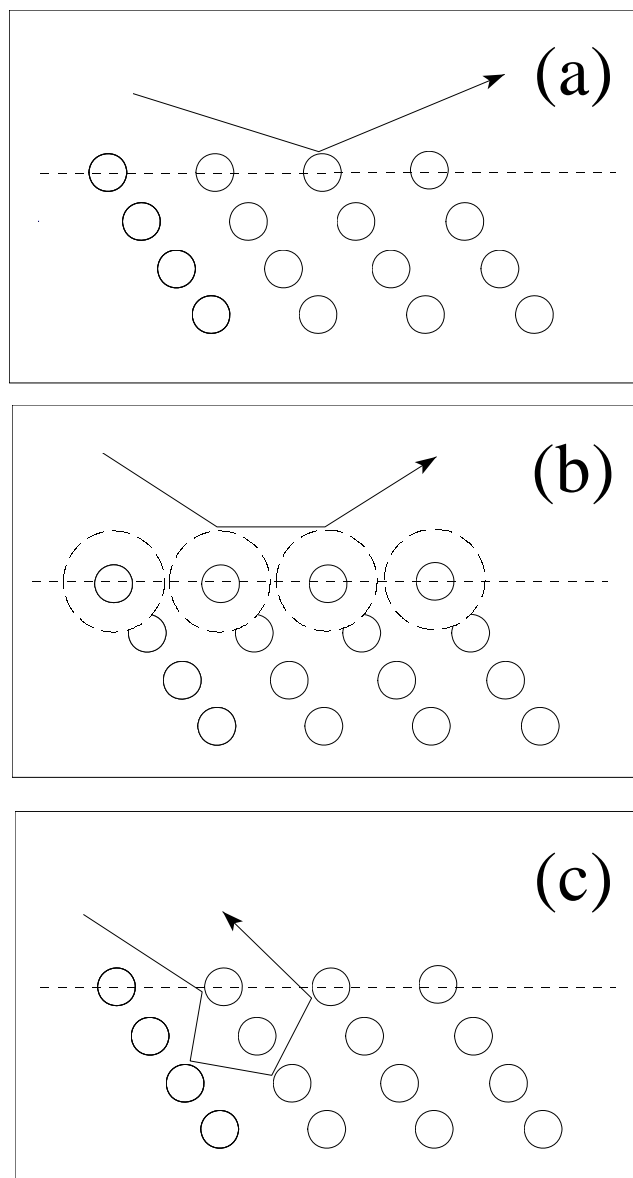
Figure 4.1 *Illustration of (a) single, (b) double and (c) multiple scattering from a well ordered surface.*

The study of the angular and energy distributions of scattered noble gas ions and alkali ions from single-crystal metal surfaces, both experimentally and with trajectory calculations, gives much information about their scattering dynamics [10,11]. A pictorial illustration of three possible trajectories is given in Fig. 4.1. We can distinguish several trajectories: the particles can make (a) a single collision, (b) a double collision, (c) or more than two collisions, i.e. multiple collisions. The single collision event is favored at high incoming energies. A double collision is more likely at lower incoming energies, as the repulsive part of interaction potential between the incident particle and surface atoms increases (schemat-

ically depicted in Fig. 4.1(b) by the dashed circular lines). The transition from single to double collision dynamics gives rise to surface rainbow scattering [9]. The maximum scattering angle in this case is given by the angle where the single and double collision peak merge. Multiple collisions become likely if penetration into the crystal lattice becomes apparent which is mostly at sufficiently high incoming energies or steep enough incoming angles.

In our experimental set-up it is possible to vary the detector position and hence perform angular resolved energy analysis of the fragment ions. By carefully studying the energy transfer to the surface and the fragmentation patterns of the incoming ion as a function of total scattering angle and incoming energy, much can be learned about the scattering dynamics. Challenging questions that need to be answered are: what are the important neutralization, dissociation and ionization mechanisms in scattering polyatomic ions from a liquid surface? How are the scattered particles spatially distributed? How is energy transferred to the surface and to internal energy of the ion? Where does the dissociation occur? What is the influence of the surface?

Recently, we studied the dissociative scattering of CF_3^+ ions from a clean Ag(111) [116] and a barium-covered Ag(111) surface [117]. We proposed an empirical model which describes the mechanisms leading to the complete break-up of the CF_3^+ ion into charged fragments. These studies showed that concerted electronic and collision-induced processes are important in the dissociative scattering of polyatomic ions from a clean metal surface. However, most of the CF_3^+ ions dissociate due to electron transfer, only a small fraction dissociates directly due to the impulsive collision. We also observed that the crystal structure has a large influence on the dissociation due to the impulsive collision. It is interesting to compare scattering from a metal surface to scattering from non-metal surfaces like SAM surfaces and perfluoropolyether surfaces.

The scattering of fluorocarbon ions at hydrocarbon, deuterated hydrocarbon and fluorocarbon SAM surfaces has been studied by mass spectrometric techniques in the group of Cooks [28,30]. They found that the perfluorinated surface most efficiently fragments the incoming ions. Approximately 17 to 20% of the incident translational energy is transferred to internal energy. For the other surfaces this value ranges from 11 to 13%. A possible reason for this difference is the larger effective mass of the perfluorinated surface which is considered to be a "hard" surface. Also neutralization is less efficient at the perfluorinated surface compared to the other surfaces, due to the higher ionization energy of this surface. The dissociation was assumed to occur via translational-to-vibrational energy transfer. The break-up of the particles occurs via statistical channels in the gas phase [118]. In those studies no angular and translational energy distributions of the scattered fragment ions were measured.

In this chapter, we present a detailed experimental study of the energy and angular distributions of positive and negative fragment ions in the scattering of 100-to 500-eV CF_3^+ ion beams from a liquid perfluorinated polyether (PFPE) surface. From our results we determine the impulsive energy transfer to the liquid molecules and to internal energy of the scattered ions as a function of incoming energy and total scattering angle. We show that the dissociation is governed by a *single* impulsive collision off -CF$_3$ groups of the liquid molecules. We demonstrate that the translational energy loss ΔE that the parent ion has suffered in the collision is the key parameter that determines the internal energy uptake.
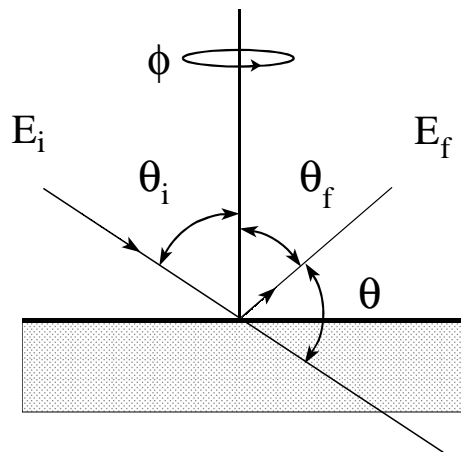
Figure 4.2 *Definition of the scattering geometry: the incoming angle θ_i, the outgoing angle θ_f and azimuthal angle ϕ.*

Our discussion ends with a comparison between dissociative scattering from *liquid* and from *metal* surfaces.

This chapter is divided into five main sections. In section 4.2 the experimental set-up and sample preparation is described. In section 4.3 the experimental spectra are presented and analyzed. The mechanisms governing ion-surface interactions are discussed in section 4.4. This chapter ends with a summary of the most important results.

4.2   Experimental

4.2.1   Apparatus

The experimental set-up is described in Chapter 2 of this thesis. Briefly, it consists of two UHV chambers. In one, the liquid scattering sample can be characterized and stored. The sample can be transferred under UHV to a two-axis goniometer in the second chamber (base pressure of 1×10^{-10} mbar). The goniometer allows rotation of the target around an axis parallel to the surface to change the incoming angle θ_i (which is measured with respect to the surface normal) and rotation around the surface normal to change the azimuthal angle ϕ. This is schematically depicted in Fig. 4.2. The total scattering angle θ is defined as: $\theta = 180° - (\theta_i + \theta_f)$ with θ_f the outgoing angle of the particles. In the scattering chamber, a differentially pumped electron impact source (VG, AG 60) is mounted which produces the CF_3^+ ions. Gaseous CF_4 was introduced into the ion source and irradiated with 110-eV electrons. The resulting positive ions are accelerated to translational energies which can be varied between 100 and 500 eV. The ion beam is purified using a Wien-filter. The scattered ions are detected with a 90° cylindrical electrostatic energy analyzer, with an energy resolution of $\Delta E/E = 0.08$. The energy spectra shown throughout this chapter have not been corrected for the energy-dependent transmission of the energy analyzer (proportional to E) to avoid an enlargement of the intensities at very low energies. When the relative intensi-

ties of the fragment ions are determined from the energy spectra, the raw energy spectra are scaled by a factor $1/E$ to correct for the energy-dependent transmission function of the analyzer. In the scattering plane the detector can be rotated from $45°$ to $180°$ with respect to the incoming beam and out of plane detection from $-15°$ to $90°$ is possible. The angular resolution of the detector is around $0.5°$. The amount of contaminants or metastables in the primary beam is less than 0.01%. Neutrals are not detected in our experiment.

4.2.2   Sample preparation

The support of the liquid surface is a stainless steel disc (diameter 10 mm, thickness 2 mm) which has been polished mechanically and has a roughness below $0.05\ \mu$m. The support is covered with a high molecular weight perfluorinated polyether, sold under the trade name krytox 16256. Its structural formula is given by: $F[CF(CF_3)CF_2O]_{63(ave)}CF_2CF_3$. Its average molecular weight is about 11000 and its vapor pressure at room temperature is about 10^{-15} mbar. We obtained a smooth thin film by allowing the liquid to sheet across the stainless steel support. This could be done under UHV conditions by changing its azimuthal orientation. All spectra in this chapter were measured with a surface near room temperature. Although we have an insulating layer, no evidence for charging was found. Reproducible data could be obtained over several days. Also no changes in the spectra were observed with changing the incoming particle flux.

4.2.3   Measurement procedure

In a typical measurement, the incoming angle θ_i and the azimuthal orientation ϕ are kept constant. The detector is kept in the scattering plane at a fixed outgoing angle θ_f. The intensity I of the positive or negative ions is measured as a function of their final energy E_f by scanning the detector voltage. This procedure is repeated for various outgoing angles. In this way a three-dimensional intensity distribution $I(\theta_f, E_f)$ is obtained.

4.3   Results and analysis

4.3.1   Spectra

Positive fragment ions

The kinetic energy distributions of positive fragment ions for the scattering of a beam of 100 eV CF_3^+ ions from a perfluoropolyether liquid surface are shown in Fig. 4.3. The data are taken at (a) $\theta_i = 70°/\theta_f = 85°$ and (b) $\theta_i = 70°/\theta_f = 75°$, respectively. We start by discussing Fig. 4.3(a) in which the total scattering angle is $25°$. Here, three peaks are clearly visible and indicated with labeled arrows. The peak at around 80 eV can be identified with backscattered CF_3^+ ions. The translational energy loss ΔE the ions suffered in the collision is approximately 20 eV. The two peaks at lower energies can be identified with CF_2^+ (57 eV) and CF^+ (34 eV), respectively. The positive ion yield was approximately 10%. For the mass assignment the parent ion and fragment ions are assumed to leave the surface with the same speed and have a final energy which is proportional to their mass. This has been applied in
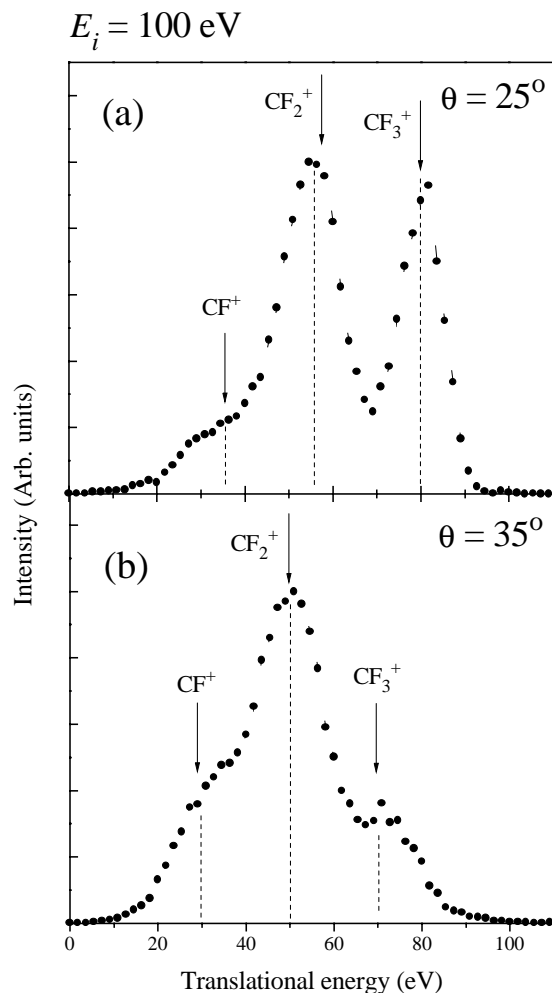
Figure 4.3 *Kinetic energy distributions for positive fragment ions formed in the scattering of 100 eV CF_3^+ from a PFPE liquid surface. The data are taken at (a) $\theta_i = 70°$ / $\theta_f = 85°$ and (b) $\theta_i = 70°$ / $\theta_f = 75°$.*

previous studies and has proven to be valid [17,80,116]. In scattering from a PFPE liquid surface we observe the survival of the parent CF_3^+ ion. This was not seen in scattering from a clean Ag(111) surface or a barium-covered Ag(111) surface [116,117].

Fig. 4.3(b) shows results of fragment ions scattered over a larger total scattering angle (35°) and here the CF_3^+ peak has decreased relative to the CF_2^+ peak. The energy positions of the peaks have shifted to lower energies. The CF_3^+ ion is observed at 70 eV. The other two peaks can again be identified with CF_2^+ and CF^+. Their final energies have also shifted to lower values. For scattering over larger angles more dissociation is observed and more energy is transferred to the surface. This is investigated in more detail in section 4.3.2. We first investigate the incident energy dependence of the scattered positive ion signal.

In Fig. 4.4 the incoming energy is varied from 100-to 500-eV. The scattering geometry is the same as in Fig. 4.3(a), i.e. $\theta_i = 70°/\theta_f = 85°$. For easy comparison, a reduced energy

$$\theta = 25^{\circ}$$
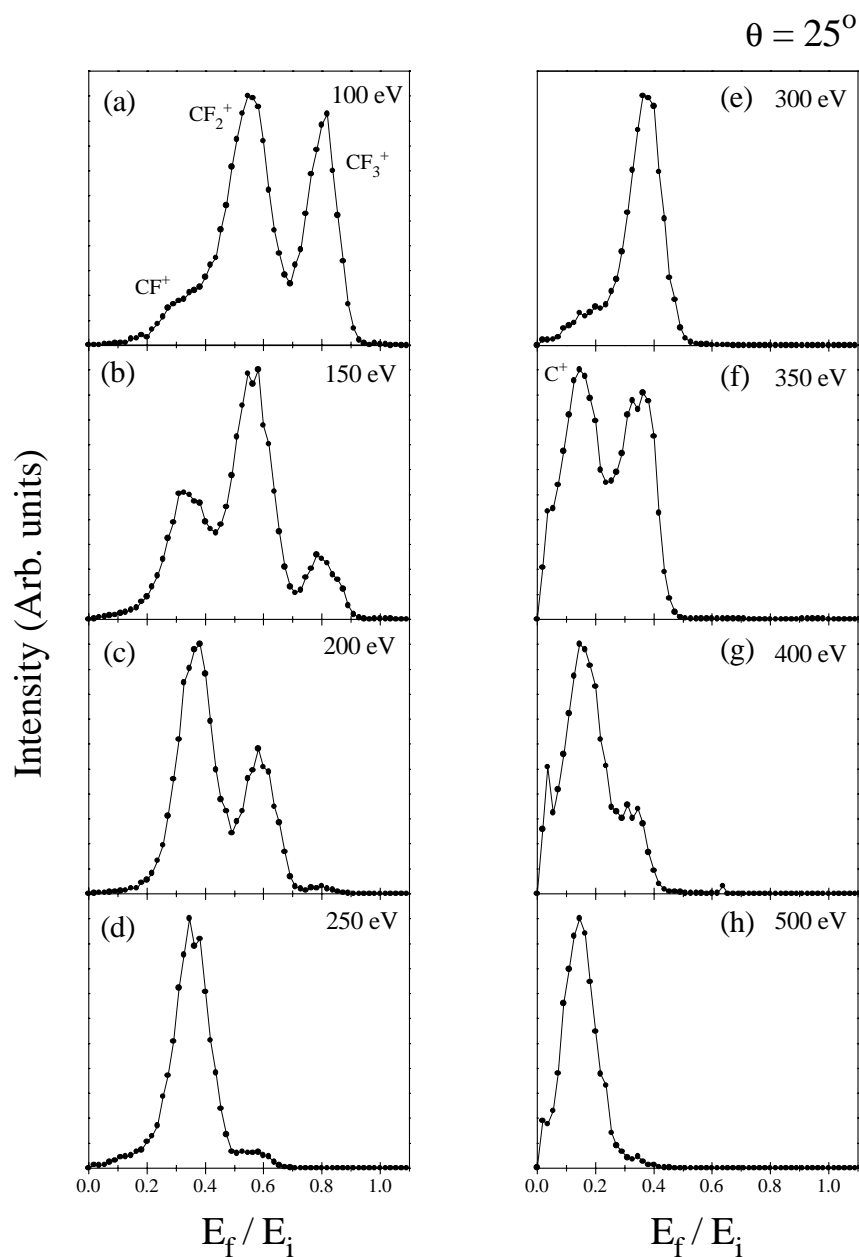
Figure 4.4 *Kinetic energy distributions for positive ions formed for $\theta_i = 70^{\circ}$ and $\theta_f = 85^{\circ}$. The incoming energies are (a) 100 eV, (b) 150 eV, (c) 200 eV, (d) 250 eV, (e) 300 eV, (f) 350 eV, (g) 400 eV, (h) 450 eV and (i) 500 eV. The measured intensities are plotted on a linear scale. No correction for the energy-dependent transmission of the energy analyzer has been made.*

scale, E_f/E_i, is used with E_f the final energy of the ions and E_i the incoming energy of the beam. This allows for direct comparison between the measured energy spectra. If the incoming energy is increased, we observe a decrease in parent ion and an increase in fragment ion signal. At $E_i = 200$ eV (c), we observe the CF_2^+ and CF^+ ions, at $E_i = 350$ eV we observe the CF^+ and C^+ ions and at $E_i = 500$ eV the incoming ion is completely fragmented and we only observe C^+ ions. The enhanced fragmentation with incoming energy indicates that the dissociation is governed by the impulsive collision. The relative widths of the peaks of the fragment ions appear to be the same over the measured incident energy range. Also the relative energies of the peaks are located at about the same positions. The latter observation indicates single collision dynamics [119–121] and is discussed extensively in section 4.3.2.

In Fig. 4.5, the three-dimensional intensity distributions $I(\theta_f, E_f)$ and corresponding contour diagrams of the backscattered positive ions are plotted for (a) 100 eV, (b) 300 eV and (c) 500 eV CF_3^+ ions incident on a PFPE liquid surface. In all three cases $\theta_i = 70°$. In Fig. 4.5(a) (E_i=100 eV) we can observe two distinct peaks: at E_f=80 eV / $\theta_f = 85°$ and E_f=57 eV / $\theta_f = 85°$. These have been assigned previously (in Fig. 4.4(a)) to CF_3^+ and CF_2^+, respectively. Also the CF^+ ion can be observed as a shoulder at the left hand side of the spectrum (E_f=34 eV / $\theta_f = 70°$). The CF_3^+ peak shows a sharp angular distribution and the ions are observed at angles larger than specular. Apparently they survive the impact in rather soft (shallow) collisions. In the case of metal surfaces, survival is mainly observed in the specular direction [86] showing that the surface can be considered flat or slightly corrugated. However, we observe survival of the parent ion at even more grazing exit angles, indicating that we scatter from a very corrugated surface or even individual end groups of the liquid. The CF_2^+ ions show a broader angular distribution compared to that of the scattered parent ions and the ions appear at larger total scattering angles, which indicates that these ions are formed in hard collisions with the surface. At larger total scattering angles the CF_2^+ ion is observed at lower energies; demonstrating that more energy is transferred to the surface. When the energy of the incoming particles is raised to 300 eV (see Fig. 4.5(b)), the CF_3^+ and CF_2^+ ions are no longer present in the spectra. We only observe the CF^+ and C^+ ions. The CF^+ peak appears at larger total scattering angles than the CF_3^+ and CF_2^+ ions observed in Fig. 4.5(a), indicating that harder collisions are needed to form the CF^+ ion. In Fig. 4.5(b), the largest scattering angle is observed for C^+ fragment ions; these are observed at $\theta_f = 60°$. The full width at half maximum (FWHM) of the angular distributions of the CF^+ and C^+ peaks are 20° and 25°, respectively. The appearance of fragment ions at larger scattering angles has been observed by Murata and coworkers in their study on the dissociative scattering of N_2^+, CO^+ and CO_2^+ from Pt(100) [86,81]. They observed that the angular distributions of the dissociation products appear at total scattering angles larger than that of the parent ion scattered non-dissociatively. They concluded that smaller impact parameters are required for dissociative scattering than for non-dissociative scattering. Similar behaviour is observed for CF_3^+ on Ag(111) and on Ba/Ag(111) [116,117].

Fig. 4.5(c) shows scattering for an incoming energy of 500 eV. Here, no backscattered polyatomic ions are observed; only scattered C^+ ions and a peak with a broad angular distribution at the low energy side are present. The shape of the energy distribution peaked around 10 eV is characteristic for sputtered particles: a sharp rise at the low energy side
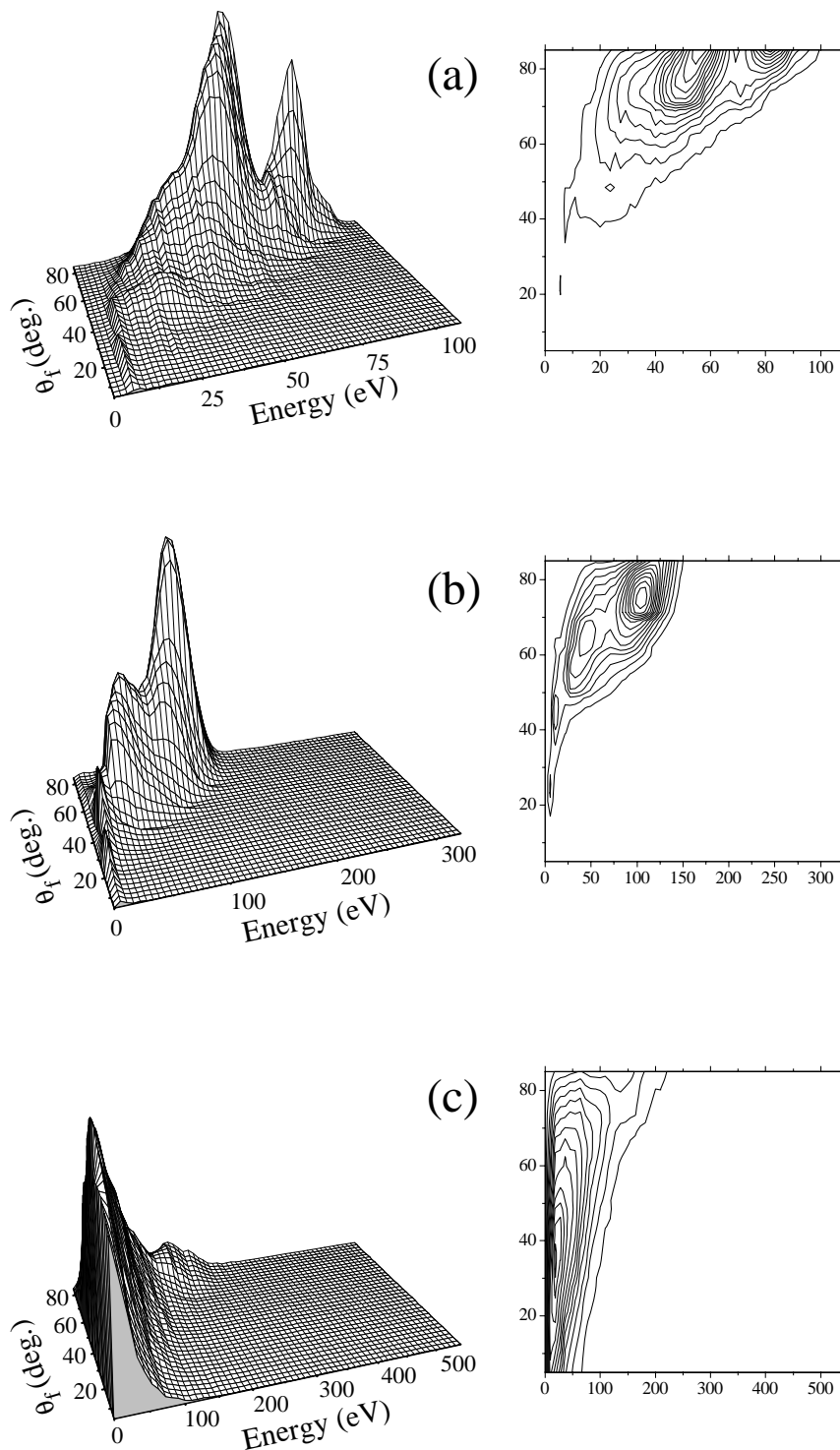
Figure 4.5 *Three-dimensional intensity distributions $I(\theta_f, E_f)$ and corresponding contour diagrams of positive ions formed in scattering of (a) 100 eV, (b) 300 eV and (c) 500 eV CF_3^+ from a PFPE liquid surface. In all three cases $\theta_i = 70°$. The measured intensities are plotted on a linear scale. No correction for the energy-dependent transmission of the energy analyzer has been made.*
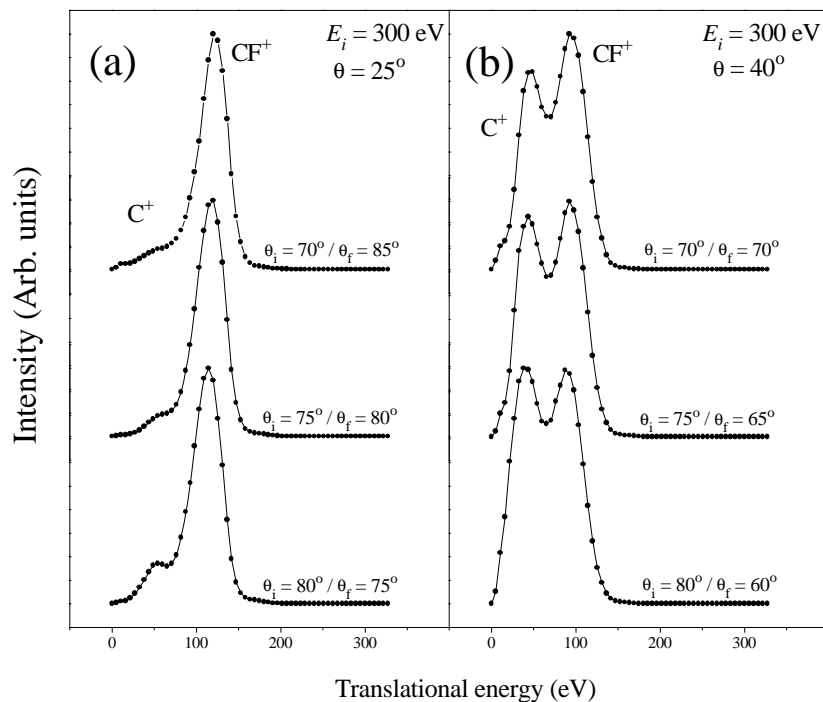
Figure 4.6 *Intensity distributions of positive fragment ions in the scattering of 300 eV* CF_3^+ *from a PFPE liquid surface. The scattering geometry is varied while the total scattering angle is kept constant. Spectra for two different total scattering angles are shown: (a) $\theta = 25°$ and (b) $\theta = 40°$, respectively. No correction for the energy-dependent transmission of the energy analyzer has been made.*

followed by a slow decay at the high energy side [97]. A maximum in intensity for the sputtered particles in the angular distribution is observed around $\theta_f = 40°$. The intensity of the C^+ ion is much lower than that of the sputtered particles and they are hard to distinguish from the background of sputtered particles. Chemical sputtering experiments on the PFPE surface with Xe^+ and Kr^+ ions show that fluorocarbon ions like CF_3^+, $C_2F_5^+$, $C_3F_7^+$ and the oxygenated product CFO^+ [110,112] leave the surface. Those experiments also show that the PFPE surface is remarkably free of hydrocarbon impurities.

The energy and angular behaviour of the backscattered fragment ions seems to indicate single hard sphere like collisions. This behaviour resembles ion-surface collisions from single crystal surfaces when the incoming energy of the ion is high enough to penetrate deep into the ion-surface interaction region to allow single collisions with the surface atoms [19]. Similar observations were made for the hyperthermal beam scattering experiments off PFPE surfaces [111]. A method to check the validity of the single collision approximation is to keep the total scattering angle θ constant while varying the incoming and outgoing angles [19]. If single collisions occur no changes in the energy spectra should be observed, as in gas phase scattering [19]. In Fig. 4.6, energy spectra are shown for a 300 eV CF_3^+ beam incident on the PFPE liquid surface for two different scattering angles: (a) $\theta = 25°$ and (b) $\theta = 40°$. The intensity distributions of the positive ions, and hence the dissociated fraction,
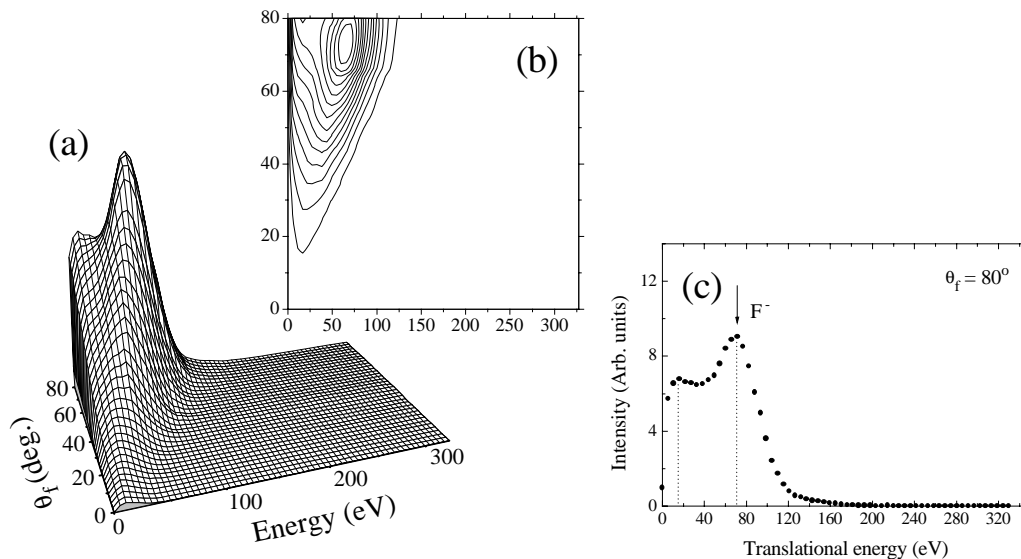
Figure 4.7   Three-dimensional intensity distributions $I(\theta_f, E_f)$ (a) and corresponding contour diagrams (b) of negative ions formed in scattering of 300 eV CF_3^+ from a PFPE liquid surface. The data are taken at $\theta_i = 75°$. (c) shows an energy spectrum for $\theta_f = 80°$. The measured intensities are plotted on a linear scale. No correction for the energy-dependent transmission of the energy analyzer has been made.

is only dependent on the total scattering angle. We conclude from the above observations that the impulsive energy transfer to the surface and to the internal energy of the incoming ion scales with the incoming energy and total scattering angle; this is studied in detail in section 4.3.2.

Negative fragment ions

In Fig. 4.7(a), the three-dimensional intensity distribution $I(\theta_f, E_f)$ and corresponding contour diagram of the backscattered negative ions are plotted for a 300 eV CF_3^+ beam incident on the PFPE liquid surface. The data are taken at an incoming angle of 75°. The peak at $E_f = 60$ eV and $\theta_f = 70°$ can be identified with F^- fragment ions. The ions leave the surface with the same speed as the positive fragment ions for this incoming energy and scattering geometry. The yield of the negative fragment ions is of the same order as that of positive fragment ions ($\sim 10\%$). No negatively charged *polyatomic* ions are observed for incoming energies ranging from 100-to 500-eV. The negatively charged ions show a very broad angular distribution and the maximum intensity is observed around $\theta_f = 70°$, which is at larger total scattering angles than that at which the parent CF_3^+ ion is observed indicating that the particles are formed in the impulsive collision with the surface, similar to the positive fragment ions. In Fig. 4.7(c) we have plotted the energy spectrum at $\theta_f = 80°$. We can clearly see two contributions to the negative ion signal, one originating from sputtered particles and one from scattered ions. The energy position of the fragment ion is observed around $E_f = 68$ eV. Again, the ions have the same speed as the positive (fluoro)carbon

fragment ions under these scattering conditions ($\theta = 25°$, see Fig. 4.4(e)). At larger total scattering angles, the sputtered particles dominate the spectrum. After the different contributions are resolved, the F^- fragment ions have an angular width (FWHM) between 35° and 40°.

The angular distributions of the F^- formed in the scattering of CF_3^+ from the PFPE liquid surface are quite different from those formed in scattering off the Ag(111) surface where the angular distributions are sharply peaked around the specular directions and the F^- are mainly formed in the dissociative scattering due to electron transfer processes [116,117]. In the case of scattering from a PFPE surface, the angular distributions of the negative fragment ions clearly show they are formed in impulsive collisions.

4.3.2 Impulsive energy transfer

From the angular and energy distributions presented in the previous sections we can extract information concerning the transfer of translational energy to the surface and to internal energy of the scattered polyatomic ion. In the following section we concentrate on both of these aspects of polyatomic ion-surface collisions. Our results are described by a simple model calculation using the binary collision model. We start by considering the translational energy transfer to the liquid molecules at a fixed total scattering angle.

Translational energy transfer to the liquid: varying the incoming energy

In our experiment we measure the energy distributions of the fragment ions as a function of incoming energy and as a function of outgoing angle. Therefore, the translational energy loss ΔE of the scattered particles is measured directly. By applying simple kinematic formulas we can determine the "effective" mass of the liquid molecules. This same procedure is applied in low-energy ion scattering (LEIS) from single crystal surfaces to perform elemental analysis of the topmost layer of the surface [10,11,34]. The formula that is used for binary scattering is given by:

$$E_f = E_i \left(\frac{\cos\theta \pm \sqrt{A^2 - \sin^2\theta}}{1 + A} \right)^2 , \qquad (4.1)$$

where $A = M_2/M_1$ and θ is the total scattering angle. This equation gives the final energy E_f of a scattered particle of mass M_1 and incoming energy E_i which strikes a target particle of mass M_2, which is initially considered to be at rest [34]. If the mass of the incoming particle is smaller than, or equal to that of the target, i.e. $M_1 \leq M_2$ and $A \geq 1$, then the positive sign in equation 4.1 is used. This is the case we will consider.

In Fig. 4.3(a) the energy distribution of the positive fragment ions for a beam of 100 eV CF_3^+ ions at $\theta_i = 70°$ and $\theta_f = 85°$ is shown; approximately 80% of the translational energy of the parent ion is retained. Consequently, 20% of the translational energy of the scattered CF_3^+ is transferred to the liquid surface. If we apply eq. (4.1), we find an effective target mass of $M_2 = 69$ (with $M_1 = 69$). This is in agreement with earlier studies which show that the surface is composed of functional groups, i.e. -CF_3 and -CF_2, which are oriented nearly perpendicular to the surface [111–114]. In our case the CF_3^+ ions scatter off the

Data: ■ CF_3^+
       ● CF_2^+
       ▲ CF^+
       ▼ C^+ ——— Binary collision model: $M_2 = 69$
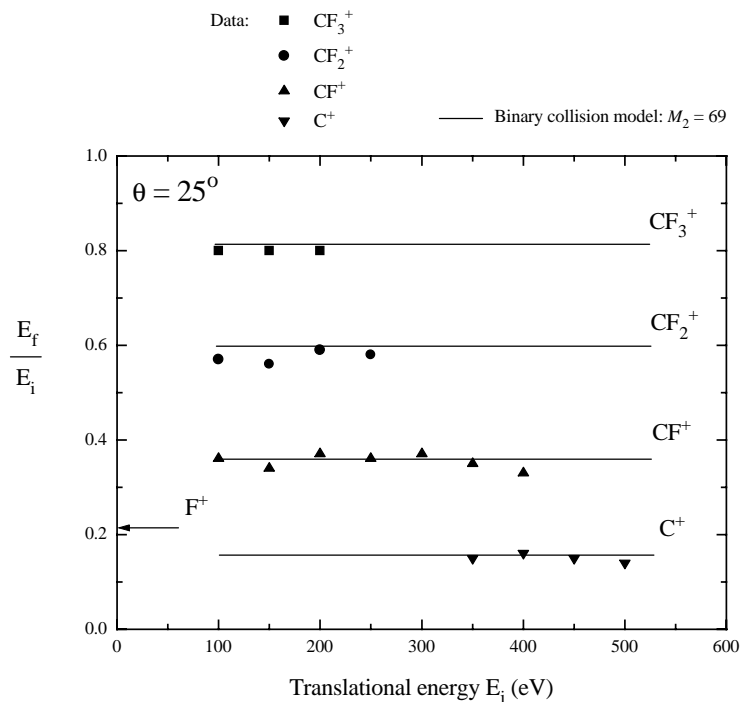
Figure 4.8 *Relative energy* (E_f/E_i) *of the four positive fragment ions as a function of incoming energy for* CF_3^+ *from a PFPE liquid surface. The data are taken at* $\theta_i = 70°$ *and* $\theta_f = 85°$. *The points are values of* E_f/E_i *from experimental data; the solid lines were calculated from eq.(4.1) (binary approximation) for the* CF_3^+-CF_3 *system.*

-CF_3 groups. The internal energy uptake is neglected since this is small compared to the total energy transfer. We now focus on the incident energy dependence of the translational energy transfer to the liquid at a constant total scattering angle.

Fig. 4.8 shows the relative energies (E_f/E_i) of the four positive fragment ions as a function of incoming energy for CF_3^+ scattering from a PFPE liquid surface. These relative energies are indicated as points in the figure. The data are taken at $\theta_i = 70°$ and $\theta_f = 85°$ i.e. at a total scattering angle θ of 25°. When the incoming energy is raised from 100-to 200-eV, the percentage of energy retained by the parent ion remains about 80%. This is indicative for *single* collisions with the liquid molecules. Note that the parent ion is not observed above 200 eV (see Fig. 4.4). In the past, this invariance of the relative energy position with incoming energy was studied extensively for noble gas ions scattered from single-crystal and polycrystalline surfaces to investigate the validity of the binary collision approximation [119–121]. In our case, a "single scattering event" was already inferred when discussing the energy distributions of the positive fragment ions at one fixed scattering θ, but for different in- and outgoing angles (see Fig. 4.6).

The relative energy positions of the other (fluoro)carbon fragment ions show the same invariance. This is especially clear for the CF^+ fragment ion, since it is observed over a wide energy range. From this graph we deduce that the energy of the fragment ions is directly proportional to their mass and, moreover, that the fragment ions leave the surface

with the same speed for incoming energies ranging from 100-to 500-eV. The relative energy position of the F$^-$ fragment ion is in agreement with these observations.

The lines in Fig. 4.8 denote the relative energy positions of CF$_x^+$ (x=0-3) fragments, using simple kinematic theory. We assume that CF$_3^+$ ions scatter off the -CF$_3$ groups of the liquid molecules in a binary collision. After scattering, the fragment ions leave the surface with the same speed. Although other effects like internal energy uptake have been ignored in this model, the calculated lines in the figure describe the relative energy positions of the fragment ions very well and indicate the validity of the binary collision approximation for this total scattering angle and this incident energy range.

Translational energy transfer to the liquid: varying the total scattering angle

We now investigate the translational energy transfer to the PFPE liquid as a function of total scattering angle. In Fig. 4.3(a) we show a translational energy loss ΔE of the scattered CF$_3^+$ ions of about 20 eV, for E_i=100 eV and $\theta = 25°$. For larger total scattering angles more energy is transferred to the surface. In Fig. 4.3(b) we see that for $\theta = 35°$ about 30 eV is transferred. The peak positions of the fragment ions have shifted to lower energies, proportional to their mass. Once again, this means that the speed of the fragment ions is the same. This observation holds for the entire energy and angular regime employed in this experimental study. Also the negatively charged fragment ions (F$^-$) show this proportionality.

In what follows, "the translational energy that is retained by the fragment particles" refers to the amount of translational energy that stays in the motion of the fragments after the scattering event. At small total scattering angles this quantity is determined directly by measuring the translational energy of the scattered parent ion. At larger total scattering angles, where the parent ion is not observed due to the enhanced fragmentation, the *speed* of the other fragment ions is determined and from this the center-of-mass energy of the scattered parent ion is deduced. We mentioned in section 4.3.2 that for the scattering conditions used in this experimental study all fragment ions leave the surface with the same speed.

In Fig. 4.9 we have plotted the translational energy that is retained by the fragment particles as a function of their total scattering angle. The incoming angle is 70° and the incoming energy 100 eV. These are identical scattering conditions to those used in Fig. 4.5(a). This graph clearly shows that more translational energy is lost at larger scattering angles. The translational energy transfer to the surface varies from 20% for a total scattering angle of 25° to about 60% for total scattering angles of about 90°. The solid line gives the translational energy of the CF$_3^+$ ions when we apply the binary scattering formula (eq. (4.1)), for a CF$_3^+$ ion scattering off the -CF$_3$ groups of the PFPE liquid molecules. At small total scattering angles the data points follow the single scattering model. However, at larger total scattering angles the single collision model with a fixed mass does not describe the data points very well and, clearly, another model should be applied. The effective surface mass appears to increase. This is discussed in more detail in section 4.4.1. and in Chapter 6 of this thesis.
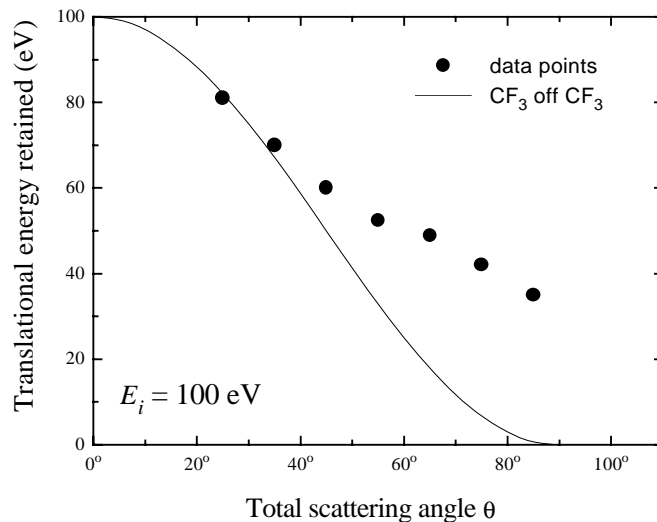
Figure 4.9 *The measured kinetic energy retained by the fragment ions as a function of total scattering angle after scattering of a 100 eV CF_3^+ beam from a PFPE liquid surface. The data are taken at $\theta_i = 70°$. The solid line was calculated from eq.(4.1) (single collisions) for the CF_3^+ on CF_3 system.*

Translational-to-Internal energy transfer: varying the incoming energy

In our experiment the total scattering angle and translational energy loss ΔE of the fragment ions are known and, assuming a single collision event, it should in principle be possible to determine the transfer of translational energy to internal energy of the projectile. Unfortunately, the resolution of our energy analyzer is limited and we are not sufficiently sensitive to accurately determine this quantity. Therefore, we apply an alternative method to determine the internal energy uptake which is based on the appearance potentials of the fragment ions.

In Fig. 4.10 the relative intensities of the CF_x^+ (x=0-3) ions as a function of incoming translational energy are plotted in a so-called breakdown diagram. The relative intensities of the fragment ions are determined from the fragment ion abundances in the energy spectra presented in Fig. 4.4. These raw energy spectra are scaled by a factor $1/E$ to correct for the energy-dependent transmission function of the analyzer. The individual peaks in the corrected energy spectra are fitted to gaussians. For each incident energy the total ion yield is normalized. The scattering conditions are identical to those of the data shown in Fig. 4.4, i.e. $\theta_i = 70°$ and $\theta_f = 85°$. The obtained breakdown curves can be used to estimate the average internal energy $<Q>$ deposition at a particular collision energy by a thermochemical method used in SID [6,122,123]. We summarize this method below and, subsequently, apply it to our results.

In Table 4.1 the appearance potentials (E_0) of the fragment ions are listed. These values are determined by electron-impact on and photo-ionization of CF_4, and are taken from Ref. [124]. From these values, the average internal energy to produce each fragment ion has been extracted [6,122,123]. The average internal energy deposition $<Q>$ can be calculated by
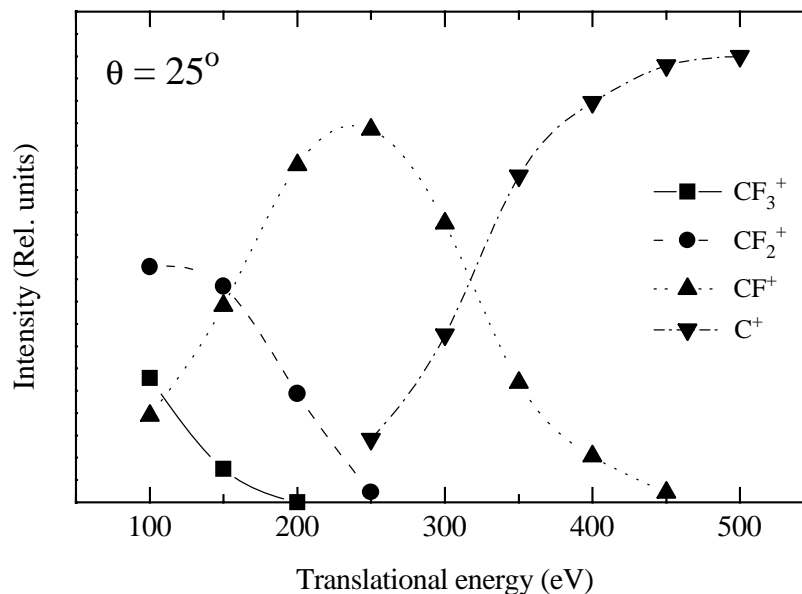
Figure 4.10 *SID breakdown curve showing the normalized relative intensities of the four positive fragment ions as a function of incoming energy for* CF_3^+ *from a PFPE liquid surface. A correction for the energy-dependent transmission of the energy analyzer has been made. The data are taken at* $\theta_i = 70°$ *and* $\theta_f = 85°$.

Table 4.1 *Appearance potentials and average internal energies of the (fluoro)carbon fragment ions*

Ion	Appearance potential[a]	average internal energy
CF_3^+	15.35	2.47
CF_2^+	20.3	6.1
CF^+	22.6	11.7
C^+	31.5	$\sim 17.3^{b}$

[a]Ref. [124].
[b]Based on the critical energy in the breakdown curves relative to ions with known appearance potentials.

determining the fragment ion abundances arising from a series of consecutive events having known critical energies (Eq. 4.2):

$$CF_3^+ \xrightarrow{E_0(1)} CF_2^+ \xrightarrow{E_0(2)} CF^+ \xrightarrow{E_0(3)} C^+ \qquad (4.2)$$
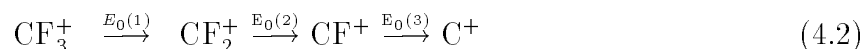
The internal energy distribution $P(E)$ at a particular incident ion translational energy is constructed by taking the relative abundance of the fragment ion CF_x^+ and dividing this by the energy interval $E_0(x+1) - E_0(x)$ over which it is present. This gives a single probability value which corresponds approximately to the average internal energy in this
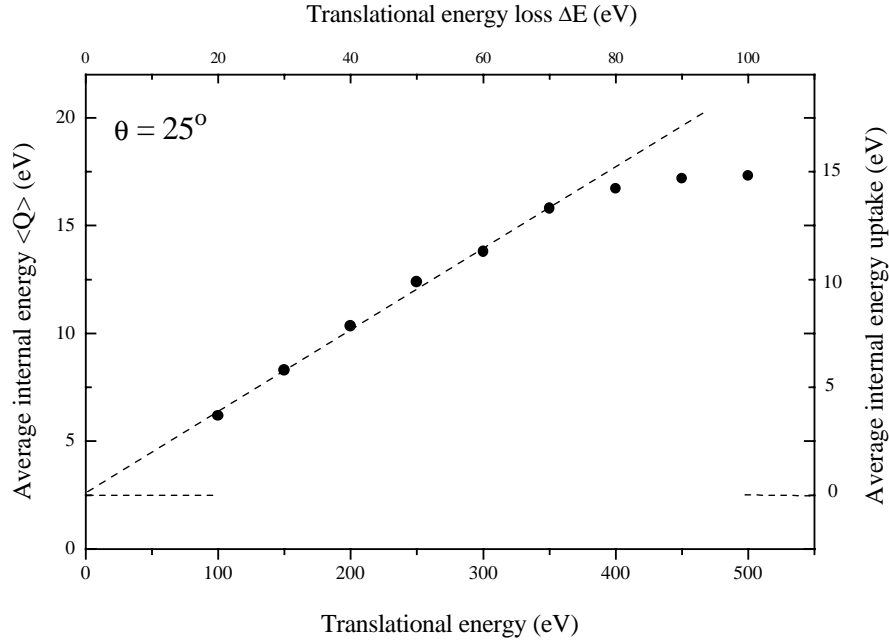
Figure 4.11 *The estimated average internal energy* <Q> *as a function of incident ion kinetic energy (lower abscissa) and kinetic energy loss* ΔE *(upper abscissa) for* CF_3^+ *from a PFPE liquid surface. The data are taken at* $\theta_i = 70°$ *and* $\theta_f = 85°$.

interval. In this way $P(E)$ is constructed and the average internal energy deposition is measured. The average internal energy deposition $<Q>$ can be determined directly by applying the following formula [123]:

$$< Q > \;=\; \sum_x \frac{N_x}{\sum_y N_y} \frac{E_0(x+1) - E_0(x)}{2},$$ (4.3)

where N_x and N_y are the relative intensities of the $CF_{x,y}^+$ (x,y=0-3) ions.

The estimated average internal energy deposition $<Q>$ as a function of incident ion translational energy (lower abscissa) is plotted in Fig. 4.11. As the translational energy loss ΔE is directly proportional to incident ion translational energy (section 4.3.2), this quantity is depicted on the upper abscissa. The plot shows a linear increase of the internal energy of the scattered ion with increasing ion translational energies. This behaviour has been observed in a number of previous studies [6,125,126]. At the highest incoming energies $(E_i > 350$ eV$)$ $<Q>$ starts deviating from this linear behaviour. This is most probably due to the method followed to determine the $<Q>$ values which inherently assumes a maximum internal energy uptake. If we extrapolate to low incoming energies we can estimate the average internal energy prior to the collision. Doing so gives a value of about 2.5 eV which is a reasonable value compared with previous studies [123]. Note that in our study electron impact energies of 110 eV are used; therefore the CF_3^+ ions will be vibrationally hot. To correct for this we have plotted on the right hand ordinate the average internal energy

uptake in the collision. The value of 2.5 eV is approximately the same as the average fragmentation energy of the parent ion ($CF_3^+ \rightarrow CF_2^+ + F$) assuming uniform distribution of internal energies, the value of which is about $4.95/2 = 2.5$ eV [126].

We can now estimate how much of the translational energy lost in the collision, ΔE, is converted into internal energy Q. This gives an efficiency of about 19%; a constant value for incoming energies between 100 and 350 eV. Note that approximately 3.8% of the total incoming energy is transferred to internal energy, because we use grazing angles of incidence in this study, the total scattering angle used is only 25°. In this kind of collision only a small fraction of the center-of-mass (c.m.) energy is transferred to the surface. The largest fraction of the c.m. energy will stay in the motion of the fragment ions. In previous studies determining the translational-to-internal energy transfer efficiencies, larger total scattering angles (about 90°) were employed giving rise to much larger total translational energy losses, ΔE, than that determined in Fig. 4.9.

Translational-to-Internal energy transfer: varying the total scattering angle

In Fig. 4.3 we showed a shift to lower energies of the fragment ion positions with increasing total scattering angles. Also more dissociation takes place at larger total scattering angles where more translational energy is transferred to internal energy. When we compare the positive fragment ion spectra of Fig. 4.3(b) and Fig. 4.4(b) we observe a striking resemblance. The relative ion abundances are comparable and, consequently, the internal energy uptake must also be comparable (both ~ 5.7 eV). In both cases the translational energy loss, ΔE, which the CF_3^+ ion has suffered in the collision, is about 30 eV. However, the scattering geometry and incident energy are quite different: for Fig. 4.3(b); $E_i=100$ eV and $\theta = 35°$, for Fig. 4.4(b); $E_i=150$ eV and $\theta = 25°$. The CF_3^+ ions are observed at $E_f=70$ eV and $E_f=120$ eV in Fig. 4.3(b) and Fig. 4.4(b), respectively. These observations indicate that the average internal energy uptake $<Q>$ is proportional to the average translational energy loss ΔE in the collision ($<Q> \propto \Delta E$), which was suggested by Uggerud and coworkers in a theoretical paper [127,128]. The present experimental study confirms this prediction using different incoming energies and scattering geometries leading to the same translational energy loss ΔE and average internal energy uptake $<Q>$.

4.4 Discussion

In the previous sections we showed the energy and angular distributions of positive and negative fragment ions in the scattering of 100-to 500-eV CF_3^+ beams incident on the PFPE liquid surface. We determined the energy transfer to the liquid molecules and estimated the average internal energy deposition in the incident particle as a function of incoming energy and total scattering angle. These results indicate single collisions off the -CF_3 groups of the PFPE molecules. The degree of dissociation scales with the incident energy and total scattering angle θ. The important parameter is the energy lost ΔE in the collision. In this section we address the scattering dynamics in more detail. We discuss the dissociation mechanism and comment on charge transfer processes. A comparison is made with measurements done on CF_3^+ scattering from Ag(111) and barium-covered Ag(111).

4.4.1   Scattering dynamics

It is quite remarkable that, at *small* total scattering angles ($\theta < 40°$), we observe a translational energy loss ΔE of the CF_3^+ ions which exactly matches the scattering off a -CF_3 group of the perfluoropolyether. Although both species are composed of 4 atoms, their interaction can be considered essentially binary. In the case of scattering diatomic ions from single crystal surfaces at total scattering angles larger than about 20°, the interaction is viewed as being binary: the total mass of the scattered diatomic ion is considered to be colliding with the metal atom(s) in a single or double collision. In the case of CF_3^+ scattering from Ag(111) the energy position of the parent negative ion was observed to correspond to the double collision position [116]. The energy transfer to the surface by larger polyatomic ions scattered from organic surfaces has also been studied. It was found that 60 to 70% of the incoming energy was lost with a total fixed scattering angle of 90° [97,122,123]. An effective surface mass corresponding to the mass of several functional groups ($CH_3(CH_2)_5$ or $CF_3(CF_2)_2$) was introduced to account for the observed translational energy losses [122,123]. In the scattering of C_{60}^+ ions from heteroepitaxial fullerite surfaces a small translational energy loss was measured [129]. In modeling the scattering process, the initial interaction is viewed as being binary, i.e. a C_{60}^+ ion collides with one C_{60} of the fullerite [130]. The surface C_{60} recoils from the incident C_{60} and subsequently rebounds from the lattice hitting the incident ion in a second collision. Consequently, the fullerite acts as a rigid wall and only a small amount of energy was lost by the scattered C_{60}; although the scattering occurred in a sequence of binary collisions. In the case of equal mass (and size) of the scatterers, the energy transfer is most effective as can be deduced from the binary scattering formula (eq. 4.1). Most presumably this is the reason a translational energy loss ΔE ($\theta < 40°$) of the CF_3^+ ions which corresponds exactly to the scattering off a -CF_3 group of the perfluoropolyether is observed.

At larger total scattering angles ($\theta > 40°$) the energy transfer to the liquid starts deviating from the single collision model (see Fig. 4.9). The fragment ions leave the surface with more final energy, i.e. less energy is transferred to the surface, than is expected on the basis of a single collision with a -CF_3 group. However, if the incoming energy is raised and the total scattering angle is kept constant ($\theta = 25°$), the same translational energy losses ΔE are seen and no deviation from the single collision model is observed (see Fig. 4.8). This observation rules out inelastic effects like electronic excitations being responsible for the deviation from the single collision model [10,11,131]. The effective surface mass appears to increase for larger total scattering angles. This phenomena is studied in detail in Chapter 6 of this thesis.

In our experiment we observe an enhanced fragmentation for particles scattered over larger total scattering angles (Fig. 4.5(a) and (b)). This enhanced fragmentation has been observed before in scattering from single crystal surfaces [81,86] and studied in more detail for scattering of CF_3^+ along different azimuthal angles of the Ag(111) surface [116]. From the experimental results presented in this chapter, a straightforward explanation can be given for the increase in fragmentation with total scattering angle. When the incident particles scatter off the surface they follow different trajectories leading to different total scattering angles. Trajectories with larger total scattering angles can be associated with smaller impact parameter collisions [11,132]. With each scattering angle a different translational

energy loss ΔE is associated; more energy transfer to the surface occurs for larger scattering angles (Fig. 4.9). The translational energy loss is directly proportional to the internal energy uptake as was demonstrated in section 4.3.2. Consequently, more fragmentation is observed at larger total scattering angles.

4.4.2 Dissociation mechanism

The dissociation of CF_3^+ on a PFPE surface is governed by the impulsive collision. The increase in dissociation yield with higher incoming energies clearly indicates collisional activation rather than a mechanism involving electron transfer. The present result greatly differs from the results of CF_3^+ from a clean and a barium-covered Ag(111) surface, where electron transfer processes dominate the ion-surface interaction and the dissociation dynamics.

Previous studies have shown that many of the same excitation processes are operative in gas phase collision-induced dissociation as in surface-induced dissociation [6,109]. In collisional activation in the gas phase, the translational energy of the parent ion is converted into vibrational energy (T-V conversion). The dissociation takes place "slowly" relative to the times scale in which the collision occurs [118]. The dissociation of polyatomic ions is claimed to occur exclusively via statistical channels at these low collision energies [118].

In the present experimental study the impulsive excitation and energy transfer to the surface occur in a *single* collision. This single collision event is supported by the invariance of the relative energy position of the fragment ions and the energy distributions of the positive ions performed at a fixed total scattering angle θ. That the internally excited ion dissociates when it has left the vicinity of the surface is supported by the fact that the fragment ions are detected with the same velocities. This is true for the positively charged (fluoro)carbon ions and the negatively charged fluorine ion. If the dissociation were to occur directly at the surface, the fragment ions would leave the surfaces with different velocities [122] and the fragment ions would display a broader angular distribution [18,133]. The exact timescale in which the dissociation takes place is difficult to determine from the present experimental findings. Unimolecular dissociation is known to occur on a μs timescale, while the collision event occurs on a femtosecond timescale.

Previously, the scattering of fluorocarbon ions (CF_3^+, $C_2F_4^+$ and $C_3F_6^+$) at hydrocarbon, deuterated hydrocarbon and fluorocarbon SAM surfaces has been studied by mass spectrometric techniques by Cooks and coworkers [28,30], who concluded that approximately 60% of the incident translational energy was transferred to the surface. The percentage of the total incident translational energy transferred to internal energy ranges from 13% for the hydrocarbon to 20% for the fluorocarbon SAM surfaces. Their scattering geometry was $\theta_i = 45°$ and $\theta_f = 45°$ or a total scattering angle of 90°. These values are in good agreement with our findings. For the same scattering conditions we observe that approximately 65% of the incident energy is lost in the collision (Fig. 4.9) of which 19% is transferred to internal energy.

Some attempts have been made to develop an impulsive collision-transfer theory for the collision between a gas *atom* and a macro*molecular* ion by Uggerud and coworkers [127,128], which has been subsequently applied to surface scattering experiments [122,123]. The theory gives an expression of the uptake of the internal energy Q, the translational

Table 4.2 *Ionization potentials and affinity levels of the (fluoro)carbon species*

particle	ionization potential	affinity level
CF_3	≤ 8.9 eV[a]	1.8 ± 0.2eV[b]
CF_2	11.4eV[a]	0.18eV[c]
CF	9.11eV[a]	0.45 ± 0.05eV[d]
C	11.3eV[a]	1.26eV[a]
F	17.4eV[a]	3.4eV[e]

[a]Ref. [134]. [b]Ref. [87].
[c]Ref. [88]. [d]Ref. [89].
[e]Ref. [90].

energy loss ΔE and the angle θ through which the macromolecular ion is scattered for the case of a *single* collision event. The important conclusions of this theory relevant to the present work are summarized here. *i*) The average translational energy loss ΔE of the polyatomic ion increases linearly with its incoming translational energy. *ii*) The average internal energy uptake, $<Q>$, increases linearly with the energy of the ion. *iii*) The average internal energy uptake, $<Q>$, is directly proportional to the average translational energy loss ΔE in the collision. In a comment following the Uggerud paper [127] it is stressed that the translational energy loss, ΔE, which characterizes any particular fragment ion, can be converted to the internal energy of the parent ion [128]. Points *i* through *iii* have been verified in our experiment. However, it is very difficult to calculate these quantities directly from the present theory for the CF_3-CF_3 collision system.

The mechanism of collision induced dissociation assumes the impulsive transfer of translational energy into rovibrational energy. This will be dependent upon the individual masses of the atoms of the incident polyatomic ions and of the surface atoms. Also the orientation of the internuclear axes of the incident polyatomic ion, its vibrational frequencies and the molecule's vibrational phase during the collision are important. A detailed understanding of these properties requires the use of classical trajectory calculations [18,22]

4.4.3   Charge-transfer

Neutralization

In the scattering from a clean Ag(111) surface all the incoming CF_3^+ ions are neutralized. No surviving CF_3^+ ions are observed. Two neutralization channels are operative: one is directly to the ground state located at 8.9 eV below the vacuum level via an Auger process and the other channel is resonant neutralization to a stable Rydberg state at 4.3 eV below the vacuum level. The energy position of this state has been calculated using *ab initio* configuration interaction calculations [98]. No other neutralization channels have been found in the calculations. Neutralization into this Rydberg state is the dominant process. The efficiency of Auger neutralization is low, as is confirmed by scattering from a barium covered Ag(111) surface [117].

These two neutralization states are not directly accessible when we scatter from a liquid

perfluoropolyether: the ionization potentials of (per) fluorinated ethers are well above 12 eV [134]. The ground state of neutral CF_3 is located at 8.9 eV below the vacuum level. The other fragment ions have comparable ionization potentials (see Table 4.2). Although about 90% of the incoming ions are neutralized, this neutralization yield is considerably less than in scattering from a clean metal surface as has been observed in a number of studies [30,31].

Negative ion formation

Negative ion formation from atomic species (H, O, F) incident on metallic and non-metallic surfaces has been studied in much detail [32,49]. The population of the affinity level of a neutral atomic species in collisions with a metal surface is inferred to occur via a resonant charge exchange process of an electron from the Fermi-level of the metal. In close approach to the surface, the affinity level of the atom shifts down due to the image force attraction and a broadening of this level due to the overlap of atomic and metallic wave functions occurs. High yields of negative ions can be obtained for low work function surfaces and/or for atoms with high affinity levels. Recently, Winter and co-workers studied the formation of negative halogen ions in scattering of positive halogen ions from alkali-halide surfaces. It was found that negative ion yields up to 100% could be obtained under certain scattering conditions [48]. However, this requires highly energetic beams (> 10 keV) in very grazing collisions. The incident energies employed in the current experimental study are several orders of magnitude lower.

Negatively charged molecular ions have also been observed in the scattering of positive molecular ions and neutral molecules from metal surfaces [17,101]. However, not only is the shift of the affinity level due to image force attraction and broadening important, but also the phase of the vibrational period of the bond is important which can cause even larger shifts of this level [17,22,82,135].

It is quite remarkable that we observe negative ions in our experiment: the ionization potentials of (per) fluorinated ethers are above 12 eV [134]. The affinity level of the F atom is located 3.4 eV below the vacuum level (see Table 4.2). This table also shows that the fluorocarbon species have affinity levels comparable to that of the fluorine atom. However, we do not observe any negatively charged *polyatomic* ions. This seems to indicate that ions surviving the surface collision are not easily neutralized at the outgoing trajectories and subsequently negatively ionized. This is in agreement with our previous conclusion that the break-up of the particle occurs at some distance from the surface. Possibly, F atoms formed in the impulsive collision can pick up an extra electron. However, the dissociation event is inferred to occur in the gas phase and, moreover, the energy shift of the affinity level required for resonant charge exchange is extremely large (> 8 eV). Another, more likely process is that a *neutral* CF_3 species is formed which dissociates due to the impulsive collision at some distance from the surface into a positively charged (fluoro)carbon species and negatively charged F ion (i.e. a polar dissociation event). In gas phase collision induced dissociation, an "ion pair" was observed in the scattering of singly charged negative ions to form a doubly charged negative ion and a positive ion [136]. This was referred to as collisionally-induced "ion pair" formation. In our case we conclude that a collisionally-excited neutral species leaving the surface forms an "ion pair". In equations 4.4 and 4.5 we have schematically depicted two possible dissociation channels of a positive (eq. 4.4) and a

neutral (eq. 4.5) collisionally-excited CF_3 particle leaving the surface, respectively. These equations can be generalized for more channels. In both cases a positive (fluoro)carbon ion is formed, in the neutral case also a negatively charged F ion is formed. The equations are given by:

$$CF_3^+ + PFPE \; \longrightarrow \; [CF_3^+]^* + PFPE \longrightarrow CF_2^+ + PFPE + F \qquad (4.4)$$

$$CF_3^+ + PFPE \; \longrightarrow \; [CF_3]^* + PFPE^+ \longrightarrow CF_2^+ + PFPE^+ + F^-, \qquad (4.5)$$
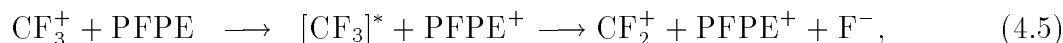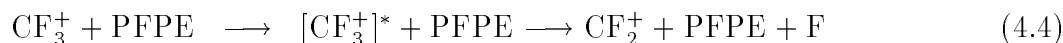
where CF_3^+ is the incoming ion which collides with the perfluoropolyether surface PFPE. In the first case the ion is collisionally excited (denoted with asterisk) after the collision. In the second case the ion is neutralized and collisionally excited and, subsequently, the dissociation occurs in the gas phase and the "ion-pair" is formed.

In the case of scattering of CF_3^+ off Ag(111) we also inferred a polar dissociation event. However, in this case an *electronically* excited species dissociates into CF^+ and F^-. The excited species $[CF_3]^*$ is formed by resonant neutralization to a Rydberg state at 4.3 eV below the vacuum level [98,116].

4.4.4 Liquid-versus-metal surfaces

In this section we make a comparison between the dissociative scattering of polyatomic ions from a liquid and from a metal surface. The main differences can be explained by the difference in electronic structure between the liquid, the perfluoropolyether, and the metal surfaces, the Ag(111) and the barium covered Ag(111) surface.

Geometric structure and effective mass of the surface

A remarkable difference in the angular distributions can be observed by comparing scattering from Ag(111) and the PFPE liquid. In the case of scattering from a metal surface, the angular distributions of the C^+ ion are distinctly broader than those measured in the scattering from a liquid surface. Looking at the final energy of those C^+ ions we observe that much less energy is transferred to the surface in the ion/metal collision. This is especially clear if we compare the energy transfer to the different surfaces as a function of outgoing angle. In the case of scattering from a clean Ag(111) surface, the energy transfer shows a much smaller decrease with larger outgoing angle than scattering from the PFPE liquid. We attribute this to the fact that the Ag atoms are much heavier (M=108) and to the fact that the single crystal surface has a much closer packing than the liquid surface. We fitted a model with a double collision with the Ag atoms to our results. In the present experimental study we showed that the average internal energy uptake, $<Q>$, is proportional to the average translational energy loss ΔE in the collision. In the case of scattering from a Ag(111) and a Ba/Ag(111) surface, the energy transfer is a weak function of the outgoing angle. Consequently, the average internal energy uptake is also a weak function of outgoing angle. Ions in trajectories over larger total scattering angles survive the collision. This leads to a broader angular distribution for the C^+ ions scattering from Ag(111). For scattering conditions similar to those employed in the current experimental study this was

about 40° (FWHM). The widths of the angular distributions of the CF^+ and C^+ peaks for similar scattering conditions are 20° and 25° (FWHM), respectively. From this we conclude that the width of the angular distributions of the product ions gives direct information concerning the energy transfer in the collision and, hence, the internal energy uptake.

Hence, scattering from an effectively heavier surface results in less dissociation because the average translational loss ΔE in the collision is less. This is contrary to what has been suggested earlier where it was claimed that scattering from a "heavier" surface results in more dissociation [122,126]. However, the energy transfer to the surface was not studied in much detail in those studies. It could well be that more energy is transferred in scattering from a fluorinated surface than a hydrogenated surfaces because of a difference in surface structure and/or distance between the -CH_3 and -CF_3 groups. However, no measurements have been done to support this.

Not only is the effective surface mass important in the scattering event but also the distance between the objects which scatter is relevant. This is demonstrated when the CF_3^+ ions are scattered along different azimuthal orientations of the Ag(111) crystal. Along all crystal azimuths, essentially a double collision occurs with the Ag atoms. However, the angular distributions of the fragment ions are quite different. In case of scattering from a perfluoropolyether the mutual distance between the -CF_3 groups is large enough to allow for single collisions.

Electronic structure of the surface

Apart from the geometric structure and effective mass of the surface, the electronic structure of the surface is also important in polyatomic ion-surface collisions [26]. In the case of scattering from a Ag(111) surface, resonant neutralization and Auger neutralization are considered, as discussed above. Essentially all CF_3^+ ions are neutralized in scattering from Ag(111) and the dissociation is mostly due to charge transfer processes. In the case of scattering from the PFPE surface the neutralization is hindered due to the high ionization potentials of the liquid molecules. The incoming ions are not easily neutralized along the incoming trajectory and dissociation due to the impulsive collision becomes apparent. The same holds for fragment ions leaving the surface; these are also not easily neutralized.

Several studies have been performed which directly compare scattering from well characterized metal and non-metal surfaces. These systems include $Fe(C_5H_5)_2^+$ on Si(100) and alkanethiol SAM surfaces [118], pyridine from clean Ag(111) and from pyridine-covered Ag(111) [76,137]. In all cases higher survival probability was found in scattering from non-metallic surfaces. These are generally surfaces with higher ionization potentials.

4.5   Summary and conclusions

We have studied the dissociative scattering of CF_3^+ ions from a liquid insulating perfluorinated polyether surface. We measured the energy and angular distributions of the scattered positive and negative fragment ions. The parent positive ion was observed as well as CF_2^+, CF^+ and C^+ ions. Their appearance was dependent on the scattering conditions. The negative ions only showed F^-; no negatively charged *polyatomic* ions were observed. We determined the transfer of translational energy to the surface and to internal energy of the

scattered polyatomic ion as a function of incoming energy and total scattering angle. The CF_3^+ ions scatter off the -CF_3 groups of the PFPE in a single collision. The dissociation is governed by the impulsive collision. The degree of dissociation scales with the incoming energy and total scattering angle. The important quantity is the energy transferred in the collision ΔE. Approximately 19% of the translational energy lost in the collision is transferred into internal energy, i.e. rovibrational energy. This translational energy transfer to the surface varies from 20% for a total scattering angle of 25° to about 60% for total scattering angles of about 90°.

The appearance of the negatively charged F ions is inferred to occur due to a collisionally-excited neutral species leaving the surface which forms an "ion-pair". The main differences in scattering from a metal and liquid surface is explained by the effective mass and the geometric- and electronic-structure of the surface. In the case of scattering from a Ag(111) surface *electronically* excited species are formed which dissociate. The ionization potentials of the perfluoropolyether are too high to allow resonant neutralization. Here, *collisionally* excited species are formed which dissociate after leaving the surface.

Chapter 5

Design and performance of a new low-energy ion beamline

Abstract

A new low-energy ion beamline capable of producing ions between 10 and 1000 eV is described. At the sample position currents between 20 and 100 nA are attained, for beam energies varying from 10-to 100-eV. Preliminary experiments are shown for Ne^+ scattering off Au(111) at low incident energies (34 eV and 77 eV). The feasibility of polyatomic ion/surface experiments is discussed.

5.1 Introduction

The dissociative scattering of molecules and molecular ions from surfaces has been a topic of ongoing research in chemistry and physics. In the thermal and hyperthermal incident energy regime, much work has been done with the help of molecular beam techniques [7]. These techniques allow the acceleration of neutral particles to incident translational energies between 10 meV and at most 10 eV, to elucidate the mechanisms leading to dissociation in particle/surface scattering. In addition, ion scattering studies in the low incident energy regime (100-to 3000-eV) have been performed on the scattering of diatomic ions from single crystal surfaces [101,106]. The ion beams can easily be produced and focused with the appropriate ion optics at these translational energies.

In the last decade, more attention has been focused on the intermediate energy regime, which is roughly between 10 and 100 eV [107,108]. This incident energy regime is relatively unexplored, because of the technical difficulties associated with the production of sufficiently intense hyperthermal ion beams. In particular, the spatial spreading of the ion beams due to the space charge effect is troublesome at these low incident energies.

The incident energy regime between 10 and 200 eV is of interest in tandem mass spectrometry, where collisions between polyatomic ions and surfaces, so-called surface-induced dissociation (SID), are used to efficiently transfer translational energy into internal energy, which leads to fragmentation for analytical purposes [6]. To study the impulsive energy transfer processes of polyatomic ions in collision with surfaces in detail, well characterized low energy ion beams, with energies between 10 and 200 eV, are necessary. The spread of the incident translational energies should be kept low. In addition, it should be possible to

produce large polyatomic ions, with high mass resolution. For a complete understanding of the scattering dynamics, energy and angular analysis of the scattered products must be performed [138].

In this chapter, we describe the design and performance of a new low-energy beamline which is capable of producing intense ion beams between 10 and 1000 eV, with a relatively low translational energy spread. In addition, sufficiently high mass resolution is achieved, allowing for the scattering of large polyatomic ions and their fragment ions. We show that the currents attained at the target position are sufficiently high, even at very low incident energies, to allow for ion/surface scattering experiments. Currents between 20 and 100 nA are measured for beam energies varying between 10 and 100 eV. In the present set-up, it is possible to perform energy and angular analysis of the scattered products. The new set-up allows for the study of the fundamental processes governing polyatomic ion/ surface scattering in the hyperthermal and low incident energy range.

This chapter is divided into four main sections. In section 3.2, a description is given of the experimental set-up and the design criteria of the new low-energy beamline are discussed. The vacuum system and the ion optics are described in some detail. In section 3.3, the instrument performance is discussed and some preliminary results are given. Section 3.4 ends with a summary of the most important results.

5.2   Instrument description

5.2.1   Experimental set-up

The experimental set-up is described in detail in chapter 2 of this thesis. Briefly, it consists of two UHV chambers. In one (base pressure of 4×10^{-11} mbar), the scattering sample can be characterized and stored. The sample can be transferred under UHV to a two-axis goniometer in the second chamber (base pressure of 1×10^{-10} mbar). The goniometer allows for the rotation of the target around an axis parallel to the surface in order to change the incoming angle θ_i (which is measured with respect to the surface normal) and rotation around the surface normal to change the azimuthal angle Φ. This is schematically depicted in Fig. 5.1. The total scattering angle θ is defined as: $\theta = 180°$ - $(\theta_i + \theta_f)$ with θ_f the outgoing angle of the particles. The scattered positive and negative ions are detected with a 90° cylindrical electrostatic energy analyzer, with an energy resolution of $\Delta E/E = 0.08$. In the scattering plane the detector can be rotated from 45° to 180° with respect to the incoming beam and out of plane detection from $-15°$ to 90° is possible. The angular resolution of the detector is around 0.5°.

5.2.2   Design criteria

The goal is to build a high-intensity low-energy ion beam line which is compatible with the existing UHV set-up. The translational energy of the primary ion beam must be variable between 10 and 1000 eV and sufficiently high ion yields (> 1 nA/cm^2) at very low incident energies (< 50 eV) must be produced. It must be possible to change the mass of the primary ion between roughly 1 and 400 a.m.u, to allow for the study of polyatomic ions which are also used in conventional mass spectrometry. Because of the limited amount
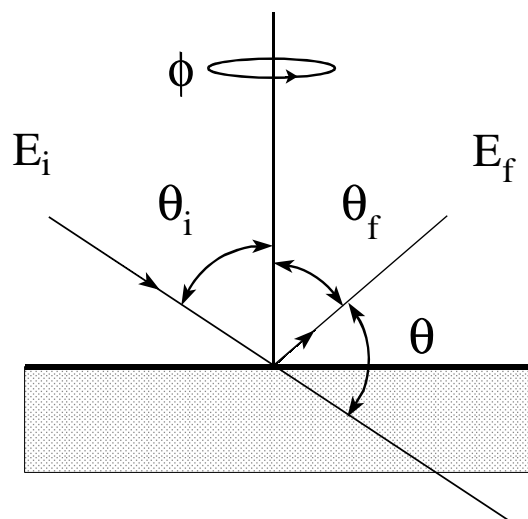
Figure 5.1 *Definition of the scattering geometry: the incoming angle θ_i, the outgoing angle θ_f and azimuthal angle Φ.*

of space available in our laboratory and the positioning of the present set-up, the total length of the beamline should be kept short. The ion source must be capable of producing high-intensity beams of noble gas ions for characterization purposes, and polyatomic ions like $C_6H_6^+$, CF_3^+, CF_2^+ and CF^+ ions for low-energy polyatomic ion/surface collisions. The important design criteria are briefly summarized below.

1. Ability to vary the translational energy of the primary ion beam from 10-to 1000-eV.

2. High mass resolution ($M/\Delta M = 400$) and low energy spread of the primary ion beam (< 0.2 eV).

3. The total length of the beamline has to be kept short.

4. Electrical guiding tubes should be present to reduce spreading of the ion beam during transport and to shield the ion beam from stray fields.

5. A bending section is required for the removal of neutrals and photons. We introduce a bending angle of 10°.

6. Ultrahigh vacuum (UHV) compatibility with the main scattering chamber, which means the introduction of several pumping restrictions in the beamline.

7. Two movable collimators for narrowing the angular divergence of the incident ion beam.

8. A current detector for measuring the ion currents just after the bending section.

9. A valve should be present between the scattering chamber and the rest of the beamline.

10. Appreciable currents at the target position (nAs) must be attained.
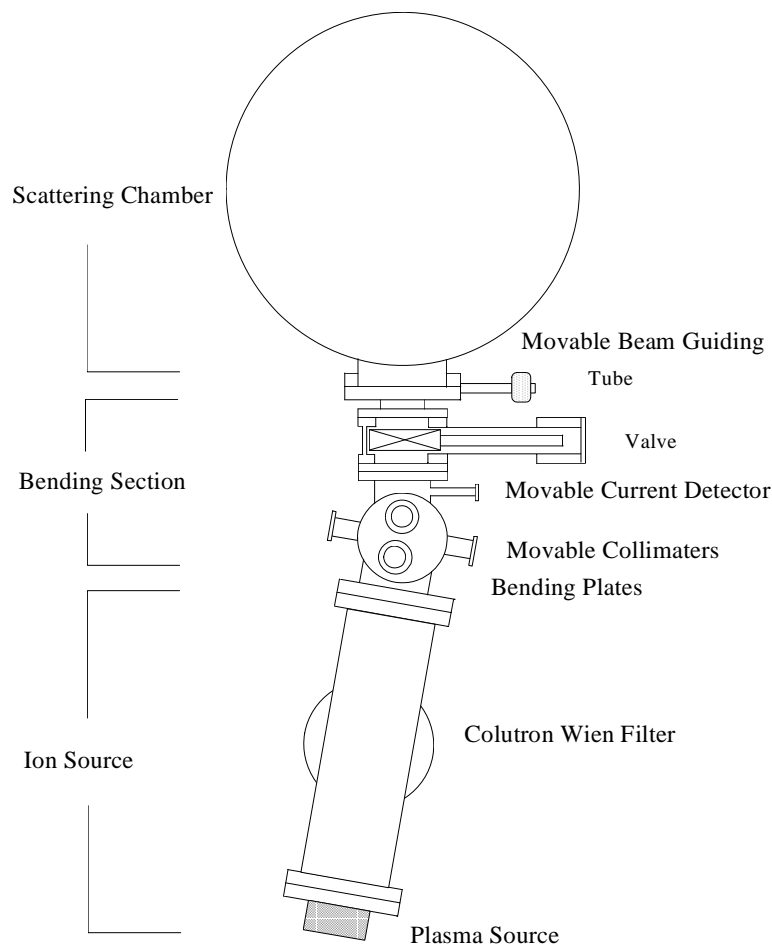
Figure 5.2 *A schematic overview of the UHV beamline housing. We can distinguish three main sections: the ion source, the bending section and the scattering chamber.*

5.2.3   Hardware and vacuum system

The UHV beamline housing is schematically shown in Fig. 5.2. We can distinguish three main sections: the ion source, the bending section and the scattering chamber. The ion source section consists of a plasma source with a narrow energy spread (< 0.2 eV) [139] and a Colutron Wien filter [140] for purification of the primary ion beam. The ion source is pumped by a Balzers 100-l/s turbo molecular pump, the bending section by a Balzers 500-l/s turbo molecular pump and the scattering chamber by a Balzers 300-l/s turbo molecular pump, a titanium sublimation pump and a ion-getter pump (400-l/s). Pumping restrictions are introduced between the ion source and bending section and between the bending section and scattering chamber. The base pressure in the source housing is 10^{-9} mbar. During operation the pressure in the ion source increased to a value between 10^{-6} mbar and 10^{-5} mbar. Operating pressure in the bending section is 10^{-8} mbar, and in the scattering chamber $1{\times}10^{-10}$ mbar.
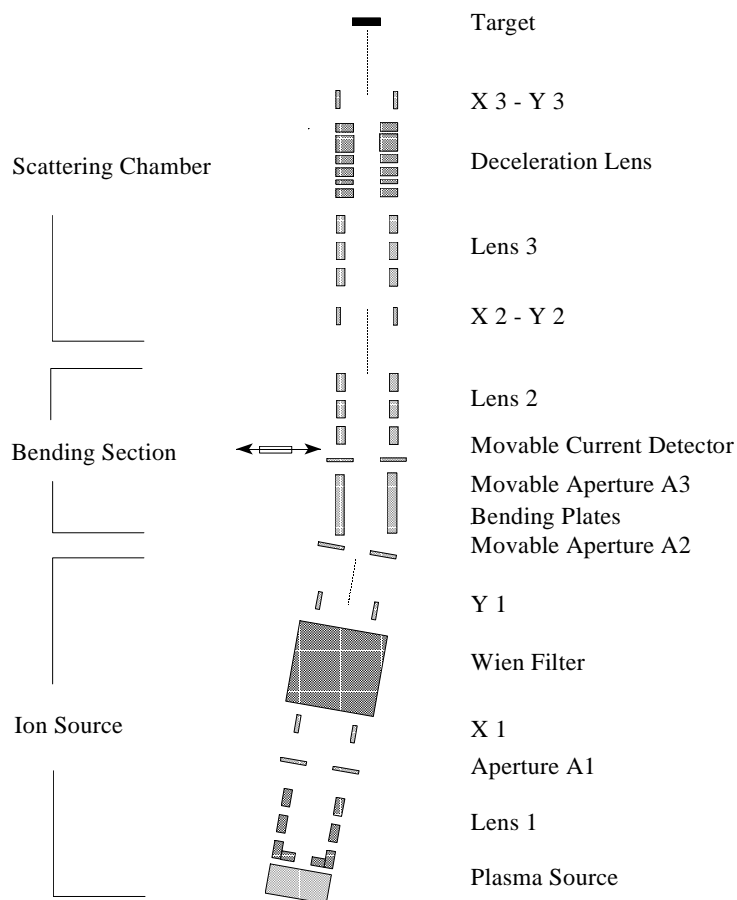
Figure 5.3 *A schematic overview of the beamline optics. The details of the lenses and operating conditions are given in the text.*

5.2.4 Ion optics

Design

The beamline ion optics have been designed with the help of calculations based on the SIMION computer code [141]. In these calculations, all the beamline optics from the source position to the sample position, including the beam guiding tubes and the bending plates, are simulated. The beamline was divided in different sections and the size of the beam cross sections and the angular divergence at the various locations in the beamline have been determined. The spreading of the beam, due to space charge effects was not considered.

Implementation

A schematic overview of the ion beamline optics is given in Fig. 5.3. The ions from the low energy spread plasma source [139] are extracted and focused by lens 1 (Colutron 200), which serves as a combination of extraction lens and Einzel lens. The ions are accelerated

to transport energies ranging from 400 eV to 1 keV, depending on the mode of operation. The ions are focused into a Wien filter (Colutron 600-B) for purification of the beam. The Wien filter has a mass resolution of 400.

The ions are transported to the bending section, where they are bent through an angle of 10° by two curved bending plates. This section removes light originating from the plasma source and neutrals particles from the beam; only charged particles can pass this section. The plates can be considered an energy filter which removes fragmented particles which have lower translational energies. Two movable collimators for narrowing of the beam size, are placed just before and after the bending section. These are plates which are composed of round holes with diameters varying from 0.5, 1.0, ... to 3.0 mm. These collimator plates are electrically raised to beam voltages. A movable current detector is placed after the second collimator allowing for determination of the current inline with the beam direction. A compact Z-translator (Caburn) allows for the probe-pen and collector plate (diameter 6 mm), which are electrically isolated, to be placed in and out of the ion beam. The probe is connected to a piccoammeter (Keithley), which is at beam voltages. A second Einzel lens is placed after the probe for focusing of the ion beam.

In the scattering chamber, a third Einzel lens is mounted, which focuses the ion beam into the deceleration lens. The deceleration lens determines the final energy and beam quality at the sample position. It is a six-element cylindrical lens of the Menzinger type (Colutron 400-L). The first two elements are at the beam voltage and elements four and six at ground potential. Elements three and five can be adjusted. The beam is decelerated in two steps, in the gaps between element two and three and between three and four. With help of element five the final focusing is achieved, which is operated in an accelerating mode.

Several X-Y deflection plates are mounted along the beamline as can be seen in the schematic overview. Also a set of X-Y deflection plates have been placed just after the deceleration lens for adjusting the final direction of the beam. The Einzel lenses throughout the beamline are operated in retarding mode.

5.2.5   Beam guiding tubes and bending section

To reduce the spreading of the ion beam due to space charge effects, the ions are accelerated to transport energies of 400 eV. During transport, the ions only "see" the deceleration voltage because from the beginning of the bending section to the deceleration lens in the scattering chamber, beam guiding tubes at the deceleration voltage are present. These beam guiding tubes are electrically isolated from the vacuum housing by ceramic rings. During operation of the ion beam, the valve between the bending section and scattering chamber is open. In order not to distort the electric fields by potentials from the vacuum housing, a movable beam guiding tube can be inserted in the open space. The deceleration lens is attached to the beam guiding tube. This approach allows the vacuum housing to be maintained at ground potential; hence no shielding of the vacuum system is required.

The bending section essentially consists of two curved plates. To reduce the perturbation of the field, two additional half plates are inserted between the plates to assure a homogeneous electrical field. These plates are electrically isolated by ceramic rings.
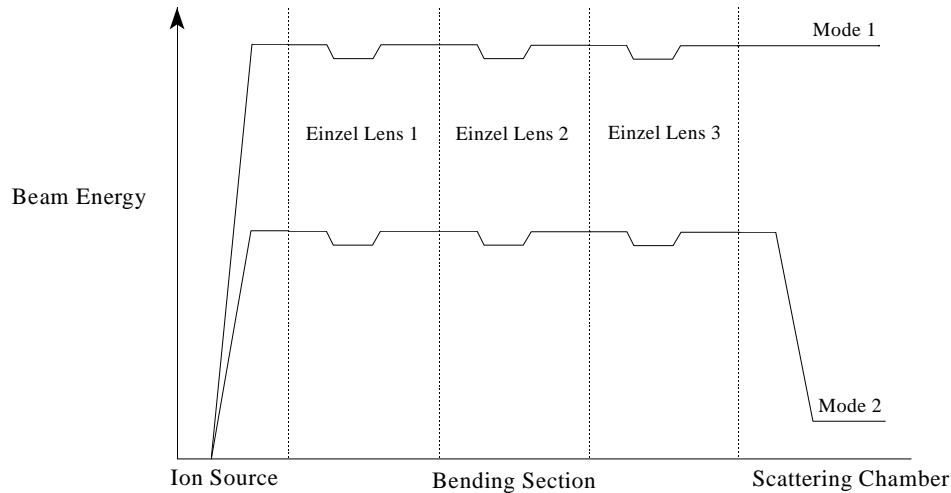
Figure 5.4 *The different modes of operation of the ion beamline: mode 1 for high energy beams (> 400 eV) and mode 2 for low-energy beams (< 400 eV). This scheme applies both to positive and negative ion beams.*

5.2.6   Modes of operation

The ion beamline can be operated in different modes of operation, which are schematically depicted in Fig. 5.4. When high-energy beams are required (> 400 eV, mode 1), the ions are directly accelerated to the desired beam energies. For low-energy ion beams (< 400 eV, mode 2), the ions are accelerated to transport energies of 400 eV. With the deceleration lens, the required final beam energies are attained. This commercially available decelerator lens is designed for an energy range from 1 eV to 1 keV. The ion beams can be decelerated to 1/200 of their initial energy without appreciable beam current loss.

By reversing the polarities on the ion optics, it is possible to produce ion beams of negatively charged particles. This is conceivable for plasma source conditions and gases which easily form negative ions, e.g. CF_3^- or H^-. The negative ion beams are operated in the operation modes depicted in Fig. 5.4.

5.2.7   Instrument control

The electronics that are used for the ion beam optics were constructed in-house. These are isolated power supplies which are used as plug-in units. The heart of this unit is powered by a Spellman-MHV12-1.0K200P power supply [142]. The units can be connected internally to a reference point to allow for the entire ion beamline optics and beam guiding tubes to be raised and referenced to the beam energy. The power supplies can either be operated in the local or remote setting. The local setting allows for setting the output voltages directly at the unit, with the remote setting these can be set by a personal computer. All the lenses have separate power supplies. The plasma source and Wien filter are powered by commercial electronics; Heinzinger (HNC 1200-500) and two Delta (SM7020-D), respectively.

5.3   Instrument performance

In the previous sections we discussed the design and construction of a low-energy ion beam-line. In this section, we comment on the performance of the new instrument. We look at the beam output along the beamline for several ions and discuss some preliminary results of experiments on ion/surface collisions.

5.3.1   Beam output

The decisive factor for ion/surface experiments is the ion beam current at the target position. We determined the ion current along the beamline. for standard operating conditions of the plasma source. The source powers was about 15 W, where the source power is the product of the discharge current and the anode voltage [139].

When the beamline is operated in mode 2, He^+ ions can be accelerated to beam energies of 400 eV. At the entrance aperture, before the bending section, a current of 1.5 μA is measured. Just after the bending section the current is reduced to 100 to 200 nA. At the exit aperture in the scattering chamber, similar currents are measured. In Fig. 5.5, the ion beam currents, which are measured at the target position as a function of deceleration voltage, are depicted. For ion beams with final energies above 50 eV, currents varying between 80 and 120 nA are measured. Below 50 eV, a loss in intensity is observed. Nevertheless, appreciable currents are measured; for an ion beam of 10 eV currents between 10 and 20 nA are attained. For neon gas, we measured currents of 70 nA at the target position. When gaseous CF_4 is introduced in the plasma source, we measure for the CF_3^+, CF_2^+, CF^+ and C^+, 1.8 nA, 30 nA, 8 nA and 1.3 nA, respectively, at the target position for final beam energies of 50 eV. These are sufficiently high yields for ion/surface experiments.

5.3.2   Low-energy ion/surface collisions

In this section we show preliminary experiments which were performed with the new low-energy ion beamline. We limit ourselves to noble gas ion scattering from a metal surface. In addition, experiments have been carried out concerning polyatomic ion/surface collisions: CF_3^+, CF_2^+, CF^+ and C^+ incident on a perfluoropolyether film at incident energies varying from 20-to 200-eV. These results are in chapter 6.

Ne^+ on Au(111)

In Fig. 5.6 the contour diagrams of the backscattered positive ions are plotted for (a) 77 eV, and (b) 34 eV Ne^+ ions incident on a Au(111) surface. In both the cases $\theta_i = 45°$. In Fig. 5.6(a) (E_i=77 eV), we can observe a distinct peak at E_f=68 eV / $\theta_f = 68°$. The angular distribution is peaked towards the surface normal, at angles larger than specular. The energy position is consistent with a Ne atom scattered off a Au atom and can be described by the binary collision formula. The dashed line gives the energy position as a function of outgoing angle calculated for the Ne^+ on Au single collision system, which describes the data points well. The peak in the angular position can be considered a rainbow peak which is the peak where the single and double collision peaks merge [9].
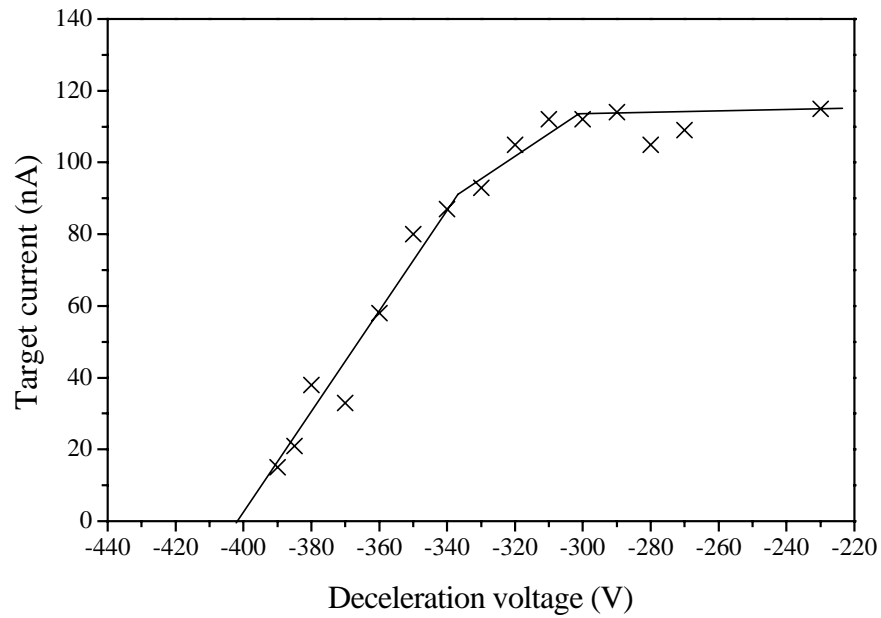
**Figure 5.5**   *The He$^+$ ion beam current measured at the target position as a function of deceleration voltage. The initial energy of the ions is 400 eV. The line is drawn to guide the eye*
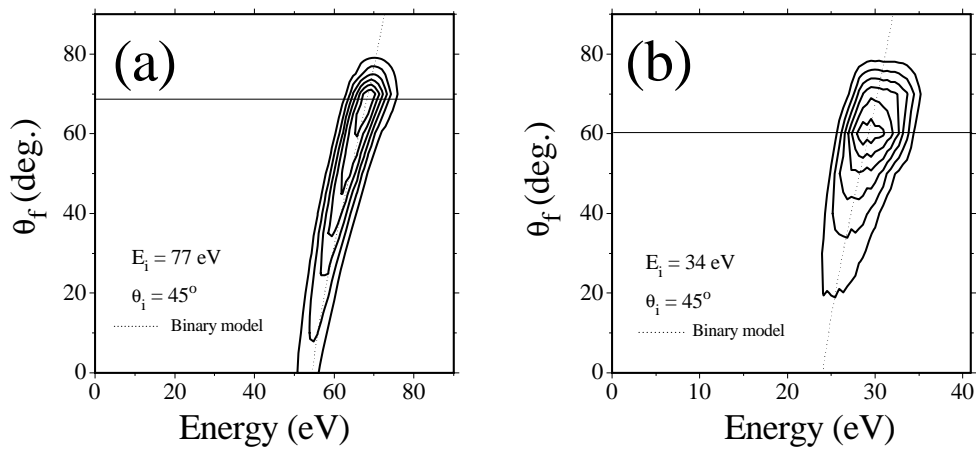
Figure 5.6   *Contour diagrams for backscattered Ne$^+$ ions obtained from (a) 77 eV and (b) 34 eV Ne$^+$ from Au(111) at $\theta_i = 45°$. No correction for the energy-dependent transmission of the energy analyzer has been made.*

In Fig. 5.6(b) the energy of the incident ion beam is lowered to 34 eV. The peak position is shifted towards the surface normal compared to scattering at $E_i=77$ eV, and is now seen at $\theta_f = 60°$. The energy position is consistent with the binary collision formula. The shift towards the surface normal reflects the change in the interaction between the ion and the surface at these low incident energies. At low incident energies the repulsive interaction potential between the incident particle and surface atoms increases giving rise to a smaller cut-off angle of the rainbow peak, Also the width (FWHM) of the angular distribution appears less broad in the case of Fig. 5.6(b).

To our knowledge, this is the first time combined energy and angular distributions of scattered noble gas ions have been determined experimentally in the incident energy range 10-to 100-eV. Some computer simulation studies have been performed for this incident energy range [143]. Experimentally, angular distributions have been determined, however not in combination with energy analysis of the scattered ions [107].

5.4   Summary and conclusions

We have designed, built and tested a new low-energy ion beamline for the production of intense atomic and polyatomic ion beams in the incident energy range 10-to 1000-eV. At the sample position we attained currents between 20 and 100 nA. The new set-up allows for a detailed study of polyatomic ion/surface collisions and determination of the mechanisms that govern the dissociation of polyatomic ions relevant for SID.

Chapter 6

Ion/liquid scattering: Energy transfer to internal energy and to the surface

Abstract

The dissociative scattering of CF^+, CF_2^+ and CF_3^+ ions from a perfluoropolyether surface is explored across the hyperthermal incident energy range 50-to 220-eV. A comparative study on internal energy uptake efficacy and on translational energy transfer to the surface in scattering from the PFPE surface is presented. In addition, measurements are performed on C^+ scattering in order to examine the energy transfer to the PFPE liquid surface in more detail. The CF_3^+ ions take up more internal energy as a function of translational energy lost in the collision than the CF_2^+ and the CF^+ ions. The incident CF_3^+ ions have more approach geometries favorable for internal energy uptake than the other two fluorocarbon ions. Furthermore, a detailed analysis and discussion is presented on the surface effective mass as a function of incident (fluoro)carbon ion mass and total scattering angle. The results are remarkably different from ion/metal surface scattering. The influence of the orientation of the target molecules is observed in ion/liquid scattering. This chapter represents the first detailed study on energy transfer to liquid surfaces in atomic and polyatomic ion scattering.

6.1 Introduction

The study of the mechanisms governing the dissociative scattering of low-energy ions from surfaces is an area of research of considerable interest. Traditionally, the interest originates from two distinct disciplines within chemistry and physics. On the one hand, there are surface scientists who study the interaction of di- and tri-atomics with well defined single crystal surfaces [10,101,106–108]. Those investigations reveal the influence of incident translational energy [15,86], surface corrugation [18,104], impact parameter (Chapter 3 of this thesis), internal energy [82] and approach geometry [21,104,144,145] on the outcome of the scattering event. Along with classical trajectory calculations, much has been learned about the details of mechanisms responsible for the break-up of the incident particles [18,22].

On the other hand, analytical chemists explore the fragmentation of "large" polyatomic ions in collisions with adsorbate covered metal surfaces [6,27,31,146]. Their interest is stim-

ulated by the desire of applying surface-induced dissociation (SID) as an alternative to generate structurally relevant fragment ions for analytical purposes. The ultimate goal is to develop a mass spectrometric technique which helps resolve structures of large (bio)molecules. The SID studies reveal that 10 to 30% of the incident translational energy is transferred to internal energy of the scattered ion. In addition, it has been shown that collisions with surfaces yield relatively narrow distributions of internal energies compared to collisions with noble gas atoms [6].

It is very interesting to combine both areas of research and this indeed has been done in recent work on the fragmentation of "small" polyatomic ions which are scattered off metal and adsorbate covered surfaces [116,147,148]. However, the transition from di-atomic to polyatomic ions remains unexplored, even though this regime gives valuable information on the fundamental excitation mechanisms, particularly on energy transfer mechanisms to the surface and to internal energy of the scattered ions. In this chapter, we study the dissociative scattering of di-atomic, tri-atomic and tetra-atomic ions off a liquid perfluoropolyether surface.

Previous work has shown that the approach geometries of incident di-atomic molecules have a large influence on translational-to-internal energy transfer in particle/surface collisions. In the scattering of oriented thermal NO molecules from surfaces by Kleyn and coworkers, this was shown experimentally [149–151]. In addition, classical trajectory calculations have been performed on hyperthermal and low-energy neutral molecule scattering from solid surfaces, such as O_2 and H_2 on Ag(111), which clearly indicate an orientational dependence in internal energy uptake [18,21]. The impulsive transfer of incident translational energy to rovibrational energy is most favorable if the diatom has its internuclear axis along the surface normal prior to surface impact. Moreover, aligned ion beam scattering experiments ($NO^+ \rightarrow$ Ag(111)) have been performed by Jacobs and coworkers [24,144]. It was shown that the break-up occurs more readily for molecules colliding "end-on" rather than "side-on" with the surface. Clearly, approach geometry effects will be present in polyatomic ion/surface collisions as well. However, it is very difficult to orient polyatomic ions; classical trajectory calculations and/or detailed comparative experimental studies of randomly oriented molecules are necessary to study these effects.

In some recent studies, the energy transfer to the surface has been explored in polyatomic ion/surface scattering (Ref. [147] and Chapters 3 and 4 of this thesis). These studies clearly indicate that most of the translational energy lost in the collision is transferred to the surface atoms. In Chapter 4, we showed that the transfer of energy to the surface is highly dependent on the total scattering angle. Traditionally, an effective surface mass has been introduced to account for the observed energy losses, e.g. the hard cube models. This approach has been applied also in polyatomic ion/surface collisions [76,137]. However, the effective mass seems to vary with incident ion [147] and with total scattering angle (Chapter 4 of this thesis). More studies are necessary to investigate these effects.

The dissociation event in polyatomic ion/adsorbate covered surface collisions is inferred to occur unimolecularly is the gas phase, on time scales much longer than the collision time. The measured translational energy distributions of the scattered fragment ions confirm this (Ref. [147] and Chapter 4 of this thesis). The translational energy of the scattered fragment ions is directly proportional to their mass and their velocities are equal.

In Chapters 3 and 4, we studied the dissociative scattering of polyatomic CF_3^+ ions from

$$CF^+ \qquad CF_2^+ \qquad CF_3^+$$
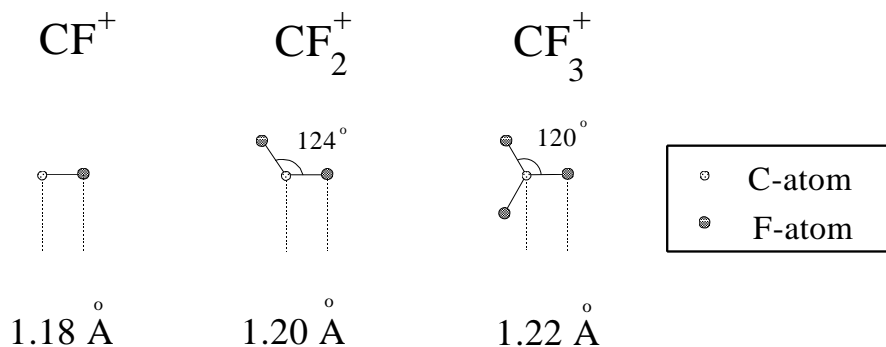
Figure 6.1 *Geometrical configurations of the fluorocarbon* CF_x^+ *(x=1-3) cations.*

metal (Ag(111) and Ba/Ag(111)) and liquid (perfluoropolyether) surfaces, respectively. In the case of scattering from the Ag(111) surface, the interaction was dominated by charge transfer processes (see Chapter 3). The CF_3^+ ions dissociate predominantly due to electron transfer processes and only a small fraction dissociates directly due to the impulsive collision. The influence of the crystal structure is clearly demonstrated in Chapter 3. In the case of scattering from a perfluoropolyether (PFPE) (Chapter 4), the dissociation is governed by the impulsive collision. The CF_3^+ ions scatter off -CF_3 groups of the PFPE in *single* collisions. The occurrence of *single* collisions are verified by keeping the total scattering angle θ constant while varying the incoming and outgoing angles [19]. No changes in the energy spectra were observed, as in gas phase scattering [19]. In addition, in the angular distribution the parent CF_3^+ ions are observed close to the surface, which shows that the differential scattering cross section is similar to those in gas phase scattering, which is forward peaked. These observations corroborate that *single* collisions occur in the scattering of small polyatomic ions off a PFPE surface and justify the use of the binary collision formula. The internal energy uptake is neglected in this approach since this is small compared to the total energy transfer. The collisions are treated as purely elastic. The effective surface mass shows a remarkable increase with total scattering angle, which appears to indicate that the structure of the liquid molecules cannot be ignored in the scattering process. Approximately 19% of the translational energy lost in the impulsive collision is transferred to internal energy, i.e. rovibrational energy.

In this chapter, we present a comparative study on the dissociative scattering of CF^+, CF_2^+ and CF_3^+ from a perfluoropolyether surface to explore the effect of increasing molecular complexity on energy transfer to the surface and to internal energy. For comparison, Fig. 6.1 displays the geometrical configurations of the CF^+ (Ref. [152]), CF_2^+ (Ref. [153]) and CF_3^+ (Ref. [91]) cations. The ionization potentials of the fluorocarbon ions are similar (see Table 4.1, Chapter 4) and the strengths (D^os) of the F-C bonds of the fluorocarbon ions are also comparable [134]. The present study gives information on the effective surface mass and on internal energy uptake efficacy, going from di-atomic to polyatomic ions. Measurements are performed on C^+ scattering from the PFPE to further investigate translational energy transfer to the surface. The present study provides insight into the role of approach geometry and effective interaction region in polyatomic ion/surface collisions. It highlights

some unique features in ion/liquid surface scattering which are not observed in ion/metal surface scattering experiments for the same scattering conditions such as the influence of the orientation of the target molecules.

6.2 Experimental

6.2.1 Apparatus

The experimental set-up is described in detail in Chapter 2 of this thesis. Briefly, it consists of two UHV chambers. In one, the liquid scattering sample can be characterized and stored. The sample can be transferred under UHV to a two-axis goniometer in the second chamber (base pressure of 1×10^{-10} mbar). The goniometer allows rotation of the target around an axis parallel to the surface to change the incoming angle θ_i (which is measured with respect to the surface normal) and rotation around the surface normal to change the azimuthal angle ϕ. This is schematically depicted in Fig. 4.2 of Chapter 4. The total scattering angle θ is defined as: $\theta = 180°$ - $(\theta_i + \theta_f)$ with θ_f the outgoing angle of the particles. In the scattering chamber, a new low-energy ion beamline is mounted which produces the (fluoro)carbon ions (see Chapter 5). The scattered ions are detected with a 90° cylindrical electrostatic energy analyzer, with an energy resolution of $\Delta E/E = 0.08$. The energy spectra shown throughout this chapter have not been corrected for the energy-dependent transmission of the energy analyzer (proportional to E) to avoid an artificial enlargement of the intensities at very low energies. When the relative intensities of the fragment ions are determined from the energy spectra, the energy spectra are scaled by a factor $1/E$ to correct for the energy-dependent transmission function of the analyzer. In the scattering plane the detector can be rotated from 45° to 180° with respect to the incoming beam and out of plane detection from $-15°$ to 90° is possible. The angular resolution of the detector is around 0.5°. Neutrals are not detected in our experiment.

6.2.2 Source operating conditions

CF_4 gas was introduced in the plasma source [139]. The pressure in the source was estimated to be around 10^{-3} mbar and the pressure in the Wien-filter housing during operations was measured to be 10^{-5} mbar. The filament current was set at 15 A (17 V). Because of the high power consumption of the plasma source, it is surrounded by a heat sink which is cooled by HFC-134 Freon (duPont). An arc-discharge current of 200 mA and anode voltage of 80 V are used during operation of the ion source. The ions are extracted by an extraction voltage of 400 V. The ion beam is mass selected by a cooled Colutron Wien-filter (M/ΔM = 400) [140]. At the target positions typical currents for CF_3^+, CF_2^+, CF^+ and C^+ of 1.8 nA, 30 nA, 8 nA and 1.3 nA, respectively, were delivered for final beam energies of 50 eV. The translational energy spread in the primary ion beam is estimated to be below 0.2 eV.

6.2.3 Sample preparation

The support of the liquid surface is a stainless steel disc (diameter 10 mm, thickness 2 mm) which has been polished mechanically and has a roughness below 0.05 μm. The

support is covered with a high molecular weight perfluoropolyether, sold under the trade name krytox 16256. Its structural formula is given by: $F[CF(CF_3)CF_2O]_{63(ave)}CF_2CF_3$. Its average molecular weight is about 11000 and its vapor pressure at room temperature about 10^{-15} mbar. We obtained a smooth thin film by allowing the liquid to sheet across the stainless steel support. This could be done under UHV conditions by changing its azimuthal orientation. All spectra in this chapter were measured with a surface near room temperature. Although we have an insulating layer, no evidence for charging was found. Reproducible data could be obtained over several days. Also no changes in the spectra were observed with changing the incoming particle flux.

6.3   Results and analysis

In the following sections, the results when mass-selected CF_3^+, CF_2^+, CF^+ and C^+ ion beams are scattered from a liquid perfluoropolyether surface are shown. The energy and angular distributions of scattered positive product ions are measured. A comparative analysis on the transfer of incident translational energy to the PFPE surface and to internal energy of the scattered (fluoro)carbon ions is presented.

6.3.1   Spectra

The translational energy distributions of positive fragment ions for the scattering of beams of 107 eV (a) C^+, (b) CF^+, (c) CF_2^+ and (d) CF_3^+ ions from a perfluoropolyether liquid surface are displayed in Fig. 6.2. The data are taken at $\theta_i = 70°$ / $\theta_f = 70°$. Fig. 6.2(a) displays C^+ scattering. The maximum in intensity is observed at E_f=88 eV. Applying the binary collision formula (eq. 4.1 Chapter 4) gives an effective surface mass of 31 a.m.u, corresponding to a -CF group. Towards lower energies, a tail in the distribution is observed. Most likely, these are particles which have made multiple collisions inside the PFPE liquid, similar to what is observed in (hyper-)thermal noble gas atom scattering from PFPE [111,154]. In what follows, we discuss the translational energy distributions when fluorocarbon ions are scattered from the PFPE surface.

In Fig. 6.2(b) for CF^+ scattering, two peaks are indicated with labeled arrows; these are identified with the scattered parent ion CF^+ (E_f=76 eV) and the fragment ion C^+ (E_f=30 eV). In the case of CF_2^+ (c) scattering, scattered CF_2^+ (E_f=73 eV) and CF^+ (E_f=46 eV) ions are observed. The CF_3^+ spectrum (d) displays three peaks which are identified with CF_3^+ (E_f=72 eV), CF_2^+ (E_f=52 eV) and CF^+ (E_f=33 eV). The spectrum of CF_3^+ is identical to those presented in Chapter 4, for the same scattering conditions. For reference, the energy positions of the incident beams prior to surface impact are shown by the dashed line in the figure. Remarkably, the energy that is retained by the scattered parent polyatomic ions is approximately the same for all the three cases; ranging from 71% for the scattered CF^+ ion, to 67% for the scattered CF_3^+ ion, indicating that the effective surface mass changes with the mass of the incident projectile. In addition, the energy spectra reveal that the degree of fragmentation is significantly higher in the case of CF_3^+ scattering than for CF^+ and CF_2^+, which display almost identical fragmentation patterns.

Fig. 6.3(a) displays the incident energy dependence of the positive ion signal for CF^+ for incident translational energies ranging from 61 to 215 eV. The data are taken at $\theta_i = 70°$
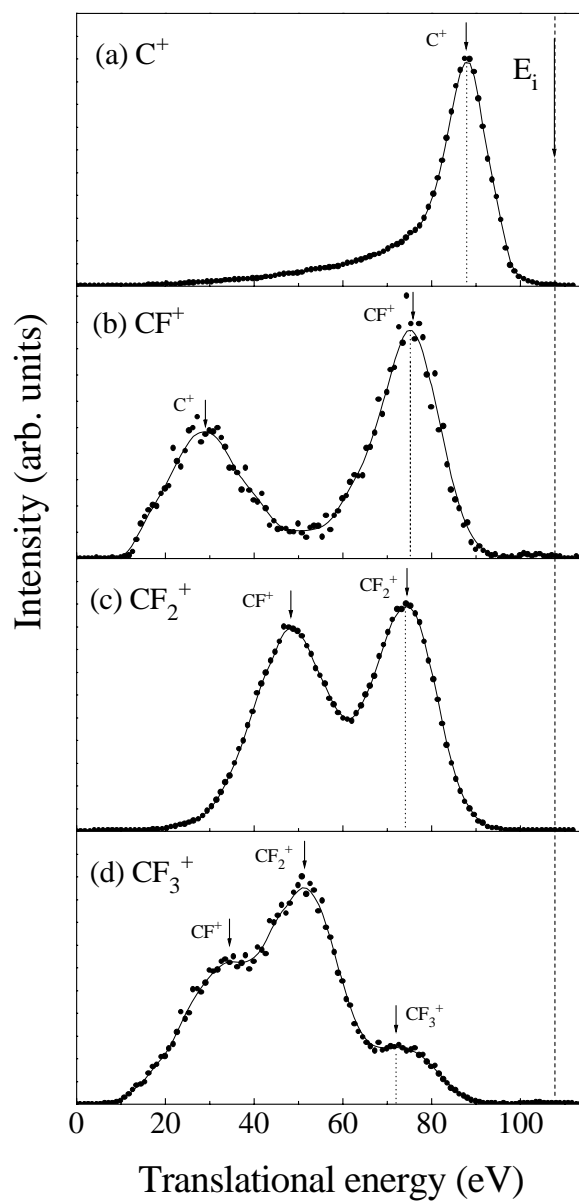
**Figure 6.2** *Translational energy distributions for positive fragment ions formed in the scattering of 107 eV (a) C^+, (b) CF^+, (c) CF_2^+ and (d) CF_3^+ from a PFPE liquid surface. The data are taken at $\theta_i = 70°$ / $\theta_f = 70°$. The dashed line indicates the energy position of the incident beams. No correction for the energy-dependent transmission of the energy analyzer has been made.*
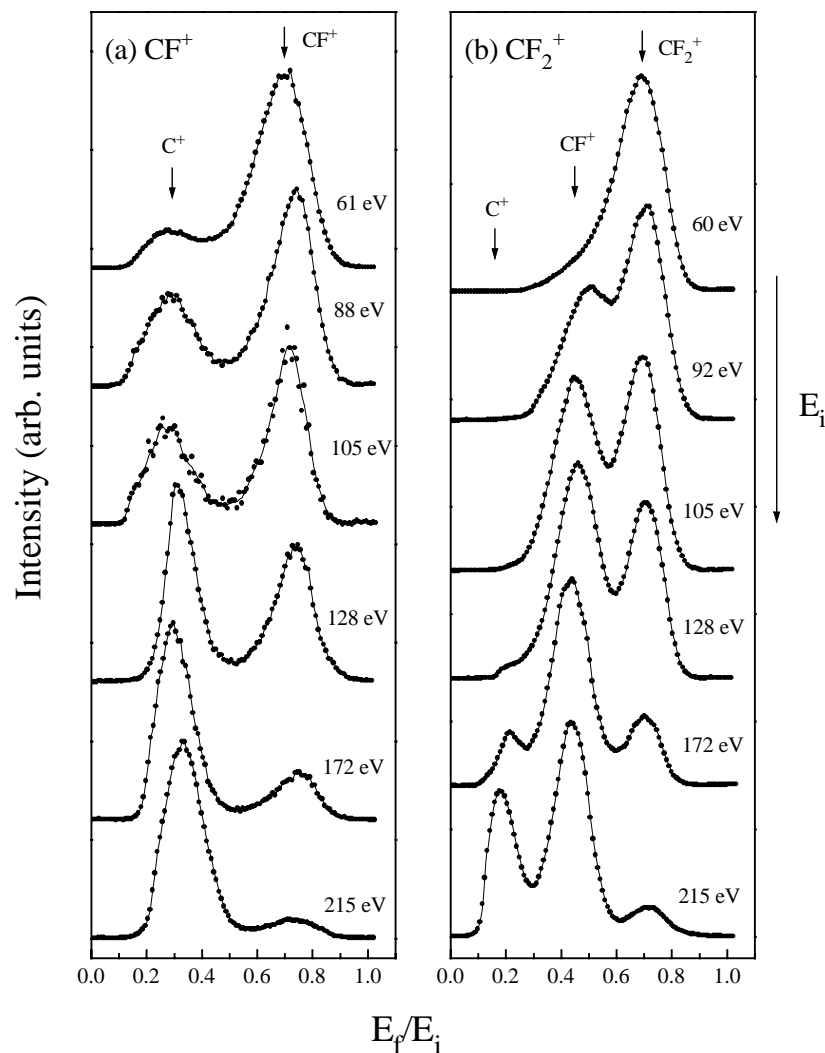
Figure 6.3 *Translational energy distributions for (a) CF$^+$ and (b) CF$_2^+$ scattered off a PFPE surface leading to positive fragment ions. The data are taken at $\theta_i = 70°$ / $\theta_f = 70°$ and the incident translational energy is varied from 60 to 215 eV. The labeled arrows give the energy positions of the fragment ions. No correction for the energy-dependent transmission of the energy analyzer has been made.*

/ $\theta_f = 70°$. In this graph, a reduced energy scale E_f/E_i is used. The energy positions of the fragment ions are indicated by labeled arrows. Clearly, more fragmentation occurs at higher incident energies, which indicates that the dissociation is governed by the impulsive collision. This is similar to CF$_3^+$ scattering off a liquid PFPE surface which was studied in Chapter 5. In Fig. 6.3(b), we have plotted the incident energy dependence of positive product ions for incident CF$_2^+$ ions. Once again, more fragmentation is observed for higher incident energies. For incident translational energies above 128 eV, the C$^+$ ion becomes apparent.

In Fig. 6.4, the three-dimensional intensity distributions I(θ_f, E_f) and corresponding

contour diagrams of backscattered positive ions are plotted for fluorocarbon ions scattered off a PFPE surface. The dashed lines give the angles for specular reflection. In Fig. 6.4(a) CF^+ and (b) CF_2^+ are scattered at $\theta_i = 70°$ and $E_i = 105$ eV. The scattered parent ions are observed at angles larger than specular: (a) CF^+ at $E_f \geq 87$ eV / $\theta_f \geq 80°$ and (b) CF_2^+ at $E_f \geq 85$ eV / $\theta_f \geq 80°$, which indicates they survive the impact in soft collisions. Previously, this was explained in terms of scattering off individual end groups of the liquid molecules (Chapter 4). The fragment ions are observed at larger total scattering angles: (a) C^+ at $E_f = 32$ eV / $\theta_f = 68°$ and (b) CF^+ at $E_f = 50$ eV / $\theta_f = 70°$. In addition, they reveal much broader angular distributions. Both these aspects indicate that the fragment ions are formed in hard collisions with the surface in which more energy is transferred. The amount of dissociation is higher in the case of CF_3^+ scattering (see Fig. 4.5(a) Chapter 4) than in the cases of CF_2^+ and CF^+ scattering, as is clearly observed in the three-dimensional intensity distributions.

In Fig. 6.4(c) CF^+ and (d) CF_2^+, the incoming angles are changed to 55°. Remarkably, the scattered parent ions are observed at angles much larger than specular: (c) CF^+ at $E_f = 73$ eV / $\theta_f = 79°$ and (d) CF_2^+ at $E_f = 63$ eV / $\theta_f = 74°$, which is again consistent with scattering off the groups of the liquid molecules in shallow collisions. The peaks of the scattered parent ions can be considered rainbow peaks which are the peaks where the single and double collision peaks merge [9]. In the three-dimensional intensity distributions, the fragments (c) C^+ and (d) CF^+ are observed at larger total scattering angles and display broad angular distributions. At the largest total scattering angles, in the case of CF_2^+ scattering, a peak is observed which can be attributed to backscattered C^+ ions. At the very low energy side, sputtered particles are detected.

Fig. 6.5 displays the three-dimensional intensity distributions $I(\theta_f, E_f)$ and corresponding contour diagrams for incident 105 eV C^+ and backscattered positive ions at $\theta_i = 70°$. Once again, the dashed line gives the angle for specular scattering. The backscattered C^+ ions display a broad angular distribution which is peaked at angles larger than specular: $E_f \geq 93.5$ eV / $\theta_f \geq 80°$. The angular distribution is significantly broader than those of the fluorocarbon ions. This can be explained by the absence of fragmentation in the case of C^+ scattering which allows the parent ion to be scattered over larger total scattering angles. Fig. 6.5 clearly indicates that more energy is lost going to larger total scattering angles.

6.3.2   Energy transfer

The energy and angular distributions presented in the previous sections allow for direct determination of the translational energy loss ΔE in the molecular ion/surface collisions. In the sections that follow, the amount of translational energy that is transferred to the liquid is determined. In addition, translational-to-internal energy transfer of the scattered fragment ions is determined by a method based on the appearance potentials of the fragment ions, which has been developed by Cooks and coworkers [6]. This method is described in detail in Chapter 4 of this thesis and elsewhere [6,122,123]. The appearance potentials (E_0) of the fluorocarbon ions are listed in Table 4.1 of Chapter 4. When the relative intensities of the fragment ions or average translational energies of the product ions are determined, the raw energy spectra are scaled by a factor $1/E$ to correct for the energy-dependent transmission function of the analyzer, similar to what is described in Chapter 4.
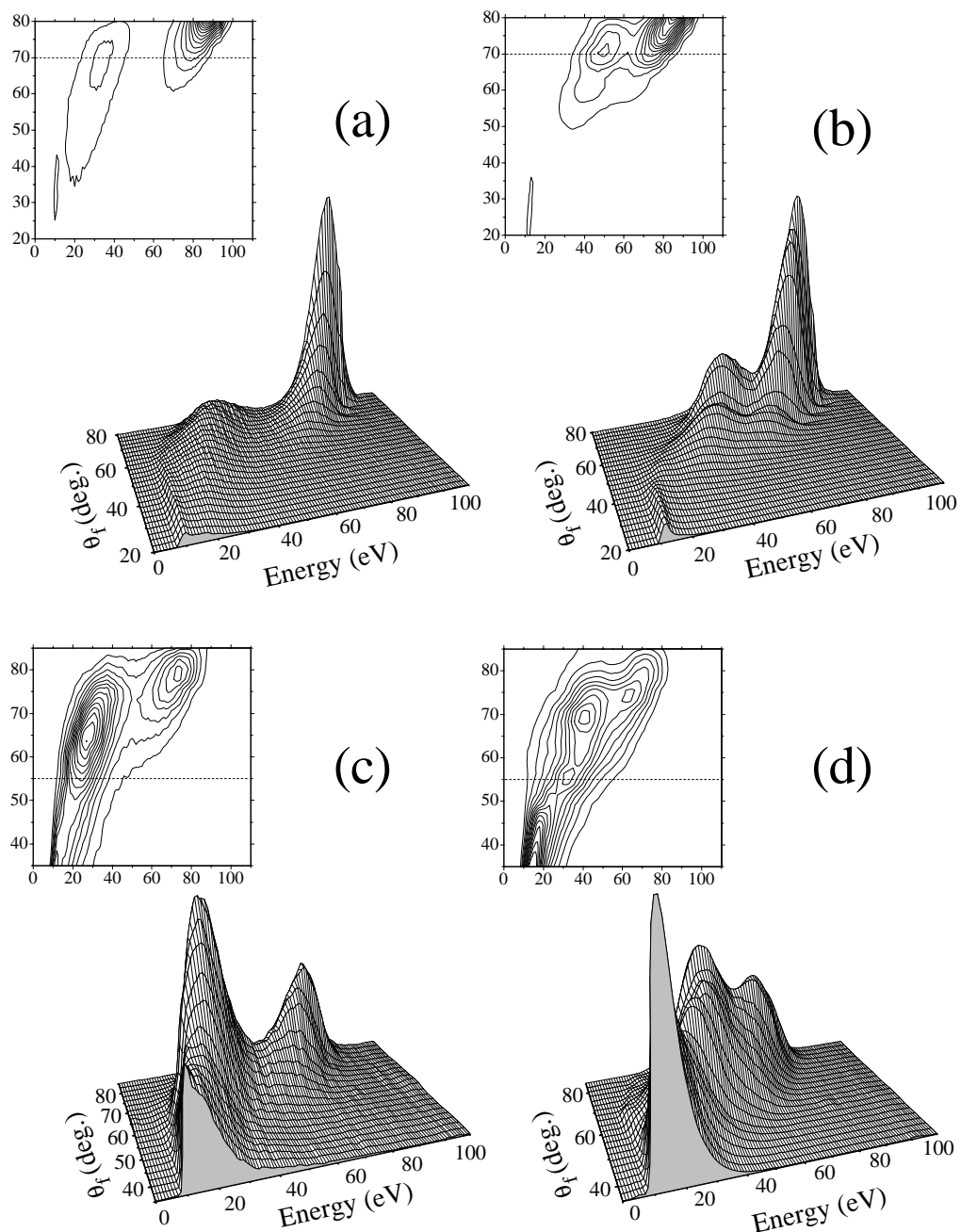
Figure 6.4 *Three-dimensional intensity distributions $I(\theta_f, E_f)$ and corresponding contour diagrams of positive ions formed in scattering of (a) CF^+ and (b) CF_2^+ at $\theta_i = 70°$ from a PFPE surface. In (c) CF^+ and (d) CF_2^+ are scattered at $\theta_i = 55°$. The incident energies are 105 eV in all the four cases. The dashed lines give the angles for specular scattering. No correction for the energy-dependent transmission of the energy analyzer has been made.*
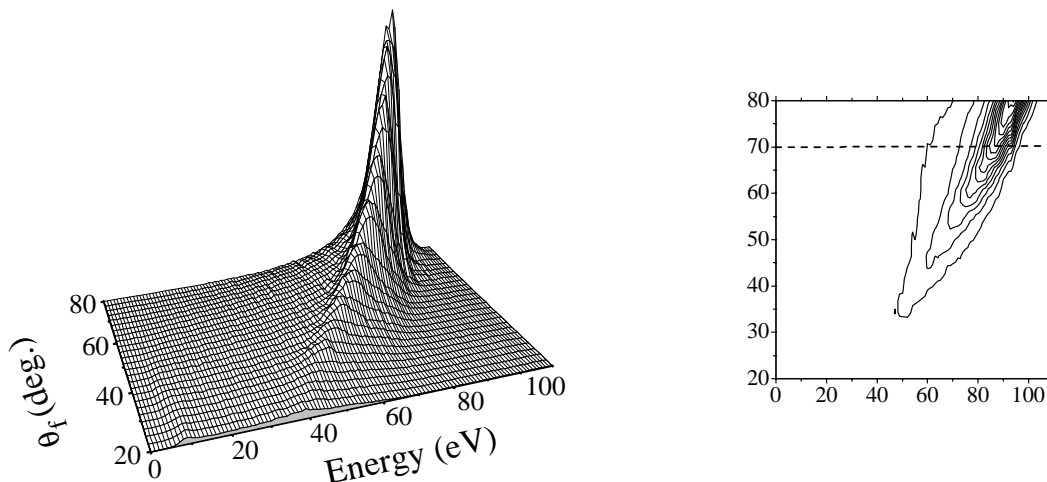
Figure 6.5   *Three-dimensional intensity distribution $I(\theta_f, E_f)$ and corresponding contour diagrams of positive ions formed in scattering of 105 eV C^+ from a PFPE liquid surface. The incident angle is 70°. The dashed line gives the angle for specular scattering. No correction for the energy-dependent transmission of the energy analyzer has been made.*

Translational energy transfer to the surface: varying the incoming energy

Fig. 6.6(a) displays the average translational energies of the scattered CF^+ and C^+ ions as a function of the incident CF^+ translational energy, for $\theta_i = 70°$ and $\theta_f = 70°$, a total scattering angle of 40°. For both product ions, the average translational energies display a linear increase with CF^+ translational energy. The lines in the figure are calculated from the binary collision model for the CF-CF (dotted line), $CF-CF_2$ (dashed line) and the $CF-CF_3$ (solid line) system. The data points are best described by the $CF-CF_2$ line. At the lowest incident energies there seems to be a deviation from the linear behavior; the surface effective mass appears to decrease. In calculating the C^+ line, we assume that the fragment ions leave the surface with the same speed. The calculated line describes the energy positions of the C^+ fragment fairly well. Note that the collisions are treated as purely elastic. The internal energy uptake is neglected.

In Fig. 6.6(b), the average translational energies of the scattered CF_2^+, CF^+ and C^+ ions as a function of the incident CF_2^+ translational energy are depicted. The scattering geometry is the same as in Fig. 6.6(a). Once again, the average energies of the product ions display a linear increase. Binary collision model calculations indicate that the scattering is best described by CF_2-CF_3 collisions; the surface appears heavier to the incident CF_2^+ ions than to the incident CF^+ ions. The lines for the CF_2^+ and CF^+ fragments are calculated based on the assumption that the ions leave the surface with the same speed; good agreement is obtained with the experimentally determined average energy values.

The calculated lines in both figures describe the energy positions of the fragment ions very well for CF^+ and CF_2^+ scattering off PFPE and indicate the validity of the binary collision approximation for this total scattering angle and this incident energy range. Moreover, it shows that the assumption that the fragment ions leave the surface with the same speed is
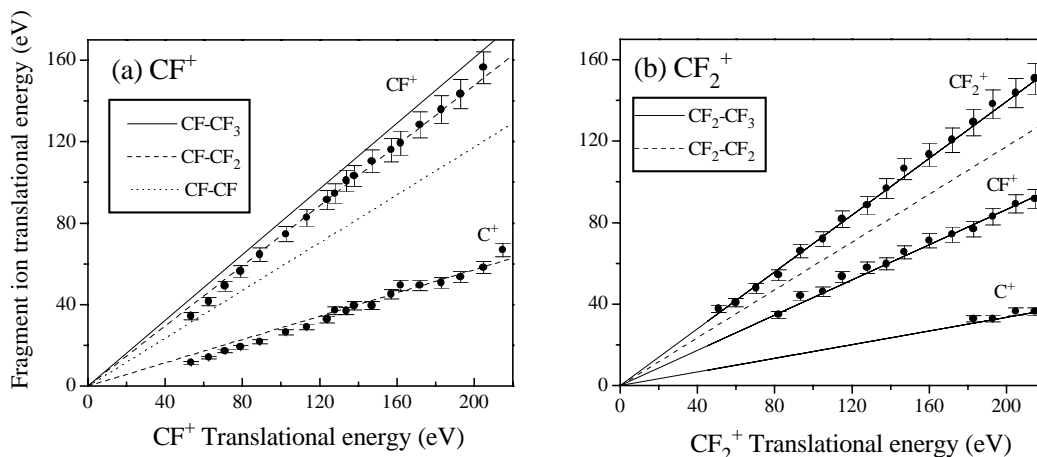
Figure 6.6 *The average translational energies of scattered (a)* CF^+ *and* C^+ *ions as a function of the incident* CF^+ *translational energy. (b) shows the average translational energy of scattered* CF_2^+, CF^+ *and* C^+ *ions as a function of the incident* CF_2^+ *translational energy. The data are taken at* $\theta_i = 70°$ *and* $\theta_f = 70°$.

correct. These results were also obtained for CF_3^+/PFPE scattering (section 4.3.2. Chapter 4).

Translational energy transfer to the surface: varying the total scattering angle

Much can be learned about the scattering dynamics, when we consider the three-dimensional intensity distributions $I(\theta_f, E_f)$ of the scattered product ions. In Fig. 6.7 we have plotted the average translational energies that are retained by the product ions as a function of total scattering angle for scattering of (a) $C^+(105 \text{ eV})(\to C^+)$, (b) $CF_2^+(107 \text{ eV})(\to CF_2^+ + CF^+)$, (c) $CF^+(53 \text{ eV})(\to CF^+)$ and (d) $CF^+(105 \text{ eV})(\to CF^+ + C^+)$ beams from a PFPE liquid surface. The detected product ions are given at the right hand side of the arrows. The data are taken at $\theta_i = 70°$. Clearly, for all cases, more translational energy is lost in the collision for scattering over larger total scattering angles. The translational energy retained by the parent ions varies for C^+ scattering (Fig. 6.7(a)); it ranges from 90% for a total scattering angle of 30° to about 53% for total scattering angles of 70°. For CF^+ scattering (Fig. 6.7(c)), these values are determined as 75% and 27%, respectively.

The lines in the figure give the translational energies of the product ions when we apply the binary scattering formula (see eq. (4.1) in Chapter 4). In the case of fragmentation, it is assumed that the product ions leave the surface with the same speed. To calculate the line for a double collision, the binary scattering formula is applied twice using total scattering angles of $\theta/2$ and the E_f from the first collision as the E_i of the second collision. In the analysis, we only consider scattering off -CF_n (n=1-3) groups and F atoms of the liquid molecules. At small scattering angles (i.e. $\theta < 40°$), C^+ scattering (a) is best described by scattering off -CF groups, CF_2^+ (b) by scattering off -CF_3 groups, CF^+ (53 eV) (c) by scattering off -CF groups and CF^+ (105 eV) (d) by scattering off -CF_2 groups. At larger total scattering angles, some remarkable differences are observed. The molecular
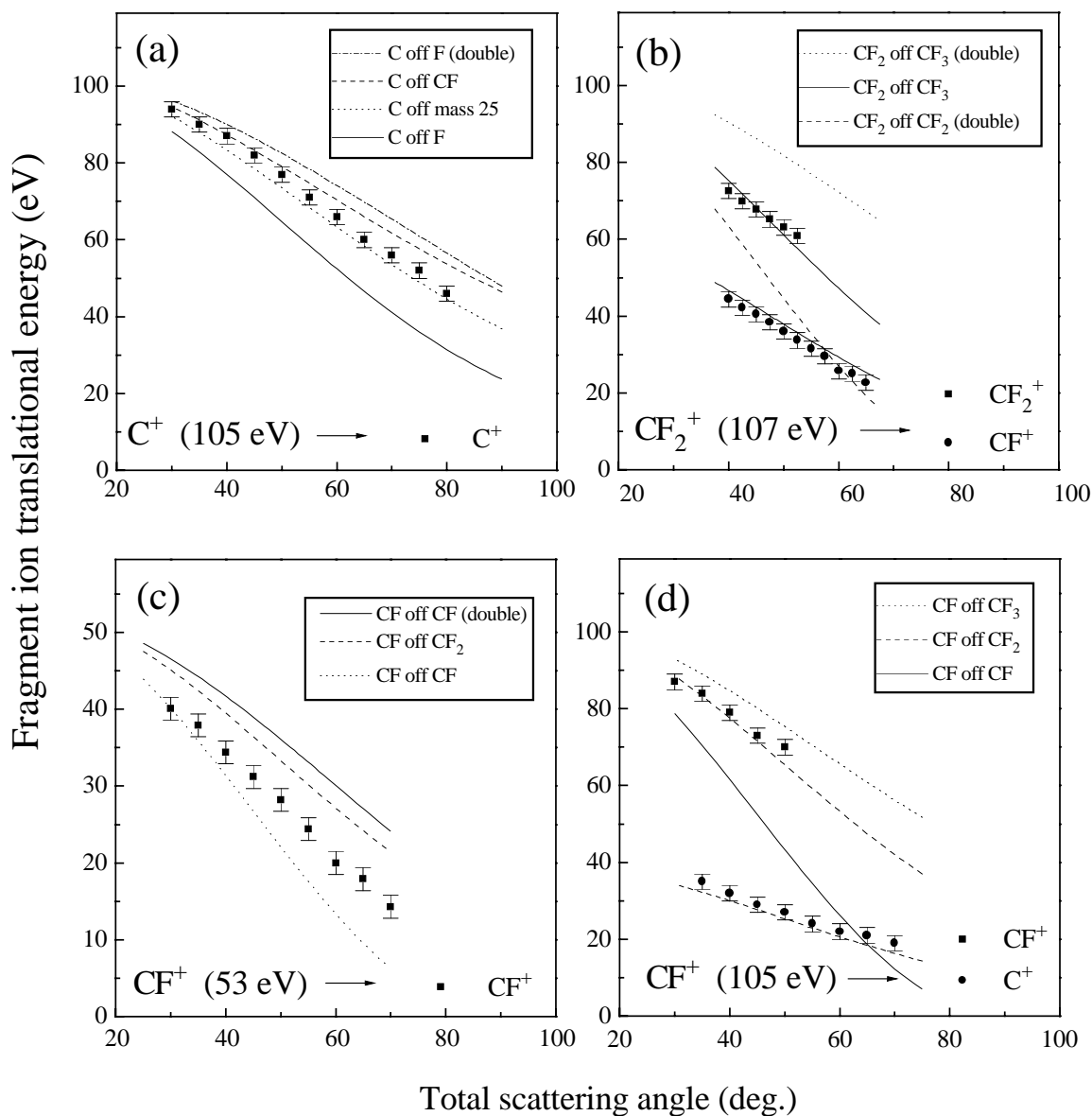
**Figure 6.7** *The average translational energies of product ions as a function of total scattering angle for scattering of (a)* C^+*(105 eV)($\to C^+$), (b)* CF_2^+*(107 eV)($\to CF_2^+ + CF^+$), (c)* CF^+*(53 eV)($\to CF^+$) and (d)* CF^+*(105 eV)($\to CF^+ + C^+$) beams from a PFPE liquid surface. The data are taken at* $\theta_i = 70°$*. The lines in the figure were calculated from the binary collision model.*
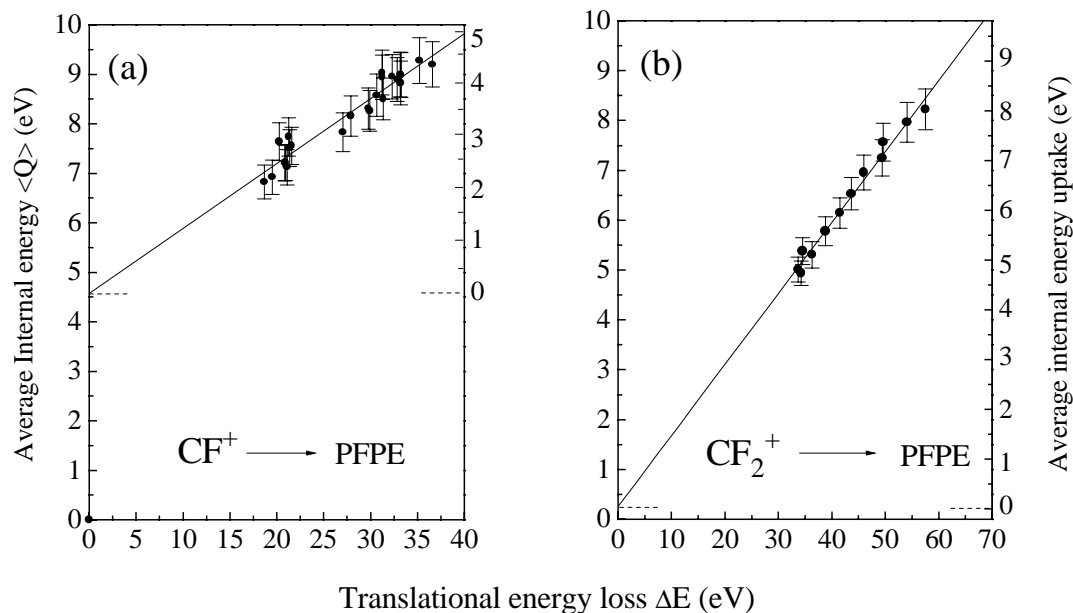
Figure 6.8 *The estimated average internal energy <Q> as a function of translational energy loss ΔE for (a) CF^+ and (b) CF_2^+ from a PFPE liquid surface. The data are taken at (a) $\theta_i = 70°$ / $\theta_f = 70°$ and at (b) $\theta_i = 70°$ and between $\theta_f = 40°/\theta_f = 70°$.*

ions leave the surface with higher translational energies than is expected on the basis of the single collision model assuming a given target mass. The same trend is observed for CF_3^+ scattering (Fig. 4.9 Chapter 4). However, the scattered C^+ ions reveal the opposite behaviour; the C^+ ions leave the surface with energies which are lower than is expected on the basis of the single collision model. Clearly, an alternative explanation must be given to clarify the different results.

Translational-to-internal energy transfer

In Chapter 4, we have shown that the translational energy loss ΔE in the polyatomic ion/surface collision is the quantity that determines the average internal energy uptake $<Q>$ and, hence, the amount of fragmentation that occurs. The experimental study revealed that approximately 19% of the translational energy that is lost in the collision is transferred into internal energy (rovibrational energy) of the scattered CF_3^+ ion. The *efficacy* is defined as: *efficacy* $= <Q>/\Delta E$, and is determined directly from the slope of the line in the $<Q>$ versus ΔE plot, which displays a linear behaviour. The present experimental results confirm the previously determined 0.19 efficacy for CF_3^+ on a PFPE surface. In the sections that follow, an estimate is made of the efficacies of CF^+ and CF_2^+ scattered off a PFPE surface.

The estimated average internal energy deposition $<Q>$ as a function of measured translational energy loss ΔE in CF^+/PFPE collisions is plotted in Fig. 6.8(a). The plot displays a linear increase of the internal energy of the scattered ion with increasing translational energy loss in the ion/surface collision. This behaviour has been observed in CF_3^+ incident

on PFPE. The line in the figure is a fit to the data points determined by linear regression. The intersection at low translational energy loss gives the average internal energy prior to the collision. On the right hand ordinate the average internal *uptake* in the collision is depicted. The slope of this line is 0.13, which reveals that 13% of the translational energy lost in the collision is converted to internal energy of the scattered parent ion; a value significantly lower than the 19% determined for CF_3^+ scattering.

Fig. 6.8(b) displays the estimated average internal energy deposition $<Q>$ as a function of measured translational energy loss ΔE for CF_2^+/PFPE collisions. Once again, a linear increase of $<Q>$ is observed with increasing ΔE and the intersection at low translational energy loss gives the average internal energy prior to the collision. On the right hand ordinate the average internal *uptake* in the collision is depicted. The slope of the line is 0.14; 14% of the translational energy loss is converted to internal energy of the scattered parent ion, which is comparable to CF^+ from the PFPE.

6.4 Discussion

6.4.1 Scattering dynamics

In Chapter 4, we discussed the scattering dynamics of CF_3^+ on PFPE. The results were interpreted in terms of binary elastic collisions with the -CF_3 groups of the liquid molecules. In the sections that follow, the angular distributions are discussed in more detail. In particular those for smaller incoming angles ($\theta_i = 55°$), because these are remarkably absent in the literature for polyatomic ion/surface scattering.

Angular distributions

It is quite remarkable that the angular distributions of the fragment ions are peaked so strongly towards the surface plane in polyatomic ion/surface collisions, even for incoming angles as "small" as 55°. In the present experiment, the parent ions are observed at outgoing angles of 80° and their fragments have a maximum in intensity between $\theta_f = 65° - 70°$ It is commonly assumed that the polyatomic ions scatter predominantly in the specular direction [148]. Schulz et al. have performed classical dynamics simulations of $Si(CD_3)_3^+$ from hexanethiolate self-assembled monolayers, which predict subspecular reflections; scattering at $\theta_i = 45°$ resulted in $\theta_f = 38°$. These results were independent of incident translational energy.

For hyper-thermal noble gas atom scattering (0.1 to 2 eV) from the PFPE surface, the same supraspecular scattering is observed as in our case; for $\theta_i = 45°$ the angular distribution showed a maximum at $\theta_f = 60°$ [111]. These results were interpreted in terms of scattering off functional groups of the liquid PFPE. The PFPE surfaces must be highly corrugated, so that the fluorocarbon ions are scattered so close to the surface plane. Molecular dynamics simulations on the liquid-vapor interface of alkane oligomers indicate that the outer edge of a liquid surface is dominated by chain ends [155]. In the case of a liquid PFPE surface, these are -CF_2CF_3 species that extend outward at the liquid's surface, making the surface plane highly corrugated [113].
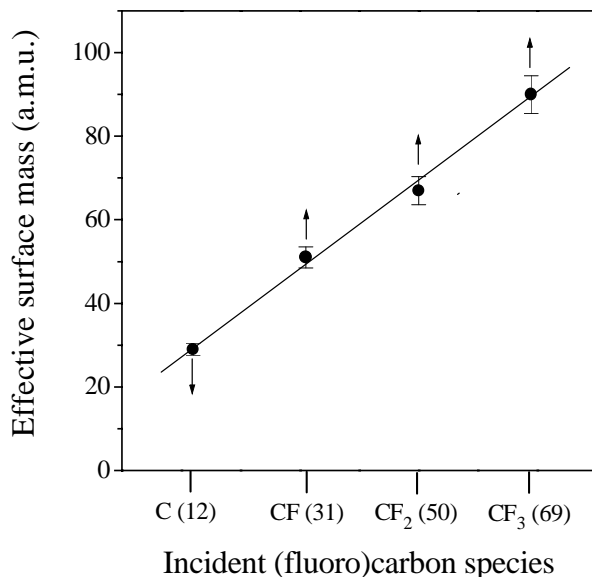
Figure 6.9 *The effective surface mass for* C^+, CF^+, CF_2^+ *and* CF_3^+ *scattering from PFPE. The incident energies of the particles is 107 eV and the effective surface mass is determined for elastic collisions at* $\theta_i = 70°$ / $\theta_f = 70°$. *The line in the figure is drawn to guide the eye. The arrows give the trend of the effective surface masses for larger total scattering angles.*

6.4.2 Effective surface mass

The experimental results reveal that the energy transfer to the surface depends sensitively on the incident (fluoro)carbon ion, its incident translational energy and its total scattering angle. In addition, remarkable differences are observed for atomic (C^+) and polyatomic (CF_n^+ (n=1-3)) scattering.

Varying the incident particle

The present experimental results clearly indicate that the effective surface mass increases with increasing mass of the incident particle. The experimental results are summarized in Fig. 6.9, which gives the surface effective mass as a function of incident (fluoro)carbon mass. The line in the figure is drawn to guide the eye. The dependence of effective surface mass upon the size of the incident ion has been observed before [147]. In our case, the dependence upon the size of the ion, or more precisely, the number of atoms in the incident particle, gives direct information on the number of atoms which impulsively recoil. For "larger" projectiles, more of the surface area is probed. In the case of CF^+ scattering, effectively the two atoms impulsively exchange energy with two atoms from the PFPE. With an increasing number of incident atoms, interaction with effectively more surface atoms occurs. This can largely be attributed to the fact that the effective size and composition of the incident particles and functional groups of the PFPE are similar.

In Fig. 6.10, we have schematically illustrated this effect for a mono-atomic and a di-atomic particle scattered off a functional group consisting of 4 atoms. To simplify the

(a)   (b)
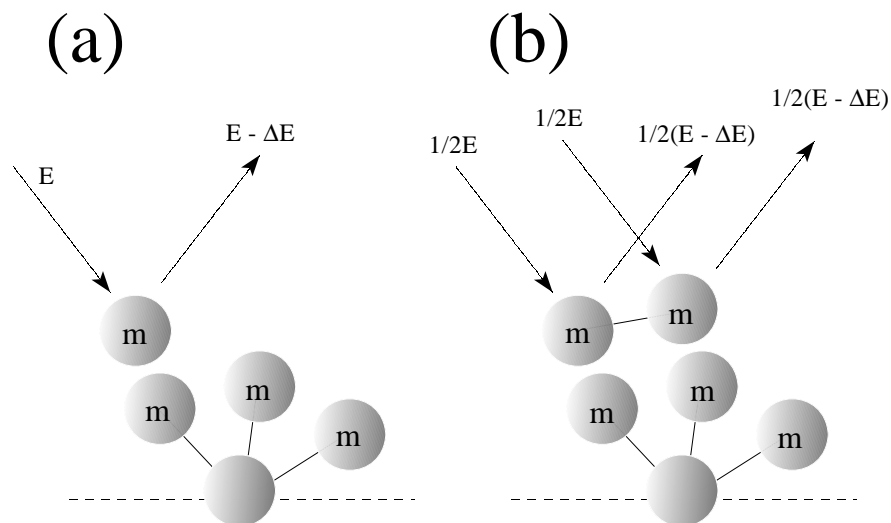
Figure 6.10 *Schematic illustration of a (a) mono-atomic and (b) di-atomic particle scattered off a functional group of the liquid PFPE surface. The incident energy of the particles is the same, resulting in the same energy loss. The effective surface mass increases from m to 2m.*

treatment, we take the mass of the atoms to be equal, i.e. a mass m. In the case of a mono-atomic (mass m) particle (Fig. 6.10(a)), effectively elastic scattering off a single atom (mass m) of the functional group occurs; the incident translational energy is E_i and the translational energy lost in the collision is ΔE. A di-atomic particle (mass 2m), with incident energy E_i has an energy per nucleus of $0.5E_i$. Each of these atoms elastically scatters off an atom of the functional group, giving rise to a total energy loss in the collision of ΔE. The effective surface mass has increased from m to 2m. This approach can be extended to tri- and tetra-atomic particle scattering. The results indicate an effective surface mass which increases linearly with increasing particle size, while the energy loss the particles suffer in the collision remains constant. This is similar to what was experimentally observed and shown in Fig. 6.9 and in Fig. 6.2, respectively. The discussion is very schematic; collisions that are depicted in Fig. 6.10(b) are rare. However, although we integrate over all orientations of the incident molecules in our experiment, the effect remains visible.

Varying the total scattering angle: C^+ scattering

The effective surface mass depends upon the total scattering angle. Going to larger scattering angles, the effective surface mass increases for the scattered polyatomic ions. However, the scattered C^+ ions reveal the opposite behaviour; the effective surface mass decreases, going to larger scattering angles. In other words, less energy is retained by the scattered C^+ ions than is to be expected on the basis of the binary scattering formula. What is the cause of this remarkable experimental observation?

Models of vibrational energy transfer employed in gas phase scattering consider two limiting situations, which are schematically depicted in Fig. 6.11, for an atom A in "head-on" collision with molecule BC. We consider the chemical bond in BC to be represented
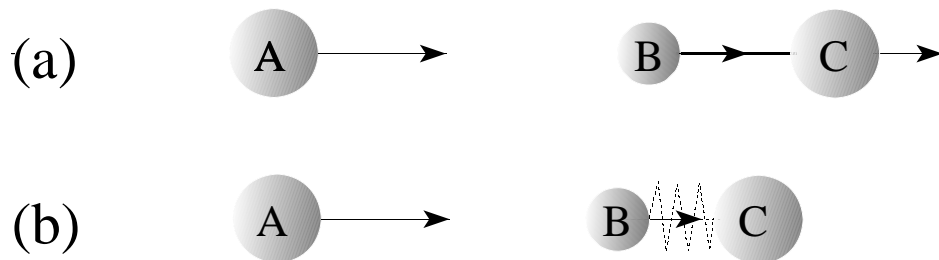
Figure 6.11 *Schematic illustration of an "head-on" collision of atom A with harmonic oscillator molecule BC. Two limiting situations are shown: (a) extremely stiff bond or adiabatic limit and (b) very loose bond or sudden limit.*

by a harmonic oscillator spring. If the spring is extremely stiff (Fig. 6.11(a)), the molecule BC can be considered a rigid body. All the energy that is lost in the collision by atom A is transferred to translational energy of molecule BC. This situation occurs at low-velocities or in the adiabatic limit. The interaction time is longer than a vibrational period of molecule BC. At high-velocities or in the sudden limit ((Fig. 6.11(b)), we can consider the case of a very loose spring. The interaction time is smaller than a vibrational period of molecule BC. All the translational energy lost in the collision by atom A is transferred to atom B in molecule BC [23]. The velocity difference between B and C is considered to be the internal energy uptake or vibrational energy transfer. The effective mass of molecule BC is larger in the case of the adiabatic limit (a) than in the case of the sudden limit (b).

The same consideration can be given when C^+ ions scatter off molecule $F-CF_2$ (the $-CF_3$ groups of the liquid molecules). The collision is neither purely adiabatic nor sudden. The effective mass is given at a total scattering angle of 30° (see Fig. 6.7(a)) by the mass of a -CF group, i.e. 31 a.m.u. At higher impact parameters, i.e. small total scattering angles, the collision will tend to be more adiabatic, because of the larger range parameter a, than collisions at lower impact parameters, i.e. large total scattering angles [95]. Hence, the effective surface mass appears to decrease with larger total scattering angles, because the collision becomes more sudden; in other words the C^+ ions transfer more translational energy in the collision than is expected on the basis of the single collision model. This is clearly observed in Fig. 6.7(a).

Scattering of noble gas ions from single crystal metal surfaces displays an entirely different behaviour. Here, the effective mass of the surface is given by the mass of a single surface atom, provided that the mass of the incident particle is less than the mass of a surface atom. The mass of the surface can be considered constant for increasing mass of the incident noble gas ion. No deviations from the single collision model are observed in Ne^+ scattering from Au(111) (Fig. 5.6 in Chapter 5) for large total scattering angles. This clearly reveals the remarkable differences in scattering from liquid surfaces and scattering from metal surfaces.
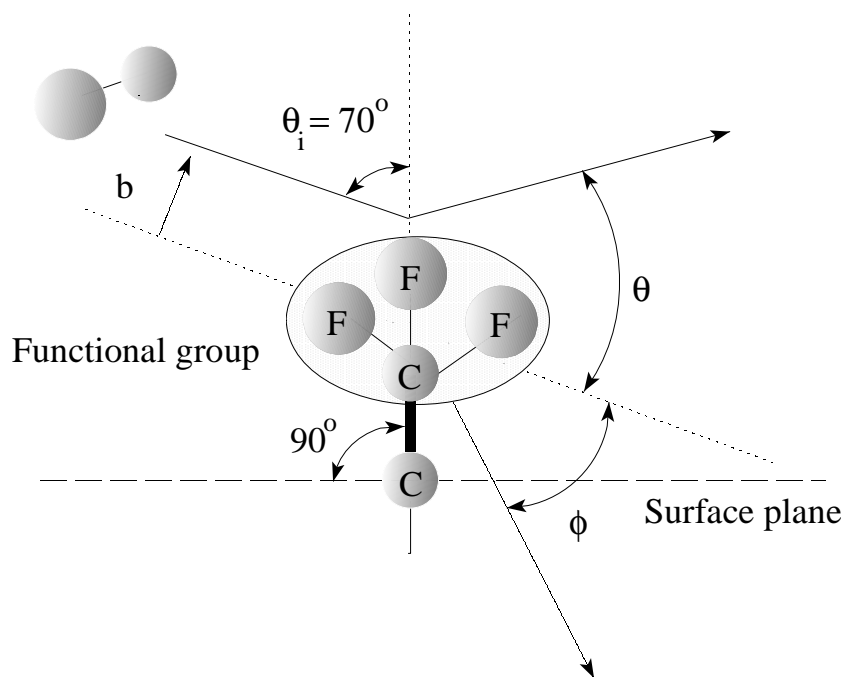
Figure 6.12 *Schematic illustration of a polyatomic ion scattered off a recoiling -CF$_3$ functional group, which is oriented perpendicular to the surface plane. The recoil angle of the functional group is defined as ϕ, the total scattering angle of the scattered particle θ. b is the impact parameter and $\theta_i = 70°$.*

Varying the total scattering angle: CF$_n^+$ (n=1-3) scattering

That the collision becomes more sudden as we go to smaller impact parameter collisions will also play a role for fluorocarbon ions scattering off the PFPE surface. However, for polyatomic ions scattered off PFPE more energy is retained by the fragment ions than is expected on the basis of the binary collision formula; the effective mass of the surface increases for CF$_n^+$ (n=1-3) scattering going to larger scattering angles. Clearly, other effects become more important, compared to those in C$^+$ scattering.

The functional -CF$_3$ groups are oriented perpendicular to the surface plane; the fluorocarbon ions basically scatter off oriented molecules. It was shown in the previous sections, that for polyatomic ion/surface scattering, interactions with more surface atoms occur than for mono-atomic scattering. Not only the F-C bonds have to be considered, as in C$^+$ scattering, but also the F$_3$C-CF$_2$ bond, which is oriented nearly perpendicular to the surface [114,115]. In Fig. 6.12 we have schematically depicted the scattering of a polyatomic ion from a -CF$_3$ group that is bonded to the rest of the liquid molecule with an angle of 90° with respect to the surface plane, which we take parallel to the macroscopic surface plane of the stainless steel disc support. The incoming angle is 70°. The total scattering angle is defined as θ and the recoil angle of the -CF$_3$ group as ϕ. For larger total scattering angles, i.e. smaller impact parameters b, the recoil angle ϕ decreases, and vice versa. The recoil direction of the -CF$_3$ groups is closer to the alignment direction of the C-C bond at small total scattering angles of the scattered particles. The liquid molecules will easily
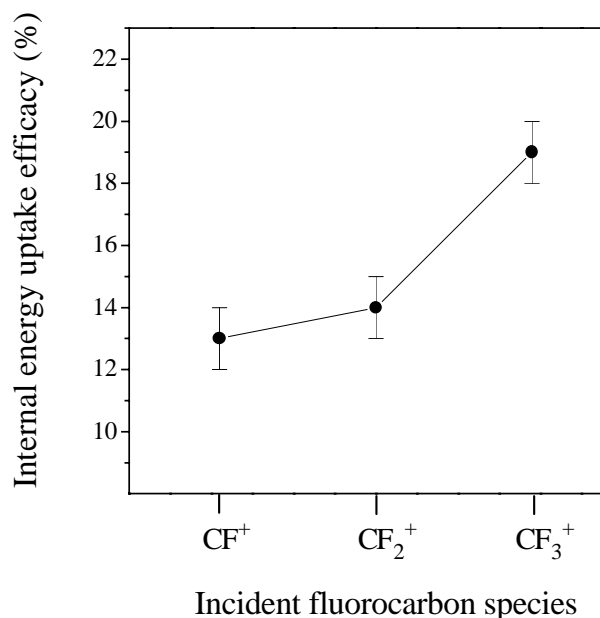
Figure 6.13 *The internal energy uptake efficacies for* CF^+, CF_2^+ *and* CF_3^+ *scattering from PFPE.*

be compressed. At small impact parameters, i.e. large total scattering angles, the recoil direction of the -CF_3 group is less aligned with the C-C bond direction, and hence the C-C bond is compressed less effectively. The effective mass of the surface increases, and less energy is transferred to the surface than is expected on the basis of the binary collision model. In a recent classical dynamics simulation study by Schultz et al., $Si(CD_3)_3^+$ ions were scattered from hexanethiolate self-assembled monolayers which have an average chain tilt of 27° with respect to the surface normal [148]. It was shown that "head-on" collisions allow for more energy to be transferred than "side-on" collisions. In "head-on" collisions the recoil directions are aligned with the bond directions. In our case, larger scattering angles, can be associated with more "side-on" collisions, in which effectively less energy is transferred.

6.4.3 Internal energy uptake efficacies

The present experimental results reveal that translational-to-internal energy transfer in CF^+ and CF_2^+ scattering occurs less readily than in CF_3^+ scattering. In Fig. 6.13, we have summarized the estimated conversion efficacies for the three fluorocarbon ions incident on the PFPE surface, which were determined from the $<Q>$ versus ΔE plots. In addition, the energy distributions presented in Fig. 6.2, for CF_3^+, CF_2^+ and CF^+ scattering from the PFPE surface, revealed more fragmentation in the case of CF_3^+ than for the other two fluorocarbon ions, for the same incident energy E_i and energy lost ΔE in the collision, corroborating the more effective internal energy uptake in the case of CF_3^+. What is the cause of the more effective internal energy uptake of the CF_3^+ ion? In what follows, we have listed a number of possible explanations.

1. The mass of the incident molecular ion can have an influence on internal energy uptake. According to an impulsive collision-transfer theory developed by Uggerud and coworkers, for the collision between a gas atom and a macromolecular ion, there is a scaling with incident ion mass [127,128]. The theories predict less internal energy uptake going to larger incident masses [147]. However, also the effective surface mass increases, which may serve to cancel the effect. The relation between the efficacy and the incident mass M_i is given by,

$$Q/E_i \propto [2M_a M_s^2 (M_i - M_a)]/[(M_a + M_s)^2 M_i^2], \qquad (6.1)$$

where M_i is the total mass of the incident ion, M_s the effective surface mass and M_a is the mass of the fragment of the incident ion that is "hit" [147]. The angular dependence has been omitted in this relation. This relation can be applied because in the case of the fluorocarbon ions $E_i \propto \Delta E$.

2. The number of internal modes available for energy uptake differs. If we consider the number of vibrational modes available for vibrational excitation, these are $3N$-6 for a non-linear N-atom species; for linear species these are $3N$-5 [156]. Clearly, more internal modes are available for molecules which are composed of more atoms.

3. There may be steric requirements for translational to internal energy transfer to occur. Some configurations of the incident molecular ion may be more favorable for internal energy uptake than others. The incident CF_3^+ ions may have more approach geometries favorable for internal energy uptake than the CF^+ and CF_2^+ ions.

The first two explanations can be dismissed on the basis of equal internal energy uptake efficacies for CF^+ and CF_2^+, although the mass and the number of internal modes differ for the ions. The third explanation seems the most likely candidate, especially considering the fact that oriented neutral beam molecule surface scattering experiments by Kleyn and coworkers [149–151] and aligned ion beam scattering experiments by Jacobs and coworkers clearly reveal an orientational effect in internal energy uptake. For the CF_3^+ ion effectively more internuclear F-C alignments are possible (3) than for CF^+ and CF_2^+ (2) (see Fig. 6.1), which can result in bond compression. In the considerations that follow, we introduce a simple model which treats the approach geometry of the incident fluorocarbon ions.

Analogous to describing reactivity in gas-phase molecule scattering (see the book by Levine and Bernstein [95]), we introduce a steric opacity function, which defines an orientational dependence in translational-to-internal energy transfer. We assume "reactive" collisions occur, when "head-on" collisions take place, which means that the F-C internuclear axis of the projectile in the collision is aligned with the (local) surface normal. "Non-reactive" collisions occur when "side-on" collisions take place. "Reactive" collisions are defined as collisions in which translational-to-internal energy occurs. Likewise, in "non-reactive" collisions, no internal energy uptake is assumed. Previous work on di-atomic scattering in classical trajectory calculations and oriented beam scattering experiments has indicated that internal energy uptake is most favorable for molecules having their internuclear axis aligned with the (local) surface normal. Furthermore, the studies indicated that
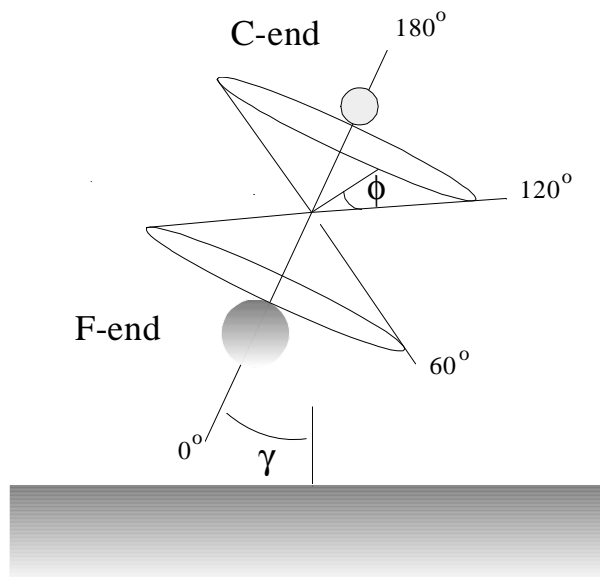
**Figure 6.14** *Schematic illustration of the step-function model with two reactive sites. The angle γ gives the angle between the (local) surface normal and the F-C internuclear axis.*
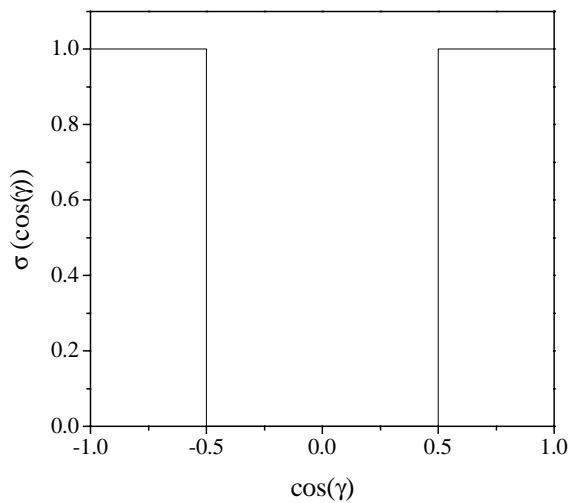

Figure 6.15 *Two-dimensional steric opacity function for CF^+. The angle γ and I are defined in Fig. 6.14 and in the text. Translational-to-internal energy transfer occurs ("reactive collision") for $\sigma = 1$.*

maximum translational-to-internal energy transfer occurs for internuclear alignment angles, γ, below 60° [24,144], where γ is the angle between the (local) surface normal and the F-C internuclear axis.

To compare the reaction probabilities for CF^+, CF_2^+ and CF_3^+ scattering from the PFPE, surface we apply the step-function model [157], which is schematically depicted in Fig. 6.14 for the CF^+ ion incident on a flat surface. In this model, the relative number of collisions N leading to "reactive" scattering is given by:

$$N = A[\int_0^{2\pi} \int_{-1}^1 \sigma(\gamma) dcos\gamma d\phi], \qquad (6.2)$$

where A is a constant which includes the total number of orientations of the incident molecule, $\sigma(\gamma)$ gives the reaction probability for certain internuclear axis alignment γ. Fig. 6.15 displays what angles of γ lead to internal energy uptake.

We now apply the step function model to the three fluorocarbon ions. Integrating over all orientations of the incident CF_3^+ ion (i.e. three-reactive sites) leads to a relative probability for "reactive" scattering of 0.75. For the CF^+ and CF_2^+ ions, each having two reactive sites, these values are determined to be 0.5, indicating that half of the collisions lead to "reactive" scattering and the other half to "non-reactive" scattering. In the case of the CF^+ ion, we take the F-end and C-end to be equally reactive (see Fig. 6.14 and Fig. 6.15). These relative probabilities indicate that 1.5 times more "reactive" collisions occur in the case of CF_3^+ scattering, than in CF^+ and CF_2^+ scattering, which was experimentally determined. In this comparative analysis, the actual area of the reactive zones seems unimportant, only the number of reactive sites is important, as long as $\gamma < 60°$. In reality, σ is a smooth function with γ [144].

The step function model oversimplifies the events that happen in reality, but it can serve as a starting point for the description of collision induced dissociation of small polyatomic ions at surfaces. In combination with classical trajectory calculations, it can provide new insights into the complicated events and processes occurring in polyatomic ion/surface collisions. Especially, the role of approach geometry [18,21], impulsive character of the collision [158,159] and orientational effects of the target molecules [148] can be explored.

6.5   Summary and conclusions

We have explored the dissociative scattering of CF^+, CF_2^+ and CF_3^+ from a perfluoropoly-ether across the hyperthermal incident energy range 50-to 220-eV. We studied the transfer of translational energy to the surface and to internal energy of the scattered fluorocarbon ions. In addition, C^+ ions were scattered from the PFPE surface to further examine the energy transfer to the PFPE molecules. The angular distributions of the fragment ions indicate scattering off individual groups of the liquid molecules; even for incoming angles as "small" as 55°, the parent ions were predominantly observed at outgoing angles of 80°. The effective surface mass increases linearly with increasing mass of the incident particle, which reveals that more atoms of the -CF_3 group participate in the interaction for incident molecules composed of more atoms.

For C^+ scattering the effective surface mass depends upon the total scattering angle; for a total scattering angle of 30°, the surface effective mass is given by the mass of a -CF group. For larger total scattering angles the effective surface mass decreases, revealing that high impact parameter collisions with the F-C group will tend to be more adiabatic than collisions at low impact parameters.

In contrast, for the polyatomic fluorocarbon ions we observe an increase of the surface effective mass going to larger scattering angles, which is explained by the fact that now the interaction occurs with a larger portion of the -CF_3 groups which are oriented perpendicular to the surface plane. Upon impact, for incoming angles of 70°, these groups more recoil easily in the direction of the C-C bond, decreasing the surface effective mass. These situations can be associated with small scattering angles of the fluorocarbon ions.

For all the three incident fluorocarbon ions the dissociation is governed by the impulsive collision. The experimental results reveal that more of the translational energy lost in the collision is transferred to internal energy in the case of CF_3^+ (19%) compared to CF_2^+ (14%) and CF^+ (13%) scattering. We have introduced a simple model which successfully describes the relative internal energy uptake probabilities for the CF^+, CF_2^+ and CF_3^+ ions. This model predicts that the incident CF_3^+ ion has more orientations favorable for internal energy uptake than the CF^+ and CF_2^+ ions; 1.5 times more "reactive" collisions occur in the case of CF_3^+ scattering.

References

1. J.M. Thomas and W.J. Thomas, Principle and Practice of Heterogeneous Catalysis (VCH Verlags-gesellschaft mbH), Germany, 1997.

2. D.P. Woodruff and T.A. Delchar, Modern Techniques of Surface Science- Second Edition (Cambridge University, 1994).

3. A. Zangwill, Physics at Surfaces (Cambridge University, 1988).

4. N. Herbots, O.C. Hellman, P. Ye, X. Wang and O. Vancauwenberghe, *Chemical reactions during thin-film synthesis by low-energy ions: Ion-beam oxidation (IBO) and ion-beam nitration (IBN) of semiconductor surfaces*, in Low Energy Ion-Surface Interactions, edited by J. W. Rabalais (Wiley, United Kingdom, 1994).

5. E. Murad, *Spacecraft interaction with atmospheric species in low earth orbit*, Journal of Spacecraft and Rockets 33 (1996), pages 131–136.

6. R.G. Cooks, T. Ast and MD.A. Mabud, *Collisions of polyatomic ions with surfaces*, International Journal of Mass Spectrometry and Ion Processes 100 (1990), pages 209; and references therein–265.

7. J.A. Barker and D.J. Auerbach, *Gas-surface interactions and dynamics; thermal energy atomic and molecular beam studies*, Surface Science Reports 4 (1984), pages 1–99.

8. S.T. Ceyer, *Dissociative chemisorption: Dynamics and mechanisms*, Annual Review of Physical Chemistry 39 (1988), pages 479–510.

9. A.W. Kleyn and T.C.M Horn, *Rainbow scattering from solid surfaces*, Physics Reports 199 (1991), pages 191–230.

10. S.R. Kasi, H. Kang, C.S. Sass and J.W. Rabalais, *Inelastic processes in low-energy ion-surface collisions*, Surface Science Reports 10 (1989), pages 1; and references therein–105.

11. H. Niehus, W. Heiland and E. Taglauer, *Low-energy ion scattering at surfaces*, Surface Science Reports 17 (1993), pages 213; and references therein–303.

12. J.F. van der Veen, *Ion beam crystallography of surfaces and interfaces*, Surface Science Reports 5 (1985), pages 199–288.

13. P. Sigmund, *Scaling laws governing the multiple scattering of diatomic molecules under Coulomb explosions* 46 (1992), pages 2596–2606.

14. K. Fukutani, M. Tsunoda, Y. Murata, K. Yamashita, H. Komaki and K. Kobayashi, *High-resolution depth analysis of hydrogen by a resonance nuclear reaction: a-Si/H/Si(001)*, Surface Science 283 (1993), pages 447–451.

15. P.H.F. Reijnen, P.J. van den Hoek, A.W. Kleyn, U. Imke and K.J. Snowdon, *The O_2-Ag(111) interaction studied by 100-3000 eV glancing incidence O_2^+ scattering*, Surface Science 221 (1989), pages 427–453.

16. J.W. Gadzuk and J.K. Nørskov, *Vibrational excitation, harpooning, and sticking in molecule-surface collisions*, Journal of Chemical Physics 81 (1984), pages 2828–2838.

17. P. Haochang, T.C.M. Horn and A.W. Kleyn, *Harpooning in surface scattering: O_2^- formation in collisions of O_2^+ from Ag(111)*, Physical Review Letters 57 (1986), pages 3035–3038.

18. P.J. van den Hoek and A.W. Kleyn, *Calculations of 1.eV–3.keV oxygen scattering from Ag(111) using ab initio pair potentials*, Journal of Chemical Physics 91 (1989), pages 4318–4329.

19. U. van Slooten, D.R. Anderson, A.W. Kleyn and E.A. Gislason, *Scattering of fast molecular hydrogen*

from Ag(111), Surface Science 274 (1992), pages 1–20.

20. U. van Slooten, E.J.J. Kirchner and A.W. Kleyn, *Classical trajectory study of fast H_2 from Ag(111)*, Surface Science 283 (1993), pages 27–35.

21. U. van Slooten and A.W. Kleyn, *Orientation dependence of dissociation in fast H_2-Ag(111) collisions*, Chemical Physics 177 (1993), pages 509–517.

22. J.S. Martin, B.T. Feranchak, J.R. Morris, J.N. Greeley and D.C. Jacobs, *Simplified classical trajectory model of dissociative scattering on surfaces: Role of incident vibrational and translational energies*, Journal of Physical Chemistry 100 (1996), pages 1689–1697.

23. B.H. Mahan, *Refined impulse approximation for the collisional excitation of the classical anharmonic oscillator*, Journal of Chemical Physics 52 (1970), pages 5221–5225.

24. J.N. Greeley, J.S. Martin, J.R. Morris and D.C. Jacobs, *The effect of internuclear-axis alignment on molecule/surface reactive scattering*, Surface Science 314 (1994), pages 97–106.

25. S. Dagan and A. Amirav, *High-efficiency surface-induced dissociation on a rhenium oxide surface*, Journal American Society for Mass Spectrometry 4 (1993), pages 869–873.

26. S.B. Wainhaus, J.A. Burroughs and L. Hanley, *Charge transfer during pyridine ion scattering off clean and oxygen modified Ni(111)*, Surface Science 344 (1995), pages 122–130.

27. V.H. Wysocki, J.L. Jones and J.-M. Ding, *Polyatomic ion/surface collisions at self-assembled monolayer films*, Journal American Society for Mass Spectrometry 113 (1991), pages 8969–8970.

28. M.R. Morris, D.E. Riederer, B.E. Winger, R.G. Cooks, T. Ast and C.E.D. Chidsey, *Ion/surface collisions at functionalized self-assembled monolayer surfaces*, International Journal of Mass Spectrometry and Ion Processes 122 (1992), pages 181–217.

29. A. Somogyi, T.E. Kane and V.H. Wysocki, *Reactions between doubly charged $[C_6H_6]^{2+}$ ions and self-assembled monolayer surfaces*, Organic Mass Spectrometry 28 (1993), pages 283–284.

30. T. Ast, D.E. Rieder Jr, S.A. Miller, .M Morris and R.G. Cooks, *Collisions of fluorcarbon ions at solid surfaces: electronic excitation, surface-induced dissociation and chemical sputtering*, Organic Mass Spectrometry 28 (1993), pages 1021–1033.

31. J de Maaijer-Gielbert, J.H.M. Beijersbergen, P.G. Kistemaker and T.L. Weeding, *Surface-induced dissociation of benzene on a PFPE liquid insulator in a time-of-flight mass spectrometer*, International Journal of Mass Spectrometry and Ion Processes 153 (1996), pages 119–128.

32. J. Los and J.J.C. Geerlings, *Charge exchange in atom-surface collisions*, Physics Reports 190 (1990), pages 133; and references therein–190.

33. B.H. Cooper and E.R. Behringer, *Scattering and charge transfer dynamics in low- and hyperthermal-energy alkali-ion-surface collisions*, in Low Energy Ion-Surface Interactions, edited by J. W. Rabalais (Wiley, United Kingdom, 1994).

34. P.G. Betrand and J.W. Rabalais, *Ion scattering and recoiling for elemental analysis and structure determination*, in Low Energy Ion-Surface Interactions, edited by J. W. Rabalais (Wiley, United Kingdom, 1994).

35. C.F.A Van Os, P.W. Van Amersfoort and J Los, *Negative ion formation at a barium surface exposed to an intense positive-hydrogen ion beam*, Journal of Applied Physics 64 (1988), pages 3863–3873.

36. K. Tsumori, W.R. Koppers, R.M.A. Heeren, M.F. Kadodwala, J.H.M Beijersbergen and A.W. Kleyn, *Large ion yields in hydrogen scattering from a graphite surface*, Journal of Applied Physics 81 (1997), pages 6390–6396.

37. M. Hou and M.T. Robinson, *Mechanisms for the reflection of light atoms from crystal surfaces at kilovolt energies*, Applied Physics 17 (1978), pages 295–301.

38. D.P. Jackson and W. Eckstein, *The scattering of keV H and He ions from tungsten and tungsten oxide*, Nuclear Instruments and Methods 194 (1982), pages 671–675.

39. W. Eckstein and J.P. Biersack, *reflection of low-energy hydrogen from solids*, Applied Physics A 38 (1985), pages 123–129.

40. R. Aratari and W. Eckstein, *Backscattering of atomic and molecular hydrogen from nickel and carbon*, Nuclear Instruments and Methods in Physics Research B 42 (1989), pages 11–18.

41. M Shi, J.W. Rabalais and V.A. Esaulov, *Neutralization and ionisation processes in the scattering of*

D^+, D_2^+ and D_3^+ on a Mg surface, Radiation Effects and Defects in Solids 109 (1989), pages 81–89.

42. H Muller, R Hausmann, H Brenten and V Kempter, *Electrons from intra- and interatomic auger processes in low-energy grazing collisions of H^+ and H_2^+ with W(110) patially covered by alkali atoms*, Surface Science 284 (1993), pages 129–.

43. U. van Slooten, W.R. Koppers, H.M. van Pinxteren, A.M.C. Moutinho, J.W.M. Frenken and A.W. Kleyn, *The adsorption of Ba on Ag(111)*, Journal of Physics: Condensed Matter 5 (1993), pages 5411–5428.

44. C. Höfner, A. Närmann and W. Heiland, *Trajectory calculations for H scattering at grazing angles from Ni(110) and Ni(111)*, Nuclear Instruments and Methods in Physics Research B 72 (1992), pages 227–233.

45. R.J. MacDonald, D.J. O'Connor, B.V King, Yaogan Shen and Gonjian Xu, *The scattering of low energy hydogen ions from surfaces*, Nuclear Instruments and Methods in Physics Research B 78 (1993), pages 56–62.

46. B.V. King, D.J. O'Conner and G. Xu, *Scattering of keV H^+ from Au(110) - comparison between experiment and simulation*, Radiation Effects and Defects in Solids 130 (1994), pages 293–300.

47. C. Auth, A.G. Borisov and H. Winter, *High fractions of negative ions in grazing scattering of fast oxygen atoms from a LiF(100) surface*, Physical Review Letters 75 (1995), pages 2292–2295.

48. H. Winter, A.G. Auth and A.G. Borisov, *Formation of negative ions in grazing scattering from a LiF(100) surface*, Nuclear Instruments and Methods in Physics Research B 115 (1996), pages 133–136.

49. M. Maasouz, L. Guillemot, S. Lacombe and V.A. Esaulov, *Electron capture processes on oxidized surfaces: H^- formation on Mg/O_2 and Al/O_2*, Physical Review Letters 77 (1996), pages 4265–4268.

50. A.D. Tenner, K.T. Gillen, T.C.M. Horn, J. Los and A.W. Kleyn, Surface Science 172 (1986), pages 90–.

51. A.D. Tenner, R.P. Saxon, K.T. Gillen, D.E. Harrison Jr., T.C.M. Horn and A.W. Kleyn, *Computer simulations and rainbow patterns of alkali ion scattering from metal surfaces*, Surface Science 172 (1986), pages 121–150.

52. C.A. Keller, C.A. DiRubio, G.A. Kimmel and B.H. Cooper, *Trajectory-dependent charge exchange in alkali ion scattering from a clean metal surface*, Physical Review Letters 75 (1995), pages 1654–1657.

53. G.E. Makhmetov, A.G. Borisov, D. Teillet-Billy and J.P. Gauyacq, *Resonant charge transfer in grazing atom-metal collisions: effect of the presence of steps on the surface*, Surface Science 366 (1996), pages L769–L774.

54. F. Wyputta, R. Zimny and H. Winter, *H^- formation in grazing collisions of fast protons with an Al(111) surface*, Nuclear Instruments and Methods in Physics Research B 58 (1991), pages 379–383.

55. A. Närmann, H. Derks, W. Heiland, R. Monreal, E Goldberg and F. Flores, *Crystallographic effects in charge exchange processes: He scattering from Ni(110)*, Surface Science 217 (1989), pages 255–266.

56. D.J. O'Connor, R.J. MacDonald, W. Eckstein and P.R. Higginbottom, *Surface structure analysis using low energy scattered and recoiling ions*, Nuclear Instruments and Methods in Physics Research B 13 (1986), pages 235–239.

57. U. van Slooten, O.M.N.D. Teodoro, A.W. Kleyn, J. Los, D. Teillet-Billy and J.P. Guayacq, *Negative ion formation in proton scattering from Ba/Ag(111)*, Chemical Physics 179 (1994), pages 227–240.

58. D. Teillet-Billy and J.P. Gauyacq, *Position and width of a negative-ion state in front of a surface - Formation of $C^-(^4s4)$ ions by electron capture*, Surface Science 239 (1990), pages 343–352.

59. W.R. Koppers, B. Berenbak, D. Vlachos, U. van Slooten and A.W. Kleyn, *H^- formation in proton (Ba)/Ag(111) collisions: effects of the surface structure*, Nuclear Instruments and Methods in Physics Research B 100 (1995), pages 417–422.

60. A. Bot, U. van Slooten, W.R. Koppers and A.W. Kleyn, *Surface diffusion during thin film annealing studied by XPS*, Surface Science 287 (1993), pages 901–906.

61. E.J.J. Kirchner, E.J. Baerends, U. van Slooten and A.W. Kleyn, *Relativistic effect on the interatomic platinum-oxygen potential and its consequences in high energy $O_2/Pt(111)$ scattering*, Journal of Chemical Physics 97 (1992), pages 3821–3830.

62. M.T. Robinson and I.M. Torrens, Physical Review B 9 (1974), pages 5008–.

63. D.L. Adler and B.H. Cooper, *Energy and angular distributions of 100- to 400-eV Na^+ scattered from Cu(110)*, Physical Review B 43 (1991), pages 3876–3892.

64. H.B. Nielsen and T.A. Delchar, *Fast He atom scattering from a tungsten (100) surface*, Surface Science 141 (1984), pages 487–499.

65. M.N. Yusuf and T.A. Delchar, *Angle-resolved fast atom scattering: He on clean Cu(111)*, Surface Science 182 (1987), pages 231–244.

66. U. van Slooten, *Excitation, dissociation and growth at surfaces*, PhD Thesis, University of Amsterdam (1993).

67. R.L. McEachern, D.M. Goodstein and B.H. Cooper, *Trajectory analysis of low-energy and hyperthermal ions scattered from Cu(110)*, Physical Review B 39 (1989), pages 10503–10513.

68. R. Lahaye, *Simulations of surface scattering*, PhD Thesis, Vrije Universiteit Amsterdam (1995).

69. R.J.W.E. Lahaye, S. Stolte, S. Holloway and A.W. Kleyn, *The scattering of Ar on Ag(111): A molecular dynamics study*, Surface Science 338 (1995), pages 169–182.

70. H.H. Andersen and J.F. Ziegler, *Hydrogen: stopping powers and ranges in all elements*, The Stopping and Ranges of Ions in Matter vol 1, edited by J. F. Ziegler (New York: Pergamon) (1977).

71. J.N.M. van Wunnik, J.J.C. Geerlings, E.H.A. Granneman and J Los, *The scattering of hydrogen from cesiated tungsten surfaces*, Surface Science 131 (1983), pages 17–33.

72. C. Höfner, A. Närmann and W. Heiland, *Energy loss spectra of H^+ and He^+ scattered off clean and K-covered Pd surfaces*, Nuclear Instruments and Methods in Physics Research B 93 (1994), pages 113–116.

73. A. Närmann, W. Heiland, R. Monreal, F. Flores and P.M. Echenique, *charge exchange and energy loss of particles interacting with surfaces*, Physical Review B 44 (1991), pages 2003–2018.

74. S. Hausman, C. Höfner, T. Schlathölter, H. Franke, A. Närmann and W. Heiland, *Energy-loss of light-ions scattered off Al(110) single crystal surfaces at low energies*, Nuclear Instruments and Methods in Physics Research B 115 (1996), pages 31–33.

75. G.M. Lamble and D.A. King, private communication (1994).

76. Q. Wu and L. Hanley, *Reactive scattering, sputtering, and dissociation of 32.eV pyridine ions colliding with clean and pyridine-covered Ag(111)*, Journal of Physical Chemistry 97 (1993), pages 2677–2685.

77. V.H. Wysocki, J. Ding, J.L. Jones, J.H. Callahan and F.L. King, *Surface-induced dissociation in tandem quadrupole mass spectrometers: a comparison of three designs*, Journal American Society for Mass Spectrometry 3 (1992), pages 27–32.

78. W. Heiland, U. Imke, S. Schubert and K.J. Snowdon, *Interaction of fast molecular ions with surfaces*, Nuclear Instruments and Methods in Physics Research B 27 (1987), pages 167–172.

79. K.J. Snowdon, R. Hentschke, A. Närmann and W. Heiland, *Auger and resonant neutralization of low energy ions near metal surfaces*, Surface Science 173 (1986), pages 581–592.

80. B. Willerding, W. Heiland and K.J. Snowdon, *Neutralization of fast molecular ions H_2^+ and N_2^+ at surfaces*, Physical Review Letters 53 (1984), pages 2031–2034.

81. H. Akazawa and Y. Murata, *Dissociative scattering of low energy N_2^+ ion beam on Pt(100)*, Surface Science 207 (1989), pages L971–L979.

82. J.S. Martin, J.N. Greeley, J.R. Morris, B.T. Feranchak and D.C. Jacobs, *Scattering state selected NO^+ on GaAs(110): The effect of translational and vibrational energy on NO^- and O^- product formation*, Journal of Chemical Physics 100 (1994), pages 6791–6812.

83. I.S. Bitensky and E.S. Parilis, *Highest rotational and vibrational excitation of swift diatomic molecules scattered by solid surface*, Surface Science 161 (1985), pages L565–L571.

84. K. Schmidt, H. Franke, T. Schlathölter, C. Höfner, A. Närmann and W. Heiland, *Scattering of swift molecules, N_2 and CO_2 from metal surfaces*, Surface Science 301 (1994), pages 326–336.

85. Y.G. Shen, L.J. Huang and W.M. Lau, *Interaction of molecular BF^+ and BF_2^+ ions with gold surfaces at low energies: neutralization, dissociation and deposition*, Journal of Vacuum Science and Technology A 11 (1993), pages 2099–2103.

86. H. Akazawa and Y. Murata, *Interaction of reactive ions with Pt(100). ii. Dissociative scattering of molecular ions near the threshold energy region*, Journal of Chemical Physics 92 (1990), pages 5560–5568.

87. H. Dispert and K. Lacmann, *Negative ion formation in collisions between potassium and fluoro- and chloromethanes: electron affinities and bond dissociation energies.*, International Journal of Mass Spectrometry and Ion Processes 28 (1978), pages 49–67.

88. K.K. Murray, D.G. Leopold, T.M. Miller and W.C. Lineberger, *Photoelectron spectroscopy of the halocarbene anions HCF^-, $HCCL^-$, $HCBr^-$, HCL^-, CF_2^-, CCL_2^-.*, Journal of Chemical Physics 89 (1988), pages 5442–5453.

89. Y. Xie and H.F. Schaefer III, *The electron affinity of CF*, Journal of Chemical Physics 101 (1994), pages 10191–10192.

90. H. Hotop and W.C. Lineberger, *Binding energies in atomic negative ions: Ii*, Journal of Physical and Chemical Reference Data 14 (1985), pages 731–742.

91. R.G.A.R. Maclagan, *A theoretical study of the ionisation potential and appearance potential of CF_3^+*, Journal of Molecular Structure (Theochem) 235 (1990), pages 21–24.

92. P. Haochang, P.H.F. Reijnen, T.C.M. Horn and A.W. Kleyn, *Harpooning in scattering of O_2^+ from Ag(111): dependence on initial beam energy and direction*, Radiation Effects and Defects in Solids 109 (1989), pages 41–46.

93. U. van Slooten, T.C.M. Horn and A.W. Kleyn, *Angular distributions and charge exchange in Na scattering fropm clean and Cs covered Ag(111)*, Surface Science 243 (1991), pages 12–22.

94. A. Amirav, M.J. Cardillo, P.L. Trevor, C. Lim and J.C. Tully, *Atom-surface scattering dynamics at hyperthermal energies*, Journal of Chemical Physics 87 (1987), pages 1796–1807.

95. R.D. Levine and R.B. Bernstein, Molecular Reaction Dynamics and Chemical Reactivity (Oxford University Press, Oxford, 1987).

96. H. Akazawa and Y. Murata, *Neutralization of very-low-energy ions on Pt(100)*, Physical Review Letters 61 (1988), pages 1218–1221.

97. B.E. Winger, H.-J. Laue, S.R. Horning, R.K. Julian, S.A. Lammert, D.E. Riederer and R.G. Cooks, *Hybrid BEEQ tandem mass spectrometer for the study of ion/surface collision processes*, Review of Scientific Instruments 63 (1992), pages 5613–5625.

98. P.J.A Ruttink, C.G. de Koster, J.H.M. Beijersbergen and T.L. Weeding, *Dissociation energies of the excited π^* and 3s Rydberg states of CF_3*, In Preparation (1997).

99. G.L. Gutsev, *A density functional investigation on the structure of the CF_n compounds, n= 1-5, and their singly charged anions*, Chemical Physics 163 (1992), pages 59–67.

100. J. Burgdorfer, P. Lerner and F.W. Meyer, *Above-surface neutralization of highly charged ions: The classical over-the-barrier model* 44 (1991), pages 5674–5685.

101. W. Heiland, *The interaction of molecular ions with surfaces*, in Low Energy Ion-Surface Interactions, edited by J. W. Rabalais (Wiley, United Kingdom, 1994).

102. Y.G. Shen, I. Bello and W.M. Lau, *Dissociative scattering of molecular BF^+ and BF_2^+ ions from Au surfaces*, Nuclear Instruments and Methods in Physics Research B 73 (1993), pages 35–40.

103. M. Vicanek, T. Schlathölter and W. Heiland, *Scattering of fast H_2 from Pd surfaces: classical trajectory simulations*, Nuclear Instruments and Methods in Physics Research B 115 (1996), pages 206–210.

104. M. Vicanek, T. Schlathölter and W. Heiland, *Molecule scattering from solid surfaces: Orientation and surface corrugation effects*, Nuclear Instruments and Methods in Physics Research B 125 (1997), pages 194–200.

105. P.H.F. Reijnen and A.W. Kleyn, *Negative ion formation in scattering of diatomic positive ions from Ag(111)*, Chemical Physics 139 (1989), pages 489–496.

106. A.W. Kleyn, *Dissociation in molecule-surface collisions*, Journal of Physics: Condensed Matter 4 (1992), pages 8375; and references therein–8394.

107. Y. Murata, *Interaction of very low energy molecular ions with metal surfaces*, in Unimolecular and Bimolecular Reaction Dynamics , edited C. Y. Ng, T. Baer and I. Powis (Wiley, United Kingdom, 1994).

108. D.C. Jacobs, *The role of internal energy and approach geometry in molecule/surface reactive scattering*, Journal of Physics: Condensed Matter 7 (1995), pages 1023; and references therein–1045.

109. MD.A. Mabud, M.J. Dekrey and R.G. Cooks, *Surface induced dissociation of molecular ions*, International Journal of Mass Spectrometry and Ion Processes 67 (1985), pages 285–294.

110. T. Pradeep, S.A. Miller, H.W. Rohrs, B. Feng and R.G. Cooks, *Surface structure of a liquid perfluoropolyether examined by reactive ion/surface scattering*, Materials Research Society Symposium Proceedings 380 (1995), pages 93–97.

111. M.E. King, G.M. Nathanson, M.A. Hanning-Lee and T.K. Minton, *Probing the microscopic corrugation of liquid surfaces with gas-liquid collisions*, Physical Review Letters 70 (1993), pages 1026–1029.

112. T. Pradeep, S.A. Miller and R.G. Cooks, *Surface-induced dissociation from a liquid surface*, Journal American Society for Mass Spectrometry 4 (1993), pages 769–773.

113. M.E. King, M.E. Saecker and G.M. Nathanson, *The thermal roughening of liquid surfaces and its effect on gas-liquid collisions*, Journal of Chemical Physics 101 (1994), pages 2539–2547.

114. T. Pradeep, *Chemical constitution of a perfluoropolyether liquid surface. A photoelectron spectroscopic study*, Chemical Physics Letters 243 (1995), pages 125–128.

115. S. Ramasamy and T. Pradeep, *Preferential molecular ordening at the surface of a perfluoropolyether revealed by x-ray photoelectron spectroscopy*, Journal of Chemical Physics 103 (1995), pages 485–486.

116. W.R. Koppers, J.H.M. Beijersbergen, K. Tsumori, T.L. Weeding, P.G. Kistemaker and A.W. Kleyn, *Dissociation of polyatomic ions at surfaces: The influence of mechanical and electronic energy transfer*, Physical Review B 53 (1996), pages 11207–11210.

117. W.R. Koppers, J.H.M. Beijersbergen, K. Tsumori, T.L. Weeding, P.G. Kistemaker and A.W. Kleyn, *Dissociative scattering of CF_3^+ from a barium covered Ag(111) surface*, Surface Science 357 (1996), pages 678–683.

118. S.A. Miller, D.E. Rieder Jr, W.R. Cooks, R.G. Cho, H.W. Lee and H. Kang, *Energy disposal and target effects in hyperthermal collisions of ferrocene molecular ions at surfaces*, Journal of Physical Chemistry 98 (1994), pages 245–251.

119. L.T. Tongson and C.B. Cooper, *Mass spectrometric study of the binary approximation in scattering of low energy ions from solid surfaces*, Surface Science 52 (1975), pages 263–269.

120. H. Niehus and E. Bauer, *Quantitative aspects of ion scattering spectroscopy(ISS)*, Surface Science 47 (1975), pages 222–233.

121. W. Heiland, H.G. Schäffler and E. Taglauer, *Energy distributions of low-energy noble gas ions backscattered from a single crystal nickel surface*, Surface Science 35 (1973), pages 381–392.

122. J.A. Burroughs, S.B. Wainhaus and L. Hanley, *Impulsive excitation of $Cr(CO)_6^+$ during surface-induced dissociation at organic monolayers*, Journal of Physical Chemistry 98 (1994), pages 10913–10919.

123. J.A. Burroughs, S.B. Wainhaus and L. Hanley, *Impulsive excitation of $FeCp_2^+$ $SiMe_3^+$ during surface-induced dissociation at organic monolayers*, Journal of Chemical Physics 103 (1995), pages 6706–6715.

124. H.M. Rosenstock, K. Drax, B.W. Steiner and J.H. Herron, *Energetics of gaseous ions*, Journal of Physical and Chemical Reference Data 6 (1977), pages –.

125. M.E. Bier, J.W. Amy, R.G. Cooks, J.E.P. Syka, P. Ceja and G. Stafford, *A tandem quadrupole mass spectrometer for the study of surface-induced dissociation*, International Journal of Mass Spectrometry and Ion Processes 77 (1987), pages 31–47.

126. K. Vekey, A. Somogyi and V.H. Wysocki, *Internal energy distribution of benzene molecular ions in surface-induced dissociation*, Journal of Mass Spectrometry 30 (1995), pages 212–217.

127. E. Uggerud and P.J. Derrick, *Theory of collisional activation of macromolecules. impulsive collisions of organic ions*, Journal of Physical Chemistry 95 (1991), pages 1430–1436.

128. H.J. Cooper, P.J. Derrick, H. Donald, B. Jenkins and E. Uggerud, *Comment on theory of collisional activation of macromolecules*, Journal of Physical Chemistry 97 (1993), pages 5443–5444.

129. Th. Lill, F. Lacher and I.V. Busman, H.-G.and Hertel, *Fusion and rainbow scattering of C_{60}^+ on*

crystalline fullerite films, Physical Review Letters 71 (1993), pages 3383–3386.

130. Th. Lill, H.-G. Busman, F. Lacher and I.V. Hertel, C_{60}^{+} *ions in collisions with crystalline surfaces: Kinematics, dynamics and rainbows*, International Journal of Modern Physics B 10 (1996), pages 11–57.

131. M. Aono and R. Souda, *Inelastic processes in ion scattering spectroscopy of solid surfaces*, Nuclear Instruments and Methods in Physics Research B 27 (1987), pages 55–64.

132. D.P. Masson, T.F. Hanisco, W.L. Nichols, C. Yan, A.C. Kummel and J.C. Tully, *Correlations between angular momentum orientation and exit velocity in gas-surface scattering: A probe of the dependence of collision dynamics on the position of impact*, Journal of Chemical Physics 101 (1994), pages 3341–3352.

133. P.J. van den Hoek, T.C.M. Horn and A.W. Kleyn, *Classical trajectories, harpooning and dissociation for O_2 scattering from Ag(111)*, Surface Science 198 (1988), pages L335–L345.

134. R.C. Weast (Ed.), *Handbook of Chemistry and Physics*, CRC Handbook of Chemistry and Physics, 75th edition, CRC Press, Boca Raton, Fl, 1994.

135. A.W. Kleyn, J. Los and E.A. Gislason, *Vibronic coupling at intersections of covalent and ionic states* 90 (1982), pages 1–71.

136. W.P.M. Maas and N.M.M. Nibbering, *Formation of doubly charged negative ions in the gas phase by collisionally-induced "ion pair" formation from singly charged negative ions*, International Journal of Mass Spectrometry and Ion Processes 88 (1989), pages 257–266.

137. Q. Wu and L. Hanley, *Pyridine ion collisions with pyridine-d_5 multilayers on Ag(111): New scattered ions and neutralization quenching*, Journal of Physical Chemistry 97 (1993), pages 8021–8025.

138. W.R. Koppers, J.H.M. Beijersbergen, T.L. Weeding, P.G. Kistemaker and A.W. Kleyn, *Dissociative scattering of polyatomic ions from a liquid surface: CF_3^{+} on a perfluoropolyether film*, To be published (1997).

139. M. Menzinger and L. Wålinn, *High intensity, low energy spread ion source for chemical accelerators*, Review of Scientific Instruments 40 (1969), pages 102–105.

140. L. Wålinn, *The colutron, a zero deflection isotope seperator*, Nuclear Instruments and Methods 27 (1964), pages 55–60.

141. D. McGilvery and R. Morrison, *Macsimion version 2.0*, Department of Chemistry, Monash University, Australia, 1991, MacSimion Version 2.0.

142. Air-Parts, Alphen aan den Rijn, The Netherlands.

143. M. Nakamura, M. Tsukada and M. Aono, *Interaction of low velocity rare-gas ions with a solid surface*, Surface Science 283 (1993), pages 46–51.

144. J.N. Greeley, J.S. Martin, J.R. Morris and D.C. Jacobs, *Scattering aligned NO^{+} on GaAs(110): The effect of internuclear-axis direction on NO^{-} and O^{-} product formation*, Journal of Chemical Physics 102 (1995), pages 4996–5011.

145. U. Heinzmann, S. Holloway, A.W Kleyn, R.E. Palmer and K.J. Snowdon, *Orientation in molecule-surface interactions*, Journal of Physics: Condensed Matter 8 (1996), pages 3245–3269.

146. S.A. Miller, H. Luo, X. Jiang, H.W. Rohrs and R.G. Cooks, *Ion/surface reactions, surface-induced dissociation and surface modification resulting from hyperthermal collisions of $OCNCS^{+}$, CH_3SiNCO^{+}, and CH_3SiNCS^{+} with a perfluorinated self-assembled monolayer surface*, International Journal of Mass Spectrometry and Ion Processes 160 (1997), pages 83–105.

147. S.B. Wainhaus, H. Lim, D.G. Schultz and L. Hanley, *Energy transfer and surface-induced dissociation for $SiMe_3^{+}$ scattering off clean and adsorbate covered metals*, Journal of Chemical Physics 106 (1997), pages 10329–10336.

148. D.G. Schultz, S.B. Wainhaus and L. Hanley, *Classical dynamics simulations of $SiMe_3^{+}$ ion-surface scattering*, Journal of Chemical Physics 106 (1997), pages 10337–10348.

149. M.G. Tenner, F.H. Geuzebroek, E.W. Kuipers, A.E. Wiskerke, A.W. Kleyn, S. Stolte and A. Namiki, *Orientation dependence of rotational excitation in NO scattering from Ag(111)*, Chemical Physics Letters 168 (1990), pages 45–50.

150. M.G. Tenner, E.W. Kuipers, W.Y. Langhout, A.W. Kleyn, G. Nicolasen and S. Stolte, *Molecular*

beam apparatus to study interactions of oriented NO and surfaces, Surface Science 236 (1990), pages 151–168.

151. F.H. Geuzebroek, A.E. Wiskerke, M.G. Tenner, A.W. Kleyn, S. Stolte and A. Namiki, *Rotational excitation of oriented molecules as a probe of molecule-surface interaction*, Journal of Chemical Physics 95 (1991), pages 8409–8421.

152. Müller. J. and H. Ågren, *Role of core hole state geometry in molecular electron spectroscopies*, in Molecular Ions Geometric and Electronic Structure, edited by J. Berkowitz and K,-J Groeneveld (Plenum Press, New York, 1983).

153. The geometrical configuration of the CF_2^+ ion has been determined by standard *Ab initio* self-consistent field molecular orbital calculations with the GAMESS system of programs [160]. For the geometry optimalization we used the spin unrestricted Hartree-Fock (UHF) formalism with the 63lg** basis set.

154. M.E. Saecker and G.M. Nathanson, *Collisions of protic and aprotic gases with a perfluorinated liquid*, Journal of Chemical Physics 100 (1994), pages 3999–4005.

155. J.G. Harris, *Liquid-vapor interfaces of alkane oligomers. structure and thermodynamics from molecular dynamics simulations of chemically realistic models*, Journal of Physical Chemistry 96 (1992), pages 5077–5086.

156. N.V. Richardson and N. Sheppard, *Normal modes at surfaces*, Vibrational spectroscopy of molecules at surfaces (Plenum Press), New York, 1987.

157. H. Ohoyama, H. Makita, T. Kasai and K. Kuwata, *Orientation dependence of the CF_3^* formation in collision energy transfer reactions: $CF_3Cl + Ar(^3P) \rightarrow CF_3^* + Cl + Ar$ and $CF_3Cl + Kr(^3P) \rightarrow CF_3^* + Br + Kr$*, Journal of Physical Chemistry 99 (1995), pages 5798–5801.

158. R.B. Gerber and R. Elber, *Centrifugal mechanism for molecular dissociation in high-energy collisions with solid surfaces*, Chemical Physics Letters 107 (1984), pages 141–144.

159. R.B. Gerber and A. Amirav, *Dynamics of dissociation and energy transfer in molecular collisions with solid surfaces*, Journal of Physical Chemistry 90 (1986), pages 4483–4491.

160. M.F. Guest and P. Sherwood, *Generalized Atomic and Molecular Structure System*, GAMESS Users's Guide and Reference Manual, Revision B.0 May 1992, Daresburry, UK (1992).

Summary

In this thesis, we present experiments on the scattering of positively charged ions from metal and liquid surfaces. Attention is focused on various aspects of ion-surface interactions such as charge transfer, the trajectories the ions follow in the ion/surface region and dissociation of incident polyatomic species through either charge transfer processes or impulsive collisions. A theme unifying this thesis is the way in which electronic and translational energy is (re)distributed during and after the ion-surface encounter.

Several positive ions, such as the atomic H^+ and C^+ ions and the polyatomic fluorocarbon ions CF^+, CF_2^+ and CF_3^+ are scattered off surfaces. The ions are created in an ion source and subsequently accelerated to the low incident energy regime between 50 to 1250 eV. The focusing of the ion beam is done with electrostatic lenses. A beam spot of 2 mm^2 on the target position can be attained. To ensure the surface is clean on an atomic scale, the experiments were performed under ultra-high vacuum (UHV) conditions. Scattered positive and negative ions are detected with a rotatable electrostatic energy analyzer. This allows energy and angular analysis of the scattered product ions, for a basic understanding of the processes occurring. The bulk of the experiments described in this thesis are concerned with polyatomic ion-surface scattering. We try to answers challenging questions such as: What are the important neutralization, dissociation and ionization mechanisms? How are the scattered particles spatially distributed? How is energy transferred to the surface and to internal energy of the ion? Where does the dissociation occur? What is the influence of the surface on the points listed above?

In chapter 2, the results of scattering a H^+ ion beam off a clean Ag(111) surface and a barium covered Ag(111) surface are shown. With help of classical trajectory calculations, the trajectories the hydrogen particles follow in the surface region are identified. The detected negatively charged particles can originate from many layers deep in the crystal. No trajectory dependence is observed in negative ion formation. Using the detection of H^-, the positions of the barium atoms on the Ag(111) surface can be determined. To our knowledge, this is the first time backscattered H^- ions are used in an ion beam crystallography study.

In chapter 3, the incident ion species is the polyatomic CF_3^+ ion. The dissociation (dynamics) of this tetra-atomic ion is explored when it is scattered from a clean and a barium covered Ag(111) surface. The results indicate that most of the CF_3^+ ions dissociate by electron transfer processes from the metal surface, before the incident positive ions reach the surface plane. This gives rise to a high yield of F^- ions. The complete dissociation of the CF_3^+ ion is possible at low (normal) incoming energies. The azimuthal orientation of the crystal has a large influence on the degree of dissociation which indicates the importance of direct momentum transfer. In this chapter we demonstrate for the first time the complete break-up of a low-energy tetra-atomic ion upon collision with a well defined solid surface.

An empirical dissociation model is proposed which explains the salient features of the data.

A remarkable difference in dissociation behaviour is observed when the collision surface is changed to an insulating liquid perfluoropolyether (PFPE). The results of CF_3^+ scattering from a PFPE surface are shown in chapter 4. The incident particles dissociate due to the impulsive collision with the surface. Dissociation by electron transfer processes, as was observed in scattering from metal surfaces (chapter 3), does not contribute. This is because of the high ionization potential of the PFPE surface. The degree of dissociation scales with the incident energy, the total scattering angle and the energy transferred in the collision. The energy transfer in the collision of the scattered parent ion indicates that they scatter off the -CF_3 groups of the PFPE molecules in single collisions. Approximately 19% of the energy that is lost in the collision is transferred to internal energy of the scattered ions. The dissociation event occurs unimolecularly in the gas phase after the scattering event. Furthermore, we demonstrate in that the translational energy loss ΔE that the parent ion has suffered in the collision, is the key parameter that determines the internal energy uptake.

The design and performance of a new low-energy ion beamline is described in chapter 5. The new beamline is capable of producing intense atomic and polyatomic ion beams in the incident ion range 10-to 1000-eV. At the sample position, currents between 10 and 100 nA are attained. In addition, sufficiently high mass resolution is achieved ($M/\Delta M=400$) to allow for the scattering of large polyatomic ions and their fragment ions.

With the new low-energy ion beamline, experiments have been performed on (fluoro)carbon ion (C^+, CF^+, CF_2^+ and CF_3^+) scattering from the PFPE surface in the hyperthermal incident energy range 50-to 220-eV. These experiments are described in chapter 6 of this thesis. A comparative study is carried out on energy transfer to the surface and to internal energy of the scattered ions. Surprisingly, the experimental results reveal that more of the translational energy lost in the collision is transferred to internal energy in the case of CF_3^+ (19%) than in CF_2^+ (14%) and CF^+ (13%) scattering. A simple model is introduced which predicts that the incident CF_3^+ ion has more orientations favorable for internal energy uptake than the CF^+ and CF_2^+ ions. The surface effective mass increases linearly with the number of atoms the fluorocarbon contains, giving information on the number of target atoms involved in the scattering event. This chapter represents the first detailed study on energy transfer to liquid surfaces in atomic and polyatomic ion scattering.

Samenvatting

Oppervlakken

Oppervlakken vormen de scheiding tussen de gassen in de lucht om ons heen en de vaste stoffen en vloeistoffen. De chemische samenstelling van deze oppervlakken kan erg verschillen van die in het materiaal. We zijn allemaal bekend met het zwart worden van zilveren theelepeltjes, het groen uitslaan van koperen munten en het roesten van ijzeren voorwerpen. In al deze gevallen reageren de gassen in de lucht met het oppervlak van de vaste stof en veranderen haar samenstelling. In een aantal gevallen vinden chemische reacties tussen gassen sneller plaats op een oppervlak dan in een gasmengsel; in sommige gevallen vinden ze zelfs alleen maar plaats op een oppervlak. We spreken dan van zogenaamde katalytische reacties. Deze reacties spelen een zeer belangrijke rol in de chemische industrieën, maar vinden ook hun toepassing in bijvoorbeeld de auto-katalysator, waar deze katalytische reacties worden gebruikt om schadelijke stoffen om te zetten in minder schadelijke. Vele eigenschappen van vaste stoffen, waaronder de eerder genoemde katalytische werking, worden bepaald door de buitenste paar atoomlagen, wat oppervlakken tot interessante studie-objecten maakt.

Dit proefschrift behandelt een aantal onderwerpen die we rekenen tot de chemische fysica. De wisselwerking tussen elektrisch geladen atomen en moleculen, ook wel ionen genoemd, en oppervlakken wordt onderzocht. De interesse voor dit onderwerp heeft te maken met de ontwikkeling van een experimentele techniek die gebaseerd is op de zogenaamde oppervlakte geïnduceerde fragmentatie. Met behulp van deze techniek is het mogelijk grote moleculen in kleinere fragmenten uiteen te laten vallen (dissociëren) door deze te laten botsen met een oppervlak. Vervolgens worden de massa's van deze fragmenten bepaald met zogenaamde massaspectrometrische technieken. Op deze manier kan men de structuren van grote moleculen onderzoeken. Tot nu toe zijn andere fragmentatie-technieken gebruikt, zoals botsingen met gasatomen of bundels elektronen. De fragmentatie door botsingen met oppervlakken is efficiënter, omdat het inkomende ion maar één keer botst met het oppervlak met een afbuighoek die instelbaar is. Dit is niet het geval in botsingen met gasatomen. Er zijn echter ook een paar nadelen verbonden aan het verstrooien van ionen aan metaaloppervlakken zoals neutralisatie, die de detectie bemoeilijkt omdat alleen elektrisch geladen deeltjes worden gedetecteerd. Daarnaast begrijpt men veel van de processen die optreden als moleculaire ionen aan oppervlakken worden verstrooid niet. In dit proefschrift willen we een antwoord vinden op een aantal intrigerende vragen, zoals: Wat zijn de belangrijke ladingoverdracht-processen en dissociatie-mechanismen? Hoe worden de deeltjes ruimtelijk verstrooid na de botsing? Hoe vindt energieoverdracht plaats naar het oppervlak en naar interne energie van het verstrooide deeltje? Wanneer vindt de dissociatie plaats: voor,

tijdens of na de botsing? En wat is de invloed van het soort oppervlak op de vragen die hierboven vermeld staan?

Het proefschrift

Dit proefschrift behandelt botsingen van positieve ionen met metaaloppervlakken en vloeistofoppervlakken. We bespreken een aantal verschillende aspecten van de wisselwerking, zoals de uitwisseling van lading (elektronen), de banen die de ionen volgen als ze van het oppervlak terugkaatsen en de dissociatie van geladen moleculen door uitwisseling van elektronen en/of door de harde botsing met de oppervlakteatomen. De centrale vraagstelling van dit proefschrift is de manier waarop elektronische en bewegingsenergie wordt (her)verdeeld tijdens en na de botsing van de ionen met het oppervlak.

We hebben gekozen voor een aantal verschillende systemen. Zo worden de atomaire waterstof (H^+) en koolstof (C^+) ionen en de moleculaire ionen koolstoffluoride (CF^+), koolstofdifluoride (CF_2^+) en koolstoftrifluoride (CF_3^+) verstrooid aan metaaloppervlakken en vloeistofoppervlakken. De ionen worden geproduceerd in een ionenbron en versneld naar energieën tussen 50 en 1250 eV. Voor het waterstof-ion komt dit overeen met snelheden tussen 350.000 en 1.800.000 km/h. De geladen deeltjes worden afgebogen en gefocusseerd met behulp van elektrostatische lenzen. Uiteindelijk bestrijkt de bundel ongeveer 2 mm^2 van het botsoppervlak. Om er zeker van te zijn dat het oppervlak "schoon" is, worden de experimenten uitgevoerd in een ultrahoog vacuüm (UHV) opstelling met een basisdruk van 1×10^{-10} mbar, een druk 10.000.000.000.000 keer zo laag als om ons heen. De terugverstrooide positief en negatief geladen ionen worden gedetecteerd met een zogenaamde roteerbare elektrostatische energie-analysator. Met behulp van deze detector kunnen we de energie en de hoek van de terugverstrooide ionen, wat ons helpt de processen te begrijpen die optreden tijdens de botsingen van de ionen met het oppervlak.

In hoofdstuk 2 bespreken we de resultaten van positieve waterstof-ionen die worden verstrooid aan een schoon zilveroppervlak (Ag) en een met barium (Ba) bedekt zilveroppervlak. We hebben de snelheden waarmee en de hoeken waaronder de negatief geladen terugverstrooide deeltjes (H^-) het oppervlak verlaten, gemeten. Het positief waterstof-ion is door de overdracht van twee elektronen uit het metaal negatief geladen geworden. Met behulp van klassieke baanberekeningen die we uitgevoerd hebben op een computer, kunnen de banen die de waterstof-deeltjes volgen tijdens de wisselwerking met het oppervlak worden geïdentificeerd. Het blijkt dat de deeltjes diep binnendringen in de vaste stof alvorens deze weer te verlaten. De ladingoverdracht processen die zich aan het oppervlak afspelen blijken niet af te hangen van de banen die de deeltjes hebben gevolgd. De ladingtoestand van de deeltjes wordt op enige afstand van het oppervlak bepaald. Met de detectie van de negatieve waterstof-ionen kunnen de posities van de barium atomen op het zilveroppervlak worden bepaald. Naar ons beste weten is dit de eerste keer dat terugverstrooide negatieve waterstof-ionen worden gebruikt in een structuur analyse.

In hoofdstuk 3 is het inkomende deeltje het CF_3^+ ion, die uit 1 koolstofatoom (C) en 3 fluoratomen (F) is opgebouwd. De dissociatie van dit vier-atomige deeltje is onderzocht wanneer het wordt verstrooid aan een schoon en een met barium bedekt zilveroppervlak. De experimentele resultaten laten zien dat de meerderheid van de CF_3^+ ionen uiteen vallen

door elektronen overdracht voordat het inkomende positieve ion het oppervlak bereikt heeft. Met onze detector worden voornamelijk negatief geladen fluoride-ionen (F^-) gedetecteerd. Het CF_3^+ ion dissociëert volkomen bij lage inkomende energieën. Het blijkt dat de ruwheid van het zilveroppervlak een grote invloed heeft op de mate van dissociatie. Bij ruwere oppervlakken verliest het CF_3^+ ion meer F-atomen door de botsing met het oppervlak. In dit hoofdstuk wordt voor de eerste keer het kompleet uit elkaar vallen van een laag-energetisch vier-atomig ion met een zeer goed gedefinieerd vaste stof oppervlak aangetoond.

We zien een opvallend ander dissociatie gedrag wanneer de CF_3^+ ionen botsen met een elektrisch niet-geleidende vloeistof ofwel een geperfluorineerde polyether (PFPE) waarvan het oppervlak uit -CF_3 groepen bestaat. De resultaten van deze studie zijn beschreven in hoofdstuk 4. Elektronenoverdracht is nu in belangrijke mate onderdrukt omdat het erg moeilijk is elektronen vrij te maken uit het PFPE-oppervlak. De inkomende deeltjes vallen nu uiteen als gevolg van de harde botsing met de oppervlakteatomen. De mate van dissociatie schaalt met de inkomende energie, de afbuighoek van het deeltje en de hoeveelheid bewegingsenergie die verloren gaat in de botsing. Het verlies in bewegingsenergie geeft tevens aan dat er een enkele botsing plaatsvindt tussen het inkomende CF_3^+ ion en een -CF_3 groep van de PFPE. Ongeveer 19% van de bewegingsenergie die verloren gaat in de botsing, wordt overgedragen naar de interne energie van de verstrooide ionen. De dissociatie zelf vindt plaats in de gasfase, nadat de botsing heeft plaats gevonden. We laten bovendien zien dat het energieverlies in de botsing de essentiële factor is die bepaalt hoeveel interne energie er door het inkomende deeltje wordt opgenomen.

Het ontwerp en functioneren van een laag-energetische ionenbundellijn wordt beschreven in hoofdstuk 5. Met dit nieuw gebouwde apparaat is het mogelijk ionenbundels te maken die bestaan uit atomaire ionen, dan wel moleculaire ionen, met bewegingsenergieën variërend van 10 tot 1000 eV. Op het oppervlak worden ionenstromen gemeten tussen 10 en 100 nA; stromen 100 miljoen keer zo klein als er door een gloeidraadje van een gewone gloeilamp worden gestuurd. Met de nieuwe opstelling is het mogelijk moleculaire ionen en hun fragmenten aan oppervlakken te verstrooien in het lage energie gebied.

Met de nieuwe ionenbundellijn zijn (koolstof)fluoride ionen (C^+, CF^+, CF_2^+ en CF_3^+) verstrooid aan het eerdergenoemde PFPE-oppervlak. De inkomende energieën zijn gevarieerd tussen 50 en 220 eV. Dit zijn snelheden tussen 40.000 en 200.000 km/h. De experimenten zijn beschreven in hoofdstuk 6. We hebben een vergelijkende studie uitgevoerd naar de overdracht van bewegingsenergie naar het oppervlak en naar interne energie van de verstrooide deeltjes. De experimentele resultaten laten zien dat veel meer van het energieverlies in de botsing naar interne energie wordt overgedragen in het geval van het CF_3^+ ion (19%) dan in het geval van de CF_2^+ (14%) en CF^+ (13%) ionen. We hebben een model opgesteld dat laat zien dat het inkomende CF_3^+ ion meer oriëntaties heeft die geschikt zijn voor interne energieopname dan de CF_2^+ en CF^+ ionen. De experimentele resultaten wijzen bovendien uit dat meer atomen van het PFPE-oppervlak deelnemen aan de interactie wanneer het aantal atomen waaruit de koolstoffluoride ionen zijn opgebouwd, toeneemt. Dit hoofdstuk vertegenwoordigt de eerste gedetailleerde studie van de energieoverdracht van atomaire en moleculaire ionen naar vloeistofoppervlakken.

Nawoord

Vele mensen hebben een bijdrage geleverd aan het tot stand komen van dit proefschrift. Ik zou ze op deze wijze allemaal hartelijk willen bedanken. Een aantal van hen zou ik graag even bij naam willen noemen.

In de eerste plaats wil ik de mensen bedanken die het dichtst bij mij staan. Mijn vader, moeder en mijn zusje Ingrid wil ik graag danken voor de manier waarop ze mij gestimuleerd hebben om mijn studie te volgen. Doutzen wil ik graag bedanken voor al haar steun, geduld en vertrouwen de afgelopen jaren. Met haar erbij is het een stuk leuker geweest.

Dank ben ik ook verschuldigd aan mijn promotor Aart Kleyn. De vrijheid die hij mij heeft gegeven in mijn onderzoek en zijn enthousiasme bij het zien van nieuwe resultaten resulteerde in een atmosfeer waar ik mij erg prettig bij heb gevoeld. Tina Weeding, co-promotor, wil ik hartelijk bedanken voor de enthousiaste wijze waarop ze telkens mijn schrijfselen heeft gecorrigeerd en het geduld waarmee ze steeds weer het 'adjective' een paar plaatsen in een zin wist te verplaatsen. Joop Los wil ik hartelijk bedanken voor de interesse die hij heeft getoond in het vloeistofwerk. De stimulerende discussies die hieruit voortkwamen zou ik niet hebben willen missen.

Udo van Slooten en Age Raukema kan ik als mijn directe experimentele opvoeders beschouwen. Zij hebben veel bijgedragen aan het werkplezier dat ik heb gehad tijdens hun verblijf op het lab en daarna. Jaap Beijersbergen heeft in de korte tijd dat ik met hem heb samengewerkt een grote invloed gehad op de inhoud van dit proefschrift. Ik ben niet meer los gekomen van het CF_3^+ ion.

During the last 4 years, several foreign guests have been working at the MOBI apparatus. Dimitrios Vlachos, Katsyuhoshi Tsumori, João Lourenço, David Conceiçao and Michael Gleeson. I would like to thank them for the very nice co-orporation, the huge dedication and our nice outings in Amsterdam. I hope we keep in touch.

De verhuizing van het apparaat MOBI in het begin van mijn promotie heeft veel voeten in aarde gehad. Iwan Snel, Michael de Wilde, Henk Timmer, Huub Kersten en André Dijkslag wil ik bedanken voor hun aandeel in het klaren van deze klus. De bouw van de nieuwe bundellijn aan het eind van mijn promotie was ook een zeer arbeidsintensieve klus waar veel mensen bij betrokken waren. Herman Ficke en Evert de Haas bedankt voor de mooie werktekeningen. Wim Brouwer, Jan van der Linden, Henk Neerings, Hildebrand Voort en Wim Barsingerhorn hebben de tekeningen omgezet in een mooie roestvrijstalen constructie. Ook hebben ze vele andere klussen uitgevoerd voor MOBI. Idsart Attema en Paul van Deenen zijn verantwoordelijk voor de mooie electronicakastjes, waarvoor mijn hartelijke dank. Hans ter Horst, Henk Dekker, Jan van Elst en Marco Wijnberg stonden altijd klaar bij het oplossen van electronica & informatica probleempjes. René Koper heeft zeer vakkundig mooie gladde kristallen gemaakt. René Maatman stond altijd klaar voor

een spoedbestelling naar de andere kant van de oceaan. Met Henk Sodenkamp in de buurt verdwenen alle kopieerproblemen als sneeuw voor de zon. Ook wil ik hem hartelijk bedanken voor de leuke groepsfoto op de achterkant van het proefschrift.

Frans Giskes heeft mij enorm geholpen met de bouw van een nieuwe detector en de nieuwe bundellijn. Met hem was het prettig samenwerken en zonder zijn grote inzet en handigheid was dit boekje ongetwijfeld een stuk dunner geweest. Hetzelfde geldt voor Richard Schaafsma. Zijn inzet bij de verhuizing en prompte acties als een van de "kastjes" het weer eens had begegeven heb ik zeer gewaardeerd. Bart Berenbak heeft in het kader van zijn doctoraalscriptie een tijdje bij MOBI doorgebracht en heeft heel wat gebouwd, gemeten en klassieke baanberekeningen gedaan. Ik wil alle andere groepsleden van de Moleculaire Bundels groep van Amolf bedanken voor de goede samenwerking en de prettige werksfeer. Eric Kirchner, Arjen Bot, Paul Dorlandt, Rob Lahaye, Arjan Wiskerke, Ruud Dirksen, Hans Jenniskens, Janine de Maaijer, Bert van Lierop, Malcolm Kadodwala, David Butler, Wouter van Essenberg, Bern Riedmüller, Dimitrios Papageorgopoulos, Laurent Phillipe en Martijn Verwoest bedankt!

Met Gerard van Rooij en António Paiva heb ik menig uurtje op de squashbaan doorgebracht. Samen met hen en anderen van de massaspectrometrie groep was het ook leuk een biertje drinken in "Brouwerij het IJ" en na achten ergens verderop in de stad.

De interesse van Luc, John en Olof in de dingen die ik op het lab uitspook heb ik zeer fijn gevonden. Ze hadden altijd een luisterend oor als de dingen niet zo liepen als ik wilde.

Maarten Bakker en zijn "reclame-team" bestaande uit Herbert van Hoogdalem, Oof Verschuren en Naïm Niebuur wil ik graag bedanken voor de prachtige voorkant en schitterende uitnodigingen. Wat als iets heel onschuldigs begon is uitgegroeid tot een heuse reclamecampagne. Gelukkig hebben we onze hoofden niet gestoten.